

Chemistry, Physical Chemistry, and Uses of Molecular Fluorocarbon—Hydrocarbon Diblocks, Triblocks, and Related Compounds—Unique “Apolar” Components for Self-Assembled Colloid and Interface Engineering

Marie Pierre Krafft^{*,†} and Jean G. Riess^{*,‡}

Université de Strasbourg, Institut Charles Sadron (SOFFT-CNRS), 23 rue du Loess, 67034 Cedex, Strasbourg, France, and Harangoutte-les-Roses, 68160 Ste-Croix-aux-Mines, France

Received July 12, 2005

Contents

1. Scope	1715	5.1. Background and Terminology	1734
2. Introduction: Yoking Together Two Antipathetic Moieties	1716	5.2. Thermal Characterization of (<i>F</i> -Alkyl)alkane Diblocks—Phase Transitions	1735
2.1. <i>F</i> -Alkyl versus <i>H</i> -Alkyl Chains	1716	5.2.1. Melting Transition	1735
2.2. (<i>F</i> -Alkyl)alkyl Diblocks: Primitive, yet Amphiphilic, Amphisteric, and Amphidynamic	1718	5.2.2. Solid State Transitions	1736
3. Synthesis of <i>F</i> -Alkyl/Alkyl Diblocks, Triblocks, and Their Precursors	1719	5.3. Solid State Structures of (<i>F</i> -Alkyl)alkyl Diblocks—Liquid Crystal Behavior	1736
3.1. Principles	1719	5.3.1. The <i>F12Hm</i> Series	1737
3.2. (<i>F</i> -Alkyl)alkanes, (<i>F</i> -Alkyl)alkenes, and Related Diblocks	1720	5.3.2. The <i>F10Hm</i> Series	1741
3.2.1. Linear <i>F</i> -Alkyl/ <i>H</i> -Alkyl Diblocks	1720	5.3.3. The <i>F8Hm</i> Series	1745
3.2.2. Unsaturated Diblocks	1721	5.3.4. Brominated and Iodinated (<i>F</i> -Alkyl)alkanes and Further Diblocks	1745
3.2.3. Branched Diblocks	1722	5.3.5. Branched <i>FnHm</i> Diblocks	1746
3.2.4. Diblocks with Heteroatoms	1723	5.4. Solid State Behavior of <i>FnHmFn</i> Triblocks and Multiblocks	1747
3.2.5. Diblocks with Heavy Halogens	1724	5.4.1. Triblocks with <i>F</i> -Alkyl and Alkyl (Aryl) Blocks	1747
3.3. Triblocks and Multiblocks	1724	5.4.2. Multiblocks and Polyphilic Mesogens	1747
3.3.1. <i>FnHmFn</i> Triblocks	1724	5.5. Some Conclusions about the “Solid” State Behavior of <i>F</i> -Alkyl/ <i>H</i> -Alkyl Diblocks and Multiblocks	1748
3.3.2. <i>HmFnHm</i> Triblocks	1725	5.5.1. Thermal Behavior	1748
3.3.3. Star-Shaped Triblocks	1725	5.5.2. Liquid Crystal Behavior— <i>F</i> -Alkyl Blocks as Smectogens	1748
3.3.4. Multiblocks and Polyaffine Compounds	1726	5.5.3. Complexity/Variability/Uncertainty	1749
4. Basic Properties of (<i>F</i> -Alkyl)alkyl Diblocks	1726	5.5.4. Triblocks	1749
4.1. The “Polarity” Issue—“Apolar”, yet Dipolar	1726	5.5.5. Some Open Questions	1749
4.2. Surfactant Properties	1727	6. The Gaseous and Liquid States	1750
4.2.1. Surfactant Effects of <i>FnHm</i> Diblocks at Interfaces with Air, Fluorocarbons, and Hydrocarbons	1728	6.1. Diblock Gases and Liquids	1750
4.2.2. Cosurfactant Effects	1730	6.2. Surface Crystallization of Liquid Diblocks	1750
4.3. Solubility Properties	1730	7. Diblock Aggregation in Solutions—Micelles and Fibrous Gels	1751
4.3.1. Solubility of Diblocks in Fluorocarbons, Hydrocarbons, and Other Diblocks	1730	7.1. Aggregation (Micelle Formation) in Solution	1751
4.3.2. Solubility of Diblocks in Carbon Dioxide	1731	7.1.1. In Fluorocarbons	1751
4.3.3. Solubility of Diblocks in Polar Media	1731	7.1.2. In Hydrocarbons	1752
4.3.4. Gas Solubilities	1731	7.1.3. In Mixed Solvents	1753
4.3.5. Solubility of Polar Substances in Diblocks	1732	7.1.4. In Supercritical Carbon Dioxide	1753
4.4. Propensity to Self-Assemble and Promote Ordering and Micro- and Nanocompartmentation in Colloids and at Interfaces	1733	7.1.5. Inclusion in β -Cyclodextrin	1753
5. Solid State: Structural Transitions and Liquid Crystal Behavior	1734	7.2. Gels	1753
		8. Diblocks at Interfaces—Adsorbed Films and Surface Self-Assemblies	1754
		8.1. Gibbs Films or Self-Adsorbed Surface Films	1755
		8.2. Langmuir Monolayers and Related Thin Films	1757
		8.2.1. Diblocks at the Air/Water Interface—Langmuir Film Stability	1757

* Correspondence: krafft@ics.u-strasbg.fr and jriess@allp.com.

[†] Université de Strasbourg.

[‡] Harangoutte-les-Roses.

8.2.2.	Diblocks at a Water/Air Interface—Electric Properties of Langmuir Monolayers	1759
8.2.3.	Diblocks at an Air/Water Interface—Film Structure and Molecular Orientation	1759
8.2.4.	Langmuir–Blodgett and Other Supported Films	1761
8.2.5.	Langmuir Monolayers of Mixtures of Diblocks with Other Compounds	1762
8.2.6.	Monolayers in Contact with Diblock Gases	1762
8.2.7.	Black Lipid Membranes	1763
8.3.	Patterned Surface Films—Surface Micelles	1763
8.3.1.	Characterization of Surface Micelles of Diblocks after Transfer of a Langmuir Monolayer onto Solid Supports	1763
8.3.2.	Direct Observation of <i>FnHm</i> Micelles on the Surface of Water	1767
8.3.3.	Surface Micelles of Diblocks Deposited on Solid Supports from Solutions in Supercritical Carbon Dioxide	1767
8.3.4.	Surface Micelles from Mixtures of Diblocks with Other Amphiphiles	1768
8.3.5.	Surface Micelle Formation: an Inherent Behavior of <i>FnHm</i> Diblocks	1768
8.4.	Diblock-Induced, Pressure-Controlled Film Dynamics	1768
9.	Diblocks at Interfaces—Discrete Dispersed Particles	1770
9.1.	Bilayer Membranes—Fluorinated Vesicles	1770
9.1.1.	Preparation and Stability	1771
9.1.2.	Structural Studies	1772
9.1.3.	Permeability—Encapsulation Stability	1773
9.1.4.	Vesicle Fusion	1774
9.1.5.	Behavior in Biological Media	1774
9.2.	Gas Bubble Dispersions and Foams	1775
9.3.	Fluorocarbon-in-Water Emulsions	1775
9.3.1.	Stabilization and Particle Size Control	1775
9.3.2.	Mechanism of Diblock-Induced Emulsion Stabilization	1777
9.4.	Other Emulsions	1779
9.4.1.	Microemulsions	1779
9.4.2.	“Apolar” Hydrocarbon-in-Fluorocarbon Emulsions	1779
9.4.3.	Reverse Emulsions and Multiple Emulsions	1779
10.	Application Potential	1779
10.1.	Research Tools	1780
10.2.	Biomedical	1781
10.2.1.	Biological Characteristics	1781
10.2.2.	Oxygen Carriers	1783
10.2.3.	Ophthalmologic Uses	1784
10.2.4.	Lung Surfactant Replacement Preparations	1784
10.2.5.	Drug Delivery Systems	1785
10.2.6.	Contrast Agents for Diagnostic	1785
10.3.	Materials Science	1785
11.	Abbreviations	1786
12.	Acknowledgments	1787
13.	References	1787



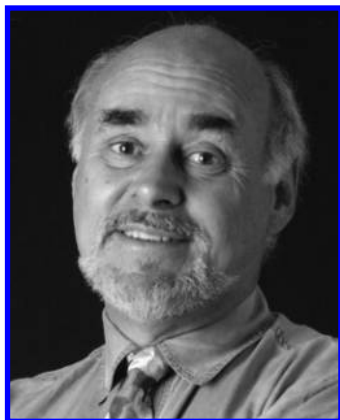
Marie Pierre Krafft is Director of Research at the University of Strasbourg, France (Institut Charles Sadron, Centre National de la Recherche Scientifique). She received her Ph.D. in chemistry from the University of Nice (1989). After postdoctoral work in Japan (Nagoya University) and in a Californian startup, she became in charge of a research team at the Laboratoire de Chimie Moléculaire in Nice. In 1997, she joined the Institut Charles Sadron, where she is now a research group leader. She focuses on the synthesis, investigation, and applications of highly fluorinated compounds, in particular amphiphiles, as components of functional self-assembled systems. Her present research includes the engineering and study of multicompartimented micro- and nano-objects, with nanocompartmentation being induced by fluorinated chains in organized self-assemblies such as monolayers, surface micelles, vesicles, tubules, microbubbles, and emulsions. The potential of such systems for biomedical applications (lung surfactant, tissue oxygenation, cell adhesion control, bioartificial pancreas, diagnosis) and in material sciences (nanopatterned surfaces) is also being explored. Dr. Krafft has published 85 articles, including 4 book chapters and 10 invited reviews. She holds 9 patents and has given numerous lectures. She sits on the Committees of the Nanosciences Program of the French National Research Agency (ANR), Nanomaterials and Health Initiative of the Pôle Matériaux et Nanosciences d'Alsace (PMNA), of the French Division of Physical Chemistry, of the International Blood Substitutes Symposia, and of the French Network of Fluorine Chemistry. She coedits the Surfactant Section of *Current Opinion in Colloid and Interface Sciences* and is on the Editorial Board of several journals.

perhydroalkyl chain (*H*-chain, C_mH_{2m+1}) (e.g., $C_2F_5C_2H_5$, not the isomeric $CHF_2CF_2CH_2CFH_2$). [The IUPAC-authorized, *italicized* prefix symbol *F*-, meaning perfluoro (as in *F*-alkyl = perfluoroalkyl), will, by extension, be used to designate entities (e.g., *F*-chains, *F*-amphiphiles, and *F*-colloids) that comprise highly fluorinated moieties or fluorocarbon (*FC*) phases, responsible for significant effects, different from those found for hydrocarbon (*HC*) analogues. Mirroring this notation, the prefix *H*-, as in *H*-alkyl, will be used for unambiguous designation of *HC* counterparts. In order to avoid any possible confusion, italics will also be used systematically to distinguish codes for moieties (e.g., $F_4 = C_4F_9$, $H_m = C_mH_{2m+1}$) from symbols for the atoms F and H within formulas (e.g., $F_4CH=CHH_m$ represents $C_4F_9-CH=CHC_mH_{2m+1}$)].

The compounds reviewed here are typically represented by the (*F*-alkyl)alkanes $C_nF_{2n+1}C_mH_{2m+1}$ (or *F*-alkyl/*H*-alkyl diblocks, *FnHm*). Characteristically, *FnHm* diblocks are devoid of hydrophilic polar function. The connection between the *F*- and *H*-chains is usually a C–C single bond, but it can occasionally be a heteroatom. Heteroatoms are sometimes also present within one or the other chain. Unsaturated *H*-chains are often encountered. *F*- and *H*-chains with less than two carbon atoms will generally not be considered, unless for context, nor will (multi)block copolymers with molecular weights (MW) exceeding about one thousand. Diblocks with branched chains are included, but usually not

1. Scope

The semifluorinated molecular diblock compounds considered here consist primarily of covalent assemblages of a linear *perfluoroalkyl* chain (*F*-chain, C_nF_{2n+1}) and a linear



First trained as a chemical engineer, Jean Riess received his Doctorat-ès-Sciences degree from the University of Strasbourg, with his mentor being Prof. Guy Ourisson. He then spent 2 years with Prof. John Van Wazer at Monsanto's Central Research Department in Saint-Louis, MO, learning some phosphorus and transition metal chemistry. In 1968, he became a Professor at the University of Nice, France, where he founded, directed, and eventually became the honorary director of the Unité de Chimie Moléculaire (associated with the Centre National de la Recherche Scientifique). Subsequently, Prof. Riess joined a Californian start-up as a VP of Research and Development and eventually retired in France as a consultant. His research successively involved organic and inorganic phosphorus chemistry, transition metal chemistry, organometallics, and eventually perfluorochemicals. His present interests are in fluorocarbons, fluorinated amphiphiles, their colloidal chemistry, and biomedical uses, including emulsions for in vivo oxygen delivery (the so-called "blood substitutes"), fluorocarbon-based contrast agents, fluorinated self-assemblies, and drug delivery systems. Prof. Riess has published about 380 papers and filed some 25 patents. He has served on numerous councils and committees, and has chaired or cochaired international conferences on phosphorus chemistry and blood substitutes. He has also worked with the Stockholm Peace Research Institute and the Pugwash Conferences on chemical weapon control. He has won awards from the French Academy of Sciences, French Chemical Society, Alexander von Humboldt Stiftung, City of Nice, Controlled Release Society, as well as Alliance's first Distinguished Contribution Award. His latest award is a 2008 Grand Prix from the French Académie des Sciences. He also held a Research Associate position at the University of California, San Diego, and sits on the Board of Directors of Alliance Pharmaceutical Corp.

those with cyclic, polycyclic, or aromatic blocks. Iodinated diblocks are included, in particular because they constitute the most frequently encountered starting materials or synthetic intermediates. The presence of heavy halogens can also be desirable, such as for conferring radiopacity or other properties to the molecule. Related linear triblocks (e.g., $C_nF_{2n+1}C_mH_{2m}C_nF_{2n+1}$, F_nHmF_n or $C_mH_{2m+1}C_nF_{2n}C_mH_{2m+1}$, $HmFnHm'$) and multiblocks will also be considered. Table 1 provides typical examples of the compounds discussed in this review. Literature coverage is until mid 2008.

Investigation of *F*-alkyl/*H*-alkyl diblock molecules and of supramolecular self-assemblies and colloidal systems involving such components has lately been very active. The studies aim at advancing our basic understanding of amphiphilic behavior, multiblock copolymer design, and self-assembled constructs involving fluorophobic effects. Many unusual features have been reported in these areas. New (self)-organized films and membranes, discrete objects, and interfaces have been obtained, and novel applications have been explored in the medical area, materials science, and other fields. In particular, *FnHm* diblocks provide unique tools and components for the engineering of compartmented micro- and nanophase molecular constructs that display specific surface patterns and confinement zones, useful as templates, reservoirs, carriers, and micro- and nanoreactors.

The purpose of this review is to collect and discuss the information available on the multiple facets, including synthesis, structure, properties, and potential uses, of *FnHm* diblocks and related compounds, and of self-assembled colloids and interfaces involving such compounds.

2. Introduction: Yoking Together Two Antipathetic Moieties

Although the basis for the radical-catalyzed synthesis of essentially any (*F*-alkyl)alkane or alkene or their immediate precursors had been laid much earlier,^{1–5} investigation of their structure and specific properties was only initiated in the 1980s.^{6,7} These studies have developed independently with two distinct purposes in mind: the design of advanced functional polymers and the quest for new types of liquid crystals.

At IBM (San José, CA), molecular *FnHm* diblocks were investigated as model molecules, the knowledge of which was expected to help predict the structure and properties of their infinite-chain macromolecular analogues.⁶ The goal was to design copolymers that would have the high thermal stability and the mechanical and dielectrical properties of poly(tetrafluoroethylene), while maintaining the processability of poly(ethylene). In the same time frame, a group at the Institut Charles Sadron (Strasbourg, France) was searching for mesogen properties in compounds that did not feature the traditional diphenyl-type mesogenic moieties and discovered that the amphiphilic *F10H10* diblock had liquid crystalline behavior.⁷ From then on, research on *F*-alkyl/alkyl diblock compounds expanded in multiple directions, including determination of phase transitions, phase structure, and phase transition mechanisms; assessment of adsorption and aggregation behavior in solution; interfacial film and membrane formation; the determination of structure and properties; the design of a wealth of self-assembled colloidal systems; and the exploration of their potential applications.

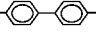
2.1. *F*-Alkyl versus *H*-Alkyl Chains

The unique properties of *FnHm* diblocks are essentially determined by the forced (covalent) pairing of "antipathetic" (or "amphipatic") *F*- and *H*-chains, resulting in an amphiphilic molecule.

The attributes of the element fluorine that determine the specific characteristics of *F*-chains include a combination of high ionization potential, extreme electronegativity, and larger size than hydrogen, comparable to that of oxygen, yet with lesser polarizability.

F-chains differ from *H*-chains in several important ways.^{8–14} The larger van der Waals radius of the fluorine atom as compared to hydrogen (1.47 vs 1.20 Å)¹⁵ entails mean volumes of the CF_2 and CF_3 groups estimated as 38 Å³ and 92 Å³, as compared to 27 Å³ and 54 Å³ for CH_2 and CH_3 , respectively. The CF_3 group is actually comparable in size to or even larger than an isopropyl group $CH(CH_3)_2$. *F*-chains are much bulkier than *H*-chains, with cross sections in the 27–30 Å² range for the former and 18–21 Å² for the latter, with the exact value depending on the packing situation. For example, a molecular area of ~27.6 Å² has been found for the hexagonally close-packed, surface normal-aligned surface-frozen monolayer of *F12H8* and *F12H14* (and ~28.5 Å² for the more disordered *F12H19*)¹⁶ as compared to 18.7 Å² in the crystal phases and ~19.7 Å² in the rotator phases of bulk *n*-alkanes.¹⁷ Molecular areas of 29.6 and 28.6 Å² were

Table 1. Examples of Common and Less Common *F*-Alkyl/*H*-Alkyl Diblocks, Triblocks, Their Precursors, and Related Compounds Considered in This Review (All Chains Linear, Unless Specified Otherwise; *E*, *Z* Isomers Sometimes Separated; See Section III for References)

$C_nF_{2n+1}C_mH_{2m+1}$ (<i>FnHm</i>)	$C_nF_{2n+1}XC_mH_{2m+1}$ ($X = O, S, S-S; FnXHm$)
$C_nF_{2n+1}CH=CH_2$	$C_nF_{2n+1}(CH_2)_mCH=CH_2$ $C_nF_{2n+1}CH=CHC_mH_{2m+1}$
$C_nF_{2n+1}CH_2CH=CHC_mH_{2m+1}$	$C_nF_{2n+1}CH=CH(CH_2)_mCH=CH_2$
$(CF_3)_2CFC_nF_{2n}C_mH_{2m+1}$	$C_nF_{2n+1}C_mH_{2m}CH(C_mH_{2m+1})C_{m'}H_{2m'+1}$
$C_nF_{2n+1}C_mH_{2m}I$ (<i>FnHmI</i>)	$C_nF_{2n+1}CH_2CHIC_mH_{2m+1}$
$C_nF_{2n+1}CH_2CHIC_mH_{2m}CH=CH_2$	$C_nF_{2n+1}CH_2CHOC_mH_{2m+1}$
$C_nF_{2n+1}CH_2CHICH_2OCH_2CH=CH_2$	$C_8F_{17}CH_2CH_2SCH_3$
$ClC_nF_{2n}CH_2CHIC_mH_{2m+1}$	$C_nF_{2n+1}C_mH_{2m}Br$
$C_nF_{2n+1}C_mH_{2m}C_nF_{2n+1}$ (<i>FnHmFn</i>)	$C_mH_{2m+1}C_nF_{2n}C_mH_{2m+1}$ (<i>HmFnHm</i>)
$C_8F_{17}CH_2CHICH_2CH_2CHICH_2C_8F_{17}$	$C_nF_{2n+1}CH=CHC_nF_{2n+1}$
$C_nF_{2n+1}CH=ClC_nF_{2n+1}$	$C_nF_{2n+1}CF=CH-CH=CFC_nF_{2n+1}$
$C_nF_{2n+1}C\equiv CC_nF_{2n+1}$	$C_nF_{2n+1}CH_2C(C_mH_{2m+1})C(C_mH_{2m+1})CH_2C_nF_{2n+1}$
$CF_3CH_2O(CH_2)_mOCH_2CF_3$	$C_nF_{2n+1}(CH_2)_2S(CH_2)_2C_nF_{2n+1}$
$CH_2CH_2(CF_2)_nCH_2CH_2I$	$BrCH_2CBr_2C_nF_{2n}CHBr_2CH_2Br$
$CH_2=CH(CF_2)_nCH=CH_2$	$HC\equiv C(CF_2)_nC\equiv CH$
$C_mH_{2m+1}(CF_2)_2O(CF_2)_2C_mH_{2m+1}$	$C_7F_{15}CH_2OCO$ —  — $OC_{11}H_{22}C_8F_{17}$
$C_nF_{2n+1}CH_2CHC_mH_{2m+1}$	
$C_nF_{2n+1}CH_2CHC_mH_{2m+1}$	

measured for $C_{10}F_{21}CH_2COOH$ (19 °C)¹⁸ and $C_{20}F_{42}$ (4 °C),¹⁹ respectively, when spread as Langmuir monolayers, assuming hexagonal close-packing. Cross-sectional areas of 29.6 Å² and 21.0 Å², respectively, have been reported for the alcohols $C_{10}F_{21}C_2H_4OH$ and $C_{14}H_{29}OH$ in Langmuir monolayers.²⁰ The length and volume of a fully stretched diblock have been calculated using typical bond lengths, bond angles, van der Waals radii, and a specific mean contribution for the CF_2-CH_2 junction.²¹ The length (Å) of an *FnHm* diblock was thus approximated as $l = n \times 1.306 + m \times 1.265 + 3.26$ and its volume (Å³), defined as the envelope of interpenetrating van der Waals spheres, as $V = n \times 21.5 + m \times 17.1 + 12$. *F*-chains also display larger surface areas than *H*-chains, which is a major contributor to their enhanced hydrophobicity and surface activity.

In spite of its nine electrons (and due to its nine protons), the tightly packed, dense electron cloud of fluorine is less polarizable than that of hydrogen ($\alpha = 0.557$ vs 0.667×10^{-24} cm³, respectively²²). Contrary to some persistent belief, fluorine atoms in perfluoroalkyl compounds usually do not engage in hydrogen bonding.^{14,23}

Due to the larger steric requirements of fluorine, *F*-chains are substantially more rigid than *H*-chains. *F*-chains also tend to adopt an *all-trans* helical (rather than planar) conformation in standard conditions.^{24,25} The 1,3 repulsive fluorine–fluorine interaction and larger van der Waals diameter of fluorine (2.94 Å), as compared to the *trans* C–C–C distance (2.62

Å), can indeed be relieved in a long *F*-chain by twisting the C–C–C chain sequence by 12° on average, resulting in a 15/7 helix, with left and right helices being in equal proportions. The thread of the helix depends somewhat on the number of CF_2 units (with the need for a helical structure increasing with chain length) and tends to become lesser when temperature or pressure increases.^{26–29} A planar zigzag conformation may actually be advantageous for short *F*-chains and could be promoted by linkage to an *H*-chain.²⁹ The planar *trans* zigzag configuration was thus determined to be the most stable for C_4F_{10} and C_6F_{14} .³⁰ A planar conformation has also been demonstrated in thin films of closely packed *F*-dodecanoic acid.³¹ Untwisting of the helices upon regular packing was no longer seen for *F*-chains longer than 12 carbon atoms. When the *F*-block adopts a helical conformation, “frozen” individual *F*-alkyl/*H*-alkyl diblock molecules are not only dissymmetric but asymmetric as well.

The conformational freedom of *F*-chains is significantly reduced as compared to that of *H*-chains. *Trans/gauche* interchange enthalpies are at least 25% higher for linear *FC*s than for the *HC* analogue. They have been determined from infrared studies to be 5.1 versus 4.0 kJ mol^{−1} for gaseous *n*- C_4F_{10} as compared to *n*- C_4H_{10} (3.0 vs 2.2 kJ mol^{−1} in the liquid state, respectively) and 4.9 versus 2.6 kJ mol^{−1} for gaseous *n*- C_6F_{14} and *n*- C_6H_{14} , respectively (2.1 and 1.7 kJ mol^{−1} for the liquids, respectively).²⁶ The hindered internal reorientation about C–C bonds and reduced occurrence of

gauche defects facilitate *F*-chain stacking, ordering, and crystallization.

F-chains are also subject to motions unfamiliar to *H*-chains, such as helix reversal and helix/planar conformational interchanges (untwisting), including in their solid state (section 5). The helix inversion activation energy is, however, low and inversion is estimated to occur rapidly at room temperature.²⁷ Increasing temperature induces a continuous slow reduction of the thread of the helix, which eventually approaches an *all-trans* form. On the other hand, the helical conformation provides a smoother, “streamlined” molecular shape that may facilitate rotation and translation (slipping) of an *F*-chain as a whole along the chain’s long molecular axis within a crystal.²⁴ Disorder arising from such movements occurs at lower temperatures in *n-F*-alkanes as compared to *n*-alkanes.³²

In their condensed states, fluorocarbons (*FCs*) display significantly lower cohesive energy densities than hydrocarbons (*HCs*). Therefore, the vapor pressures of *FCs* are much higher than those of *HCs* of comparable MW and the liquid domain of an *F-n*-alkane is significantly narrower than that of the corresponding *n*-alkane. The boiling point of *n-F*-hexane (57 °C) is lower than that of *n*-hexane (69 °C), in spite of a four times larger MW. *FCs* also display lower surface energies (surface tensions), refractive indexes (polarizabilities), and dielectric constants, but higher densities, compressibilities, viscosities, and critical temperatures than their *HC* analogues. These specificities essentially reflect the stronger *intramolecular* bonding and weaker *intermolecular* interactions found in *FCs* relative to the corresponding *HCs*.

F-chains are considerably more hydrophobic than *H*-chains and are substantially lipophobic as well. The outstanding hydrophobicity of *F*-chains has been related primarily to their larger surface area.^{33–37} The incremental changes in free energy of adsorption for the transfer of one CF_2 group from water to the air/water interface or to a *FC*/water interface are about twice those of a CH_2 group (5.10 vs 2.60 kJ mol^{-1} , respectively, at 25 °C); likewise for their transfer from water

to an *F*-hexane/water interface (5.35 vs 2.88 kJ mol^{-1}).^{36,38} On the other hand, the free energies of transfer of a CH_2 group from a *HC* to a *FC* phase ($\sim 1.1 \text{ kJ mol}^{-1}$) and of a CF_2 from a *FC* to a *HC* phase ($\sim 1.4 \text{ kJ mol}^{-1}$) amount to about one-third of the energy needed to transfer a CH_2 from a *HC* to water (3.7 kJ mol^{-1}).³⁹

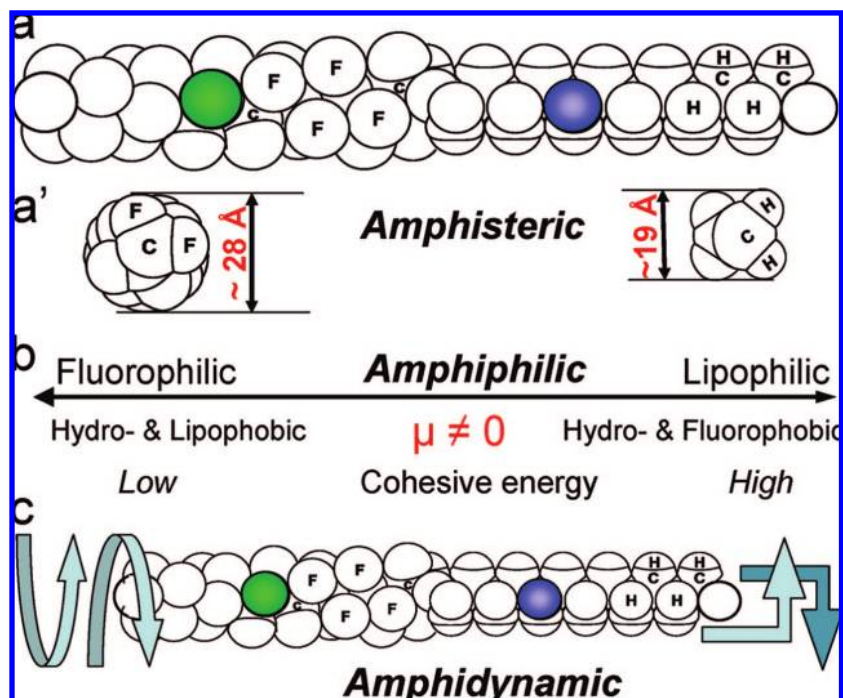
Due to the disparity in cohesive energy densities between *FCs* and *HCs*, the mixing of liquid *FCs* and *HCs*, and likewise of *F*-chains and *H*-chains, is highly nonideal.^{33,39–45} Binary phase diagram studies found no cosolubility of *F*-alkanes ($\text{C}_n\text{F}_{2n+2}$, $n = 12–20$) with alkanes ($\text{C}_m\text{H}_{2m+2}$, $m = 19$ and 20) in either the liquid or the solid phase.⁴⁴ *F*-chains and *H*-chains therefore tend to phase separate, inducing the formation of distinct micro- and nanosize domains in solutions, monolayers, membranes, and colloids. *F*-chains show an enhanced tendency to segregate, self-assemble, and collect at interfaces and, hence, generate surface activity and molecular organization, and they help to exclude both hydrophilic and lipophilic solutes.

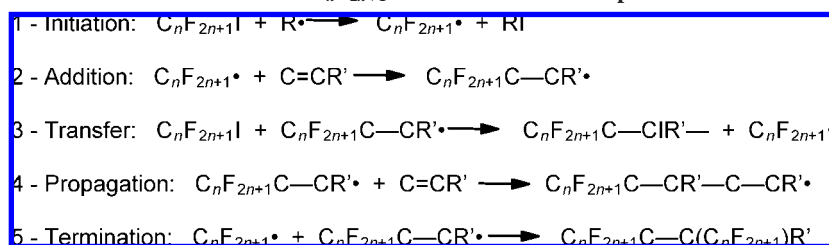
The specific physical chemistry of *FCs* and *F*-chains, their outstanding thermal stability and chemical inertness, low intermolecular cohesiveness and high gas-dissolving capacity, aptitude for enhancing surface activity, and outstanding capacity for promoting self-assembly have been discussed previously.^{10–13,46–53}

2.2. (*F*-Alkyl)alkyl Diblocks: Primitive, yet Amphiphilic, Amphisteric, and Amphidynamic

Yoking together an *F*-chain and an *H*-chain via a covalent bond generates energetic and steric frustrations and, hence, specific properties, different from those of both parent moieties. In spite of their structural simplicity, which led to them being dubbed as “primitive” surfactants,⁵⁴ linear *F_nH_m* diblocks are not only *amphiphilic* (the *F*- and *H*-moieties exhibit different affinities) but also *amphisteric* (the two chains have different conformations, cross sections, and space requirements) and *amphidynamic* (they have distinct dynamic

Scheme 2.1. Linear *F_nH_m* Diblocks Are (a) Amphisteric (a': Cross Sections of the *F*- and *H*-Blocks), (b) Amphiphilic, and (c) Amphidynamic (Schematic)



Scheme 3.1. Mechanism of Free Radical Addition of $C_nF_{2n+1}I$ to Unsaturated Compounds

Hydrogens are omitted for clarity. From ref⁵ with permission.

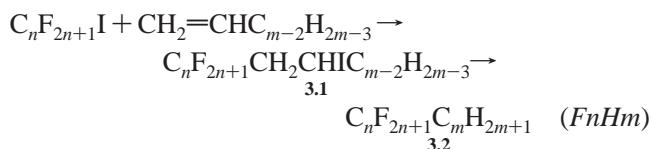
regimes: one is stiff, rodlike, and prone to crystallization, yet “slippery”; the other is more flexible and prone to kinks and defects) (Scheme 2.1). Consequently, *F*-chains manifest a higher tendency, as compared to *H*-chains, to produce layered structures with longer-range order. The ~30% smaller cross-sectional area of hexagonally packed *H*-chains, as compared to similarly packed *F*-chains, facilitates conformational disordering of the *H*-segments both in the bulk and in self-assemblies. The activation energy for many dynamic processes (e.g., conformational changes, melting) is usually lower for the *H*-chain than for an *F*-chain of comparable length, and the onset of these processes occurs, accordingly, first in the *H*-chain when temperature is raised. On the other hand, such movements as translations and rotations within a collection of molecules may be facilitated for *F*-chains due to their more streamlined shape.

3. Synthesis of *F*-Alkyl/Alkyl Diblocks, Triblocks, and Their Precursors

This section provides a nonexhaustive overview of synthetic approaches to molecular *F*-alkyl/alkyl diblocks and triblocks and their precursors or potential precursors. Examples of preparations of related diblock halides, ethers, and thioethers, as well as of some multiblocks, are also given.

3.1. Principles

The synthesis of linear *F*-alkyl/*H*-alkyl diblocks is usually straightforward. The most popular approach involves the free radical addition of *F*-alkyl iodides, $C_nF_{2n+1}I$, to a multiple bond, followed by reductive dehalogenation of the resulting iodinated adduct. (The same product number will be used for all homologues and isomers of a same structural family.)



The synthesis of triblocks follows essentially the same lines.

F-Alkyl chain free radical chemistry has been a major development in organic fluorine chemistry.^{1–5,55} The reactivity of *F*-alkyl free radicals is substantially different from that of their hydrocarbon counterparts.⁵⁶ Due to fluorine’s extreme electronegativity, *F*-alkyl radicals are electron-poor, σ -inductive, and electrophilic. They have also potentially strong π -electron donor capacity. Contrary to *H*-alkyl radicals, *F*-radicals have a pyramidal (rather than planar) structure, with a significant barrier to inversion.

Although free radical *F*-alkylation is the most frequently used route to diblock synthesis, nucleophilic and electrophilic *F*-alkylation methods have also been developed.

The commercially available *F*-alkyl iodides, $C_nF_{2n+1}I$ ($n = 4, 6, 8, 10$), usually obtained by telomerization of tetrafluoroethylene, $CF_2=CF_2$, with C_2F_5I ^{55,57–60} are preferred starting materials for access to both *F*-alkyl radicals and electrophilic *F*-alkylation reagents. Methods for generating free radicals from *F*-alkyl iodides include thermal and photochemical homolysis, use of free radical initiators or electron transfer procedures, and electrochemical initiation of the free radical chain process.^{5,56,59,61} Direct homolysis of the C–I bond requires relatively high temperatures or prolonged photolysis times that can result in extensive loss to tar and release of iodine, as well as rearrangements and fragmentations.⁵ Free radical initiators allow use of lower temperatures and proved very effective in iodo-diblock synthesis. Single electron chemical reduction using metals or anionic species^{62–64} and electrolytic *F*-alkyl radical formation procedures are also useful.^{65–68} Use of phosphanes, phosphites, or hydroxylamine as catalysts proved very effective.^{69,70}

The terminally iodinated diblocks $C_nF_{2n+1}C_mH_{2m}I$ (*FnHmI*) **3.3** that result from telomerization of $C_nF_{2n+1}I$ with ethene obviously represent further convenient starting materials that open access to a wide range of *F*-alkylated products.⁵ Some of these compounds, with $m = 2$ and 3, for example, are commercially available. A practical synthesis of *F6H3I* has been reported.⁷¹ When $m \geq 2$, the reactivity of *FnHmI* compounds is close to that of nonfluorinated iodoalkanes. *F*-Alkyl sulfonyl halides and *F*-alkanoic acids can also be envisaged as starting materials for access to *FnHm* diblocks.

The addition of *F*-alkyl free radicals to unsaturated systems is strongly exothermic, since a π bond is broken and replaced by a stronger σ bond; also, a CF_2-C bond is formed that is generally stronger than a CH_2-C bond. Addition takes place regioselectively onto the terminal, least substituted carbon of an olefin, as in a Markovnikoff addition. This addition is usually much faster for *F*-radicals than for their *HC* free radical counterparts. For example, addition of $C_3F_7^\bullet$ and $C_7F_{15}^\bullet$ to 1-hexene was $3-4 \times 10^4$ times faster than that for an *n*-alkyl radical, mainly because of higher electrophilicity of the *F*-alkyl radical.⁷² Hydrogen abstraction from $HsSnBu_3$ was also about 100 times faster for *F*-radicals than for their *H*-counterparts.

The mechanism by which an *F*-alkyl iodide reacts with alkenes and alkynes is depicted in Scheme 3.1.^{5,58} After the first radicals have been formed, whatever the initiation procedure, the first step of the chain reaction consists of the abstraction of iodide from $C_nF_{2n+1}I$ to produce a $C_nF_{2n+1}^\bullet$ radical. This radical then adds exothermically and irreversibly to the alkene (or alkyne) to give an intermediate adduct radical. Step 3 involves the transfer of the iodine atom from another $C_nF_{2n+1}I$ molecule to give the final addition product, $C_nF_{2n+1}CH_2CHIC_{m-2}H_{2m-3}$ and a new $C_nF_{2n+1}^\bullet$ radical that

allows continuation of the chain reaction. With highly polymerizable monomers or when an excess of unsaturated substrate is present, propagation of a polymer chain reaction may occur as shown in step 4. The reaction is terminated by radical coupling, such as in step 5, or another process. The mechanisms of electrochemically induced nucleophilic substitution of *F*-alkyl halides have also been discussed in detail.^{66–68,73}

The reaction of $C_nF_{2n+1}I$ with $CH_2=CHC_{m-2}H_{2m-3}$ ($m = 3–16$) has provided over 90% of end-substituted adduct with no more than 1% of the regioisomer. There were no telomers formed when proper conditions were used. *F*-alkyl radical rearrangements, such as cyclizations, have been observed, in particular with the *F*-alkyl heptenyl radical.^{74,75} Hydrogen abstraction from a substrate by *F*-alkyl radicals can compete with addition.⁵⁶ Unlike for alkyl radicals, this hydrogen scavenger behavior was very effective for $C_nF_{2n+1}^{\bullet}$ radicals ($n = 3, 6, 8$).⁶⁶

Reductive dehalogenation of the iodo-diblock intermediate $C_nF_{2n+1}CH_2CHIC_{m-2}H_{2m-3}$ **3.1** has commonly been performed with zinc powder and gaseous HCl in ethanol or another alcohol,^{6,76–78} acetic acid,⁷⁶ or aqueous HCl.⁷⁹ Tributyltin hydride⁷⁶ and $LiAlH_4$ /ether^{3,76} have also been used extensively. Unsaturated diblocks can be converted to saturated ones using standard catalytic (rhodium or palladium on charcoal) hydrogenation procedures under pressure.

Several other reviews on *F*-alkyl free radical formation, reactivity and reaction mechanisms, conditions for $C_nF_{2n+1}I$ addition to unsaturated compounds, and further practical information on the synthesis of *FnHm* diblocks and related compounds are available.^{5,56,61,67,75,80,81}

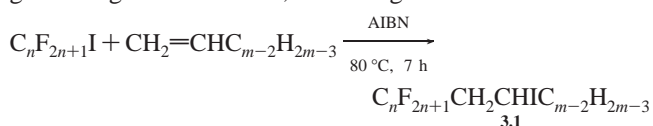
Electrophilic *F*-alkylation, although more difficult to achieve than electrophilic alkylation, due to the difficulty in generating *F*-alkyl cations, has been successfully realized using (*F*-alkyl)phenyliodonium trifluoromethanesulfonates (FITS) and their analogues as reagents.^{82,83}

Thorough purification of the *FnHm* diblock compounds is indispensable, especially when physicochemical investigation or biomedical applications are intended. It is usually achieved by distillation or recrystallization, sometimes followed by sublimation or passage over an alumina column. Filtration over activated alumina is strongly recommended when elimination of traces of potentially toxic material is essential.⁸⁴ Some diblocks (e.g., *F8H18*) have been purified based on their capacity to form gels in organic solvents.⁸⁵

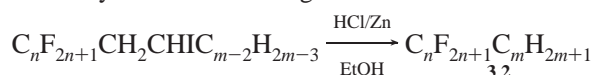
3.2. (*F*-Alkyl)alkanes, (*F*-Alkyl)alkenes, and Related Diblocks

3.2.1. Linear *F*-Alkyl/*H*-Alkyl Diblocks

The saturated linear *FnHm* diblocks **3.2** have most generally been obtained by addition of $C_nF_{2n+1}I$ onto a terminal alkene in the presence of an azonitrile-type radical-generating chain initiator, according to



followed by reductive dehalogenation of adduct **3.1**:



In practice, the most commonly used free-radical initiator has been the readily available 2,2'-azobis(isobutyronitrile)

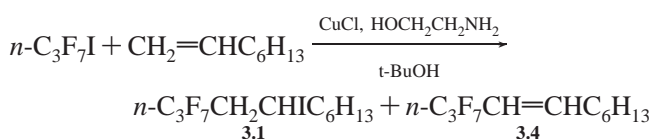
(AIBN), at relatively elevated temperatures^{3,6,58,75} (see also the patent literature, in particular^{86,87}). Yields commonly exceeded 90%. Excess alkene should be avoided in order to prevent further addition reactions and the formation of $C_nF_{2n+1}CH_2CH(C_{m-2}H_{2m-3})CH_2CHIC_{m-2}H_{2m-3}$ (Scheme 3.1, step 4). On the contrary, a slight excess of $C_nF_{2n+1}I$ can be desirable, as the unreacted *F*-alkyl iodide is easily recovered. Standard addition reaction conditions include the following: equimolar reactant ratio, 1–2% of AIBN, and reflux at 70–100 °C under an inert atmosphere for 1–10 h.⁵ It is essential that the *F*-alkyl iodide be free of radical chain inhibitors such as iodine or HI.

Other free-radical generating initiators have been used. 2,2'-Azobis(2,4-dimethylpentanenitrile) and 2,2'-azobis(2-methylbutyronitrile) have been recommended on the basis of lesser toxicity than AIBN.⁵ 2,2'-Azobis(cyclohexanecarbonitrile), di-*tert*-butylperoxide and benzoyl peroxide have also been used. Excellent yields have been obtained with azonitrile and bisulfite initiators in a biphasic system.⁵

Effective catalysis of *F*-alkyl iodides addition onto 1-alkenes has also been achieved in the presence of an ammonium salt⁸⁸ or of triphenylphosphane, tributylphosphane, triethylphosphite, and hydroxylamine,⁶⁹ providing numerous diblock iodides $F_nCH_2CHIH(m-2)$. Addition of $n-C_8F_{17}I$ on $CH_2=CHC_6H_{13}$ to give $n-C_8F_{17}CH_2CHIC_6H_{13}$ has, for example, been achieved at room temperature in excellent yield in the presence of triphenylphosphane.⁷⁰

Room temperature addition of *F*-alkyl iodides to double bonds has also been promoted by tin(0)–silver(I) acetate or tin(0)–copper(I) chloride salts.⁸⁹ The tin(0)–aluminum(0) system was slightly less reactive.

The following reaction exemplifies the reductive initiation of the addition of an *F*-alkyl iodide (and of polyhaloalkanes in general) to an olefin using copper(I) chloride and ethanolamine; however, significant HI abstraction, possibly by ethanolamine, was seen.⁶²

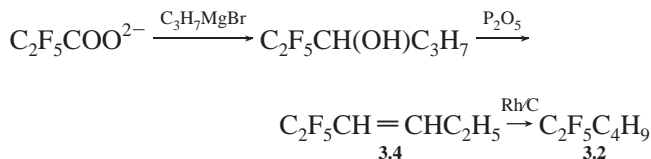


Better results were achieved when *F*-alkyl iodides were added to alkenes in the presence of catalytic amounts of Ti(0) generated in situ from $TiCl_4$ and Zn.⁹⁰

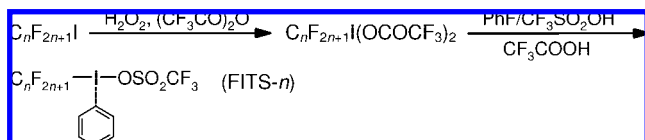
A large variety of reductively induced additions of $C_nF_{2n+1}I$ to alkenes and alkynes have been reported that can provide access to *FnHm* diblocks. The reductants used included Mg, Sn, Fe, Raney Ni, $TiCl_4Cp_2$, $Fe_3(CO)_{12}$, $Ni(CO)_2(Ph_3P)_2$, $Pd(Ph_3P)_4$, $PhSO_2Na$, Bu_4NI , and many others.^{56,91}

Use of activated copper bronze in DMSO led to a mixture of the desired (*F*-alkyl)alkanes with the alkenes $C_nF_{2n+1}CH=CHC_{m-2}H_{2m-3}$ **3.4**, requiring reduction of the latter product.⁹² The reaction likely involved formation of a $C_nF_{2n+1}Cu(I)$ intermediate and eventually a radical chain process.

Reaction of Grignard reagents with *F*-alkylcarboxylates has provided a series of light diblocks, including *F2H4*, *F3H2*, *F4H2*, *F4H3*, *F6H2*, *F8H2*, as well as some branched and other isomers.⁷⁹ For example,



Efficient electrophilic *F*-alkylation has been achieved using (*F*-alkyl)phenyliodonium trifluoromethanesulfonates (FITS). The FITS reagents were synthesized by allowing (*F*-alkyl)phenyliodonium salts⁹³ to react with superacidic trifluoromethanesulfonic (triflic, Tf) acid:⁸³



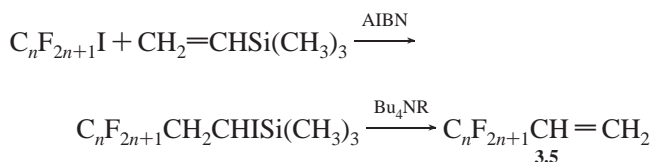
Reaction of FITS with carbanions produced saturated diblocks. For example, *n*-C₈H₁₇M (M = MgCl, Cu, Li) reacted with FITS-*n* to yield C_nF_{2n+1}C₈H₁₇ under very mild conditions (−78 °C, 2 h), with the highest yields being obtained with M = MgCl.⁸³

Examples of useful detailed procedures for diblock synthesis include, for the medium-sized compounds, *F7H16*,⁷⁶ *F8H8*,⁹⁴ *F8H16*,⁷⁸ *F8H18*,⁸⁵ *F10H8*,²¹ *F10H10*,^{21,95,96} and *F12H8*.⁶

3.2.2. Unsaturated Diblocks

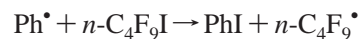
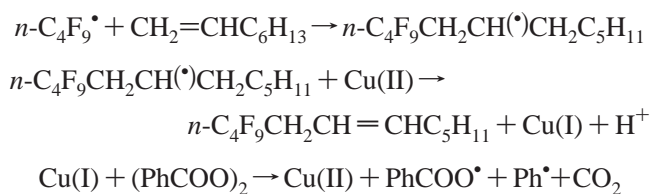
Terminally unsaturated diblocks have been obtained from the iodinated diblocks C_nF_{2n+1}C_mH_{2m}I **3.3** (*n* = 3, 4, 6, 7; *m* = 2, 3, 4, 8) by dehydrohalogenation with a strong base, typically NaOH/EtOH.⁷¹ With *m* = 2, only elimination of HI to C_nF_{2n+1}CH=CH₂ **3.5** was observed. With *m* = 3, both elimination and, predominantly, substitution (i.e., formation of C_nF_{2n+1}CH₂CH₂CH₂OH) occurred. Isomerization of C_nF_{2n+1}CH₂CH=CH₂ **3.6** to *E*-C_nF_{2n+1}CH=CHCH₃ **3.4** was also observed. Compounds of type C_nF_{2n+1}CH₂CHIC_mH_{2m+1} **3.1** underwent solely elimination, principally toward the *F*-chain, yielding C_nF_{2n+1}CH=CHC_mH_{2m+1} **3.4**, predominantly as the *E*-isomer.

Another access to **3.5** has involved an unusual fluoride-induced elimination–desilylation reaction:⁹⁷



The allylic diblocks C_nF_{2n+1}CH₂CH=CH₂ (*n* = 6, 8) **3.6** have been prepared by addition of *F*-alkyl iodides to allyl alcohol, followed by dehalogenation using Zn/AcOH.⁹⁸

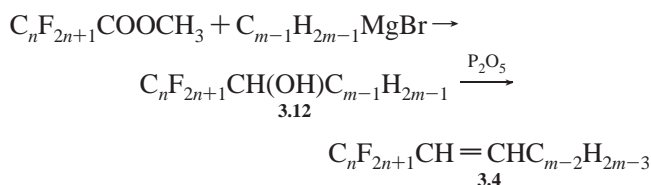
F-Alkylation of 1-octene through a double chain reaction involving Cu(II)-induced oxidation of an intermediate radical and Cu(I)-induced decomposition of benzoyl peroxide has been reported.⁹⁹ In this procedure, it is the phenyl radical that abstracts iodine from the *F*-alkyl iodide.⁸⁰



The products were *E*-(*n*-C₄F₉)CH₂CH=CHC₅H₁₁ **3.7** (83%), *Z*-(*n*-C₄F₉)CH₂CH=CHC₅H₁₁ (16%), and a trace of *n*-C₄F₉CH=CHC₆H₁₃.

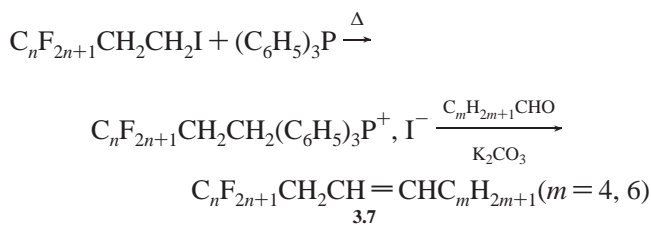
Reaction of *F*-alkyl iodides with nonconjugated terminal dienes in the presence of an azonitrile initiator led to addition of one or two *F*-alkyl groups in proportions depending on reactant mole ratio. Thus, addition of C_nF_{2n+1}I to CH₂=CH(CH₂)_mCH=CH₂ (*n* = 3, 4, 12; *m* = 1, 2, or 4) gave diblock C_nF_{2n+1}CH₂CHI(CH₂)_mCH=CH₂ **3.8**, plus triblock C_nF_{2n+1}CH₂CHI(CH₂)_mCHICH₂C_nF_{2n+1} **3.9**.⁷⁵ Zinc and acid reduction of **3.8** afforded C_nF_{2n+1}(CH₂)_{m+2}CH=CH₂ **3.10**.⁷⁶ Dehydrohalogenation of **3.8** (*n* = 4, *m* = 2, 4) with NaOR led to *E,Z*-C_nF_{2n+1}CH=CH(CH₂)_mCH=CH₂ **3.11**, with the *E*-isomer being largely predominant. Extensive cyclization was observed in the case of addition of C_nF_{2n+1}I to 1,6-heptadiene.⁷⁵

Unsaturated diblocks C_nF_{2n+1}CH=CHC_{m-2}H_{2m-3} **3.4** have also been prepared by allowing *F*-carboxylic acid methyl esters to react with alkylmagnesium bromides, followed by treatment of alcohol **3.12** with P₂O₅:⁷⁹

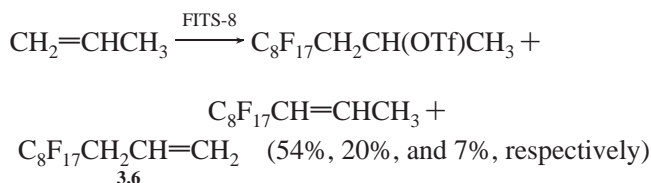
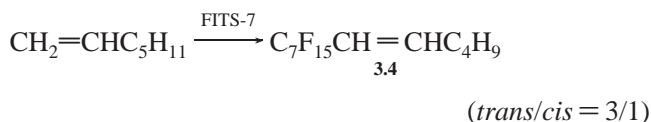


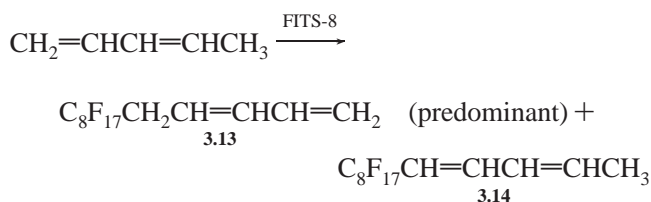
Subsequent hydrogenation with a Rh/C catalyst afforded the corresponding saturated diblocks **3.2**.

The alkenes **3.7** (*n* = 4, 6, 8) have been obtained as a mixture of *Z* (predominant) and *E* isomers through a Wittig reaction with aldehydes in the presence of hydrated K₂CO₃:¹⁰⁰



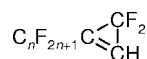
Electrophilic *F*-alkylation of CH₂=CHMgBr and CH₂=CHCH₂MgBr with FITS-8 yielded C₈F₁₇CH=CH₂ **3.5** and C₈F₁₇CH₂CH=CH₂ **3.6**, respectively.⁸³ Examples of direct *F*-alkylations of alkenes and alkadienes using FITS reagents include the following:^{82,83}





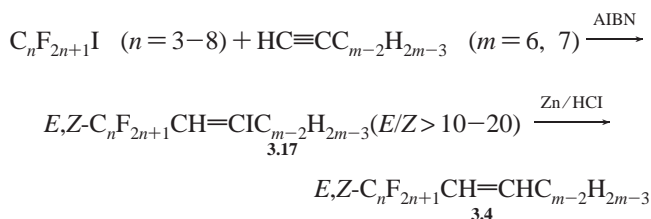
Addition of *F*-alkyl iodides to alkynes has been achieved using thermal or photochemical^{11,101,102} activation, free radical initiators,^{3,5,103} electrochemical activation,⁶⁵ transition metals complexes,^{63,104} etc.

The light-induced addition of CF₃I and C₂F₅I to acetylene yielded predominantly the *trans* adduct,¹⁰² while addition of *i*-C₃F₇I gave a slightly higher proportion of the *cis* isomer. Dehydrohalogenation of the latter provided *i*-C₃F₇C≡CH. Addition of difluorocarbene (from Me₃SnCF₂) to C_{*n*}F_{2*n*+1}C≡CH **3.15** produced cyclopropenes. Reaction of C₃F₇I or C₃F₇I onto acetylene, initiated with



AIBN or benzoyl peroxide, gave the corresponding C_{*n*}F_{2*n*+1}CH=CHI **3.16** adducts.⁵

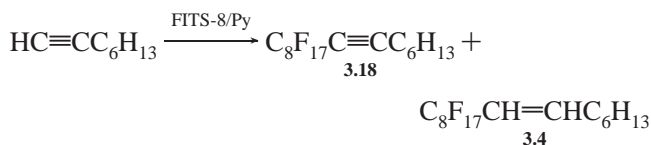
Free radical addition of C_{*n*}F_{2*n*+1}I to substituted alkynes with AIBN initiation gave the iodide **3.17** in high yields.⁵ The *E* isomer was largely predominant. Reduction by Zn/HCl in ethanol afforded *E,Z*-C_{*n*}F_{2*n*+1}CH=CHC_{*m*-2}H_{2*m*-3} **3.4**, the same product as from HI elimination from C_{*n*}F_{2*n*+1}CH₂CHIC_{*m*-2}H_{2*m*-3}.



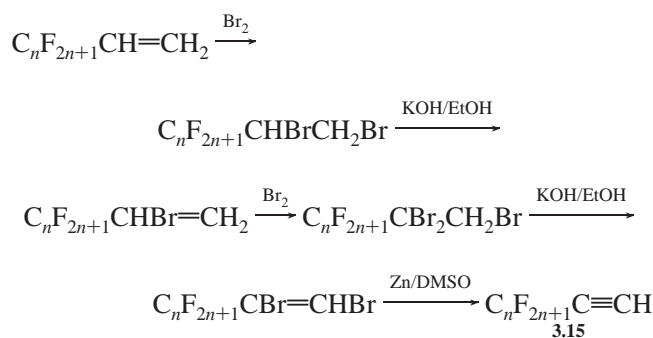
Transition metal-catalyzed addition of C₈F₁₇I to phenyl acetylene provided access to C₈F₁₇CH=CIC₆H₅.⁶³

C₈F₁₇CH=CIC₃F₁₁, C₃F₇CH=CISiMe₃, and C₃F₇CH=CICH₂SiMe₃ have been obtained from *F*-alkyl iodides and alkynes or Me₃Si-substituted alkynes using iron, cobalt, or ruthenium carbonyl complexes as catalysts.¹⁰⁴ C_{*n*}F_{2*n*+1}CH₂CHISiMe₃ (*n* = 1, 3, 8) were produced from Me₃SiCH=CH₂ under similar conditions.

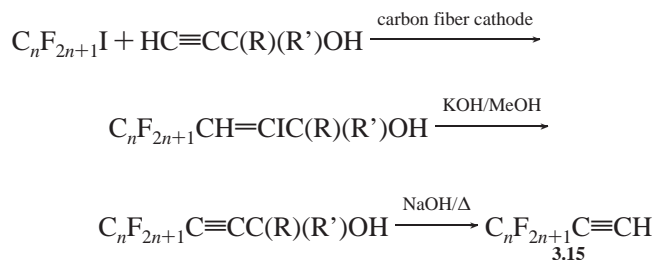
Electrophilic *F*-alkylation of alkynes is represented by⁸³



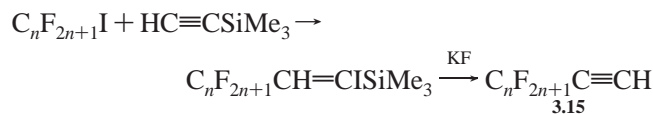
The short chain (*F*-alkyl)alkyne C₂F₅C≡CH has been prepared by reaction of C₂F₅I and acetylene under UV activation, followed by dehydroiodination by KOH.¹⁰¹ Use of acetylene for the preparation of (*F*-alkyl)alkynes **3.15** can be avoided by applying a sequence of successive bromination, dehydrobromination, and debromination steps to a terminal *F*-alkene.^{101,105} The longer homologues (*n* = 4, 6, 8) have been prepared using a similar route.¹⁰⁶



(*F*-Alkyl)alkynes **3.15** (*n* = 4, 6) have also been obtained through electrochemically catalyzed addition of *F*-alkyl iodides to hydroxylalkynes, followed by dehydroiodination and thermal cleavage in basic medium.⁶⁵



A further approach to **3.15** involved use of the trimethylsilyl blocking group.¹⁰³



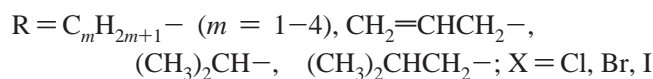
CF₃C≡CCH₃ and CF₃C≡CCD₃ have been prepared from CF₃I and HC≡CCH₃ (or HC≡CCD₃) followed by treatment with KOH.¹⁰⁷ Further unsaturated diblocks include C_{*n*}F_{2*n*+1}C≡CSiMe₃, C_{*n*}F_{2*n*+1}C≡CC₆H₅, and C_{*n*}F_{2*n*+1}CH=CHOMe.¹⁰³

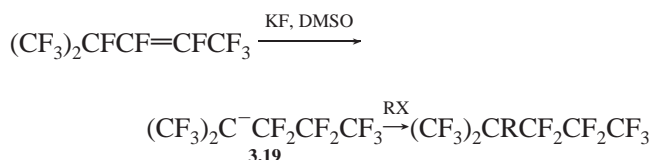
3.2.3. Branched Diblocks

Warning. Some compounds or precursors containing branched *F*-alkyl groups are highly toxic. High inhalation toxicities (LD₅₀, 1 h, < 100 ppm in mice) have, in particular, been reported for (CF₃)₃CI, (CF₃)₂C=CFC₂F₅, C₂F₅(CF₃)₂CI, C₃F₇(CF₃)₂CI, C₃F₇(CF₃)₂CBr, C₃F₇(CF₃)₂CH, and C₃F₇(CF₃)C=CF₂.¹⁰⁸

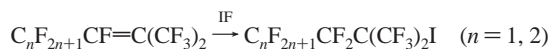
(*F*-Alkyl)alkyl compounds or precursors with a branched *F*-chain have mostly involved the *F*-isopropyl (*Fi3*) group.^{5,75} Detailed procedures have been provided for the preparation of the lighter branched diblocks *Fi3H2* and *Fi3Hi3*.⁷⁹ It is noteworthy that *i*-C₃F₇I reacted with olefins much faster than *n*-C₃F₇I, due to greater electrophilicity of the branched radical.^{5,56}

Branched diblocks with longer *F*-chains include (CF₃)₂CF(CF₂)_{*n*-3}C_{*m*}H_{2*m*+1} (*n* = 7, 9).^{109,110} *F*-4-Methylpentene-2, upon reaction with KF or CsF, added a fluoride ion, forming an *F*-carbanion **3.19** that reacted with alkyl halides, affording diblocks with the tertiary *F*-block CF₃CF₂CF₂(CF₃)₂C⁻.¹¹¹



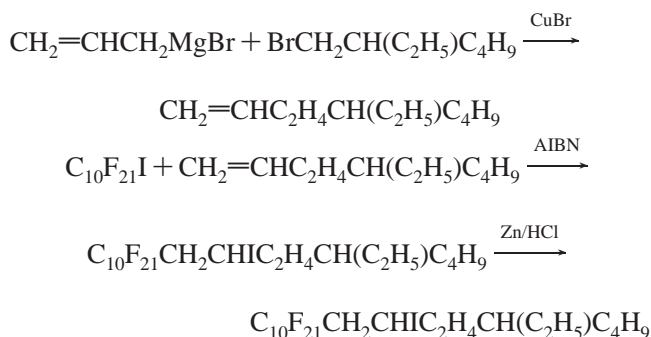


F-Alkyl iodides with *F*-methyl branches located near the iodine atom have been obtained from *F*-alkenes using KF/IF₅ at relatively high temperatures:¹⁰⁸



Subsequent addition of unsaturated substrates led, for example, to C_nF_{2n+1}CF₂C(CF₃)₂(CH₂CH₂)_nI and C_nF_{2n+1}CF₂C(CF₃)₂CH=CISiMe₃.

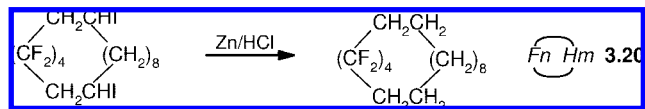
Compounds of type **3.1** and **3.2** with branched *H*-chains are represented by C_nF_{2n+1}CH(CH₃)₂ (*n* = 2–4),⁷⁹ C₅F₁₁CH₂Cl(CH₃)₂,⁴ C₅F₁₁CH₂Cl(CH₃)C₂H₅,⁶⁴ C₁₂F₂₅CH₂CH(CH₃)C₉H₁₉,¹⁰⁹ and C₁₀F₂₁C₄H₈CH(C₂H₅)C₄H₉.²¹ The latter compound resulted from the following sequence of reactions:



Triphenylphosphane-catalyzed addition of C₈F₁₇I onto C₄H₉C(CH₃)=CH₂ afforded C₈F₁₇CH₂Cl(CH₃)C₄H₉.⁷⁰

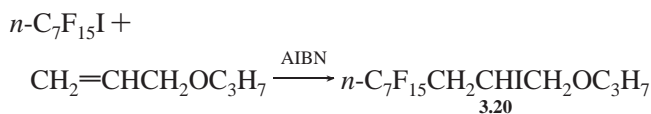
Compound C₈F₁₇(C₃H₇)C=CHC₃H₇ has been obtained by reacting alkyne C₃H₇C≡CC₃H₇ with FITS-8 in pyridine.⁸³

One example of a cyclic *F_nH_m* diblock, **3.20**, has recently been obtained by addition of α,ω-diodo-*F*-alkane onto α,ω-dodecadiene in two steps in the presence of triphenylphosphane or AIBN, followed by Zn/HCl deiodination in ethanol:¹¹²



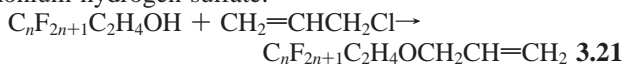
3.2.4. Diblocks with Heteroatoms

Diblocks such as **3.20** with an ether oxygen in the *H*-block were obtained through free radical addition of C_nF_{2n+1}I to allylic ethers,⁵ for example:

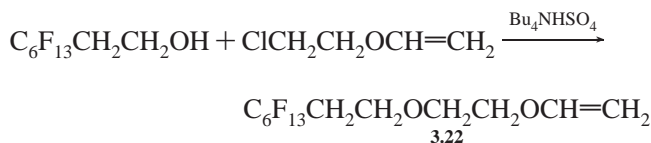


Addition of C₄F₉I to CH₂=CHOC₄H₉ under electrochemical activation afforded C₄F₉CH₂CHIOC₄H₉.⁶⁸

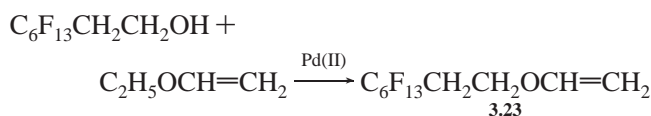
The *F*-alkylated allylic ethers **3.21** have been prepared in high yields using phase-transfer catalysis with tetrabutylammonium hydrogen sulfate:¹¹²



The terminally unsaturated *F*-alkylated diether **3.22** has been obtained from the (*F*-alkyl)ethyl alcohol using the same phase-transfer-catalyzed reaction:¹¹³

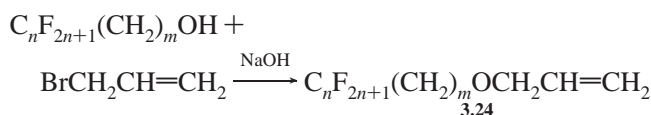


while transesterification of the alcohol with C₂H₅OCH=CH₂ in the presence of mercury acetate or of a Pd(II) complex yielded vinyl ether **3.23**:

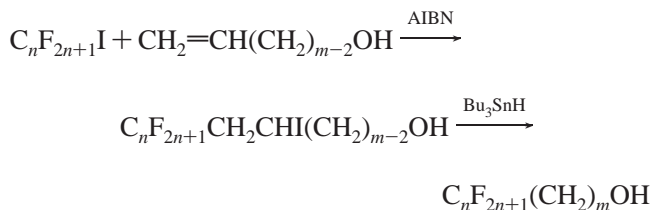


The second approach also provided the C₈F₁₇CH₂CH₂OCH=CH₂ homologue.¹¹⁴ These *F*-alkylated vinyl ethers were destined for the production of poly(vinyl ethers) with *F*-alkyl pendent groups.

A series of allyl ethers C_nF_{2n+1}C_mH_{2m}OCH₂CH=CH₂ **3.24** (*n* = 8, 10, 12; *m* = 4, 6, 10) has been synthesized by reacting the alcohols C_nF_{2n+1}(CH₂)_mOH with allyl bromide or chloride using phase transfer catalysis conditions:¹¹⁵



The (*F*-alkyl)alkanols needed for this synthesis were obtained according to

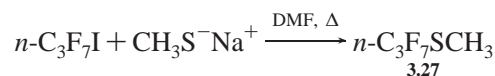


Some of these semifluorinated allyl ethers were subsequently connected to polymethylhydrosiloxanes by hydrosilylation.

The saturated diblock ethers C₈F₁₇CH₂OC_mH_{2m+1} **3.25** and C₈F₁₇CH₂CH₂OC_mH_{2m+1} **3.26** (*m* = 14 and 16) were prepared from *F*-alkyl alcohols and α-haloalkanes using the Williamson ether synthesis under basic conditions.¹¹⁶ The branched ether C₆F₁₃CH₂CH₂OCH(CH₃)CH₂(CH₃)₂ was obtained by heating C₆F₁₃CH₂CH₂OH with CH₃C(O)CH₂(CH₃)₂ under a stream of H₂ in the presence of Pd on carbon, with water being trapped during the reaction.¹¹⁷

Ethylene reacted with FITS-8 in the presence of methanol, which acted as a nucleophile, providing C₈F₁₇CH₂CH₂OCH₃.⁸³

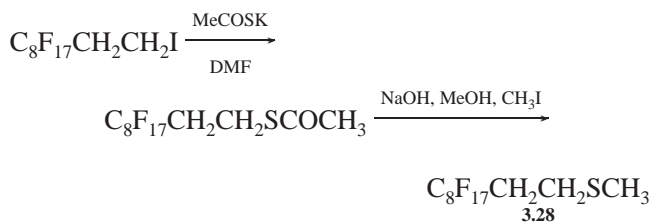
Diblocks with a sulfur junction between blocks **3.27** have been prepared by reacting an *F*-alkyl iodide with a thiolate ion:



Diblocks with a sulfur atom in the *H*-chain, C₆F₁₃CH₂CH₂SC_mH_{2m+1} **3.28** (*m* = 6, 12), have been obtained in excellent yields from C_nF_{2n+1}CH₂CH₂I and the

appropriate thiol in water, using phase transfer catalysis conditions.¹¹⁸

Displacement of iodide from $C_8F_{17}CH_2CH_2I$ by potassium thioacetate, followed by saponification and concomitant alkylation, also led to thioethers of type **3.28** in good yield:¹¹⁹



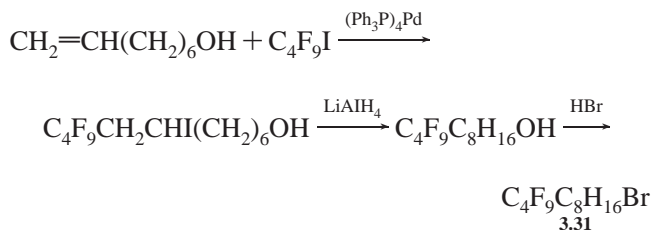
The preparation of $C_3F_7CH_2SC_mH_{2m+1}$ and of their dichloro derivatives $C_3F_7CCl_2SC_mH_{2m+1}$ ($m = 2-4$) has also been reported.¹²⁰

3.2.5. Diblocks with Heavy Halogens

In addition to the various iodinated diblock precursors encountered above and of the commercial $C_nF_{2n+1}C_2H_4I$ compounds, several other series of diblocks incorporating halogens heavier than fluorine have been reported.

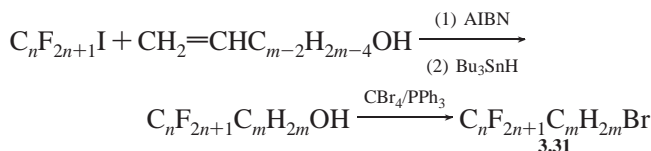
Diblock precursors with a chlorine-ended *F*-block, including $ClC_nF_{2n}CH_2CHIC_mH_{2m+1}$ **3.29** ($n = 4, 6; m = 4, 5$) and $ClC_4F_8CH_2CHICH_2CH_2CH=CH_2$ **3.30**, have been prepared by Raney nickel-catalyzed addition of $ClC_nF_{2n}I$ onto the appropriate alkenes.⁶⁴ Further diblock iodides of type **3.29** ($n = 4, 6; m = 4, 6$) have been obtained using PPh_3 as the catalyzer.⁶⁹

The terminally brominated diblocks $C_4F_9C_8H_{16}Br$ **3.31** and $C_8F_{17}C_4H_9Br$ have been synthesized by radical addition of $C_nF_{2n+1}I$ onto an ω -alkene-1-ol:⁹¹

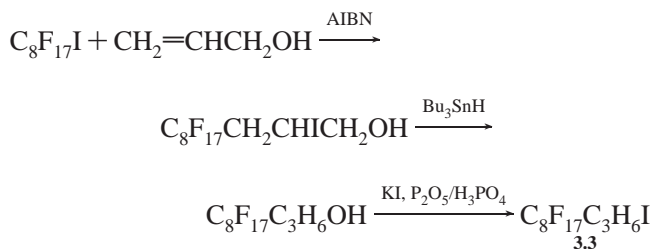


$(Ph_3P)_4Pd(0)$ catalysis allowed use of very mild conditions (0–20 °C, 1 h).

A large series of terminally brominated diblocks *F_nH_mF_n* **3.31** ($n = 8, m = 2, 4, 6, 10; n = 10, m = 10; n = 12, m = 10$) has also been obtained with AIBN catalysis:²⁹



Addition of $C_8F_{17}I$ to allyl alcohol, followed by reductive deiodination and iodination of the alcohol, was used to prepare the terminally iodinated diblock $C_8F_{17}C_3H_6I$:¹²¹



The higher homologue $C_8F_{17}C_4H_8I$ has been obtained under similar conditions.¹²²

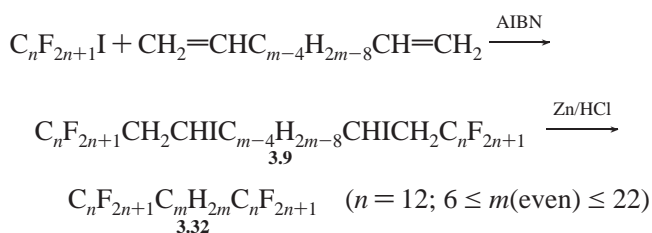
The rather inert, internally iodinated diblocks $C_nF_{2n+1}CH=CIC_6H_{13}$ ($n = 6, 8$) **3.17** have been prepared via the radical addition of *F*-alkyl iodides to alkynes for use as stabilizers of radiopaque emulsions.¹²³ Further diblocks with heavy halogens include the following: $C_nF_{2n+1}CBr=CH_2$, $C_nF_{2n+1}CBr_2CH_2Br$, $C_nF_{2n+1}CBr=CHBr$,¹⁰⁶ $C_nF_{2n+1}CBr=CBr_2$, $C_nF_{2n+1}CI=CH_2$, and $C_nF_{2n+1}CHICH_2Cl$.¹²⁴

$C_nF_{2n+1}C\equiv CMgI$, when treated with Br_2 , afforded $C_nF_{2n+1}C\equiv CI$ rather than $C_nF_{2n+1}C\equiv CBr$, and $C_nF_{2n+1}C\equiv CMgBr$, when treated with Cl_2 , gave $C_nF_{2n+1}C\equiv CBr$.¹²⁵

3.3. Triblocks and Multiblocks

3.3.1. *F_nH_mF_n* Triblocks

The synthesis of saturated triblock compounds of type *F_nH_mF_n* **3.32** has implemented the same procedures as for related diblocks, generally involving the free radical addition of *F*-alkyl iodides onto terminal alkadienes.^{75,126} Subsequent dehalogenation of intermediate **3.9** with zinc and acid afforded **3.32**:⁷⁷



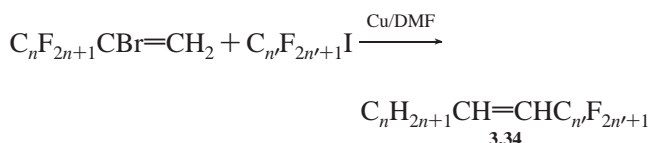
Some difficulties were encountered for the longer compounds (e.g., $C_{12}F_{25}I + CH_2=CH(CH_2)_{18}CH=CH_2$) during the dehalogenation step due to lack of solubility of intermediate **3.9** in ethanol. Higher boiling alcohols (e.g., propanol or butanol), a cosolvent (e.g., *n*-octane), excess of zinc, and long reaction times were required.⁷⁷ The reaction of C_3F_7I with 1,6-heptadiene (but not 1,5-hexadiene or 1,7-octadiene) in the presence of AIBN resulted in extensive cyclization to cyclopentane derivatives, in addition to formation of some mono- and diadduct.¹²⁶

The reaction rates for the addition of electrophilic *F*-alkyl radicals onto the “reluctant” alkenes $C_4F_9CH=CH_2$ **3.5** and $C_4F_9CH_2CH=CH_2$ **3.6** were, as expected, much slower than those with *n*-hexene.¹²⁷

The synthesis of shorter *F_nH_mF_n* triblocks, with $n = 6$ or 8 and $m = 4, 6, \text{ or } 8$, has recently been reported.¹²⁸ The compounds with $m = 4$ were obtained by treating two molecules of $C_nF_{2n+1}C_4H_8I$ with zinc in a Wurtz-type coupling reaction, and those with $m = 6$ or 8 were obtained by radical addition of $C_nF_{2n+1}I$ onto dienes, followed by reductive deiodination. Some unsaturated addition products, $C_nF_{2n+1}CH=CH(CH_2)_{m-4}CH=CHC_nF_{2n+1}$ **3.33**, were also formed. The diido precursor $C_8F_{17}CH_2CHICH_2CH_2CHICH_2C_8F_{17}$ has been prepared from the *F*-alkyl iodide and hexadiene using Ph_3P as a catalyzer.⁷⁰

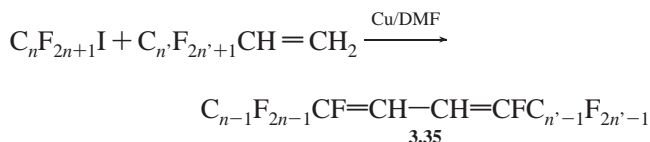
A series of remarkably inert unsaturated $C_nF_{2n+1}CH=CHC_nF_{2n+1}$ triblocks **3.34**, destined to serve as oxygen carriers (sections 9.4 and 10.1), has been synthesized by AIBN-initiated addition of $C_nF_{2n+1}I$ to $C_nF_{2n+1}CH=CH_2$, **3.5**, followed by dehydroiodination with $KOH/EtOH$.^{129,130} Only the *vic*-disubstituted compounds were formed. The yields were good in spite of the relatively electron depleted character of the substrates. Alternatively, these triblocks have

been prepared by reacting *F*-alkylcopper compounds with 1-bromo-1-*F*-alkylethenes in the presence of copper powder.¹³¹



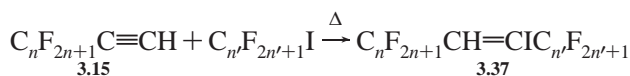
Branched members of the series, featuring isopropyl *F*-blocks, have also been reported.¹³²

A series of symmetrical and dissymmetrical dienes featuring the $-CF=CH-CH=CF-$ pattern has been synthesized by allowing *F*-alkyl iodides to react with (*F*-alkyl)ethenes in the presence of copper:¹³³



Depending on experimental conditions, the monounsaturated triblocks $C_{n-1}F_{2n-1}CF=CHCH_2C_nF_{2n+1}$ **3.36** and saturated triblocks $C_nF_{2n+1}CH_2CH_2C_{n'}F_{2n'+1}$ **3.32** were also obtained.

Thermal addition of *F*-alkyl iodides onto *F*-alkyl alkynes has provided a large series of internally iodinated compounds $C_nF_{2n+1}CH=CIC_{n'}F_{2n'+1}$ **3.37**:^{124,134}



Treatment with NaOH yielded the alkynes $C_nF_{2n+1}C\equiv CC_{n'}F_{2n'+1}$ **3.38**.¹²⁴ Bromination of **3.38** led to the internally brominated $C_nF_{2n+1}CBr=CBrC_{n'}F_{2n'+1}$ **3.39**, which were intended to serve as radiopaque material.

Triblocks with a rigid aromatic core, $F_nC_6H_4F_n$ ($n = 6, 7, 8, 10,$ and 12), have been produced¹³⁵ by addition of an *F*-alkyl copper reagent to an aromatic halide.¹³⁶

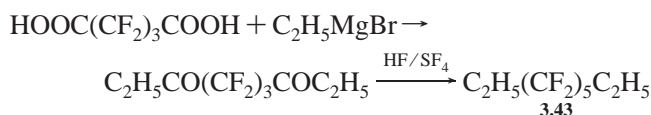
Triblock diethers $CF_3CH_2O(CH_2)_mOCH_2CF_3$ **3.40** with variable *HC* spacer length ($m = 3-10$) have been synthesized for ophthalmologic uses (section 10.2).¹³⁷

Access to triblock sulfides $C_nF_{2n+1}(CH_2)_2S(CH_2)_2C_6F_{13}$ **3.41** ($n = 4, 6$) has been achieved using a phase transfer catalysis procedure.¹¹⁸ Disulfide triblocks ($C_nF_{2n+1}C_2H_4S$)₂ ($n = 6, 8$), potentially useful for self-assembled monolayer studies, have been conveniently prepared through base-catalyzed oxidation of thiols $C_nF_{2n+1}C_2H_4SH$ by hydrogen peroxide.¹³⁸ Several synthetic routes to symmetrical triblock sulfides ($C_nF_{2n+1}C_mH_{2m}$)₂S **3.41** and disulfides ($C_nF_{2n+1}C_mH_{2m}$)₂S **3.42** ($n = 4, 6, 8; m = 2, 11$) have been investigated using the reaction of the appropriate iodides with sodium thiophosphate, sodium thiosulfate, or sodium hydrogen sulfide.¹³⁹ Sulfides $C_8F_{17}(CH_2)_mS(CH_2)_mC_8F_{17}$ **3.41**, with $m = 2$ and 3 , were prepared by allowing Li_2S to react with $C_8F_{17}(CH_2)_mI$ in THF.¹⁴⁰ These sulfides served as ligands to produce metal complexes for catalytic fluoros chemistry. Triblock sulfides and disulfides $C_nF_{2n+1}S(CH_2)_mSC_nF_{2n+1}$ and $C_nF_{2n+1}S(CH_2)_mSS(CH_2)_mSC_nF_{2n+1}$ ($n = 4$ or $6; m = 2, 3$) have also been reported.¹⁴¹

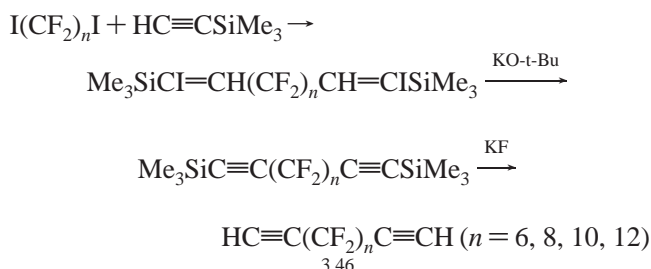
3.3.2. *HmFnHm* Triblocks

The “reverse” *HmFnHm* triblocks **3.43**, with a central *F*-block flanked by two *H*-blocks, are still scarcely represented. They can be derived directly from “telechelic” α,ω -

F-dialkanoic acids. The small reverse triblock *H2F5H2* has thus been prepared from *F*-glutaric acid and a Grignard reagent, followed by fluorination of the resulting diketone:⁷⁹



The diiodides $I(CF_2)_nI$ and, after bis(ethylenation), the α,ω -diiodinated triblocks $ICH_2CH_2(CF_2)_nCH_2CH_2I$ **3.44** or, after bis(dehydroiodination), the α,ω -divinyl-*F*-alkanes $CH_2=CH(CF_2)_nCH=CH_2$ **3.45** constitute further valuable starting materials for multiblock synthesis.^{103,142,143} Likewise for the α,ω -diacetylenic compounds **3.46**:¹⁰³



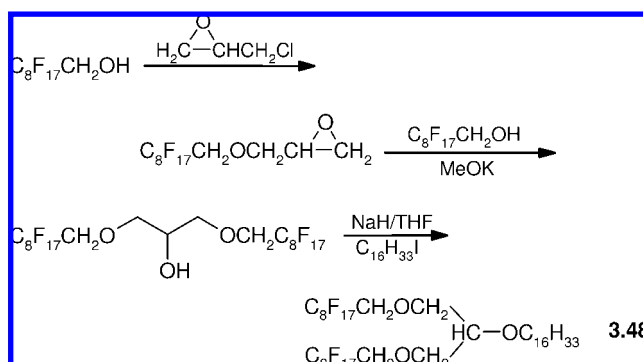
Triblocks with aromatic rings on both sides of an *F*-alkyl chain have been prepared from α,ω -diodo-*F*-alkanes and iodoaromatics in the presence of copper in a polar aprotic solvent.¹³⁶

Several *HmFnHm* triblocks ($n = 6, 8, 10; m = 6, 10, 14, 16$) have been obtained in good yield using the classical AIBN-induced addition of $I(CF_2)_nI$ on 2 equiv of the appropriate olefin, followed by Zn/HCl deiodination in ethanol.¹⁴⁴ Likewise, the “reverse” triblock ethers $C_mH_{2m+1}(CF_2)_2O(CF_2)_2C_mH_{2m+1}$ **3.47** ($m = 5, 12$) have been obtained from $I(CF_2)_2O(CF_2)_2I$ and $C_{m-2}H_{2m-3}CH=CH_2$, followed by deiodination.

Successive brominations and dehydrobrominations of $CH_2=CH(CF_2)_nCH=CH_2$ **3.45** led to the polybrominated triblocks $BrCH_2CHBrC_nF_{2n}CHBrCH_2Br$, $CH_2=CBrC_nF_{2n}CBr=CH_2$, $BrCH_2CBr_2C_nF_{2n}CBr_2CH_2Br$, and $BrCH=CBrC_nF_{2n}CBr=CHBr$.¹⁰³

3.3.3. Star-Shaped Triblocks

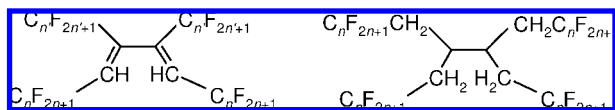
Star-shaped triblocks of type **3.48** with two *F8* chains and one *H*-chain on a glycerol triether linkage have been synthesized according to¹¹⁶



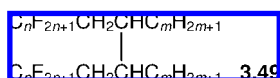
Analogous with a C_2H_4 segment between the *F*-chains and the ether junction or with a branched phytol *H*-chain were also produced.

3.3.4. Multiblocks and Polyaffine Compounds

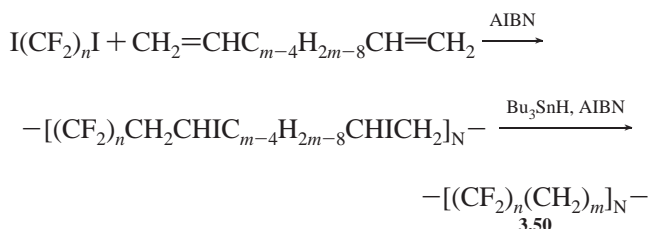
The iodinated triblocks $C_nF_{2n+1}CH=CIC_nF_{2n+1}$ **3.37**¹³⁴ and $C_nF_{2n+1}CH_2CHIC_nF_{2n+1}$,⁹⁸ after coupling using copper or zinc, yielded “pentablocks” (or interconnected triblocks) with four *F*-chains attached to a hydrogenated core.



Multiblocks of type **3.49** with two *F*-chains and two *H*-chains grafted on a *H*-core ($n = 8, 10; m = 6, 12, 14, 16, 18, 20$) have been prepared in good yield by coupling of iodinated diblocks $C_nF_{2n+1}CH_2CHIC_mH_{2m+1}$ using activated zinc in acetic anhydride.¹⁴⁵ These fused-diblock compounds can be viewed as “primitive” gemini surfactants (or as consisting of a flexible $H(2m + 2)$ chain fitted with two pendent adjacent rigid $F8CH_2$ chains).

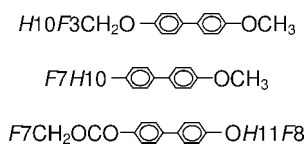


By extension, microblock polymers with regular repeating $-[FnHm]_N-$ sequences ($n = 4$ or $6; m = 6-14$) should be mentioned. They have been obtained when α, ω -diiodo-*F*-alkanes (e.g., $I(CF_2)_nI$, $n = 4, 6$) were allowed to react with α, ω -dienes:¹⁴⁶



Small multiblocks, such as $CF_3CH_2CH_2CF_3$, $CF_3CH_2CF_2CH_3$, and $CF_3CH_2CF_2CH_2CF_3$, with alternating one or two carbon *F*- or *H*-fragments, have also been synthesized.⁷⁹

Linear “polyphilic” multiblocks combining various sequences of *F*- and *H*-blocks along with a rigid aromatic core, for example, a diphenyl block flanked by two different side chains, as in



which display mesomorphic and ferroelectric properties (section 5), have been constructed. Multiaffine molecules comprising *F*- and *H*-blocks and a PEG chain, all bound to the same double bond in a starlike configuration, have been reported.¹⁴⁹ The controlled synthesis of well-defined polymers with semifluorinated segments, side chains, or chain ends has recently been reviewed.¹⁵⁰

4. Basic Properties of (*F*-Alkyl)alkyl Diblocks

The basic properties of *F**nH**m* diblocks reflect their amphisteric, amphiphilic, and amphidynamic characters. While many of the physical properties of (*F*-alkyl)alkyl diblock compounds, including their density, surface tension, refractive index, and compressibility, fall in between those

Table 2. Physical Properties of Linear *n*-Hexanes (Used with Permission from Refs 10 and 11)

property	C_6F_{14}	$C_3F_7C_3H_7$	C_6H_{14}
molecular weight	338	212	86
boiling point (°C)	57	64	69
heat of vaporization, ΔH_v (kJ mol ⁻¹)	28	33	29
critical temperature, T_c (°C)	174	200	235
density, d^{25} (g cm ⁻³)	1.672	1.265	0.655
compressibility, β , at 1 atm (10 ⁻⁶ atm ⁻¹)	254	198	150
viscosity, η^{25} (cP)	0.66	0.48	0.29
surface tension, γ^{25} (mN m ⁻¹)	11.4	14.3	17.9
refractive index, n_D^{25}	1.252	1.290	1.372
dielectric constant, ϵ	1.69	5.99	1.89

of their *FC* and *HC* counterparts, other important characteristics can differ substantially from those of the parent compounds. The latter is illustrated, in the case of *n*- $C_3F_7C_3H_7$, by a heat of vaporization that is higher and a dielectric constant that is much higher than those for both *n*- C_6F_{14} and *n*- C_6H_{14} (Table 2).^{10,11} *F**nH**m* diblocks also manifest properties, such as the existence of a dipole moment (2.3 D for *n*- $C_3F_7C_3H_7$) and surface activity, that are essentially absent in the parent *FC* and *HC*.

The CF_2-CH_2 bond at the junction between the two blocks is reinforced, as illustrated by a bond dissociation energy of 423 kJ mol⁻¹ for CF_3-CH_3 as compared to 371 and 413 kJ mol⁻¹ for CH_3-CH_3 and CF_3-CF_3 , respectively.¹⁵¹ The C—C bond is also shorter in the mixed ethane CF_3-CH_3 (1.494(3) Å), as compared to C_2F_6 (1.545(2) Å) and C_2H_6 (1.532(1) Å).¹⁵² Most importantly, this junction is the seat of a strong dipole moment.

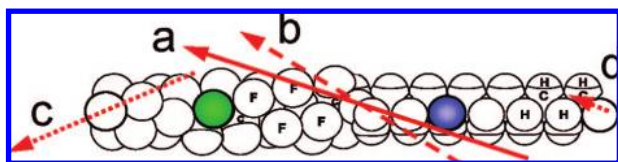
The incompatibility between *F*- and *H*-chains engenders important effects on the solubility, segregation, packing, aptitude at self-assembly, dynamics, and other properties of *F**nH**m* diblocks. The ~30% smaller cross-sectional area of hexagonally packed *H*-chains as compared to similarly packed *F*-chains facilitates conformational disordering of the *H*-block. As expected, the impact on properties of an *H*-segment located at the end of an *F*-chain is more pronounced than when such a segment is buried within the molecule (e.g., diblock $C_8F_{17}CH=CH_2$ vs triblock $C_4F_9CH=CHC_4F_9$). The shape of the molecule (e.g., *E*- $F6CH=CHF6$ vs $F6CH_2CH_2F6$) can also have an effect on certain properties, for example gas solubilities.

The physical properties of *F**nH**m* diblocks are strongly interrelated. Polarity, surface activity, solubility, and self-aggregation behavior, and their consequences, will be discussed separately only for the sake of clarity.

4.1. The “Polarity” Issue—“Apolar”, yet Dipolar

(*F*-Alkyl)alkyl diblocks are generally viewed as being apolar molecules in the sense that they do not have a polar—hydrophilic—moiety, do not dissolve in protic solvents, and display dielectric constants lower than those of their *HC* counterparts. Although this is indeed the case, *F**nH**m* compounds, because their C—F bond dipoles do not all cancel out and are stronger and oriented opposite to those of typical C—H dipoles, have nevertheless significant dipolar character. The *F*-alkyl chain is strongly electron-withdrawing, thus causing substantial displacements of electronic charges and creating an electric dipole at its junction with the *H*-alkyl chain (Scheme 4.1). This dipole is a definite source of anisotropy. The terminal CF_3 group and, to a lesser extent, the terminal CH_3 group, also contribute dipoles. Since the axes of these CF_3 and CH_3 groups are at an angle with the

Scheme 4.1. *F*-Alkyl/*H*-Alkyl Diblocks Host a Strong Dipole (a), with Components Arising from (b) the *F_n–H_m* Junction, (c) the Terminal CF₃, and (d), to a Much Lesser Extent, the Terminal CH₃



axis of the molecule, the total dipole moment of the molecule is not aligned with the axis of the molecule. The exact orientation of the molecular dipole of *F_nH_m* diblocks is also expected to be sensitive to the parity, even or odd, of the number of carbons in the two blocks.

Dielectric constants (a common gauge for solvent polarity) of *F_nH_m* diblocks range up to 6.5. Table 2 exemplifies the case of *F3H3*, for which the dielectric constant ($\epsilon = 5.99$) is over three times larger than that for its *FC* and *HC* counterparts. The dielectric constant diminishes as the length of the blocks increases. Thus, a dielectric constant of 4.47 has been reported for *F6H6* at 25 °C (as compared to 1.87 and 2.02 for C₁₂F₂₆ and C₁₂H₂₆, respectively).¹⁵³ As an example of a practical consequence, some diblocks are more soluble in methanol than *FC*s and *H_mC*s of similar length.¹⁵⁴

While the existence of a substantial dipole moment for *F_nH_m* diblocks is unquestionable, the exact values of this moment and of its group contributions remain uncertain. The molecular dipole moment of CF₃–CH₃ has been determined by microwave spectroscopy (hence as a dilute gas) to be 2.32 ± 0.03 D.¹⁵⁵ The following group dipole moments have been calculated for *F*-chains from experimental data obtained for the corresponding *F*-acid methyl esters *F_nCOOMe*: CF₃, 2.30 D; C₂F₅, 2.46 D; C₃F₇, 2.46 D; and C₄F₉, 2.47 D.¹⁵⁶ These values leveled off rapidly as the chain length increased.

The dipole moment of *F8H18* has been calculated ab initio to be 3.1 D¹⁵⁷ or 3.4 D,¹⁵⁸ based on semiempirical calculations. The dipole moment of an extended series of *F_nH_m* diblocks ($n = 4–12$, $m = 1–20$) has been evaluated to 2.8 ± 0.1 D, regardless of n and m using semiempirical calculations in vacuum.¹⁵⁹ The angle between the dipole moment vector and the diblock's long axis was estimated at a large and uniform 35°. Similar calculations provided a value of 2.9 D for the total dipole moment of an isolated *F10H19* diblock, with an inclination of 51° with respect of the axis of the molecule.¹⁶⁰ The dipole moments of several 2-to-4-carbon atom gaseous hydrofluorocarbons have been determined.¹⁶¹

Dipole moments of diblocks have also been calculated from surface potential measurements on Langmuir monolayers. However, these values represent minimum values of the apparent dipole moments μ_{\perp}/ϵ , with ϵ being the permittivity of the monolayer, and they depend on compression (section 8). A value of 0.30–0.35 D is generally retained for μ_{\perp} (the vertical component of the dipole moment vector, also called the “effective” dipole moment) of the terminal CH₃ group of a fatty acid in a compact monolayer.^{162–164} A value of 1.9 D has been mentioned for the CF₃ group.¹⁶²

As for the contribution of the CF₂–CH₂ junction, there appears to be no reliable direct evaluation available yet. The CF₂–CH₂ dipole was found to increase the wettability of surfaces coated with monolayers of molecules featuring CF₂–CH₂ junctions as compared to perfluorinated analogues.¹⁶⁵ Increasing the length of the *F*-chain reduced this

effect by removing the electric center of gravity of the dipole further from the surface of the adsorbed monolayer. A similar variation has been observed for self-assembled monolayers of (*F*-alkyl)alkanethiols on gold.¹⁶⁶

Molecular orientation correlations within liquid *F_nH_m* diblocks are also influenced by the presence of the CF₂–CH₂ dipole.¹⁶⁷ For a given total diblock length, short *F*-chains ($n = 1–4$) were found to strongly hinder orientational correlations, while this trend was reversed when n reached 6. Dipole–dipole interactions among molecules can bring about unusual properties, absent from both *n*-alkanes and *F*-*n*-alkanes, for example ferroelectric properties.¹⁶⁸ Likewise, it is largely the CF₂–CH₂ dipole that confers to diblocks their unique ability, among small molecules, to self-assemble into large monodisperse and stable surface micelles¹⁶⁹ (section 8.3).

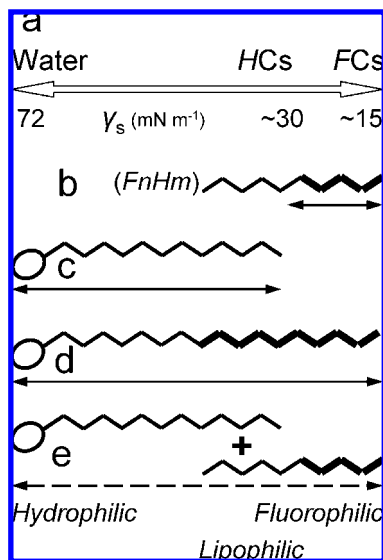
Electric dipole–dipole interactions can obviously influence the packing of diblock molecules and, hence, their macroscopic properties. Conversely, dipole moments are sensitive to molecular constitution, conformation, and packing, and they can therefore be used to probe the environment of a diblock molecule and assess conformational changes associated with a phase transition. Dielectric spectroscopy has thus been used to investigate the solid state behavior of diblocks (section 5).¹⁷⁰ For example, the dipole moment of *F12H8* was, surprisingly, 2.3 times larger than that of *F10H10*, and the dielectric relaxation activation energies of the two compounds were significantly different in the mesophases found below their melting point, indicating packing differences.¹⁷¹ The influence of the dipole on solid state structure and behavior is expected to diminish as the length of the diblock increases.

The relative polarity of a solvent is of utmost importance when practicing synthesis and product separation using fluorous media.¹⁷² Solvent polarity has been characterized, in particular, by a spectral polarity index (P_s) based on the shift of the maximum UV–visible absorption of an *F*-alkylated dye that is soluble in a wide range of solvents, including highly fluorinated ones.^{11,173} *FC*s display the lowest polarity of all solvents. They are essentially insoluble in water¹⁷⁴ and are poor solvents except for other *FC*s and other material with low cohesive energies, such as gases.^{175,176} Due to their dipole moment, higher P_s values are expected for *F_nH_m* diblocks than for perfluorinated compounds. A P_s value of 4.01 has been reported for *F4H2*, as compared to 0.00 for C₆F₁₄ and 2.56 for C₆H₁₄.¹¹ Diblocks have, therefore, the capacity for modulating the relative polarity and partition of solutes between a “fluorous” and an organic phase.^{177,178} “Fluorophilicity” has also been characterized using the Hildebrand solubility parameter and the partition coefficient of the test material between *F*-methylcyclohexane, a representative fluorous solvent, and toluene at 25 °C; a “specific” fluorophilicity was defined to account for volume differences among solvents.¹⁷⁹ The fluorophilicity of *F8CH=CH₂* was higher than that of C₁₀F₂₁I on this specific fluorophilicity scale.

4.2. Surfactant Properties

Surface activity requires the association, within a molecule, of moieties (or blocks) that have different cohesive energy densities, resulting in amphiphilic character. *F_nH_m* diblocks are fluorophilic (and lipophobic) at one end and lipophilic (and fluorophobic) at the other. Because neither moiety is hydrophilic, these diblocks were called “primitive surfac-

Scheme 4.2. Schematically Represented on the Hydrophilic/Fluorophilic (Hydrophobic) Scale (a), along with Typical Surface Tension Values γ_s , Are the Surface Activity Ranges of (b) a Lipophilic/Fluorophilic *FnHm* Diblock, as Compared to (c) a Standard Hydrophilic/Lipophilic *H*-Surfactant and (d) an *F*-Surfactant with a Hydrocarbon Spacer. Part e Depicts the Cosurfactant Effect Anticipated between an Appropriate *FnHm* Diblock and a Standard *H*-Surfactant^a



^a The double-headed arrows depict the surface tension reductions achieved. From ref 379.

tants”,⁵⁴ as opposed to conventional surfactants that comprise a hydrophilic polar head and a hydrophobic chain. In standard fluorinated surfactants (*F*-surfactants), the polar head is opposed to an *F*-chain (with, optionally, but frequently, a hydrocarbon spacer in between).^{12,35,49–51,180} *FnHm* diblocks, when investigated as model surfactants in alkanes or *F*-alkanes, have the advantage over standard surfactants in aqueous media of involving a much simpler set of interactions. In particular, the absence of strong electrostatic interactions with water is expected to facilitate the investigation and understanding of the surfactant behavior of amphiphilic molecules. Conversely, *F*-surfactants that include an *H*-spacer can be viewed as diblocks fitted with a polar head. Interestingly, the micellization and adsorption properties of such surfactants is dominated by the *F*-chain, while the *H*-block tends to behave as if it were shorter by a factor of about three and, hence, plays only a minor role in these processes.¹⁸¹

Scheme 4.2 represents the realm of surface activity of *FnHm* diblocks, as compared to that of standard *H*- and *F*-surfactants. It also envisages the association of a diblock with a conventional *H*-surfactant (Scheme 4.2e). Properly chosen *FnHm* diblocks can indeed act as cosurfactants and amplify the interfacial activity of a nonfluorinated surfactant.

Surface activity involves the spontaneous adsorption of a film of surfactant molecules at interfaces (section 8.1) and the formation of micelles or micelle-like aggregates when the concentration of surfactant exceeds a critical value (section 7.1).

4.2.1. Surfactant Effects of *FnHm* Diblocks at Interfaces with Air, Fluorocarbons, and Hydrocarbons

The surface tension γ_s measures the molecular forces per unit length on a liquid surface that oppose expansion of the

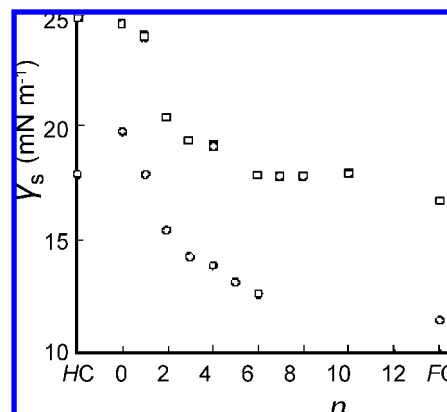


Figure 4.1. Surface tension γ_s , at 25 °C, of neat liquid *FnHm* diblocks decreased with increasing weight of the *F*-chain in the *FnH*(12-*n*) and *FnH*(6-*n*) series, and it leveled off at about 17.9 and 12.5 mN m⁻¹, respectively. From ref 154 with permission.

surface area. *FCs* have the lowest γ_s values of any organic liquid and completely wet any solid surface. *FCs* have lower surface tensions than *HCs* of similar length because of their lower cohesive energy density. For example, *n*-C₆F₁₄ has a surface tension γ_s of 11.4 mN m⁻¹ at 25 °C, as compared to 17.9 mN m⁻¹ for *n*-C₆H₁₄.¹¹ The same difference is found for polymers, with surface tensions of 18.5 versus 31 mN m⁻¹ for $-(CF_2CF_2)_n-$ and $-(CH_2CH_2)_m-$, respectively. The surface tensions of *FnHm* diblocks lie in between those of their *FC* and *HC* parents. Thus, C₃F₇C₃H₇ has a surface tension of about 14 mN m⁻¹ at 25 °C¹⁵⁴ as compared to 11.4 and 17.9 mN m⁻¹ for C₆F₁₄ and C₆H₁₄, respectively. In this context, it should also be noted that *FC/HC* mixtures can produce lower surface tensions than both individual components.¹⁸²

The surface tension of neat liquid *FnHm* diblocks has been shown to decrease, as expected, when the weight of the *F*-chain increased in the *FnH*(12-*n*) series and leveled off at about 17.8 mN m⁻¹ at 25 °C (Figure 4.1).¹⁵⁴ For the shorter *FnH*(6-*n*) series, leveling off occurred at about 12.5 mN m⁻¹.

When dissolved in a *HC*, *FnHm* diblocks are expected to adsorb at the *HC*/air interface and form a monolayer (Gibbs film) with the *F*-blocks pointing toward air, thus reducing the surface tension to a value typical of a *FC*. Reduction of the surface tension γ_s of *HCs* by addition of *FnHm* diblocks is indeed well documented.^{39,183–187} Paralleling the behavior of “complete” *F*-surfactants at the air/water interface, increasing *F*-chain length in diblocks resulted in increased surface tension reduction effectiveness. The surface tension depression of *n*-dodecane solutions increased with increasing total chain length in the *F12Hm* (*m* = 4, 8, 14, and 18) series, reaching 4 mN m⁻¹ for *F12H18* (Figure 4.2).¹⁸³ Surface tension depression of diblock solutions in Vaseline oil also increased with increasing *F*-chain length.¹⁸⁴

Conventional surfactants with a polar head and a *HC* tail typically reduce the surface tension γ_s of pure water from 72 mN m⁻¹ to about 30 mN m⁻¹, which is the typical surface tension at a *HC*/air surface, while *F*-surfactants allow reduction of γ_s of water to 25–15 mN m⁻¹.^{51,188} The maximum surface tension reduction expected for *FnHm* diblocks at a *HC*/air surface is essentially the difference between the γ_s at *HC*/air and at *FC*/air surfaces, which is on the order of 10 mN m⁻¹.¹⁸⁵ *FnHm* diblocks are thus expected to be much less effective than conventional surfactants in terms of surface tension reduction capacity, but the interfaces at which they can exercise their activity are different.

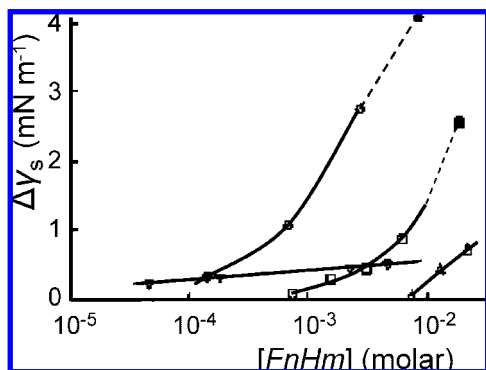


Figure 4.2. Surface tension reduction $\Delta\gamma_s$ for *n*-dodecane solutions induced by addition of *F12Hm* diblocks, as a function of diblock concentration: (∇) $m = 4$; (Δ) $m = 8$; (\square) $m = 14$; (\circ) $m = 18$; solid signs denote samples in which a small amount of gel phase was present; lines added. From ref 154 with permission.

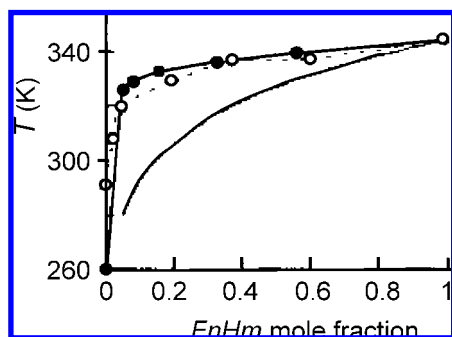


Figure 4.3. Temperature dependence of the solubility of *F10H16* in $C_{16}H_{34}$ (open circles) and in C_9F_{18} (filled circles). Strong deviation from ideal solution behavior (lower solid curve) is seen, reminiscent of Krafft behavior of conventional surfactants. From ref 189 with permission.

The amphiphilic strength of a solute in a solvent is reflected by the extent to which the temperature dependence of the solubility deviates from ideality. Thus, the solubility of *F10H16* in both *FCs* (*F*-nonane, *F*-decalin) and *HCs* (hexadecane, eicosane) as a function of temperature deviated strongly from ideal behavior (Figure 4.3).³⁹ A sudden increase in solubility at a given temperature was noted. This means that *FnHm* diblocks display a “Krafft point” similar to that found for conventional surfactants in water, but not as sharp. At the Krafft temperature (the temperature at which monomer solubility equals the critical micellar concentration (CMC), the concentration above which micelles begin to form in the solvent), the solubility of the surfactant increases sharply due to micelle formation in which the molecules are highly soluble. The Krafft temperature of *FnHm* solutions was seen to increase with the length of the diblock and solvent molecules.¹⁸⁹

The surface tension of *F12H16* in hexadecane has been determined as a function of temperature and concentration below the Krafft point.¹⁹⁰ It indicated a surfactant behavior (including Gibbs film behavior, section 8.1) similar to that of fatty alcohols at water/air or water/oil interfaces. Further measurements of the temperature dependence of surface tension for diversely concentrated solutions of *F12H18* in dodecane (pendant drop method) also showed a sharp change in slope of γ_s at a transition temperature that increased with diblock concentration.¹⁸⁷ Above the transition temperature, a slight linear decrease of γ_s indicated a weak adsorption of diblock at the free surface of the *HC*. Below the transition, the temperature dependence of γ_s became strongly positive.

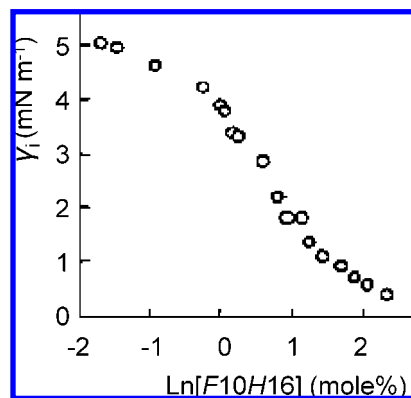


Figure 4.4. Variation of the interfacial tension γ_i at equilibrium between *F*-nonane and hexadecane upon addition of *F10H16*, demonstrating the adsorption of the diblock at the interface. The $C_9F_{20}/C_{16}H_{34}$ weight ratio was 2.3, corresponding to equal volumes; the temperature was 64 °C, i.e., above the Krafft temperature. From ref 189 with permission.

The mean area per diblock molecule at the dodecane surface was estimated at $34 \pm 2 \text{ \AA}^2$, which is $\sim 20\%$ larger than that for a close-packed *F*-chain (28 \AA^2).

The surface tension of 1,1,2,2-tetrachloroethane was significantly depressed by addition of the allyl ether diblocks $FnHmOCH_2CH=CH_2$.¹¹⁵ For $n = 12$ and $m = 6$, γ_s was reduced by about 11 mN m^{-1} , from 34.4 mN m^{-1} to 23.5 mN m^{-1} , for a concentration of 0.25 wt %. Sharp breaks in the surface tension versus concentration curves indicated a critical micellar concentration (section 7.1).

On the other hand, *FnHm* diblocks *cannot* reduce the surface tension of a *FC*, since it would increase, rather than decrease, the *FC*'s surface energy. Thus, addition of 7 wt % of *F8H16* to *F*-octane at 41 °C did not decrease γ_s below that of pure *F*-octane.³⁹

At a *FC/HC* interface, diblocks are expected to behave like standard surfactants behave at a *HC*/water interface. They reduce the energy (reflected by the interfacial tension γ_i) that opposes extension of the contact surface area, thereby facilitating dispersion of one of the immiscible phases in the other. Diblocks form monolayers at *FC/HC* interfaces that can stabilize such dispersions (e.g., *HC*-in-*FC* emulsions, section 9). Figure 4.4 shows the variation of γ_i between *F*-nonane and hexadecane observed upon addition of *F10H16*, demonstrating the adsorption of the diblock at the interface.

Critical micellar concentration values, a key characteristic of surfactant behavior, have been determined, using fluorescence probe solubilization and light scattering experiments, to be 5.8 wt % for *F8H12* in *F*-tributylamine and ~ 4.5 wt % for *F8H16* in *F*-octane.⁵⁴ These values are high but can also be encountered with conventional surfactants. The aggregation numbers of about 4–6 are low but on the same order as those observed, for example, in bile salt micelles.

Further manifestations of the amphiphilic character and surface activity of *FnHm* diblocks include their aptitude at forming liquid crystalline phases in the bulk (section 5), their tendency for self-aggregation as micelles in solutions (section 7.1) and as hemimicelles on a surface (section 8.3), their ease of formation of stable Gibbs (section 8.1) and Langmuir monolayers at interfaces (section 8.2), their aptitude at serving as foaming agents, and their capacity for reinforcing bilayer membranes (section 9.1) and stabilizing *HC*-in-*FC* emulsions as the sole surfactant (section 9.4).

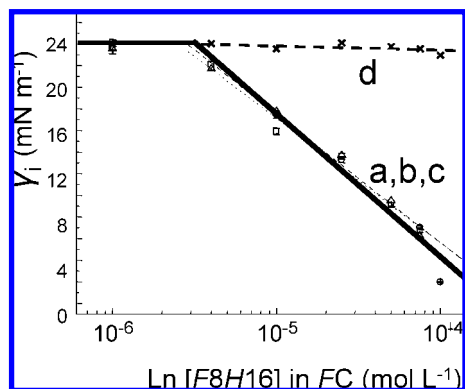


Figure 4.5. (a, b, c) Variation of the interfacial tension, γ_i , between solutions of *F8H16* in $C_8F_{17}Br$ and solutions of various phospholipids in water, as a function of the logarithm of the concentration of *F8H16* in $C_8F_{17}Br$; the linear segments of the curves were fitted with a straight line. The phospholipid solutions investigated were of DMPC (a, triangles, 1.66×10^{-11} mol L^{-1} ; dashed line), DLPC (b, squares, 1.25×10^{-9} mol L^{-1} ; dotted line), and PLC8 (c, circles, 3.73×10^{-5} mol L^{-1} ; solid line); (d) variation of γ_i between solutions of $C_{10}F_{21}Br$ in $C_8F_{17}Br$ and a DMPC solution (1.66×10^{-11} mol L^{-1}); see also section 9.3. From ref 191.

4.2.2. Cosurfactant Effects

The surface activity of a diblock can complement that of a conventional nonfluorinated surfactant in binary surfactant mixtures, thus decreasing a surface or interfacial tension well below what is achievable with the conventional surfactant alone (Scheme 4.2). The γ values attained should become comparable to those attained with an *F*-surfactant, which are on the order of 15–20 mN m^{-1} .

Definite evidence for a cosurfactant effect at the water/*FC* interface has been provided by the observation of a dramatic decrease in *FC*/water interfacial tension, typically from about 24 to about 2 mN m^{-1} (pendant drop method) between a *FC* and an aqueous phospholipid solution, when a diblock was added to the *FC* phase.¹⁹¹ Figure 4.5 depicts the variation, with the logarithm of *F8H16* concentration in *F*-octyl bromide ($C_8F_{17}Br$), of the interfacial tension γ_i between aqueous solutions of dimyristoylphosphatidylcholine (DMPC), dilaurylphosphatidylcholine (DLPC), or dioctanoylphosphatidylcholine (PLC8) and the *FC*. It shows that γ_i decreases strongly and linearly with *F_nH_m* concentration, which establishes the cosurfactant activity of the diblock and, hence, its presence at the phospholipid/*FC* interface.

The coadsorption of diblock *F8H2* with a series of phospholipids (DLPC, DMPC, DPPC) has also been investigated at the air/water interface.¹⁹² Surface tension γ_s was measured at the interface between variously concentrated phospholipid dispersions and a rising bubble of *F8H2*-saturated air. *F8H2* was found to cause a dramatic acceleration of the adsorption of the phospholipids investigated. Moreover, for any given phospholipid concentration, γ_s at equilibrium was lower than that measured in the absence of the diblock. This lowering increased with the phospholipid's chain length, suggesting that long phospholipid chains accommodated the diblock more easily. In another series of experiments, γ_s was measured between air and a dispersion, in a buffer, of small unilamellar vesicles made of a DMPC/*F6H10* 1:1 mixture. The diblock was again found to accelerate the adsorption of the phospholipid at the air/water interface and to lower the equilibrium surface pressure. See also section 9.3 for the increase in amount of phospholipids

adsorbed on *FC*-in-water emulsion droplets upon addition of a diblock compound.¹⁹³

4.3. Solubility Properties

This section will briefly consider the solubility of *F_nH_m* diblocks: first in *FCs*, *HCs*, other diblocks, and CO_2 ; then in polar media and water; then the solubility of gases in diblock compounds; and eventually that of polar substances in such compounds.

The disparity in cohesive energy densities between *FCs* and *HCs* (which largely determines their lack of mutual solubility) is reflected by a difference in Hildebrand parameter ($\delta = \Delta H^{1/2} V_m^{-1/2}$, where ΔH is the molar vaporization energy and V_m the molar volume, $MPa^{1/2}$) between *FCs* (~ 6 hildebrands) and *HCs* ($7-9$ hildebrands). For comparison, the Hildebrand parameters for O_2 and water are 5.7 and 23.4 hildebrands, respectively. This means that *FCs* are choice solvents for O_2 and that, on the contrary, their solubility in water and polar solvents is extremely low. The highly nonideal mixing of liquid *FCs* and *HCs*, and likewise of *F*-chains and *H*-chains, translates into *F*-chains being lipophobic and *H*-chains being fluorophobic, which promotes their separation.

4.3.1. Solubility of Diblocks in Fluorocarbons, Hydrocarbons, and Other Diblocks

4.3.1.1. Binary Systems. *F_nH_m* compounds usually show some finite solubility in both *FCs* and *HCs*. Phase diagrams are available for binary mixtures involving *F8H12*, *F10H12*, and *F12H_m* ($m = 6, 8, 10, 12$),⁴⁴ and *F8H16* and *F12H16*⁷⁸ with *F*-alkanes and alkanes. As diblock concentration increases, adsorption at interfaces increases and the formation of a surface monolayer (Gibbs film) is generally observed (section 8.1). Some, usually limited, aggregation (micelle formation) can occur in the solution (section 7.1). At still higher concentrations, *F_nH_m* diblocks eventually precipitate from the solution and form gels (section 7.2).

While *FCs* and *HCs* having seven carbon atoms or more are not totally miscible at room temperature, some comparatively large *F_nH_m* diblocks are miscible in *FCs* and *HCs*, provided chain lengths are similar. For example, isotropic liquid phases have been observed in *HCs* (e.g., for *F8H12*/ $C_{20}H_{42}$ mixtures) or in *FCs* (e.g., *F12H8*/ $C_{20}F_{42}$ mixtures), i.e., when the weight of the *H*- or *F*-block, respectively, of the diblock is sufficient.⁴⁴ Vapor pressure osmometry data indicated that *F12H14*/ $C_{20}H_{42}$ and *F12H14*/benzil (1,2-diphenylethanedione) solutions behaved ideally up to the solubility limit (~ 2.3 and 0.8 mol %, respectively).¹⁸⁵ Formation of solid solutions (usually grossly nonideal for the low-temperature form) from diblock combinations required that the *F*- and *H*-blocks of the components be of similar length (e.g., *F12H6* with *F12H8* or *F12H8* with *F12H12*).⁴⁴ The *F10H12*/*F12H10* system was partially fractionated at low temperature, whereas the more asymmetric *F12H8*/*F8H12* system was a eutectic. However, even the closely related *F8H10Br* and *F10H10Br* were not miscible in the solid.²⁹

A semiempirical solubility parameter has been defined that allows prediction of the solubility of *HCs* in hydrofluorocarbon compounds.⁷⁹ Within an isomeric or close-to-isomeric family (e.g., $C_3F_7C_2H_5$ vs $CF_3CH_2CF_2CH_2CF_3$), the best solvents for *HCs* were the compounds having the maximum

separation of fluorines from hydrogens, that is the *FnHm* diblock compounds.

The affinity for *HCs* (lipophilicity) of a large variety of *FnHm* compounds ($4 \leq n \leq 10$; $2 \leq m \leq 16$) has been characterized using a critical solution temperature of the diblocks in *n*-hexane (CST_{hex} , defined as the temperature at which equal volumes of diblock and hexane form a single isotropic phase) or in *n*-bromohexane ($CST_{\text{Br-hex}}$) for the more lipophilic compounds.¹⁹⁴ The lipophilic character of diblocks was seen to increase with increasing *m/n* ratio. The effect of a C_2H_5 block (as in $C_8F_{17}C_2H_5$, *F8H2*) on the lipophilicity of an *FC* was comparable to that of one terminal bromine atom (as in $C_8F_{17}Br$) or of two terminal chlorines (as in $C_8F_{16}Cl$). Branching (as in an isobutyl block) caused a decrease in lipophilicity, which was assigned to the more compact character of the isobutyl group relative to the linear *n*-butyl group.¹⁹⁴ The CST_{hex} values for a series of *FnCH=CHFn'* triblocks increased exponentially with MW and were, as expected, closer to those of linear *FCs* than to those of *FnHm* diblocks.¹⁹⁵

Solubility of *FCs* and *FnHm* diblocks in olive oil (as a model for circulating chylomicrons, responsible for lipid transport in the blood) has been used to characterize the lipophilicity of highly fluorinated compounds and predict their organ retention half-life and excretion rate when administered in the blood circulation as emulsions.¹⁹⁴ As expected, the olive oil solubility of diblock *F8H2* (29 mM at 25 °C) was much larger than that of C_8F_{18} (4.8 mM) and on the same order as that for $C_8F_{17}Br$ (37 mM). The latter compound is substantially more lipophilic than C_8F_{18} , due to its well exposed, polarizable terminal bromine atom.¹⁹⁶

The excess thermodynamic functions of mixtures of *F6H12* or *FnCH=CHHm* ($n = 6, m = 10$; $n = 8, m = 6, 10$) diblocks with $C_8F_{17}Br$ or with triblock *F4CH=CHF4* have been measured.¹⁹⁷ Complex, component, and molar ratio-dependent deviations from ideality, different from those found for typical *FC/FC*, *HC/HC*, and *FC/HC* mixtures, were seen. Thermodynamic stabilization (negative excess Gibbs energy) was, for example, observed when small amounts of *F8CH=CHH6* were added to $C_8F_{17}Br$.

Simple models have been used to predict, from a molecular perspective, the phase behavior of selected binary mixtures of *FnHm* diblocks with *n*-alkanes and *F-n*-alkanes.¹⁹⁸ However, the lack of experimental data did not allow validation of these predictions. A subsequent paper provided experimental partial molar volumes at infinite dilution for *F6H6*, *F6H8*, *F8H18*, and *F10H8* in *n*-octane at 25 °C.¹⁹⁹ The molal volumes were larger than those calculated using CF_2 , CF_3 , CH_2 , and CH_3 group contributions, and the differences were assigned to the CF_2-CH_2 junction. The values were in good agreement with values obtained by modeling the *FnHm* diblocks using the hetero-SAFT-VR equation of state. The latter thus allowed prediction of the volumetric behavior of the diblocks.

The solubility of (*F*-alkyl)alkyl diblocks can be improved by introducing structural elements that hinder crystallization, for example heteroatoms. Thus, the allyl ethers $C_nF_{2n+1}(CH_2)_mOCH_2CH=CH_2$ were substantially more soluble in organic solvents than the compounds without an oxygen atom.¹¹⁵

The partial miscibility of certain *FnHm* diblocks (e.g., *F6H8*) with silicon oils (e.g., silicone oil 5000) should be mentioned, as it has applications in ophthalmology (Section 10.2).^{200–203}

4.3.1.2. Ternary Systems. Partition coefficient studies of a series of *FnCH=CHHm* diblocks ($n = 6$ or 8 ; $m = 6, 8$, or 10) between *F*-decalin, *F*-octyl bromide, or *E-bis*-1,2-(*F*-butyl)ethene and hexadecane showed that the diblocks distributed themselves without marked preference (or phobicity) for either phase.²⁰⁴ The relative solubility in the *HC* increased, as expected, with increasing *m/n* ratio. Partition of the diblock was generally slightly in favor of the linear and slightly lipophilic *F*-octyl bromide, followed by the linear triblock *F4CH=CHF4*, as compared to the more compact bicyclic *F*-decalin. The *E* isomers of the diblocks showed higher affinity for the *FC* phase than the *Z* isomers. The affinity difference between isomers was the largest in the case of *E-F4CH=CHF4* and the lowest with *F*-decalin, possibly indicating easier insertion of the diblock among molecules of similar shape and configuration.

Addition of small amounts of a diblock (e.g., *F8H16*) to an immiscible *FC/HC* mixture (*F*-octane/isooctane) significantly reduced the phase separation temperature of this mixture.¹⁷⁷ From a practical standpoint, incorporation of *FnHm* compounds can help modulate the solubility and phase separation behavior of *FCs*. A mixture of *n*- $C_4F_9OCH_3$ and *i*- $C_4F_9OCH_3$ (HFE-7100), as well as further mixtures of the latter with hexanes (*FC*-72), have been used to tune partition coefficients of fluoros molecules between fluoros and nonfluorous organic phases.¹⁷⁸ Dramatic changes in partition efficacy were obtained, which were further enhanced by addition of small amounts of water to the organic phase, thus increasing its fluorophobicity.

The branched ether diblock $C_6F_{13}CH_2CH_2OCH(CH_3)-CH_2CH(CH_3)_2$ was found to be miscible with a wide range of common solvents, from ethanol to hexane, and partitioned about equally between acetone and *F*-hexanes.¹¹⁷

4.3.2. Solubility of Diblocks in Carbon Dioxide

High pressure phase diagrams have been established for *F10H10* and *F12Hm* ($m = 8, 12$, and 20) in dense CO_2 , and the solubilities of the diblocks at the multiple-phase pressure were measured at 25 °C.²⁰⁵ The lowest multiple-phase pressure and highest liquid CO_2 solubility were found for *F10H10*. Solubility decreased from 73% to less than 1% with increasing *H*-chain length in the series investigated: *F12H8* > *F12H12* >> *F12H20*. Such CO_2 solutions led to gels upon isothermal expansion at room temperature (section 7.2).²⁰⁶

4.3.3. Solubility of Diblocks in Polar Media

The solubility of *FnHm* diblocks in water is very low. No direct measurements appear to be available, as these solubilities are below the detection limit of conventional methods. Calculations from the Ostwald ripening rates of diblock-in-water emulsions¹⁷⁴ gave the following values (mol L⁻¹): *F8H2* (7.7×10^{-9}), *F6H10* (3.4×10^{-11}), and *F8H8* (5.1×10^{-12}).²⁰⁷ The solubility of triblock *F6CH=CHF6* in water has likewise been estimated at 2.7×10^{-15} mol L⁻¹.²⁰⁸

Little data is published on the solubility of diblocks in other polar media. It has been noted that *FnH(6-n)* ($n = 0-4$) and *FnH(12-n)* ($n = 1-3$) were more soluble in 10% aqueous methanol than *n*- C_6H_{14} and *n*- $C_{12}H_{26}$, respectively.¹⁰

4.3.4. Gas Solubilities

The solubility of oxygen, carbon dioxide, nitric oxide, xenon, and other gases in highly fluorinated liquids has been

Table 3. Oxygen and Carbon Dioxide Solubilities (vol %, 37 °C^a) in Neat (*F*-Alkyl)alkyl Diblocks and Triblocks

compound	O ₂	CO ₂	ref
C ₄ F ₉ CH ₂ CH=CHC ₈ H ₁₇	31		435
C ₃ F ₇ (CF ₃) ₂ CC ₃ H ₇	46.7		218
<i>F6H2</i>	46.1		359
	3.6×10^{-3} (27 °C) ^b	17×10^{-3} ^b	219
<i>F6H4</i>	44.8		359
<i>F6H6</i>	43.4		359
	4.0×10^{-3} (27 °C) ^b	22×10^{-3} ^b	219
<i>F6H8</i>	40.3		359
<i>F6H10</i>	35.0		359
C ₈ F ₁₇ CH ₂ CH=CHC ₄ H ₉	43		435
<i>F8H2</i>	47.1 (28 °C)		211
	45.6		359
	47.0	213	209
	4.3×10^{-3} (27 °C) ^b	23×10^{-3} ^b	219
	39 (28 °C) ^c	204 ^c	220
<i>F8CH=CH₂</i>	44.5 (28 °C)		211
	47.5	216	209
<i>F8H8</i>	52.2 (28 °C)		211
<i>F10H2</i>	43.4		359
<i>F2CH=CHF4</i>	56.2		130
<i>F2CH=CHF6</i>	51.2	232	209
<i>iF3CH=CHiF3</i>		236	132
<i>iF3CH=CHF4</i>	52	243	132
<i>F4CH=CHF4</i>	50.3	232	130
<i>F4CH=CHF5</i>	49.0	224	209
<i>iF3CH=CHF6</i>	50	224	132
<i>F4CH=CHF6</i>	47.9	207	130
<i>iF3CH=CHF8</i>	45	216	132
<i>F6CH=CHF6</i>	42.8	181	130
	61.4 (28 °C)		211
<i>F6CH₂CH₂F6</i>	46.8 (28 °C)		211
(CF ₃) ₃ C(CH ₂) ₃ C(CF ₃) ₃	35.8		218
C ₈ F ₁₇ Br	52	210	210
	40 (27 °C) ^b	213	220
C ₈ H ₁₈	33		
<i>F</i> -decalin	41.1–43	140–145	176 and 210

^a Unless specified otherwise. ^b From molecular simulations, given in molar fractions. ^c From molecular simulations, given in vol %.

investigated from a fundamental standpoint, in a search for specific interactions, and because of its application potential, for example as biocompatible O₂/CO₂ or NO carriers.^{175,176,209,210} *FCs* and gases both have low cohesive energy densities, as reflected by very close Hildebrand parameters. The solubilities of O₂ in various liquid *F_nH_m* compounds are collected in Table 3. The solubility of O₂ in *F_nH_m* diblocks lies in between those of linear *FCs* and *HCs* of the same length. The solubility of O₂ in *F_nCH=CH_n'* triblocks was similar or higher than that in the linear *FC* analogues of the same total length, and it was substantially higher for *F4CH=CHF4* than for the more compact bicyclic *F*-decalin, in spite of close MWs (464 and 462, respectively).²⁰⁹ Within homologous series, gas solubilities decreased steadily with increasing MW and molecular volume (Figure 4.6). For *F_nH_m* diblocks, O₂ solubility decreased more rapidly with increasing *m* than with increasing *n*.

An NMR study that included the linear diblocks *F8H2*, *F8CH=CH₂*, and *F8H8*, and the triblocks *F6CH=CHF6* and *F6CH₂CH₂F6* established a correlation between O₂ solubility and the extent of perturbation of the T₁ relaxation rate of the solvent's ¹³C nuclei by the paramagnetic O₂ molecule.²¹¹ The diblock compounds essentially fell in line with linear *FCs*. The higher O₂ solubility found for *F6CH=CHF6* as compared to *F6CH₂CH₂F6*, while there was no difference in O₂ solubility between *F8CH=CH₂* and *F8CH₂CH₃* (Table 3), may again indicate that the shape of the solvent molecule

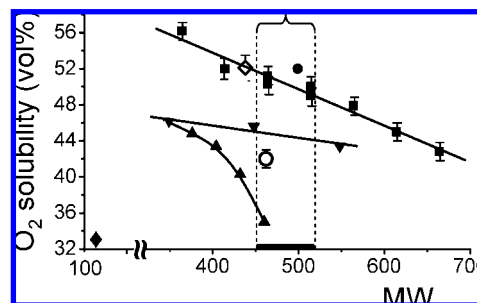


Figure 4.6. Oxygen solubility as a function of molecular weight within a homologous series of *F_nH_m* diblocks (▼, *F6H_m*; ▲, *F_nH₂*) and *F_nCH=CH_n'* triblocks (■) at 37 °C. Reference data points: ●, C₈F₁₇Br; ◇, C₈F₁₈; ○, C₁₀F₁₈ (*F*-decalin); ◆, C₈H₁₆. The O₂ solubilities of the triblocks align with those of linear *FCs*; those of diblocks decrease rapidly as the *H*-block increases in length. The bracket indicates the MW range acceptable for parenteral use for *FCs* and *F_nCH=CH_n'* triblocks (section 10); this range is extended to the right for the more lipophilic diblocks. Adapted from ref 209 with data from ref 360 and Table 3.

is an important factor. The “notch” created by the rigid *trans* double bond in *F6CH=CHF6* would facilitate the formation of the cavities that, according to the scaled particle theory,^{211,212} would host the O₂ molecules. No evidence was found in this study for specific intermolecular interactions between solute and solvent.

It is noteworthy that O₂ solubility per volume of diblock was substantially increased when diblocks *F8CH=CH₂*²¹³ or *F8CH₂CH=CHC₄H₉*²¹⁴ were in the form of a microemulsion in an aqueous medium.

F-Alkyl chains are known to be CO₂-philic.^{215–217} The solubility of gaseous CO₂ in liquid diblocks and triblocks was typically 4–5 times larger than that of O₂, a situation also found for *FCs*.^{176,209} It should be noted, however, that solubility of CO₂ in any solvent is typically ten times larger than that of O₂.

O₂ solubility, along with energy of vaporization (hence, an estimate of vapor pressure) and molar volume (hence, density), have been calculated, using an empirical group additivity system, for various branched diblocks and triblocks (e.g., CF₃CF₂CF₂(CF₃)C_{*m*}H_{2*m*+1}, CF₃CF₂CF₂(CF₃)CCH₂CH(CH₃)₂, or (CF₃)₃CC_{*m*}H_{2*m*}C(CF₃)₃).²¹⁸

Molecular simulation of the solubility of O₂, CO₂, and H₂O in *F6H2*, *F8H2*, *F6H6*, and, for comparison, C₈F₁₇Br has been achieved using full atomistic force fields.²¹⁹ The outstanding affinity of highly fluorinated compounds for CO₂ was explained in terms of classical, nonpolarizable potential models, without specific interactions.²²⁰

4.3.5. Solubility of Polar Substances in Diblocks

The solubility of water in liquid diblocks is likely higher than that in comparably sized *F*-alkanes due to the presence of the dipole. The solubility of water in *F6H2*, *F8H2*, *F8H8*, and, for comparison, C₈F₁₇Br has been calculated by molecular simulation to be on the order of 3×10^{-6} in mole fraction.²¹⁹ Water was somewhat more soluble in *F6H2* than in the longer compounds.

Nonfluorinated polar substances are generally very poorly soluble in highly fluorinated solvents. The solubility of series of carboxylic acids, diacids, aminoacids, and sugars in *F6CH=CHF6* usually diminished rapidly as their MW increased.²²¹ Interesting exceptions were, however, noted.

Thus, CF_3COOH was miscible in all proportions with $F_6\text{CH}=\text{CHF}_6$ at room temperature, as well as with $F_8\text{H}_2$, $F_8\text{CH}=\text{CH}_2$, and $n\text{-C}_8\text{F}_{18}$. CH_3COOH was only miscible with $F_8\text{CH}=\text{CH}_2$; it was highly soluble but not miscible with $F_8\text{H}_2$ and $F_4\text{CH}=\text{CHF}_4$; and it was poorly soluble in C_8F_{18} . On the other hand, HCOOH was almost insoluble and CCl_3COOH much less soluble in these solvents than the average perfluorinated carboxylic acids $F_n\text{COOH}$ ($n = 2-7$). The solubility of CH_3COOH was 25 times larger in $F_8\text{H}_2$ than in $n\text{-C}_8\text{H}_{18}$. These apparent abnormalities likely reflect the outstanding capacity for F -acetic and acetic acids to form hydrogen-bonded cyclic dimers in nonpolar solvents. These dimers essentially expose CF_3 or CH_3 groups to their environment. The much larger solubility of CH_3COOH in $F_4\text{CH}=\text{CHF}_4$ as compared to $n\text{-C}_8\text{F}_{18}$ may reflect easier formation of a cavity capable of hosting the solute molecule when the F -solvent presents a structural “defect”. Considerable amounts of the very poorly soluble formic acid could be dragged into $F_4\text{CH}=\text{CHF}_4$ using equimolar amounts of CF_3COOH , presumably in the form of mixed dimers. Conversely, in spite of its miscibility with $F_4\text{CH}=\text{CHF}_4$, CF_3COOH could easily be extracted from the F -solvent by water; partition in water was 33 times larger than that in the F -solvent at 37 °C.²²¹ Another study found that the excess thermodynamic functions were large and of opposite signs for $\text{CF}_3\text{COOH}/F_6\text{CH}=\text{CHF}_6$ and $\text{CH}_3\text{COOH}/F_6\text{CH}=\text{CHF}_6$ binary mixtures, reflecting attractive forces in the former case and repulsive forces in the latter.¹⁹⁵ Formation of dimers of the acids was confirmed by infrared spectroscopy.

4.4. Propensity to Self-Assemble and Promote Ordering and Micro- and Nanocompartmentation in Colloids and at Interfaces

Because of their combined amphiphilic, amphisteric, and amphidynamic characters, F_nH_m diblock compounds constitute unique building blocks for the engineering of self-assembled films and colloidal constructs and, hence, for controlled access to complex matter.^{13,222}

The role of the “hydrophobic effect” in self-assembly (e.g., formation of micelles, bilayer membranes, vesicles, fibers, etc.) is well established.^{223–226} F -Chains provide the ultimate in terms of hydrophobic (or “super”hydrophobic) effect. Additionally, F -chains are substantially lipophobic (or oleophobic or solvophobic) and, hence, can contribute a lipophobic effect as well. Therefore, they tend to phase separate from H -chains, as well as from polar moieties and media. Moreover, the rigid-rod character of F -chains favors ordered packing and crystallization. However, F -chains need generally to be longer than four carbon atoms in order to effectively override the weaker cohesiveness among F -chains, as compared to H -chains and, in the case of F_nH_m diblocks, the negative influence of the $\text{CF}_2\text{—CH}_2$ junction on orientational molecular correlations. Incorporation of F -chains in colloids and interfaces then develops an effective driving force for stable, compartmented supramolecular self-organization.^{13,52,222,227} The enhanced thermodynamic stability of fluorinated self-assemblies is generally accompanied by increased kinetic inertness as well.^{228,229} Molecular dynamics simulations of clusters of 128–184 molecules have demonstrated the higher tendency for F -alkanes, as compared to alkanes, to arrange into layerlike structures with a certain long-range in plane order.²³⁰ It has

been concluded, however, that this tendency may be somewhat hindered by the H -chain in diblocks (e.g., for $F_{10}H_{10}$ vs $\text{C}_{20}\text{H}_{42}$).

The powerful driving force for self-association conferred by F -chains is demonstrated by the ability of single chain F -amphiphiles to produce stable, heat-sterilizable vesicles,²³¹ flexible fibers, and rigid tubules,^{232,233} while, in the absence of supplementary forces (e.g., hydrogen-bonding, ion-pairing, etc.), nonfluorinated analogues yield only micellar solutions. The ability of F -chains to enhance ordering, and in particular to produce lamellar structures, is further exemplified by the observation that attachment of F -chains onto liquid crystal-forming molecules and polymers induced transformation of less ordered nematic mesophases into more highly ordered smectic ones.^{234,235} The introduction of semifluorinated alkyl chains into discotic systems strongly affected the thermodynamic, structural, and dynamic properties of the mesophases they formed.²³⁶ Grafting F -chains at the end of alkane substituents of tapered discotic mesogens resulted in a dramatic enhancement of their ability to self-assemble and of the stability of the resulting columnar mesophases.^{91,237} It can also induce new mechanisms of ferroelectricity.¹⁶⁸ The superior self-assembling capacity of F -chains also results in stable, densely packed Langmuir and Gibbs monolayers. Incorporation of highly fluorinated amino acid residues dramatically enhanced the stability of peptides.^{238,239} More generally, it allowed templated biosynthesis of abiotic fluorinated peptides, stabilization of protein folding, selective protein–protein recognition and assembly, DNA recognition and binding, and the modulation of biological processes.²²²

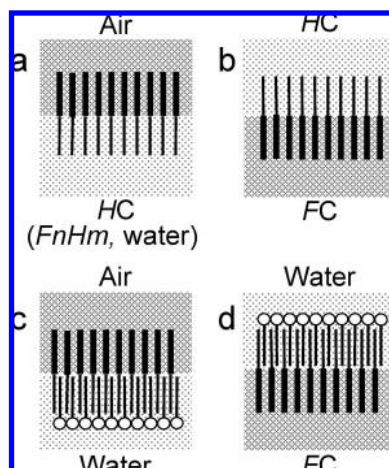
Many fluorinated surfactants comprise an H_m spacer between the F -chain and the polar headgroup and can thus be considered as “functionalized” diblocks. The H_m segment ($m \geq 2$) serves multiple critical purposes, such as screening the functional end from the electron withdrawing effects of the F -chain and introducing conformational mobility. It can also facilitate incorporation of F -chains (and their properties) in a construct or formulation due to the affinity of the H -block for other H -components.

Scheme 4.3 depicts simple examples of fluorinated interfaces involving F_nH_m diblocks. The structures, properties, and uses of such systems will be discussed in sections 6–10.

Structural studies of diblock-based systems benefit from the large electron density difference between F -alkyl and alkyl chains, which provides or greatly enhances contrast in transmission electron microscopy and X-ray scattering experiments. They also benefit from the high sensitivity of the ^{19}F nuclei in NMR, second only to ^1H NMR. Slower dynamics can allow NMR monitoring of exchange processes (e.g., monomers/micelles) in a more easily accessible temperature range.²²⁸ On the other hand, the low refraction index of FCs , around 1.33, close to that of water, hinders the use of light scattering-based methods in water.

Investigation of the structure and dynamics of condensed bulk F_nH_m phases, solutions, self-assembled films, membranes, and colloidal systems involving F_nH_m diblocks has involved a large combination of techniques, including differential scanning calorimetry (DSC), polarization optical microscopy, Brewster angle microscopy (BAM), freeze-fracture and cryogenic transmission electron microscopy (FF-TEM and cryo-TEM), atomic force microscopy (AFM), quasi-elastic light scattering (QELS), small- and wide-angle X-ray scattering (SAXS and WAXD), grazing incidence (small-angle) X-ray scattering (GI(SA)XS) using synchrotron

Scheme 4.3. Diblocks at Air/Liquid or Liquid/Liquid Interfaces: (a) At the Surface of a HC, Playing the Role of a Primitive Surfactant Such as, for Example, in a Spontaneously Formed Gibbs Film (Section 8.1) or in a Surface Frozen Monolayer When the Lower Phase Is the Liquid Diblock (Section 6.2) or, if the Lower Phase Is Water, as a Langmuir Monolayer Spread on Water (the Fragment Represented Is Then Part of a Surface Micelle, Section 8.2); (b) as a Surfactant at a HC/FC Interface Such as, for Example, in a HC-in-FC Emulsion (Section 9.4.2); (c, d) Associated with a Standard Surfactant with a Polar, Hydrophilic Head, (c) as Part of a Mixed Langmuir Monolayer (Section 8.2) or, Possibly, on the Surface of a Gas Bubble (Section 9.2) or (d) as a Cosurfactant in the Interfacial Film of a FC-in-Water Emulsion or Water-in-FC Reverse Emulsion (Section 9.3–4)



radiation, specular X-ray reflectivity, small-angle neutron scattering (SANS), Fourier-transform infrared (FTIR) spectroscopy, Raman spectroscopy, magic angle solid (MAS) ^{13}C NMR, refractometry, isothermal monolayer compression studies (Langmuir trough and Langmuir–Blodgett techniques), surface potential measurements, and pendant drop interfacial tension analysis. Further, less commonly implemented methods used for probing the structure and behavior of *FnHm* diblocks included modulated DSC, vapor osmometry, dielectric spectroscopy, dilatometry, dynamic rheology, Brillouin spectroscopy, etc.

5. Solid State: Structural Transitions and Liquid Crystal Behavior

The solid state structure of *FnHm* diblocks has been extensively investigated since the mid-eighties, initially for the purpose of providing clues for the development of new polymers or liquid crystals. *FnHm* diblocks and *FnHmFn* triblocks constitute indeed simplified models of semiflexible alternating mixed microblock polymers of type $-(\text{CF}_2)_n(\text{CH}_2)_m)_x-$.⁶ These large tonnage copolymers combine a thermal stability approaching that of poly(tetrafluoroethylene) $-(\text{CF}_2\text{CF}_2)_x-$, PTFE, Teflon) and the processability of polyethylene $-(\text{CH}_2\text{CH}_2)_x-$, PE). The ethylene-tetrafluoroethylene copolymer $-(\text{CF}_2\text{CF}_2-\text{CH}_2\text{CH}_2)_x-$ (ETFE) and poly(vinylidene fluoride) $-(\text{CF}_2\text{CH}_2)_x-$ (PVDF) are examples of commercially available polymers that offer high thermal stability, outstanding mechanical and dielectric properties, and solubility in a number of solvents.

Independently, it has been found that *F10H10* was capable of forming a smectic B liquid crystal phase.⁷ Classical smectogens (compounds that form smectic liquid crystals)



Figure 5.1. Characteristic optical microscopy texture, between crossed polars, of a smectic B liquid crystalline phase, showing typical bâtonnet texture: *F10H10* at 57.5 °C, i.e., for the high temperature mesophase. From ref 259 with permission.

typically comprise a polarizable rigid core (e.g., biphenyl or dialcyne groups) bearing one or more flexible side chains. The concept that the very existence of smectic phases was related to amphiphilicity^{240,241} suggested that substitution of the diphenyl or dialcyne rigid core by a rigid linear fluorinated block in appropriate amphiphilic compounds should provide a new approach to liquid crystals, which was indeed confirmed experimentally using *FnHm* diblocks.

5.1. Background and Terminology

Different cultures and objectives tend to engender different languages. Some authors, including scientists from the soft-condensed matter community, have described the structure and behavior of solid-state *FnHm* diblocks in terms of mesophases, smectic phases, liquid crystals, plastic phases, clearing point, etc., while others, including crystallographers, have reported about melting point, solid–solid or crystal–crystal phase transitions, layered crystals with more or less disordered packing, and rotator phases, while investigating the same or similar compounds.

The liquid crystal state is intermediate between a frozen, ordered crystal state and the disordered isotropic liquid state (melt); it is a so-called mesophase.^{242–245} In liquid crystals, molecules lose their positional order but retain part of their orientational order. The converse situation is found in the so-called “plastic” phases, where position is preserved, while orientational order is lost. Liquid crystals have generally a waxy appearance, are easily sheared, and tend to flow when pressure is applied. Transmitted polarization optical microscopy is a simple means of identifying liquid crystals that has not always been used in the earlier studies of *FnHm* diblocks. The liquid crystals formed by the rod-shaped (or calamitic) amphiphilic *FnHm* molecules are essentially of the smectic type, i.e., consist of mesophases in which the molecules are arranged in layers. In the highly ordered smectic B phase, the molecules exhibit long-range orientational order, but only short-range positional order within the layer, and are in principle oriented parallel to the normal to the layer. When examined by optical microscopy between crossed polarizers, smectic B liquid crystals show characteristic bâtonnet-type textures (see Figure 5.1), with large black homotropic areas that turn bright when the sample is sheared or tilted, or focal-conic fan-type textures.

Phase transitions in the solid have also been categorized as crystal–crystal or order–disorder transitions. In the latter, the lattice structure is preserved, but the conformational order of the molecule is modified. In the former, the lattice is changed, but molecular conformation is essentially preserved. In this terminology, rotator phases, often found for diblocks, and well documented for *n*-alkanes^{246–249} and alkane mixtures,²⁵⁰ *F*-*n*-alkanes,^{251,252} and other calamitic molecules,²⁵³ consist of layered structures in which the molecules are oriented normal to the layer (as in a smectic B phase), packed in a hexagonal array (which is typical for cylinders), and rotate about their long axis. The position of the individual molecules is maintained, but their long-range orientational order about their long axis is lost. Rotator phases are thus related to plastic phases, rather than liquid crystals. In rotator phases, order is preserved when moving from one layer to the next one, while this is not the case in smectic phases. *n*-Alkanes and *F*-*n*-alkanes display numerous phase transitions and rotator phases that differ in their short-range correlations. The high symmetry, first rotator phase (R_{II}) encountered upon cooling a sample below the melting point has often been described as “very similar” to a liquid crystal phase or as displaying freedom “like in a liquid crystal”, with stacked layers of parallel molecules as in a smectic (usually smectic B) phase, whether in *n*-alkanes,^{248,249} *F*-*n*-alkanes,²⁵² other linear molecules,²⁵³ or *F**nHm* diblocks.^{254,255} For example, $C_{20}F_{42}$ presents a phase below melting that has been described as a “soft crystalline layered phase with close similarities with smectic liquid crystals” that involved rotational, translational, and conformational motions, including helix reversal.²⁵² The smectic B-like behavior of $C_{20}F_{42}$ displays indeed several of the features characteristic of liquid crystals, including hexagonal symmetry and extremely weak coupling between molecular layers.²⁵⁶ The residual difference between the “very similar to” smectic or rotator phases or liquid crystals and the “true” items has not always been clearly spelled out.

Rotator-type behavior was not unexpected for *F**nHm* diblocks, since such behavior was well-known for *n*-alkanes and *F*-*n*-alkanes. On the other hand, liquid crystal behavior has not always been immediately identified, as such character had not been reported for the parent alkanes. A smectic liquid crystal phase has eventually been detected in mixtures of *n*-alkanes.²⁴⁸ This phase occurred between the R_{II} phase and a lower temperature (R_I) layered, plastic crystalline rotator phase. Some *F**nHm* diblock phases, first described as crystalline with motional freedom similar to that of a rotator phase,⁶ then as similar to smectic B,²⁵⁵ have eventually been identified as genuine smectic (i.e., liquid crystalline) phases.¹⁰⁹

5.2. Thermal Characterization of (*F*-Alkyl)alkane Diblocks—Phase Transitions

Investigation of thermal behavior allows detection of phase transitions and provides clues on the structure of solid samples. In addition to a strong and sharp melting endotherm, the differential scanning calorimetry thermograms of *F**nHm* diblocks exhibit, for certain values of *n* and *m*, one or more, weaker and broader endotherms (Figure 5.2), reflecting solid/solid phase transitions. It can then also be considered that melting occurs in several successive steps.

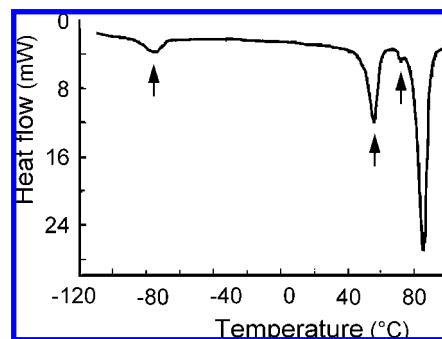


Figure 5.2. Example of a DSC thermogram for an *F**nHm* diblock, *F*12*H*8, which shows three endotherms (arrows) in addition to and below the strong melting endotherm seen on the right. From ref 6 with permission.

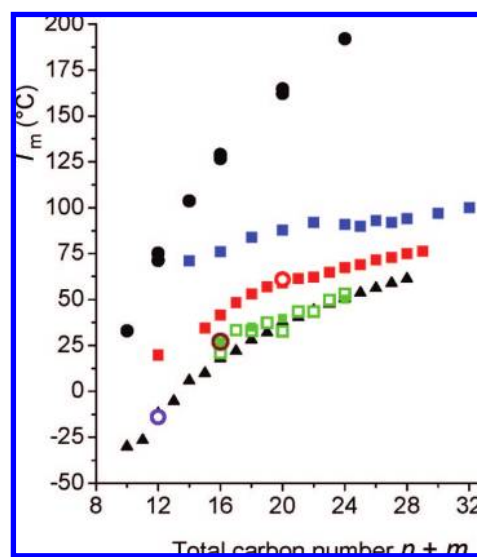


Figure 5.3. Melting temperatures T_m of *F**nHm* diblocks as a function of their total length $n + m$: blue squares, *F*12*Hm*;^{255,260} red squares, *F*10*Hm*;²⁵⁹ green squares, *F*8*Hm*: filled⁴⁵ or open;²⁵⁸ and, for reference, black circles, *F*-alkanes;^{45,251} and black triangles, alkanes.⁴⁶⁷ Open circles denote individual data points for *F*10*H*10 (red),⁷ *F*8*H*8 (brown),⁶ and *F*6*H*6 (mauve).⁴⁵

5.2.1. Melting Transition

Melting temperatures T_m , as measured by DSC (Tables 4 and 5), have been plotted against total number of carbon atoms for large series of *F**nHm* diblocks and compared to those of related *n*-alkanes and *F*-*n*-alkanes (Figure 5.3).^{6,7,45,254,255,257–259} The melting points of the diblocks increased with *m* and, in the *F*12*Hm* and *F*10*Hm* series, fell in between those of the *n*-alkanes and *F*-*n*-alkanes of the same length. The melting points of the *F*8*Hm* diblocks were very close to those of the corresponding *n*-alkanes. Increasing the length of the *F*-chain had, as for *F*-*n*-alkanes, a dominant influence on melting temperature and melting entropy, indicating that this transition was primarily associated with disordering of the *F*-blocks. Each CF_2 unit contributed to the melting entropy, ΔS_m , by an average $5.4 \text{ J K}^{-1} \text{ mol}^{-1}$, comparable to the $6.8 \text{ J K}^{-1} \text{ mol}^{-1}$ measured for the melting of PTFE.²⁵⁵ On the other hand, in the *F*12*Hm* series, the melting enthalpy and entropy (Figure 5.4) depended only little on the length of the *H*-block, until *m* reached 14, indicating that the organization of the *F*-block of the diblock remained similar to that of the *FC* compound. A sudden jump of ΔH_m and ΔS_m between $m = 14$ (26 kJ mol^{-1} and $73 \text{ J K}^{-1} \text{ mol}^{-1}$, respectively) and $m = 15$ (44.3 kJ mol^{-1} and

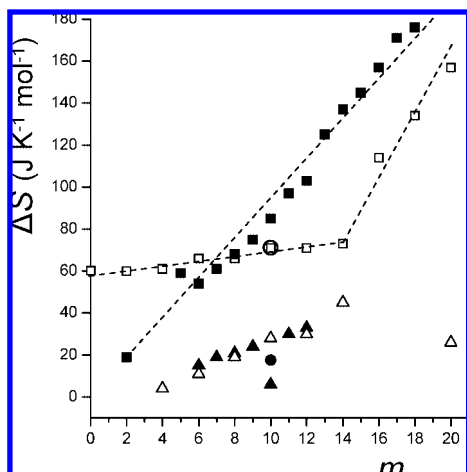


Figure 5.4. Changes in entropy at the melting point (squares) and at the solid–solid phase transition (triangles) as a function of m for $F10Hm$ (filled symbols)²⁵⁹ and $F12Hm$ (open symbols)²⁵⁵ diblocks, circles: data from ref 7 for $F10H10$; dotted lines added.

$122 \text{ J K}^{-1} \text{ mol}^{-1}$)^{254,255,260} indicated a marked change in molecular packing, which would no longer be similar to that of the FC , and reflected the onset of an outweighing influence of the H -chain.

A substantially different picture was seen for the $F10Hm$ series, where the melting entropy varied in a monotonous way throughout the series.²⁵⁹ The plot of ΔS_m versus m (Figure 5.4) emphasizes the difference between the two series. Contrary to the $F12Hm$ series, where ΔS_m remained almost constant until m reached 14, ΔS_m increased regularly with the number of CH_2 groups for $F10Hm$ and remained close to the melting entropies of n -alkanes; above $m = 14$, the variation of ΔS_m in the two series became roughly parallel. While melting had been assigned primarily to disordering of the F -block for the $F12Hm$ series,²⁵⁵ it was proposed that melting of the $F10Hm$ involved disordering of the whole molecule, not only of the F -block.²⁵⁹ Such marked differences in behavior between so closely related series are certainly puzzling and may indicate differences in the transition process. Further thermal data can be found for $F8Hm$ and isolated shorter diblocks,^{45,258} as well as for series of brominated $F_nHm\text{Br}$ ²⁹ and iodinated $F12\text{CH}_2\text{CHIH}(m-2)$ ²⁶¹ compounds.

No transitions other than melting have been reported for $F12Hm$ samples cooled from the melt when m was 16, 18, and 20 (but for a sample of $F12H20$ crystallized from solution) or in the $F10Hm$ series for $m \geq 13$. However, the melting entropies, although higher than those for smaller m values, were lower than what would have been expected for melting of a fully ordered crystal, indicating that considerable disorder was retained below the melting point.¹⁰⁹

5.2.2. Solid State Transitions

In addition to melting, several solid state transitions have been reported for numerous diblock compounds. For the $F12Hm$ series, a weaker, broader endotherm has consistently been found for $4 \leq m \leq 13$ when cooling a sample below its melting point (Figure 5.2, Table 4).^{6,254,255,260} Contrary to the melting transition, the temperature T_1 , enthalpy ΔH_1 , and entropy ΔS_1 of the first endotherm below melting increased regularly and strongly (ΔH_1 by $\sim 1.05 \text{ kJ mol}^{-1}$ per CH_2

added) in the $F12Hm$ series as m increased from 4 to 12 (Figure 5.4). The regularity of the increase suggested that the same transition mechanism would operate, regardless of m . The H -chain length dependence of ΔS_1 indicated that, whereas the melting transition was essentially governed by disordering of the F -segment, the transition at T_1 , the first below melting, was primarily controlled by disordering of the H -block. Mobility of the H -block is indeed facilitated by the difference in cross section between the F - and H -chains.

Sample history can have a significant impact on thermal behavior. It may be responsible for the spread of values sometimes found in the literature. For example, in the case of $F10H10$, T_1 and ΔS_1 were reported as $39 \text{ }^\circ\text{C}$ and $17.6 \text{ J K}^{-1} \text{ mol}^{-1}$,⁷ $46.9 \text{ }^\circ\text{C}$ and $23 \text{ J K}^{-1} \text{ mol}^{-1}$ on first heating and $37.3 \text{ }^\circ\text{C}$ and $7 \text{ J K}^{-1} \text{ mol}^{-1}$ on second heating,⁹⁵ and $48.5 \text{ }^\circ\text{C}$.⁹⁶ In the case of $F12H20$, melt-crystallized material only showed the melting endotherm, while a solution-crystallized sample exhibited at least two additional transitions (Table 4).¹⁰⁹

For the $F10Hm$ series, a transition below melting was consistently found for $6 \leq m \leq 12$ (Table 5) with an irregular dependence of T_1 (Figure 5.5) and a regular increase of ΔS_1 (Figure 5.4) with m (but seemingly with an exception for $F10H10$).^{7,96,259,262} Repeated heating/cooling cycles sometimes produced a shift, a broadening, or the disappearance of the solid-phase transition, reflecting again the importance of sample history (recrystallization or precipitation from solution or cooling from the melt) and indicating kinetic control of the transition.^{95,109} The rate of the phase transformation can be very slow, for example in the case of $F10H10$ ^{7,259} or $F8H16$.¹⁷⁰ The reason why $F10H10$ stands out of the $F10Hm$ homologous series (see also Figure 5.4) is not yet understood.

Additional solid phase transitions were often recorded upon further cooling. For example, a second transition was found (in the -126 to $-57 \text{ }^\circ\text{C}$ range) for solvent-recrystallized diblocks of the $F12Hm$ series when $4 \leq m \leq 12$ (Table 4).²⁵⁵ Likewise, three transitions were identified for $F8H16$ ($-15 \text{ }^\circ\text{C}$, 1.5 and $24 \text{ }^\circ\text{C}$) below melting at $52 \text{ }^\circ\text{C}$.¹⁷⁰

5.3. Solid State Structures of (F -Alkyl)alkyl Diblocks—Liquid Crystal Behavior

The forced covalent yoking of F - and H -chains within F_nHm diblocks engenders an interplay of unfavorable energetic interactions (related to the antipathy that drives F - and H -chains to repel each other and segregate) and entropic effects (related to the difference in cross section and stiffness of the two blocks). To be acceptable, molecular conformations and packing arrangements need to reduce the energetic mismatch between blocks and fill the available space most effectively. Multiple molecular arrangement possibilities and phase transition mechanisms have been proposed that depended strongly on the relative length of the F - and H -blocks.

The solid state structures of linear F_nHm diblocks have one essential feature in common with those of linear n -alkanes and F - n -alkanes: the molecules tend to form layers with their long axes parallel to each other and more or less parallel to the layer normal. These layers are stacked to build layered crystals. However, the additional frustrations due to the amphiphilic and amphisteric characters of F_nHm diblocks are expected to promote increased disorder. A further feature that is shared with other rod-shaped molecules is their tendency to pack in

Table 4. Melting Temperature T_m and Lower Phase Transition Temperatures T_1 and T_2 , and Corresponding Enthalpy and Entropy Values for Linear $F12Hm$ Diblocks (Data from Refs 109, 255, and 260)

m	T_2 (°C)	ΔH_2 (kJ mol ⁻¹)	ΔS_2 (J K ⁻¹ mol ⁻¹)	T_1 (°C)	ΔH_1 (kJ mol ⁻¹)	ΔS_1 (J K ⁻¹ mol ⁻¹)	T_m (°C)	ΔH_m (kJ mol ⁻¹)	ΔS_m (J K ⁻¹ mol ⁻¹)
0							72	21.0	61
2							71	20.4	60
4	-126	0.7	5	41	1.4	4	76	21.0	61
6	-109	0.5	1	43	3.5	11	84	23.4	66
8	-81	2.4	12	56 ^c			88	23.7	66
10	-66	1.0	6	69			92	25.3	71
12	-57	1.8	3	79			91	25.3	71
13				84			90	27.2	75
14				90			93	26.1	73
15				87			92	44.3	122
16							94	41.3	114
18							97	49.7	134
20 ^a	-23	4.2	17	35	7.9	26	100	58.5	157
20 ^b							100	59	157

^a Crystallized from solution. ^b Crystallized from the melt. ^c A value of 51 °C was reported in ref 251.

Table 5. Melting Temperature T_m and Lower Transition Temperature T_1 , and Corresponding Entropy Values for Linear $F10Hm$ Diblocks (Data from 259)

m	2	5	6	7	8	9	10	11	12	13	14	15	16	17	18	19
T_1 (°C)			30.5	29.8	25.0	32.9	32.5	50.5	59.6							
ΔS_1 (J K ⁻¹ mol ⁻¹)			15	19	21	24	6	30	33							
T_m (°C)	19.8	34.5	41.5	48.3	53	57	59.8	61.4	62.3	63.2	64.8	67.4	69.1	71.5	75.1	76.2
ΔS_m (J K ⁻¹ mol ⁻¹)	19	59	54	61	68	75	85	97	103	125	137	145	157	171	176	186

hexagonal arrays and undergo rotator phase behavior, that is “free” rotation around their main axis in the solid. Conformational disordering of the H -segment upon transition to a smectic liquid crystalline phase should be facilitated by the smaller cross-sectional area of hexagonally packed H -chains as compared to similarly packed F -chains and by the fact that F -chains are helical rather than planar.

The most extensive data basis on bulk solid structure and liquid crystalline behavior of molecular F_nH_m compounds is provided by studies of extended suites of $F12H_m$ (m even-numbered from 0 to 20) diblocks,^{6,109,186,254,263} and $F10H_m$ (even and uneven m) diblocks,^{7,95,96,257,259,262} and, to a lesser extent, $F8H_m$ diblocks.^{6,170,258,264} The solid-state behavior of further diblocks, including branched,^{109,258} brominated,²⁹ and iodinated compounds²⁶¹ has also been investigated.

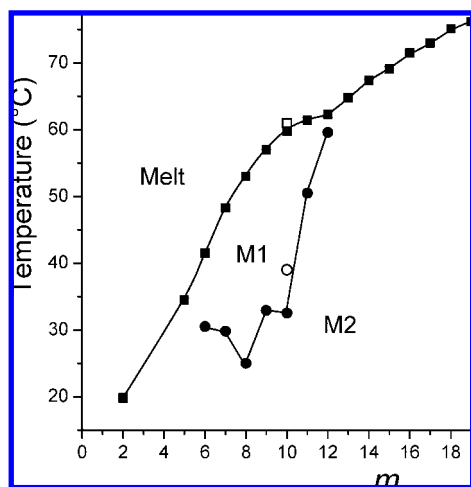


Figure 5.5. Solid–solid phase transition temperatures (circles) and melting temperatures (squares) in the $F10H_m$ diblock series as a function of m ;²⁵⁹ open symbols: data from ref 7. M1 and M2 denote the mesophases seen above and below the solid–solid phase transition (see text).

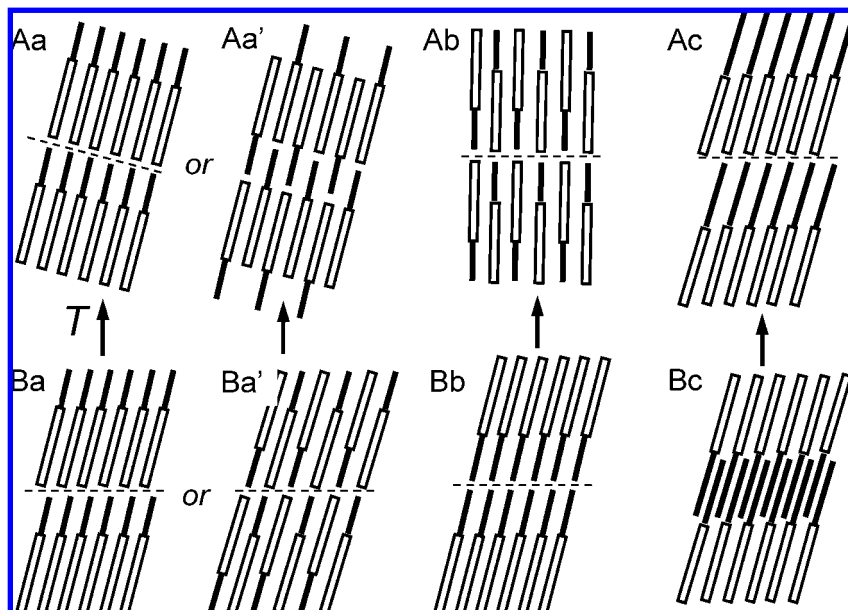
5.3.1. The $F12H_m$ Series

The diblocks of the $F12H_m$ series (even m values) have been categorized into distinct groups ($m = 2$; $4 \leq m \leq 6$; $8 \leq m \leq 14$; and $m > 14$), depending on phase behavior. The earlier studies relied heavily on Raman spectroscopy, which indicated, for all the compounds investigated, considerable motional freedom and loose packing in a hexagonal structure that was described as similar to the rotator phase known for odd n -alkanes below their melting point.^{6,254} Subsequent papers in part confirmed and in part invalidated the initial findings.^{255,263} A specific study revealed a behavior of its own for solution-crystallized $F12H2$.¹⁰⁹

5.3.1.1. Short H -Chain Diblocks. $F12H2$ was reported to behave essentially like F - n -alkanes²⁵¹ at ambient temperature, adopting a hexagonal packing in a rhombohedral unit cell.¹⁰⁹

For $m = 4$ and 6, one²⁵⁴ and subsequently a second²⁵⁵ phase transition were recorded for $F12H_m$ diblocks prior to melting. At room temperature (below the first transition temperature T_1), the SAXS profiles (large q values) for $m = 2, 4$, and 6 showed only one sharp reflection with a Bragg spacing d slightly shorter than or equal to the molecular length.^{6,254} The structure below T_1 was inferred to consist of lamellar crystals with molecular monolayers as the repeating motif. Because the Bragg spacing was less than the molecular length, the axes of the molecules had to be tilted with respect to the normal of the crystal. However, the SAXS data were compatible with two different molecular packings, parallel and antiparallel. In the parallel packing, the F -segments would be aligned so as to maximize F -chain/ F -chain contacts (Scheme 5.1.Ba). In the antiparallel packing, the arrangement would display extensive, a priori unfavorable, F -chain/ H -chain contacts, but would reduce the “void” related to the difference of cross section of the two blocks (Scheme 5.1.Ba’). Experimental discrimination between these two structures was not possible, due to the insufficient angular range over which the SAXS data were collected, the use of a powder specimen, prohibiting absolute intensity measure-

Scheme 5.1. Model Molecular Packings Proposed for the $F_{12}H_m$ Diblocks. The open elongated rectangles represent the F -blocks and the solid bars the H -blocks. The arrows indicate increasing temperatures. A and B depict model structures proposed above and below the first solid-solid phase transition T_1 below melting, respectively. Aa and Ba, Aa' and Ba' correspond to the tilted parallel and antiparallel packings, respectively, proposed for $m = 4$ and 6. Ab and Bb represent the molecular arrangements proposed for $m = 8, 10, 12,$ and 14; the molecules are tilted below the transition, but no longer above. Adapted from ref 254 with permission. The bilayer arrangement Bb is also found in the ripple phase represented in Scheme 5.2.¹⁸⁶ Ac and Bc are the packing models proposed in ref 267 (assuming that there is no change in tilt angle at T_1)



ments, and the tilt of the molecular axis away from the crystal normal. Semiempirical energy calculations, primarily for $F_{12}H_6$, slightly favored the parallel arrangement.²⁵⁴

Subsequent, better resolved SAXS data for $F_{12}H_6$, obtained over a larger angular range and, in part using synchrotron radiation, provided additional details, including the presence of three equidistant peaks in the SAXS profile, and, hence, clear evidence for a tilted monolayered lamellar structure.²⁶³ The possibility that the F - and H -segments might have different tilt angles was, however, not excluded.

Heating samples of $F_{12}H_4$ or $F_{12}H_6$ caused a new peak to emerge at smaller angles, i.e., larger Bragg spacings, in the X-ray diffraction pattern, while the peak at larger angles progressively disappeared.²⁵⁴ Above T_1 , only the peak corresponding to the larger spacing remained. The repeating distance increased with temperature and eventually reached the length of the fully extended molecule. It was proposed that the transition could be achieved by translating the molecules along their axes via a screw motion, until their extremities formed a plane perpendicular to the molecular axis, whether the packing geometry was parallel or antiparallel (Scheme 5.1.Aa and Aa'). The molecules would then no longer be tilted. A lamellar structure consisting of untilted stacked monolayers, similar to a rotator phase, was proposed.

Single peak WAXD profiles also confirmed the transition toward an untilted phase upon heating above T_1 and a lamellar structure consisting of stacked monolayers in a rotator phase.²⁶³ The Bragg peak position coincided with that of the PTFE peak, indicating a similar structure, i.e., a hexagonal arrangement of untilted F -chains. The d spacing was, however, slightly smaller than the length of the extended molecule, suggesting that the H -segments were in the liquid state. Disordering of the H -chain results indeed in a decrease in "effective" H -chain length.

5.3.1.2. Medium-Length H -Chain $F_{12}H_m$ Diblocks ($m = 8, 10, 12, 14$). When the two blocks were of comparable

length ($8 \leq m \leq 12$), initially one²⁵⁴ and subsequently a second^{186,255} phase transition were found below T_m for $F_{12}H_m$ diblocks (Table 4). $F_{12}H_{13}$ and $F_{12}H_{14}$ exhibited only one transition below T_m .²⁶⁰ Raman spectroscopy for $F_{12}H_8$ was interpreted to indicate, both below and above the first transition temperature T_1 below T_m , loose packing and considerable motional freedom for the H -segment (but without *gauche* conformations) in a hexagonal structure that was reminiscent of the rotator phase of odd n -alkanes.^{6,254} The fact that heating the sample above T_1 produced little change in the Raman spectra suggested that the molecule remained fully extended and that the transition likely involved a change in lattice packing, without change of molecular conformation. On the other hand, the SAXS profiles were substantially different from those of the $m \leq 6$ homologues.

Below T_1 , three reflections (two first-order and one second-order reflections) were observed in the SAXS profiles (see Figure 5.6 for $F_{12}H_8$).²⁵⁴ Heating caused the intensity of the peak corresponding to the shorter Bragg distance to increase, whereas that for the larger distance decreased. Only the former reflection remained above T_1 . It was proposed that two distinct structures or phases (a high- and a low-temperature phase) might coexist over a wide temperature range below T_1 and that heating increased the proportion of the high-temperature structure. As the low-temperature Bragg spacings were larger than the molecular length (actually proportional to $m + 2n$), a bilayered structure was proposed. A tilted bilayer structure was deemed necessary in order to maintain the colinearity of the F - and H -chains mandated by the Raman data (Scheme 5.1.Bb).

Wide-angle X-ray diffraction below T_1 indicated that the intermolecular distances within a same lamella were predominantly governed by the F -segments, as these spacings were close in magnitude to those found for n - $C_{20}F_{42}$.^{6,254} In particular, the spectrum of $F_{12}H_8$ displayed a reflection at

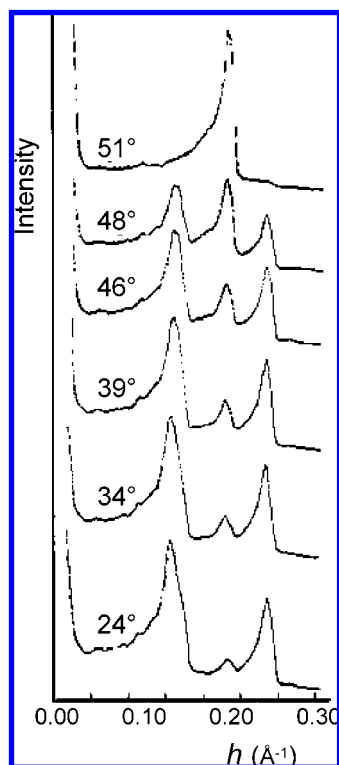


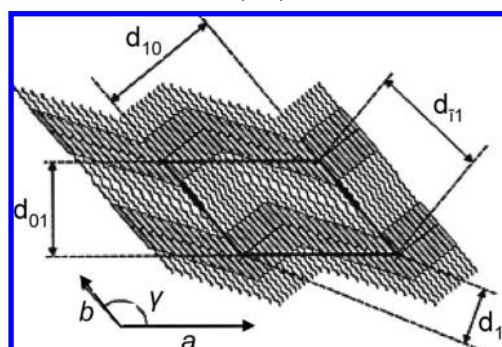
Figure 5.6. Small-angle X-ray scattering profiles of the $F12H8$ diblock; intensity at various temperatures ($^{\circ}\text{C}$). The solid–solid phase transition temperature was reported as 51°C . The peak at the larger distance ($\sim 0.28\text{ \AA}^{-1}$) is a second-order peak. From ref 254 with permission.

5.015 \AA , comparable to the peak at 4.935 \AA of $n\text{-C}_{20}\text{F}_{42}$ and differed substantially from those of the triclinic $n\text{-C}_{20}\text{H}_{42}$ and orthorhombic $n\text{-C}_{19}\text{H}_{40}$. The dominance of the reflection at 5.015 \AA diminished with increasing Hm block length. The WAXD data were also interpreted in terms of at least two structures being present. The slight increase in spacing and diffuse nature of the $F12H8$ diffraction pattern were deemed consistent with the Raman evidence for a rotator phase. However, the diffraction spectra did not allow hkl indexing. Semiempirical energy calculations gave similar energies for different packing models. As m increased, the diffraction patterns became more and more diffuse. Although this phase allowed for considerable freedom for the molecules to rotate about their long axis, it was considered as essentially crystalline. The possibility that it might actually consist of a liquid crystal phase was acknowledged in a subsequent paper.⁹⁵

Above T_1 , only the peak at shorter distance remained in the SAXS profiles. As temperature increased, the repeating distance decreased to a value corresponding to the fully extended molecule.²⁵⁴ This provided evidence for a simple lamellar structure made of stacked molecular monolayers. In the WAXD spectra, the absence of reflections other than that attributable to the intermolecular distance indicated that molecules rotated along their long axis, while maintaining lateral alignment. The transition was proposed to occur through translation of the molecules along their axes, yielding an antiparallel packing layered crystal structure with rotator behavior (Scheme 5.1.Ab).

The solid state behavior of $F12Hm$ diblocks was subsequently revisited using improved and additional techniques.^{109,186,255,263} The SAXS data confirmed the earlier conclusions concerning the *high* temperature phase. How-

Scheme 5.2. Two-Dimensional “Ripple Phase” Structural Model and the Corresponding Oblique Unit Cell (Parallelogram) Proposed for the Low-Temperature Solid Phase of $F12Hm$ with $m = 8, 10,$ and 12^a



^a The shaded straight rods depict the F -blocks and the undulated lines the H -blocks. From ref 186 with permission.

ever, the textures seen for $F12H8$ and $F12H10$ by microscopy between crossed polarizers for the mesophases at 65 and 71°C , respectively, were described as similar to those exhibited by textbook smectic B phases.²⁵⁵ Eventually, this first mesomorphic state below melting for the $F12Hm$ diblocks ($6 \leq m \leq 14$) was identified as a smectic liquid crystalline phase, rather than a crystallized bilayer with rotator behavior.^{109,186,263} In the SAXS study of $F12Hm$ ($6, 8, 10$), the number of lamellae that contributed coherently to the scattering was low (≤ 40), indicating also liquid crystalline rather than crystalline order in the *low*-temperature phase.

Magic-angle spinning (MAS) ^{13}C NMR spectra of $F12H12$ showed isotropical chemical shifts, giving evidence for a liquid-like structure for the H -chains below T_m and even below T_1 (Figure 5.7).²⁵⁵ These NMR data, as well as the magnitudes of the transition entropies, were inconsistent with the conclusions of the earlier Raman and SAXS studies. NMR indicated indeed that, in the *high* temperature “solid” phase of $F12H12$, the H -chain exhibited a nearly liquid-like *gauche/trans* ratio, in contradiction with the absence of *gauche* defects inferred from the Raman spectrum of $F12H8$. The initial hypothesis that the transition was associated with a change in lattice packing and not in molecular conformation was therefore also contradicted.

Further SAXS studies of the *low*-temperature phase of the $F12Hm$ diblocks, using an improved X-ray setup, also recognized distinct behaviors for $m = 6, 8 \leq m \leq 12$, and $m \geq 14$.^{186,263} However, for $m = 8$ and 10 , the study concluded against the initial two-phase coexistence hypothesis and tilted bilayer model below T_1 . The general appearance of the X-ray diffraction spectra, and in particular the nonequidistant Bragg peak pattern, reflected a more complex structure than a simple mono- or bilayered arrangement. An oblique two-dimensional unit cell was deemed necessary to account for the observed peak pattern. A molecular arrangement was proposed that consisted of double-layered undulating lamellae (Scheme 5.2). These undulating bilayers, or “ripple phase”, were similar to the liquid crystalline structures found in certain block copolymers²⁶⁵ and lecithin bilayers.²⁶⁶ Such a “ripple” or “zig-zag” lamellar structure could accommodate a large amount of *gauche* defects. SAXS spectra containing simultaneous contributions from the *high*- and *low*-temperature phases have been observed for $m = 6$ and 8 , probably reflecting slow transition kinetics and nonequilibrium states.²⁶³ No information on lateral structure within

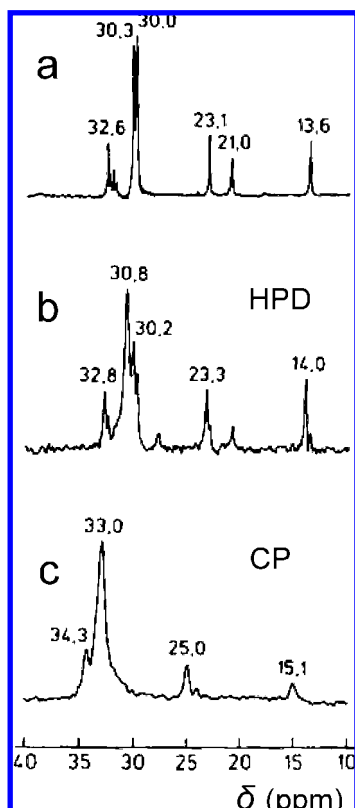


Figure 5.7. High resolution MAS ^{13}C NMR spectra of $F12H12$: (a) of the melt (95 °C), (b) above (86 °C) and (c) below (−53 °C) the upper solid state phase transition. CP refers to a cross-polarization spectrum and HPD to a spectrum obtained with 90° carbon pulses with high power ^1H – ^{13}C decoupling. From ref 255 with permission.

lamellae could be extracted from the still poorly resolved wide-angle region of the SAXS spectra. The WAXD spectra contained 7–10 peaks in the d spacing range of 0.40–0.50 nm, which excluded a hexagonal rotator phase for the low temperature phase.

Above T_1 , the new X-ray study confirmed most of the earlier findings and in particular that the diblocks formed a monolayered lamellar structure, with close-packed untilted F -blocks and disordered, liquid-like H -blocks.²⁶³ For each of the three $F12Hm$ diblocks ($m = 6, 8,$ and 10) investigated, the SAXS pattern consisted indeed of a single peak, matching that measured for PTFE, which originates from crystalline regions of close-packed $(\text{CF}_2)_n$ chains. The d spacings were slightly smaller than the length of the fully extended molecules calculated from interatomic distances and bond angles. The WAXD pattern, which consisted of a single peak, showed a structure similar to that of PTFE, i.e., a hexagonal arrangement of untilted F -chains. Rather than to a tilt, the fact that the interlamellar distances were somewhat shorter than molecular length was attributed to a high number of *gauche* defects in the H -chains. The *high*-temperature phase was definitely identified as a smectic liquid crystalline phase.¹⁸⁶

A very recent study of $F12H12$ ²⁶⁷ also detected a first-order solid–solid transition at T_1 below melting at T_m and confirmed in part the earlier structural hypothesis.^{186,254} The main new finding was the detection of the surprisingly prolonged transient dynamic coexistence of solid (smectic) and amorphous (liquid) regions of submicrometer size within the mesophase between T_1 and T_m .²⁶⁷ The proposed packing (Scheme 5.1) for the *lower* temperature solid phase (Bc)

consists of stacked tilted FC bilayer lamellae separated by densely packed interdigitated (at variance with earlier proposals) HC layers. Indexation of the SAXS profile suggested a complex internal lattice. The mesophase, between T_1 and T_m , was found to be heterogeneous and to comprise a well-packed smectic monolayer arrangement (Ac), composed of phase-separated crystallized FC and more mobile HC layers, in coexistence with a liquid phase. High resolution Brillouin light scattering (BLS, which probes the propagation of thermal phonons through the medium) detected indeed two sound velocities in this mesophase and was used to elucidate the dynamics of the system. The dynamic coexistence of the liquid and solid phases (>12 h at a temperature about 5 °C below T_m) in a finite temperature range indicated surprisingly slow kinetics for the system to reach equilibrium. A two stage mechanism was proposed for the melting of the highly anisotropic intermediate smectic phase: at T_1 , in addition to the transition from bilayer FC to monolayer arrangement, a film-surface melting would occur, whereas T_m would be associated to the grain-boundary/crystallite-surface melting.

5.3.1.3. Long H -Chain Diblocks $F12Hm$ with $16 \leq m \leq 20$. For $m = 16$ – 20 , the DSC thermograms of the $F12Hm$ diblocks did not show evidence for solid–solid transitions in the early studies. However, the jump in melting enthalpy (from 21 to 26 kJ mol^{-1} for $m = 2$ – 14 , to 41.3 kJ mol^{-1} for $m = 16$) clearly indicated a fundamental change in molecular packing.²⁵⁴

Only one single sharp reflection was present in the SAXS profile (a second diffuse maximum appeared, however, at smaller angles for $m = 20$), with a Bragg spacing increasing with m and somewhat less than twice the molecular length, which was attributed to a bilayer type crystal packing.^{6,254} Substantial differences in the Raman spectra and diffraction profiles also supported a considerable change in structure for H -chains larger than 14. The diffraction profiles indicated highly disordered structures that could not be elucidated.^{186,263}

5.3.1.4. The Case of $F12H20$. The phase behavior of $F12H20$ illustrates, among others, the dependence of diblock structure on sample history. DSC experiments showed indeed that a higher degree of order was achieved when $F12H20$ was crystallized from a solvent, as compared to from the melt.¹⁰⁹ While the latter material only showed the melting endotherm at 100 °C, a solution-crystallized sample exhibited two additional solid–solid transitions (Table 4). Crystallization from solution below 35 °C (the first transition below melting) yielded a polymorphic form that underwent a reversible transition at −23 °C. Upon heating, this stable form changed at 35 °C into a less ordered one that was similar to that obtained from material cooled from the melt. The latter transformation was not reversible, presumably due to hindered kinetics in the absence of solvent. MAS ^{13}C NMR of solution-crystallized material confirmed that packing of the H -block was temperature-dependent and resolved two different conformations of the H -block below −23 °C.

Scanning electron microscopy on melt-recrystallized $F12H20$ gave direct evidence for a fibrillar morphology for the *high* temperature solid phase, with bundles of fibrils aligned in one preferential direction (Figure 5.8).¹⁰⁹ A periodical distance of 24 nm (Figure 5.8a) was detected by freeze–fracture transmission electron microscopy that did not originate from a lamellar structure but from the surface of a layer of cylinders of uniform diameter of 24 nm (Figure 5.8b). A model was proposed that consisted of cylinders

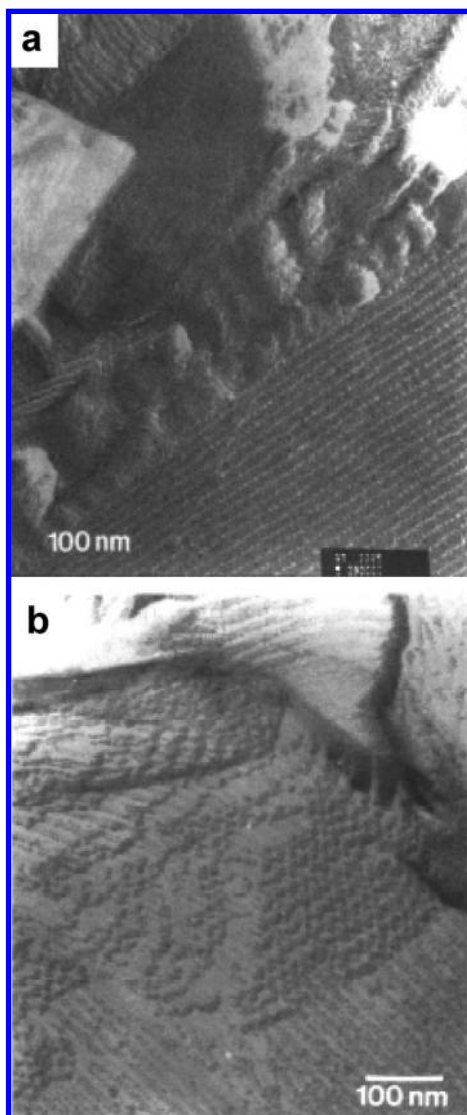


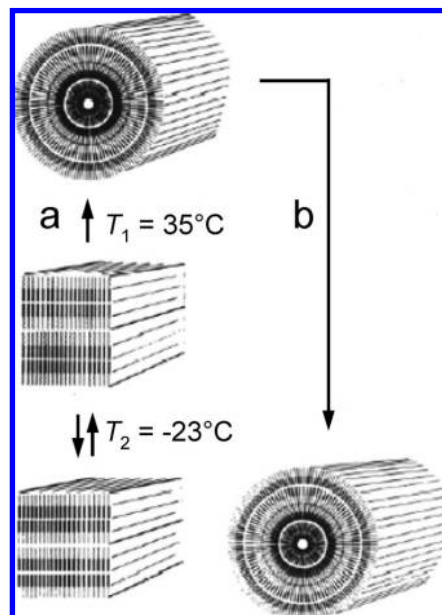
Figure 5.8. Transmission electron microscopy from a replica taken from a freeze–fracture surface of melt-crystallized *F12H20*. Part a shows 24 nm stripes and 6 nm stripes. Part b shows that the 24 nm stripes are formed by layers of cylinders. From ref 109 with permission.

made of three concentric single layers of extended diblock molecules, each 4 nm thick (Scheme 5.3). Bending diblock lamellae provides indeed a means of solving the problem of the regular packing of such amphiphilic molecules. This arrangement implied a gradual change in packing as a function of distance from the center of the cylinder that could explain the broadness of the X-ray diffraction signals. A straight lamellar morphology with a 6 nm periodicity was also observed, which could correspond to the better ordered modification obtained from solution crystallization and would, at 35 °C, bend to form the concentric lamellae that lead to the cylindrical morphology (Scheme 5.3).

5.3.2. The *F10Hm* Series

A pioneering study of *F10H10*, aimed at identifying new liquid crystal forming compounds, had found a smectic B liquid crystal phase between ~38 and 39 °C and melting at 61 °C.⁷ Formation of a liquid crystal was expected from the amphiphilic and amphiphilic characters of the diblock. The X-ray diffraction pattern of the mesophase (three sharp reflections at 50 °C in the low-angle region) indicated a

Scheme 5.3. Hypothetical Model for the Morphologies Encountered for (a) Solution-Crystallized and (b) Melt-Crystallized *F12H20*^a

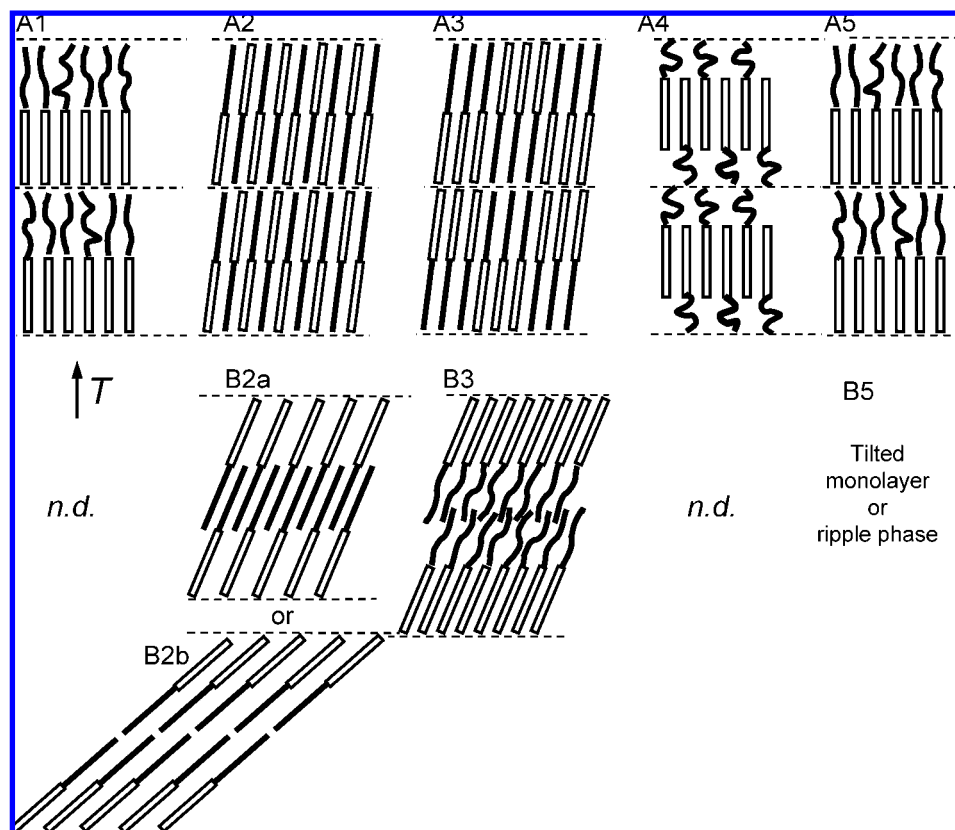


^a The higher ordered modification obtained by solution crystallization undergoes a reversible phase transition at –23°C (likely reflecting disordering of the *H*-block) and transforms at 35°C into a modification that behaved identically with the melt-crystallized sample. In the latter, the molecules are arranged in concentric bilayers and form cylinders of uniform diameter. From ref 109 with permission.

layered lamellar structure with a layer spacing of 28 Å. The second- and third-order reflections indicated a sharp interface between the *F*-decyl and *H*-decyl sublayers. The wide-angle region showed a very narrow reflection at 4.75 Å, emerging from a diffuse band around 4.5 Å, consistent with *disordered H*-blocks and a two-dimensional hexagonal packing of *segregated* rigid *F*-blocks oriented perpendicular to the layer planes (Scheme 5.4.A1). The reflection at 4.75 Å corresponded to a distance of 5.48 Å between two neighboring molecules, comparable to those reported for *F*-alkanes (5.70–5.73 Å)^{268,269} and PTFE.²⁷⁰ No information was given on the lower temperature structure.⁷ A Raman spectroscopy study of *F10H10*, along with other *F_nH_m* diblocks, indicated rotator behavior *below* the solid phase transition.⁶

A subsequent study determined that *F10H10* actually formed two liquid crystalline phases, with a reversible transition that occurred over a large 37–47 °C range, depending on thermal history.⁹⁵ Both the high temperature LC1 and low temperature LC2 phases consisted of smectic layered structures. The molecules were proposed to be *antiparallel* and *interdigitated* for LC1 and possibly also for LC2, *tilted* in both cases relative to the layer normal (Scheme 5.4.A2) and packed in a pseudohexagonal fashion, but with differences in tilt angle and interdigitation between LC1 and LC2. The SAXS data provided layer thicknesses of ~27.4 Å (in agreement with the earlier study)⁷ and ~34.1 Å, respectively. The tilt was inferred, in particular, from the observation that the layer thickness (after deduction of a “void” between layers that was postulated in order to facilitate lateral layer displacement) was slightly less than the length of the fully stretched molecule, meaning that the possibility for the *H*-chains to be disordered, and hence shorter, was probably not considered. One should also note that the antiparallel packing is a priori energetically unfavor-

Scheme 5.4. Successive Suggested Models for the Structure of the Liquid Crystalline Mesophases Found for *F10H10* and Related *F10*-Diblocks (the Structures Are Viewed in a Section Perpendicular to the Layers): (A) Above the Solid State Phase Transition Temperature: (A1) Untilted, Parallel Molecules with Segregated *F*- and *H*-Blocks, Smectic B Arrangement with Rodlike Ordered *F*-Chains and Disordered *H*-Chains, According to Ref 7; (A2) Tilted, Antiparallel, Nonsegregated, Extended Molecules, According to Ref 95; (A3) Partial, Checkerboard Segregation of Tilted Molecules, According to Ref 271; (A4) Nontilted, Antiparallel, Segregated, Smectic B Arrangement with Rodlike *F*-Chains and Highly Disordered *H*-Chains, as Determined by Ref 21; and (A5) Untilted, Parallel, Segregated Smectic B Packing, According to Ref 259 (A1 and A5 Are Essentially Identical). (B) Low Temperature Phase: (B2) Two Suggested Arrangements—(B2a) (Preferred) Tilted ($\sim 30^\circ$), Parallel Interdigitated Diblocks with Segregated Blocks, and (B2b) Tilted ($\sim 50^\circ$) Bilayer of Non-interdigitated Extended Molecules with Segregated Blocks—According to Ref 95 a Mixture of Two Structures Has Also Been Proposed; (B3) Tilted Bilayer of Non-interdigitated Diblocks with Partially Disordered *H*-Blocks, According to Ref 271; and (B5) Monolayers of Tilted Parallel Molecules, and a Possible Ripple Lamellar Phase, Have Been Proposed But Not Represented;²⁵⁹ *n.d.*, Not Determined



able. The LC1 to LC2 transition was suggested to consist of an increase in molecular tilt, followed by a change in the extent to which the molecules were interdigitated. Transmitted polarized light microscopy of LC1 showed typical mosaic textures, which were also assigned to slightly *tilted* ($\sim 5^\circ$) smectic G (or J) liquid crystals. The WAXD data for LC1 were discussed in terms of *antiparallel* chain packing (Scheme 5.4.A2), by similarity with that suggested for *F12H12*, and of a triclinic unit cell, but the spectra could not be indexed.

The SAXS data for LC2 indicated increased layer spacing (34.1 Å), greater than molecular length, that would be compatible either with layers of tilted ($\sim 30^\circ$), interdigitated molecules (Scheme 5.4.B2a), or with bilayers of even more markedly tilted ($\sim 50^\circ$) molecules with segregated blocks (Scheme 5.4.B2b). The former alternative was selected on the basis of WAXD data, although indexing was not possible, because it would require smaller changes in tilt angle and longitudinal displacement of molecules to achieve the LC1/LC2 transition. It should be noted that this model is different from the tilted bilayer model proposed for the crystalline phase of *F12H12* (Scheme 5.1.Bb).²⁵⁴ LC2 was considered as consisting of a mixture of two structures, both derived from LC1 by an increase in tilt angle. In one the

tilted molecules would also have undergone a longitudinal displacement, yielding the interdigitated arrangement shown in Scheme 5.4.B2a.⁹⁵

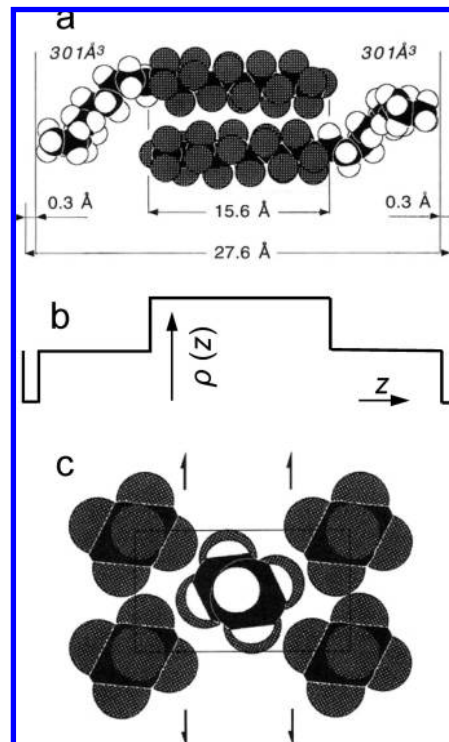
The above structural arrangement for *F10H10* was challenged on the basis of Monte Carlo simulations (united-atom force field).²⁷¹ The study emphasized a strong dependence of liquid crystal phase behavior on *F*-chain stiffness. Two types of smectic phases were calculated to optimally accommodate the energetic and entropic constraints specific to *FnHm* diblocks, but the existence of a smectic–smectic transition could not be confirmed. A *tilted*, microsegregated checkerboard pattern was proposed for LC1 (Scheme 5.4.A3), while a tilted bilayer with *H*-blocks not fully stretched was proposed for LC2 (Scheme 5.4.B3). This simulation curiously suggested that the *H*-chains should be more disordered at low temperature than at high temperature. However, the relevance of the new models to the actual phase behavior of *F10H10* could not be conclusively determined, given the approximate nature of the force-field adopted and uncertainties in the interpretation of the experimental data. An all-atom force field and a properly chosen mixing rule for the cross-interaction parameters should provide more reliable predictions for smectic behavior for *FnHm* diblocks.

Diblocks *F10H9* and *F10H11* also presented liquid crystalline properties with a reversible transition between tilted smectic phases.²⁶² The transition on cooling was proposed to occur, as for *F10H10*, in two stages: first an increase in molecular tilt angle and second a change in the relative interdigitation of the diblocks within layers.

The two above proposed *tilted* diblock models^{95,271} were disproved on the basis of an X-ray diffraction study (powder samples) of the mesophases of *F10H10*, *F10H8* and of the branched diblock $C_{10}F_{21}(CH_2)_4CH(C_2H_5)(C_4H_9)$, which supported yet a further structural hypothesis.²¹ At low angles, all three compounds displayed a series of 00*l* Bragg reflections (first to third order, and even fourth order for the branched diblock), indicating a layered arrangement (repeating distances of 27.60, 24.78, and 26.68 Å for *F10H10*, *F10H8*, and the branched analogue, respectively). At large angles, some *hk0* and *hkl* reflections were identified. The in-plane 110 reflexions occurred at very close angles for the three diblocks, indicating close smectic B structures and that the same structural model should apply to all three compounds. The main difference between the three compounds was the relative reflection intensities with respect to background. Interestingly, it was the branched diblock that presented the highest number of in-plane reflections, indicating higher order and allowing indexation with a rectangular unit cell (*pg* was retained as the 2D space group). The presence of *hkl* lines, which indicate positional correlations between the smectic planes, was checked for the branched diblock only. These lines were only compatible with a 3D orthorhombic cell. Since the three compounds had similar smectic B structures, the same cell geometry was proposed for *F10H8* and *F10H10*. It is noteworthy that the cell parameters of the branched diblock were only slightly larger than those for *F10H8* and *F10H10*, providing evidence that the cell dimensions were determined by the close-packing of the *F*-chains.

Based on these observations, a structural model, different from the previously reported ones, was proposed in which fully stretched *F*-chains, compactly packed in a hexagonal in-plane ordering, and *perpendicular* to the smectic layer, formed a *segregated* sublayer in the middle of each smectic lamella (Schemes 5.4.A4 and 5.5a).²¹ In this model, two adjacent diblock molecules are oriented oppositely. The area per molecule was 27 Å². The space available for each *H*-block was, therefore, 54 Å², meaning that the *H*-chains that flank the *F*-sublayer needed to have a highly disordered conformation in order to fill the space on either side of the *F*-sublayer. A liquid-like conformation for the *H*-chains was also supported by the halo observed for all compounds around 5.2 Å in the X-ray pattern. The new model, which alternated electron-rich and electron-poor sublayers, implying a crenel-shaped electron density profile (Scheme 5.5b), was also strongly supported by the structure factor analysis of the 00*l* reflections, which was incompatible with the earlier model that had nonsegregated *F*- and *H*-chains.⁹⁵ A model with interdigitated stretched *F10* and *H10* chains would indeed result in constant electron density. An infrared dichroism study of homeotropically oriented specimens of *F10H10* confirmed that the rigid *F*-chains were perpendicular to the smectic layers and that the *H*-chains were in a quasi-molten state.²¹ The packing compatible with the *pg* space group retained was the rectangular herringbone-type arrangement of *F*-chains shown in Scheme 5.5c. The two molecules in the unit cell have up and down alternating *H*-chains.

Scheme 5.5. (a) Segregated Arrangement for Diblock *F10H10* with Stretched Rigid, *F*-Chains Stacked in the Middle of the Smectic B Layer, and Disordered, Quasi-Molten Flexible *H*-Chains Filling the Space Available on Both Sides, Based on Experimental Lattice Parameters and Calculated *F*-Chain Length (an Interlayer Gap of 0.6 Å Was Assumed); (b) Crenel-Shaped Electron Density Profile $\rho(z)$ along the Layer normal, Corresponding to the above Segregated, Stacked *F*-Chain Model (Interdigitated Stretched *F*- and *H*-Chains Would Result in Constant Electron Density); (c) Schematic Top View of the Herringbone-Like Arrangement of the *F*-Chains (the *H*-Chains Are Pointing up and down Alternatively^a)



^a From ref 21 with permission.

Thorough multitechniques experimentation on an extended series of *F10Hm* diblocks ($2 \leq m \leq 19$, including the uneven *m* carbon numbers) further supported an *untilted, segregated F*-chain ordering for the first mesophase below melting (labeled M1), but with *parallel*⁷ rather than *antiparallel*²¹ arrangement of adjacent molecules (Scheme 5.4.A5).²⁵⁹ Thermal analyses and optical textures determined a first-order liquid crystal–liquid crystal phase transition for $6 \leq m \leq 12$ that was assigned to a change in packing. The high temperature M1 phase was identified by polarized light microscopy as a smectic B phase, with untilted molecules undergoing fast rotation about their long axis. For the low temperature M2 phase, the aspect of the samples depended on *m*, varied with thermal history and over time, and indicated slow transition kinetics. M2 was regarded as a *tilted* smectic phase, possibly a smectic G phase. No liquid crystalline properties or mesophase transitions were found for *F10Hm* compounds with $2 \leq m \leq 5$ and $13 \leq m \leq 19$.²⁵⁷ *F10H5* exhibited a sharp reflection in the small-angle region of the X-ray pattern, characteristic of crystal packing.²⁵⁹ The WAXD pattern of diblocks with $m \geq 13$ showed increased disorder in their molecular orientation.

WAXD data for *F10H9* indicated well-developed layers for M1, the thickness of which corresponded closely to molecular length.²⁵⁹ The intermolecular spacing (~ 5.53 Å)

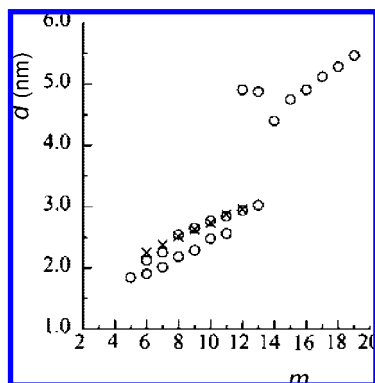


Figure 5.9. Layer spacings, calculated from X-ray diffraction data, as a function of H -block length m in the $F10Hm$ series. The open circles represent the spacings found for the M2 phase, i.e., below the phase transition temperature, and the crosses those measured for the M1 phase above this transition. From ref 259 with permission.

was again reminiscent of that of the hexagonal structure of PTFE. A parallel molecular arrangement was proposed that minimized fluorine/hydrogen contacts. For the lower temperature M2 phase, two different structures appeared to coexist for $6 \leq m \leq 12$, consisting of partially and fully transformed phases. Two possible models were proposed for M2: a tilted smectic phase (possibly a smectic G) and a ripple phase similar to that proposed for $F12H8$.²⁶³ The smectic–smectic phase transition was assigned to a change in packing.²⁵⁹ Figure 5.9 shows the layer spacings, as determined by X-ray diffraction above and below the M1/M2 transition as a function of the length of the H -block. It illustrates the coexistence of two different layer spacings in the M2 phase for $6 \leq m \leq 13$. For $5 \leq m \leq 11$, these spacings were shorter than the fully extended molecule, which was assigned to monolayers of tilted molecules. For $F10H12$ and $F10H13$, the layer spacings were longer than the molecular length and slightly less than three times the longer segment, indicating a tilted bilayer structure.

Density measurements as a function of temperature (Figure 5.10) confirmed first-order phase transitions for both the melting and M1/M2 transitions. The densities of diblocks $F10Hm$ with $6 \leq m \leq 12$ were seen to decrease and the molecular volumes to increase (Figure 5.10a) with increasing m .²⁵⁹ The calculated molar volume per CH_2 were 19.38 and $17.04 \text{ cm}^3 \text{ mol}^{-1}$ for the melt phase and the M1 phase, respectively. The authors noted that the latter value is comparable to the $17.10 \text{ cm}^3 \text{ mol}^{-1}$ value found for the smectic B phase of the classical smectogen series of 4-bromo- N -(4- n -alkyloxybenzylidene)anilines. An even/odd effect has been noted in the volume jump measured at the M1/M2 transition, with the compounds with an odd number of carbons in their H -block exhibiting a larger jump than the even-numbered ones.²⁵⁹

Striking differences in melting entropy (Figure 5.4), density, and dielectric relaxation behavior suggested differences in structure and phase transition mechanisms between the $F10Hm$ and $F12Hm$ series. Dielectric relaxation spectroscopy, which reflects the mobility of the moieties surrounding the dipole, can provide information on molecular dynamics within liquid crystals (reorientations of the whole molecule, short-range hindered rotational motions, and more local motions). Dielectric experiments (measurements of the frequency dependence of the dielectric loss factor over a range of frequencies (150 to 10^7 Hz)) performed on bulk

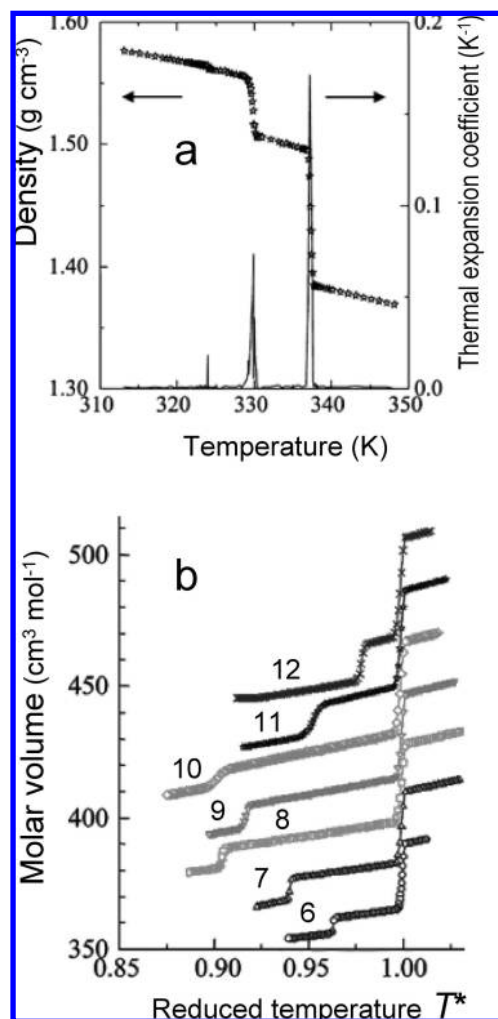


Figure 5.10. (a) Example of density (star symbols) and thermal expansion coefficient (solid line) variations as a function of temperature for $F10H11$ upon heating. From right to left: melting, smectic–smectic phase transition, and a further lower temperature transition, found solely for this diblock, which may reflect a change in unit cell structure. (b) Variation of the molar volumes as a function of the reduced temperature T^* for the $F10Hm$ series upon cooling; the number on each curve is the value of m . From ref 259 with permission.

$F10H10$ and $F12H8$ showed considerable differences in dielectric loss and activation energy between the two diblocks at the liquid crystal/liquid crystal phase transition.¹⁷¹ Rotation of the F -chain was established in the liquid crystalline state for both diblocks. However, the activation energy associated with this rotation was significantly less for $F12H8$ ($\sim 66 \text{ kJ mol}^{-1}$) than for $F10H10$ ($\sim 135 \text{ kJ mol}^{-1}$). This difference was tentatively assigned to different packings and tilt angles of the two compounds. The surprisingly large difference between the dipole moments of $F12H8$ and $F10H10$ ($\mu_{F12H8}/\mu_{F10H10} = 2.29$) further supported a difference in packing modes. The kinetics of the rotational motion of the F -chains was also different. Similar dielectric experiments have been performed on a series of $F10Hm$ ($m = 6\text{--}14$) diblocks.⁹⁶ An even/odd effect was seen for the total integrated dielectric intensity but not for the transition temperatures.

Also noteworthy is that $F10H10$ appears to behave differently from its homologues within the $F10Hm$ series, a deviant behavior that was not found for $F12H8$ (same total length) or $F12H12$ (same block length). In particular, the solid state transition entropy for $F10H10$ was smaller and

out of line with the values measured for the other *F10Hm* diblocks (Figure 5.4). The phase transition rate was also much slower for *F10H10* than for the other diblocks investigated.²⁵⁹

Molecular dynamics simulations for *F10Hm* ($m = 6, 8, 10,$ and 12), using an atomistic potential model, led to highly ordered layered structures upon cooling from an isotropic random layout (256 molecules).²⁷² The mixture of monolayer and interdigitated bilayer structures inferred from experimental X-ray data for *F10H12* (and not for the other compounds investigated) was reproduced. Molecular dynamics calculations confirmed a much higher tendency for *FCs* than for *HCS* to form ordered layered structures.²³⁰ In *FnHm* diblocks, this tendency was, however, significantly limited by the attached *H*-chain.

The evolution of our understanding of the structure of the first mesophase (LC1 or M1) found below melting for *F10H10* is summarized in Scheme 5.4. Eventually, the most convincing available data point to a smectic B liquid crystal structure with segregated rigid *F*-blocks, parallel to the layer normal and segregated disordered *H*-blocks, as depicted in Schemes 5.4.A1 and A5 or A4, most likely the latter arrangement. The structural models proposed for the phase *below* the first solid phase transition (LC2 or M2) remain largely speculative.

5.3.3. The *F8Hm* Series

Early thermal analysis and Raman spectroscopy data indicated that *F8H8* fell in line with homologous diblocks.⁶ *F8Hm* diblocks with $m = 8–11$ exhibited a mesophase, and polarized light microscopy showed textures similar to those found for the *F10Hm* series, suggesting smectic B liquid crystalline phases. Differences in thermal behavior were noticed between *F8H10* and *F8H11*.²⁵⁸ No liquid crystalline behavior was found when $m \geq 12$. No even/odd effect was observed in this series.

The solid state behavior of *F8H16* has been thoroughly investigated using temperature-modulated scanning calorimetry (TMSC, which allows studying the kinetics of a phase transition and the determination of its equilibration time and reversibility), dielectric spectroscopy, and NMR.¹⁷⁰ For samples crystallized from the melt, TMSC found two solid phase transitions for *F8H16* at 1.5 and 24 °C, while three transitions were observed by dielectric spectroscopy at about $-15, 2,$ and 24 °C, below the melting temperature (52 °C) (Figure 5.11). The three latter transitions were confirmed by ^1H and ^{19}F free induction decay (FID) NMR analysis on samples crystallized both from the melt and from solution. Wide-line ^1H and ^{19}F NMR suggested that the transition at -15 °C was related to the onset of a dynamic process in the *H*-chains only. The *H*-chains were, however, also involved in the transition at 2 °C, while the *F*-chains were involved in the transitions at 2 and 24 °C. The motional processes involved in all the phase transitions were quite slow, occurring over a rather large temperature range, especially for the transitions at -15 and 24 °C.

Also noteworthy is that fibers of *F8H16*, crystallized within an *F*-octane/isooctane mixture, were determined by SAXS experiments to adopt a ribbon-like lamellar arrangement, different from the cylindrical arrangement reported for *F12H20* (see section 7.2).^{177,264}

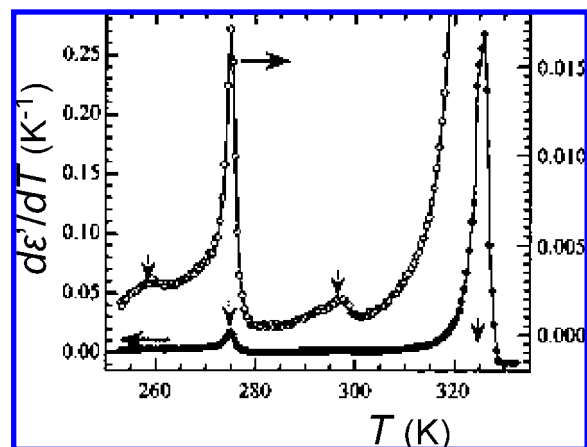


Figure 5.11. Dielectric spectroscopy data for *F8H16*: variation over time of the real part ϵ' of the complex dielectric constant ϵ (double scale) as a function of temperature at a frequency of 14.67 kHz. The arrows mark the transitions. From ref 170 with permission.

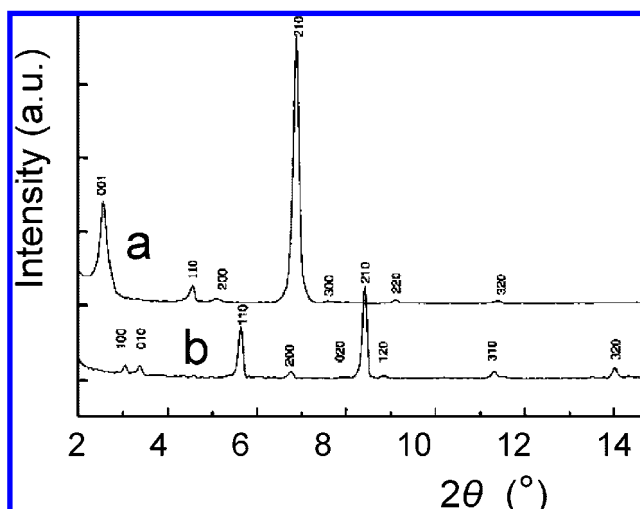
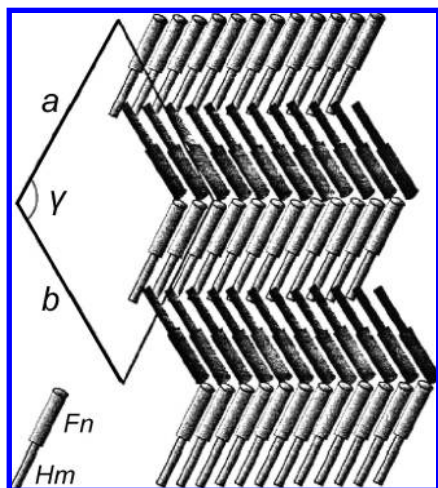


Figure 5.12. X-ray diffraction plots of (a) *F8H10Br* and (b) *F8H4Br*. All the peaks of the small angle region have been indexed by a large planar lattice and indicated a layered structure of low symmetry. From ref 29 with permission.

5.3.4. Brominated and Iodinated (*F*-Alkyl)alkanes and Further Diblocks

A thorough study of a series of terminally brominated (*F*-alkyl)alkanes $\text{C}_n\text{F}_{2n+1}\text{C}_m\text{H}_{2m}\text{Br}$ ($n = 8, m = 2, 4, 6, 10;$ and $n = 10$ or $12, m = 10$) provided further interesting clues. The melting points were higher than those of the nonbrominated analogues (44.0 °C for *F8H10Br* vs 35 °C for *F8H10*; 70.7 °C for *F10H10Br* vs 59.8 °C for *F10H10*; 96.5 °C for *F12H10Br* vs 92 °C for *F12H10*), and only *F12H10Br* exhibited a solid state transition with a strong endotherm at 80.1 °C.²⁹ The melting enthalpy increased regularly with m (by 3.1 kJ mol⁻¹ per CH₂). Interestingly, the melting enthalpy *decreased* significantly (from 38.5 to 21.9 kJ mol⁻¹) when the number of CF₂ groups went from 8 to 12, probably indicating increased disorder in the *F*-chain and, in turn, in the *H*-chain. This phenomenon has not been observed in the *F12Hm* or *F10Hm* series. FTIR data were interpreted as indicating a dominant planar zigzag conformation for the *F8* block (*F8HmBr*, $m = 4, 6,$ and 10), a mixture of planar and helical conformations for *F10* (*F10H10Br*), and a

Scheme 5.6. Structural Model Proposed for *F_nH_mBr* Diblocks with Alternating Tilted Layers and Antiparallel Head-to-Head Packing (Bromine Atoms Not Represented)^a



^a From ref 29 with permission.

dominance of helix conformation for *F12* (*F12H10Br*) with a number of helix defects that increased with *F*-chain length.²⁹

The small-angle region of the X-ray diffraction plots (Figure 5.12) has been fully indexed for *F8H_mBr* ($m = 4, 6, \text{ and } 8$) and *F_nH10Br* ($n = 10 \text{ and } 12$) and indicated a layered structure of low symmetry. The most plausible space groups were P_1 or P_2 . As the unit cell parameters were larger than the molecular length and smaller than a bilayer length, a noncentrosymmetric lamellar structure model was proposed with alternating tilted layers and antiparallel head-to-head packing in a herringbone fashion (Scheme 5.6). Single crystal Laue diffraction patterns exhibited wide-angle diffraction rings at 4.9–5.0 Å, including some sharp diffraction spots, typical of plastic crystals. The diffuse halo at 5 Å in the wide-angle region of the X-ray diffraction plots also indicated that the compounds were not perfect crystals.²⁹

Only *F12H10Br* displayed a transition prior to melting. Polarized light microscopy showed a mixture of focal-conic and mosaic textures characteristic of highly ordered smectic phases. FTIR monitoring of conformational changes during the transition were in line with substantial conformational changes of the *H*-chain at the solid phase transition and of the *F*-chain at melting. Time-resolved WAXD data were interpreted to mean that *F12H10Br* was crystalline below T_1 with hexagonal packing of the *F*-chains and rotation of the molecules about their long axis. The combination of X-ray and FTIR results led the authors to consider the transition as a plastic crystalline to smectic B transition. Above T_1 , the *H*-chains were melted and the *F*-chains packed in a hexagonal lattice, but with local conformational disorder.²⁹

The above findings (high melting points and enthalpies, distinct solid state behavior) may indicate that introduction of a large terminal bromine atom, by reducing the amphisteric and amphiphilic characters of the diblock, reduced the driving forces for liquid crystal phase formation. The absence of a liquid crystal phase for *F10H10Br* differs strikingly from the observation of a smectic B phase, throughout the series investigated ($6 \leq m \leq 12$), for the *F10CH₂CHIH(m-2)* diblocks, which have an internally located iodine,²⁶¹ probably indicating that, in the latter case, the *H*-chain remains very flexible beyond the iodine-bearing carbon.

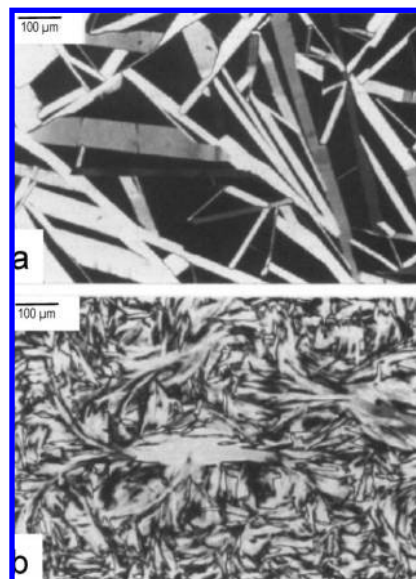


Figure 5.13. Mesophase textures at 20 °C of diblocks (a) with a branched *H*-block, $C_{12}F_{25}CH_2CH(CH_3)C_9H_{19}$, and (b) with a branched *F*-block, $(CF_3)_2CF(CF_2)_6C_{10}H_{21}$, as observed by optical microscopy between crossed polarizers. The first consists of a bâtonnet texture, and the second is of the broken focal conic type; compare also with Figure 5.1. From ref 109 with permission.

The existence for the *F10CH₂CHIH(m-2)* ($6 \leq m \leq 12$) series of a very narrow, less ordered smectic A phase between the smectic B phase and the isotropic melt was inferred from the texture seen by transmitted polarized light microscopy.²⁶¹ Contrary to the case of the *F10H_m* series, there was very little variation in T_m with m , reflecting a dominating role for iodine in the intermolecular interactions.

A liquid crystalline phase has been observed for the vinyl ether *F8H2OCH=CH₂* but not for its *F6* homologue.¹¹⁴ No evidence for a liquid crystal phase appears to be available for diblocks with $n < 8$.

The *F*-alkylated allyl ethers *F_nH_mOCH₂CH=CH₂* ($n = 8, 10, 12; m = 4, 6, 10$) all exhibited at least one and most generally two solid–solid transitions below melting.¹¹⁵

5.3.5. Branched *F_nH_m* Diblocks

Introducing branched segments, and hence, disorder, in either *F*- or *H*-blocks has been used to help assign the onset of disordering to a given block. Branched *F*-blocks (e.g., $(CF_3)_2CF(CF_2)_n C_m H_{2m+1}$, $n = 4 \text{ or } 6$, $m = 10 \text{ or } 12$) caused substantial lowering of both the melting point and the mesomorphic phase transition temperature.¹⁰⁹ Branching also changed the lamellar arrangement of the smectic phase. While bâtonnet textures were always observed by optical polarization microscopy with linear *F*-segments (Figure 5.13a), a broken focal conic-type texture was found for *F*-isononyl-*n*-decane $(CF_3)_2CF(CF_2)_6 C_{10} H_{21}$ (Figure 5.13b). On the other hand, *H*-block branching, as in $C_{12}F_{25}CH_2CH(CH_3)C_9H_{19}$, had little effect on T_m (which is primarily governed by *F*-chain melting) but significantly decreased T_1 (i.e., affected *H*-block packing). It also increased the stability of the liquid crystalline phase. Thus, the mesomorphic state of $C_{12}F_{25}CH_2CH(CH_3)C_9H_{19}$ spans over 60 °C, while that of *F12H12* spans over 12 °C only. *H*-Block branching did not appear to alter the mesomorphic phase structure, which showed the same type of bâtonnet structure as for linear diblocks.¹⁰⁹ The fact that *F*-block branching

affected the liquid crystal structure, while *H*-block branching left it essentially unaffected, confirmed that the former were regularly packed in the mesophase, while the latter were already conformationally disordered.

The branched $C_{10}F_{21}C_4H_8CH(C_2H_5)C_4H_9$ diblock displayed a smectic B phase at room temperature, until melting at 32.7 °C.²¹ Similar compactness was again found for the branched and nonbranched (*F10H8* and *F10H10*) compounds, indicating that the bulky ethyl side chain could be easily accommodated within the disordered alkyl chain regions (Scheme 5.5a). Actually, this asymmetric *F10H11* diblock presented a higher number of in-plane reflections, which allowed indexation with a rectangular unit cell.

In view of the preceding two reports, it is puzzling that a study of the same and additional *F*-isononyl-*n*-alkanes, $(CF_3)_2CF(CF_2)_6C_mH_{2m+1}$ ($m = 7-16$) found no solid state phase transition or liquid crystal phase for *F*-branched diblocks.²⁵⁸

5.4. Solid State Behavior of *F_nH_mF_n* Triblocks and Multiblocks

5.4.1. Triblocks with *F*-Alkyl and Alkyl (Aryl) Blocks

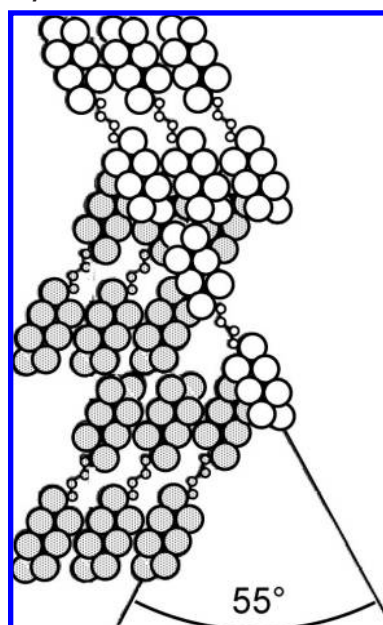
F_nH_mF_n triblocks comprise a flexible *H*-block flanked by two rigid *F*-blocks. Thermal studies of a series of *F12H_mF12* ($6 \leq m \leq 22$) triblocks initially found only one single endotherm corresponding to melting.⁷⁷ A phase transition was subsequently reported at a lower temperature (~ 14 °C) for *F12H10F12*, which was assigned to a rearrangement of the chains within the unit cell.²⁷³ Raman spectroscopy indicated that *F12H10F12* may exist below its melting point in a hexagonal-like structure, similar to the R_{II} rotator phase of odd *n*-alkanes. The phase below 14 °C was characterized by a decrease of molecular mobility, related to an increase of intermolecular coupling, and may be similar to the orthorhombic R_I phase of *n*-alkanes.

A further study reported two transitions, in addition to melting, for *F12H10F12* and one for *F10H8F10*.²⁵⁵ MAS ^{13}C NMR experiments and smaller transition entropies than those measured for diblocks indicated liquid-like behavior for the central *H*-block with, however, lesser mobility than that in diblocks because motion was restricted by the two adjacent rigid *F*-blocks. The lower transition appeared to involve no significant change in chain conformation or packing.

Eventually, liquid crystalline (smectic B) behavior was identified by polarized light microscopy for *F10H10F10*, *F12H8F12*, and *F12H12F12* over a very narrow temperature range (~ 0.4 °C).²⁷⁴ The transition between the smectic B and crystal phases was slow and appeared to involve tilting of the molecules.

Remarkable structural differences were noted between the short triblock *F6H4F6* and its *F*-alkane and alkane analogues (e.g., $C_{16}F_{34}$, $C_{20}F_{42}$, $C_{33}H_{68}$).²⁷⁵ Single crystals of *F6H4F6*, grown from cyclohexane at 30 °C (β phase), underwent, at 37 °C, a monotropic phase transition to a plastic crystalline phase (also named “orientational disordered crystalline” or α phase), prior to melting at 50 °C. A further, lower temperature equilibrium transition was detected at -128 °C, as well as two nonequilibrium transitions. Above the α/β solid state transition at 37 °C, a layered structure with tilted molecules ($\sim 42^\circ$), arranged in a slightly distorted hexagonal lattice, was found. However, the crystallographic data did not allow determination of the crystal system. In the *low*

Scheme 5.7. Proposed Packing of Triblock *F6H4F6* at Room Temperature (β Modification)^a



^a Projection of some molecules along an axis that is perpendicular to the molecular long axis. The molecules are of two consecutive “strata” (white and gray), in which they have different orientations, with the angle between their long axes being 55°. From ref 275 with permission.

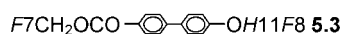
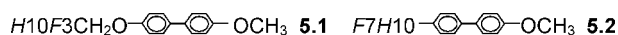
temperature phase (β phase, thermodynamically stable at room temperature), *F6H4F6* crystallized in the monoclinic system and displayed an unusual arrangement of a molecular layer that contained two subsets of molecules with different orientations of their long axes. This structure was regarded as consisting of “strata” of parallel molecules, with the strata being stacked with alternating orientations, with the angle of the molecular axes of adjacent strata close to 55° (Scheme 5.7). This crossed arrangement was further supported by optical and elastic properties measurements. A layered structure with strongly tilted molecules was suggested for the more disordered, melt-crystallized α phase.²⁷⁵ Solid phase transitions were also recorded for *F_nH_mF_n* triblocks with $n = 6$ or 8 and $m = 4, 6,$ or 8.¹²⁸

The effect of a stiff phenyl unit on cooperative motion between *F*-segments has been investigated in a series of *p*-bis(*F*-alkyl)benzene triblocks, $F_nC_6H_4F_n$ with $n = 6, 7, 8, 10,$ and 12.¹³⁵ The DSC thermograms were characterized by a single melting endotherm, except for *F7C6H4F7*, which presented an anomalously high melting point and a second, weaker endotherm, denoting a solid/solid transition. The crystal structure was not determined.

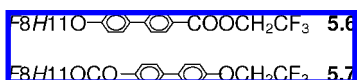
5.4.2. Multiblocks and Polyphilic Mesogens

Investigation of the solid-state behavior of alternating multiblock copolymers provided further illustration of the mesogenic properties of a rigid *F*-segment. Microblock polymers with a regular repeating $-(CF_2)_n(CH_2)_m-$ sequence ($n = 4$ or 6; $m = 6-14$) generally showed two transitions below their melting point and a mesophase with liquid crystalline behavior.^{146,276} An even/odd effect was seen in the melting temperatures. The liquid crystalline phase appeared to be of the smectic B type. The behavior of closely related di- and triblocks with embedded ester junctions has also been investigated.²⁷⁷

A word about polyphilic compounds, that is compounds comprising several fragments differing in their chemical nature, (e.g., compounds **5.1–4**), is also in order in this context. These compounds have been investigated as a generalization of the concept according to which compounds needed to be amphiphilic in order to display mesogenic qualities.^{240,241} The polyphilic compounds synthesized for this purpose usually comprised *F*- and *H*-blocks and the classical mesogenic biphenyl moieties, and possibly also polar junction units, that were arranged sequentially, as in **5.1–3**^{147,148} or in a starlike manner,¹⁴⁹ or in the strongly dipolar “swallow-tailed” compounds **5.4** and **5.5**.²⁷⁸ Segregation of the unlike fragments was expected to induce formation of mesomorphic phases.



A diversity of mesomorphic structures was indeed obtained, depending on molecular structure and, in particular, on whether the *F*-segments were in central or terminal positions (e.g., compounds **5.1** and **5.2**).¹⁴⁷ Mixtures of **5.6** and **5.7** generated smectic phases with ferroelectric properties.¹⁶⁸



5.5. Some Conclusions about the “Solid” State Behavior of *F*-Alkyl/*H*-Alkyl Diblocks and Multiblocks

Not surprisingly, the amphiphilic, amphisteric, and amphotodynamic characters of (*F*-alkyl)alkyl diblocks cause their solid state behavior to be rather more complex than those of *n*-alkanes and *F*-*n*-alkanes. Realistic molecular conformations and packing arrangements need to minimize the unfavorable *F*-chain/*H*-chain contacts and optimize space filling. Additional complexity may result from the possible temperature-dependent interconversion of helix and zigzag *F*-chain conformations and from mutual *F*-chain/*H*-chain inducement of helix reversal, and *trans/gauche* and other conformational changes.

5.5.1. Thermal Behavior

It is now generally accepted that the melting transition is primarily related to breakdown of the lattice of *F*-blocks, while the *H*-blocks are already in a conformationally disordered liquid-like state. A variable number of additional transitions have been observed in the solid state at lower temperatures, especially when the *F*- and *H*-blocks were of comparable length. In both the mesomorphic and crystalline states the *F*-blocks tend to remain regularly packed, while the *H*-blocks are disordered to various extents. There is still some disagreement about the extent of conformational disorder of the *F*-chains. While some authors believe that the *F*-chains remain stretched and rigid in the melt (the small entropy change during melting appears, for example, consistent with rigid-rod characteristics that persist in the liquid),

others think that there is already considerable conformational disorder of the *F*-chains in the solid. However, the specific intramolecular motions of *F*-chains, including helix reversal and helix/planar defects, appear to be less of a hindrance to organized packing than the *gauche* defects that are more typical of *H*-chains. The respective involvement of the *F*- and *H*-blocks in the various phase transitions is not always clear-cut.

5.5.2. Liquid Crystal Behavior—*F*-Alkyl Blocks as Smectogens

In their solid state, *F**nHm* diblocks, like *n*-alkanes and *F*-*n*-alkanes, form layered crystals, with the molecules being arranged in stacks of lamellae with their long axes parallel to each other and more or less parallel to the layer normal. Within the lamellae, molecular packing is, however, frustrated by the difference in cross section between *F*- and *H*-blocks. This mismatch can be mitigated by various degrees of molecule (or block) tilting and interdigitation, *H*-chain disordering (liquidification), layer curvature, etc. In the absence of *F*-chain/*H*-chain interdigitation, each lamella comprises an *F*-sublayer and an *H*-sublayer.

The most important and distinctive feature of *F**nHm* diblocks is their ability, when the *F*- and *H*-blocks are of comparable length, to form smectic liquid crystals. Liquid crystal occurrence is indeed only marginal for *n*-alkanes or *F*-*n*-alkanes. On the contrary, liquid crystal behavior was consistently found for *F**nHm* diblocks when the *m/n* ratio was between ~0.6 and ~1.25 in all three presently documented series ($8 \leq m \leq 14$ for *F*12*Hm*; $6 \leq m \leq 12$ for *F*10*Hm*; and $8 \leq m \leq 10$ for *F*8*Hm*). This definitely establishes that *F*-blocks can play the role of the rigid core required, along with more supple elements, in order to constitute a layered mesophase, and, hence, can substitute for diphenyl or dialcyne moieties as smectogens. In the liquid crystalline arrangement, the linear *F*-block provides the ordering element, while the *H*-block introduces the disordering component.

When the molecular axes are parallel to the layer normal, the result is a smectic B phase. The *F*-chains are then arranged in a two-dimensional hexagonal close-packed array, while the *H*-chains tend to adopt a liquid-like arrangement with numerous *gauche* defects. Conformational disordering of the *H*-segment upon transition to the smectic liquid crystalline phase is obviously facilitated by the smaller cross section of *H*-chains as compared to that of similarly hexagonally packed *F*-chains. Like *n*-alkanes and *F*-*n*-alkanes, *F**nHm* molecules have considerable freedom of rotation about their long axes, in both the low and high-temperature phases. Rotator phase behavior, similar to that described for *n*-alkanes, has also been identified for diblocks in their solid phases.

The solid state structures and phase transition characteristics depend strongly on the relative length of the blocks. As the *m/n* ratio increases, diblocks tend to become more and more disordered, meaning that the influence of the order-inducing *F*-block diminishes. The solid–solid phase transitions are often gradual and sometimes very slow. No liquid crystal phases are seen when one block outweighs the other substantially. Not unexpectedly, when the *H*-block is very short, the diblock’s behavior resembles that of an *F*-alkane, while the alkane character prevails when the *H*-block is much longer than the *F*-block.

Branching of the *F*-block can substantially alter the existence domain and structure of the mesophase. On the other hand, *H*-block branching does not affect the structure of the mesophase much and can, by reducing the difference in steric demand between the two blocks, induce higher order and stabilize a liquid crystalline phase. A similar ordering effect was observed upon introduction of the better space-filling bromine atom at the end of the *H*-block.

5.5.3. Complexity/Variability/Uncertainty

Another prevalent feature of section 5 is the impression of complexity, extreme variability, and uncertainty that it conveys. We believe that this impression truly reflects such complexity, in addition to still limited understanding of the solid state behavior of *FnHm* diblocks and the fact that some experimental data have been interpreted differently or described in different terms by different research groups. Masking this situation by drawing unwarranted generalizations should be avoided.

Except for one single study of a brominated compound,²⁹ no single crystal structure of an *FnHm* diblock has been resolved yet. The WAXD spectra did generally not allow *hkl* indexation. The only definite information provided by the single strong peak seen in most WADX spectra reflects the distance between two parallel *F*-segments (~ 5.5 Å). The intensity of this peak decreases as *m* increases. WAXD studies are difficult due to the intrinsic complexity of the *F*-segment. SAXS profiles give access to the repeating distances, provided that a layered structure is assumed. The only models that were found to fit the SAXS data are the oblique two-dimensional unit cells found for *F12Hm* with $8 \leq m \leq 12$ below T_1 ²⁶³ and the ribbon-like, bilayered structures with interdigitated *H*-blocks reported for *F8H16*.²⁶⁴

Puzzling marked differences in mesophase structures and transition kinetics have been observed between closely related diblocks (e.g., *F10H10* vs homologous *F10Hm* compounds) and diblocks series (e.g., *F10Hm* vs *F12Hm*). Substantially different molecular arrangements have been proposed, often selected on tenuous arguments, for the same or closely related molecules. A wealth of polymorphs has been proposed that could mitigate the energetic and steric mismatch between the dissimilar blocks. They all consist of layered structures, but with differences in arrangement (e.g., parallel vs anti-parallel), molecular tilting, amount of interdigitation, layer or bilayer alternation and curvature, extent of disordering of the *H*-block, etc. These diverse arrangements generally involve only small energy differences. Complex arrangements, involving cylinders and ribbons, double-layered undulating lamellae, herringbone arrangements, etc., have been reported. The coexistence of two structural arrangements or of a solid and a liquid at a given temperature has also been encountered. “Solid” *FnHm* phase behavior also depends strongly on sample history, in particular crystallization conditions. The sensitivity of structure to sample history and the sometimes very slow equilibration kinetics also call for caution when comparing literature sources. An even/odd effect has been observed in the *F10Hm* and *F8Hm* series.

5.5.4. Triblocks

FnHmFn triblocks, not unexpectedly, tend to be more ordered than diblocks made of comparable blocks, as the disorder-prone *H*-block is constrained at both ends by rigid,

order-inducing *F*-blocks. Flexibility and *gauche* defects are primarily localized in the central segment. Liquid crystalline mesophases have been identified for *FnHmFn* compounds having similar *H*- and *F*-block sizes ($n = 10$ or 12 ; $m = 8, 10, \text{ or } 12$) but over a very narrow temperature range. Smectic B mesophases have also been identified in (*F*-alkane)alkane multiblocks.

The solid phases of *FnHmFn* triblocks certainly deserve further attention, as well as the more disorder-prone *Hm-FnHm* triblocks with their central *F*-block flanked by two more mobile *H*-blocks.

5.5.5. Some Open Questions

Despite intensive research, spanning over two decades, and despite the implementation of increasingly sophisticated experimental and calculation techniques, the structural arrangement of *FnHm* diblock molecules in their solid state and the mechanisms of the observed phase transitions remain largely hypothetical.

For a given *F*-chain length, the diblocks with relatively short *H*-chain length are better understood than those with longer *H*-chains that tend to be more disordered. Also, when liquid crystal/liquid crystal transitions were identified, the higher temperature mesophase has generally been relatively well documented but the lower-temperature phase much less so. The structure and mechanisms of the still lower-temperature solid–solid transitions, for example those occurring in the -126 to -57 °C range in the *F12Hm* series, remain essentially unknown.

Particular arrangements, such as the high temperature bilayer-based cylinders formed by *F12H20*, need further investigation. No information could generally be provided on the lateral structure within lamellae. It could not be determined whether the *H*- and *F*-segments within a same diblock always have the same tilt angle. Little information is available for *F12Hm* diblocks with odd *m* numbers. While *H*-chain disorder is rather well established, the nature and extent of disorder in the *F*-block, in particular helix reversal, and the reciprocal induction of order/disorder effects between blocks remain to be ascertained. Frequent discrepancies between conclusions inferred from data acquired through different experimental methods (e.g., Raman and X-ray diffraction) or between experimental data and computer simulations require resolution. So far, even the most sophisticated computer simulations have generally remained inconclusive.

For the time being, prediction of phase behavior for diblocks and diblock series other than those actually investigated is, at best, risky. Investigation of further diblocks may reward the researcher with further types of unforeseeable behavior and structural arrangements. It is not certain whether the unique behaviors found, for example for *F12H20* or *F8H16*, as compared to closely related homologues, denote intrinsic out of line cases or are the result of specific sample treatment or of closer scrutiny.

Single crystal X-ray diffraction studies are badly needed in order to reach a satisfactory understanding of the molecular organization(s) of *FnHm* diblocks and *FnHmFn* triblocks in their condensed state and, hopefully, allow general rules with reliable predictive value to be drawn.

Table 6. Comparison of C–C and C–F Bond Length in $\text{CF}_n\text{H}_{3-n}-\text{CF}_m\text{H}_{3-m}$ (A–B) Molecules (in Å, with Estimated Standard Deviations in Parentheses) (From Ref 152)

	B = CF_3	B = CHF_2	B = CH_2F	B = CH_3
C–C Bond Length in A–B				
A = CF_3	1.545(2)	1.517(10)	1.501(4)	1.494(3)
A = CHF_2		1.518(5)	1.500(5)	1.498(4)
A = CH_2F			1.502(3)	1.502(7)
A = CH_3				1.532(1)
C–F Bond Length in A Group				
A = CF_3	1.326(1)	1.335(5)	1.334(2)	1.340(2)
A = CHF_2	1.335(5)	1.350(2)	1.353(4)	1.364(2)
A = CH_2F	1.389(6)	1.387(8)	1.384(1)	1.397(5)

6. The Gaseous and Liquid States

Little is published about the gaseous and liquid states of F_nH_m diblocks, whether pure or in mixtures with other compounds. The surface crystallization phenomenon observed on neat liquid diblocks has captured more attention.

6.1. Diblock Gases and Liquids

Gas-phase electron diffraction studies of the primary, two-carbon diblock CF_3-CH_3 and of some related hydrofluorocarbons (e.g., 1,1,1,2-tetrafluoroethane CF_3-CFH_2 , etc.) have provided precious data on the effect of progressive fluorination on C–C, C–F, and C–H bond lengths in such A–B molecules (Table 6).^{152,279} The data clearly established that the C–F bond length diminishes as the number of fluorine atoms on the carbon involved increases. They also indicated that there is a slight, but detectable, increase in C–F bond length in group A as the number of fluorine atoms in group B diminishes; thus, the C–F bond is the longest in CF_3-CH_3 . The data further indicated that A–B molecules in which A equals B have longer C–C bonds and that there is a decrease in C–C bond length as the difference (or dissymmetry) in the numbers of F atoms in groups A and B increases; thus, the shortest C–C bond in the series is found in CF_3-CH_3 .

Vapor–liquid equilibrium data for mixtures of $F4H2$ with octane and of $(\text{CF}_3)_2\text{CFOCH}_3$ with heptane have been determined at 101.3 kPa as part of a study on new, chlorine-free cleaning solvents.²⁸⁰

A combined experimental and simulation study of the thermodynamic properties of diblocks $F6H6$ and $F6H8$ in their liquid state focused more particularly on density and molecular volume.²⁸¹ The density of these diblocks, measured as a function of temperature and pressure, was higher than that of an equimolar mixture of F -hexane and hexane. The results were interpreted using a molecularly based equation of state. The F_nH_m diblocks were modeled using parameters developed earlier for the parent FC s and HC s, complemented by parameters related to the intra- and intermolecular interactions between the two types of chains. The densities predicted for different temperatures and pressures were in good agreement with the experimental data.

The equilibrium structure and thermodynamics of the free liquid surface of the pure symmetrical diblocks $F5H5$ and $F10H10$ have been investigated using molecular dynamics simulation (MD) and compared to those of the FC and HC of the same length.¹⁵³ The model failed, however, to take into account the dipole moment associated with the CF_2-CH_2 junction. The density of the diblock melt (1.37, exp: 1.35 at 27 °C) was calculated to be closer to that of the FC melt (1.61, exp: 1.58 at 127 °C) than to that of the HC

melt (0.63, exp: 0.64 at 127 °C). In contradiction with this result, the authors stated, however, that the molar volume of the diblock was larger than the average of the molar volumes of the FC and HC of the same length. Segregation of the F -blocks to the free surface was predicted, as well as their orientation perpendicular to the surface, in line with the weaker FC/FC interactions, as compared to HC/HC interactions, and larger F -chain volume and rigidity. Due to the connection of the F -blocks to H -chains, the density profiles of the F - and H -blocks were predicted to oscillate, inducing HC -rich regions and nonmonotonic decay from the liquid phase to the gas phase. The surface tension of the diblock melt was predicted to be less than those of the melts of the FC and HC of the same length. However, the calculations failed to predict a difference between the surface tensions of the FC and HC . More recent atomistic molecular dynamic simulations provided good agreement with experimental liquid density and surface tension data for $F4H12$, $F5H5$, $F8H8$, $F12H4$, and $F12H12$.²⁸² They confirmed preferential segregation of F -chains at the interface with preferential orientation normal to the interface, resulting in surface tensions close to those of FC s.

The process of aggregation of $F10H10$ into clusters of up to 128 molecules has been investigated using MD calculations and compared to those of $\text{C}_{10}\text{F}_{22}$, $\text{C}_{10}\text{H}_{22}$, $\text{C}_{20}\text{F}_{42}$, and $\text{C}_{20}\text{H}_{42}$.²³⁰ For the FC clusters, the marked stiffness of the F -chain resulted in domains with layer-like structures of extended F -chains and a certain long-range order. For the HC clusters, conformational flexibility resulted in disordered folded chains with *gauche*-like arrangements. For the diblock, formation of organized layer-like structures by the F -moieties was impeded by the covalently bound H -moieties. The formation of microphase domains of F -chains within the $F10H10$ cluster was suggested.

Torsion potential energy profiles and force field parameters, useful for MD simulation studies of diblocks, have been developed for the description of the torsion of bonds near the F - and H -block junction.²²⁰ Using these tools, molecular dynamics simulations for liquid $F8H2$ yielded density values and O_2 and CO_2 solubilities.

6.2. Surface Crystallization of Liquid Diblocks

Surface crystallization (or surface freezing) consists of the formation of an ordered, crystalline mono- or bilayer at the surface of the less ordered bulk liquid a few degrees above the freezing temperature of the bulk liquid.¹⁷ This designation is usually reserved to single component systems, while formation of ordered adsorbed films at the surface of a solution (binary and multicomponent systems) is referred to as Gibbs film formation, which will be discussed in section 8.1. The surface crystallization phenomenon is much less frequently encountered than the opposite situation, surface melting (where the surface is less ordered than the bulk and melts first upon heating), and is, as yet, restricted to chain molecules.

The melted $F12Hm$ diblocks ($m = 8, 14, \text{ and } 19$) have been examined a few degrees above their freezing points using X-ray reflectivity, grazing incidence X-ray diffraction, and surface tension measurements.¹⁶ Two types of surface crystallization behaviors were observed, depending on m . For $m = 8$ and 14, a fully crystalline layer was found to form and melt abruptly at the free surface of the melt (reversible first-order transition). The surface tension versus temperature curve changed slope abruptly. The crystalline surface layer

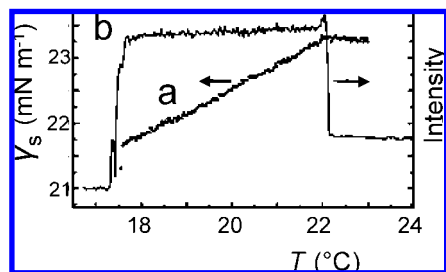


Figure 6.1. (a) Temperature dependence of the surface tension, γ_s , and (b) X-ray reflected intensities (arbitrary units) at a fixed surface-normal momentum transfer ($q_z = 0.23 \text{ \AA}^{-1}$) for *F8H8*. Note the sharp breaks observed at the formation of the surface-frozen monolayer at $\sim 22 \text{ }^\circ\text{C}$ and at bulk freezing at $\sim 17.5 \text{ }^\circ\text{C}$, and the exceptionally large temperature domain of existence of the frozen monolayer. From ref 283 with permission.

was a single-molecule thick, with surface-normal aligned, hexagonally packed molecules with, possibly, some staggering. The data were consistent with a monolayer comprising two slabs of distinct densities. The higher density upper slab was consistent with ordered *F*-blocks pointing toward the vapor phase, while the less dense lower slab grouped the disordered *H*-blocks that extended more loosely into the bulk liquid. A high (over $\sim 1000 \text{ \AA}$) coherence length was determined for the in-plane order. However, a bilayer model with 20–30% coverage in the lower layer was also consistent with the experimental data.

A fundamentally different behavior was found for *F12H19*. In this case, surface tension versus temperature showed considerable hysteresis. Melting involved a second-order-like continuous transition. The surface freezing layer had only short-range in-plane order, and its structure varied with temperature. Rather than crystalline, this layer was considered as a smectic-like single layer of a thermotropic liquid crystal. The possibility of a “dome”-covered surface was evoked to account for the relatively low density of the upper slab. A parallel may perhaps be drawn with the formation of surface micelles discussed in section 8.3.

The exceptionally broad temperature range of existence of the surface-frozen monolayers found for some diblocks ($4.5\text{--}5.5 \text{ }^\circ\text{C}$) allowed investigation of the structure and thermal expansion of the surface-frozen crystal using X-ray reflectivity and surface tension measurements.²⁸³ While the structural properties, and in particular the thermal expansion of the surface-frozen film, were expected to be essentially dominated by the thicker and more rigid *F*-block, investigation of *F8H8*, *F10H8*, and *F10H6* showed an unexpected, strong dependence of the structure on *H*-block length and *n/m* ratio. Figure 6.1 shows the temperature dependence of surface tension, γ_s , and X-ray reflectivity data for *F8H8*. The formation of the surface-frozen layer upon cooling at $22 \text{ }^\circ\text{C}$ is indicated by a sharp (first-order transition) change in slope of γ_s . Bulk freezing was accompanied by a sharp drop of γ_s at $17 \text{ }^\circ\text{C}$. The X-ray reflectivity data established that the *FnHm* molecules were totally stretched and normal to the surface. The *H*-blocks appeared to be organized on and by the 2D lattice formed by the *F*-blocks. The linear expansion coefficients for the three diblocks investigated were close to those of surface-frozen monolayers of alkanes and much higher than that reported for the bulk thermal expansion of PTFE. An increase in *F*-block length (from *F8H8* to *F10H8*) reduced molecular separation but retained the same expansion coefficient. Surprisingly, an increase in *H*-block length (from *F10H6* to *F10H8*) not only decreased intermolecular separa-

tion but also increased the expansion coefficient. This “softer” crystallinity may reflect lesser dominance of the *F/F* versus *H/H* interactions. The molecular area in the surface frozen monolayer was found to be sensitive to the *H*-block. It increased from 26.6 \AA^2 for *F10H8* to 27.9 \AA^2 for *F10H6* at $55 \text{ }^\circ\text{C}$, demonstrating that the *H*-blocks also influenced the 2D lattice, even though the *F*-blocks dominated the structure. It was also noticed that the measured nearest-neighbor distance was somewhat smaller ($\sim 5.5 \text{ \AA}$) than that typically observed for the 2D packing of *F*-blocks in Langmuir monolayers ($\sim 5.8 \text{ \AA}$). The molecular area decreased with increasing *F*-block length (from *F8H8* to *F10H8*) in the surface-frozen monolayers, while the opposite trend had been noted in Langmuir monolayers (from *F8H16* to *F12H16*), possibly indicating some fundamental differences in molecular conformation and intermolecular interactions between surface-frozen and Langmuir monolayers.²⁸³

7. Diblock Aggregation in Solutions—Micelles and Fibrous Gels

As for conventional surfactants, the amphiphilic character of *FnHm* diblocks leads to aggregation when the concentration in a solution, including in *FCs* and *HCs*, exceeds a certain critical value (section 7.1). Gel formation has been observed upon cooling diblock solutions above the solubility limit (section 7.2).

7.1. Aggregation (Micelle Formation) in Solution

The amphiphilic character of *FnHm* diblocks can manifest itself in a solvent that preferentially dissolves either *HCs* or *FCs*, leading to aggregation when the critical micelle concentration (CMC) is exceeded. Some authors prefer to use a critical aggregation concentration (CAC) at the Krafft temperature to describe the phenomenon, on the basis that the aggregates could be different from the micelles formed by conventional surfactants.³⁹ In the resulting micelles (or aggregates), one block forms a central core that is surrounded by a corona (or shell) made up from the block most compatible with the solvent. Micelles of *FnHm* diblocks with an *H*-chain corona are thus expected to form in *HCs* and micelles with an *F*-chain corona in *FCs*. However, the tendency for *FnHm* diblocks to aggregate in *FC* or *HC* solvents is weak, evidence for micelle formation is sparse, and the aggregation numbers are much lower than those for conventional surfactants in water. The physical characteristics of diblock solutions generally vary slowly with concentration, in contrast with the brusque changes usually seen for classical surfactants at their CMC. Like for classical surfactant micelles, aggregates of *FnHm* diblocks in solution are dynamic systems in which there is a rapid exchange of molecules with the surrounding medium. Contrary to aqueous systems, where the hydrophobic interactions are of entropic nature, it has been assumed that the association of diblocks in nonaqueous systems is solely due to enthalpic effects.²⁵⁵ Consequently, raising the temperature results in the dissociation of the aggregates.

7.1.1. In Fluorocarbons

Clear evidence for micelle formation in the *F8H12/F*-tributylamine system has been obtained by fluorescence probe solubilization and static light scattering experiments.⁵⁴ A sharp break in the fluorescence intensity versus *F8H12*

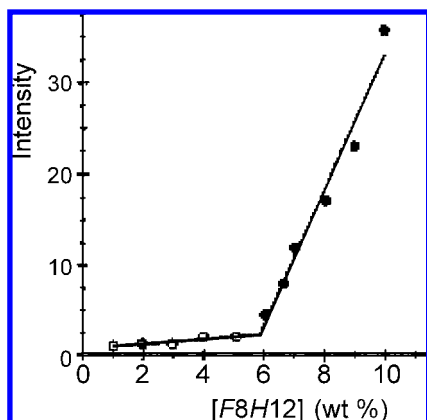


Figure 7.1. Fluorescence intensity (arbitrary units) of a steroidal fluorescence probe versus concentration of *F8H12* in *F*-tributylamine. Excitation was at 475 nm, and emission intensity was monitored at 510 nm. From ref 54 with permission.

concentration plot marked the CMC (5.8 wt %; ~ 24 °C) (Figure 7.1). In these micelles, the *H*-blocks formed an *HC* core, while the *F*-blocks, located at the micelle's periphery, faced the *FC* solvent molecules. The concentration range over which the micellar system was stable was rather narrow (about twice the CMC), and rough estimations indicated that the aggregation number prior to phase separation was quite small (~ 4 – 6). Micelle formation, with aggregation numbers of about 4–6, was also reported for *F8H16* in *F*-octane at 40 °C with a CMC around 4.5 wt %. On the other hand, no aggregation was detected for *F8H12* in *F*-hexane at concentrations up to 10 wt %, reflecting lesser "antipathy" between diblock and solvent.

The behavior of *F8H16* and *F12H16* in *F*-octane and isooctane has been investigated using viscosity and dynamic light scattering and small-angle neutron scattering techniques.⁷⁸ *F8H16*, when mixed with *F*-octane (up to 12 wt %), produced fairly monodisperse, nearly spherical aggregates with an *F*-corona. The reported aggregation number was quite high: about 95 diblock molecules at concentrations above the CMC of 4–5 wt %. This number was questioned on the basis of vapor pressure osmometry measurements that indicated much lower aggregation numbers, in the 2–10 range,³⁹ comparable to those reported earlier.⁵⁴ Substantial penetration of the solvent into the outer *F*-corona and even into the *HC* core of the micelles was observed.⁷⁸ SANS measurements indicated a micelle core radius of ~ 13 Å. The liquid–gel phase transition diagrams established for *F8H16* and *F12H16* in *F*-octane and isooctane reflected strong interactions between the outer corona and the solvent.

Significant deviations from ideal solute behavior were reported for *F8H16* and *F10H16* in *F*-heptane, *F*-octane, *F*-nonane, and *F*-decalin.³⁹ A definite breaking point in the solubility versus temperature curves corresponded to a critical aggregation concentration (Figure 7.2). The trends in CAC for *F_nH_m* diblocks (in the 0.05–0.14 molar fraction range) basically reflected the antipathy between diblock and solvent. For example, vapor pressure osmometry determined more pronounced aggregation for *F10H16* as compared to *F10H10* in *F*-nonane, reflecting the greater demixing tendency of the *H16* block with *C₉F₂₀*. The average, concentration-dependent aggregation numbers, measured above the Krafft point, were low, generally in the 2–10 range. Light scattering experiments also estimated low aggregation numbers for *F8H16* in *C₉F₂₀* (10 ± 8) and *F10H16* in *C₉F₂₀* (56 ± 4). Aggregation occurred progressively with increasing diblock

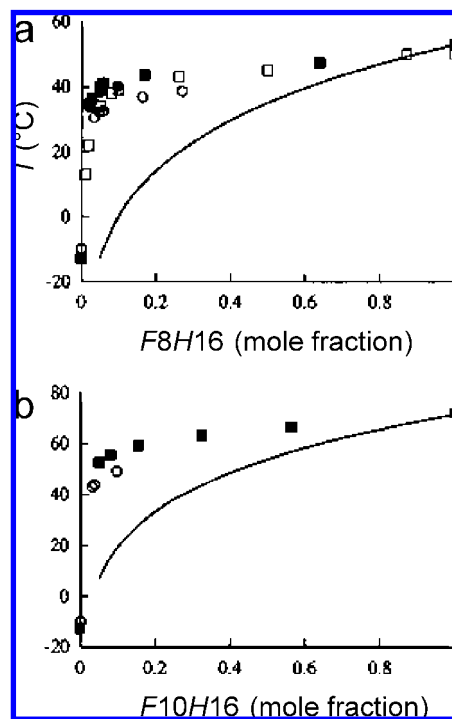


Figure 7.2. Temperature variation of the solubility of (a) *F8H16* and (b) *F10H16* in various *FC* solvents (■, *F*-nonane; □, *F*-octane; ●, *F*-heptane; ○, *F*-decalin; the solid lines represent ideal behavior). The extent of the deviation from ideality reflects the amphiphilic strength of the solute. From ref 39 with permission.

concentration rather than at a sharply defined concentration as for classical surfactants.

For *F10H_m* in *C₉F₂₀*, the CAC values estimated from solubility data and expressed as diblock molar fractions fell from 0.14 to 0.08 as *m* increased from 10 to 16.³⁹ The incremental molar free energy associated with aggregation in *H*-core aggregates (~ 0.3 kJ per CH_2 at 25 °C) was significantly less than that associated with the solubility of $\text{C}_m\text{H}_{2m+2}$ in *C₉F₂₀*, suggesting incomplete separation of the *H_m* chains from the *FC* solvent. The CAC for *F_nH16* in *C₉F₂₀* was not expected to vary with *n*, as confirmed experimentally for *n* = 8 and 10, since aggregate formation should be driven by the antipathy of the *H16* chain for the *FC*, which remained constant. The virtual independence of the CAC values of *F8H16* from the chain length of the *FC* solvent reflects the independence from *n* of the free energy of transfer of *H10* into $\text{C}_n\text{F}_{2n+2}$.

7.1.2. In Hydrocarbons

A light scattering study of *F12H10* in octane gave preliminary evidence for the presence of aggregates with aggregation numbers of about 130 at 35 °C.²⁵⁵ This observation has subsequently been questioned, since no micelle formation was seen in short alkanes.¹⁸⁵ Indeed, surface tension and vapor pressure osmometry measurements on various diblocks (in particular *F12H14*) in *H_C*s (octane, dodecane, pentadecane, toluene) showed no evidence for micelles in the *H_C*, meaning either that they do not form or that the concentration range in which they occur, preceding the solubility limit, is very narrow.¹⁸⁵ No aggregation was seen for *F12H14* in octane, toluene, or dodecane below the Krafft point (an aggregation number around 2 was estimated above that point in dodecane) or for *F6CH=CHH10* in octane.

Other preliminary evidence indicated micelle formation in toluene for *F8H16* and *F10H16*,⁵⁴ and *F12H10* with a large aggregation number of around 130 at 35 °C.²⁵⁵ A rather high aggregation number of 250 ± 200 has been determined (with, however, a large experimental error) for *F8H16* in $C_{16}H_{34}$.³⁹ The fact that, against expectations, the CAC of *F10Hm* in $C_{16}H_{34}$ decreased (from molar fractions 0.10 to 0.05) as *m* increased from 10 to 16 was speculated to arise from more favorable aggregate packing.

The behavior of *F8H16* solutions in isooctane at 40 °C was nearly ideal, as in the absence of micelles, reflecting the poor tendency for demixing of the *F8* block in the short alkane.^{39,189} Some evidence for aggregation was found for this diblock in $C_{10}H_{22}$ and $C_{16}H_{34}$. Deviation from ideality was, as expected, more pronounced for *F10H16* than for *F8H16* and was more pronounced in longer *HC* solvents (e.g., $C_{16}H_{34}$, $C_{20}H_{42}$), but the aggregation numbers remained low (~ 3 – 4).

Micelle formation was also observed in dodecane for star-shaped triblocks having two *F8* chains and one *H16* chain connected through ether bonds.¹¹⁶ The CMC values were relatively low and the micelle radii were between 1.8 and 3 nm, corresponding to low aggregation numbers. No micelles were seen in the solutions of analogous ethers with only one *F8* chain and one *H16* chain.

Altogether, the aggregation behavior of diblocks in *HCs* was consistent with *FC* in *HC* solubility data. In short, the data indicated that micelle formation from *F_nH_m* diblocks in *HCs* is either absent or occurs only over a narrow concentration range, and then with small aggregation numbers. Formation of micelles in *HCs* requires aggregation of a core of *F*-chains, which may be hindered by the rigidity and large cross section of the *F*-chains. Hindering or suppression of micelle formation is also consistent with a lack of repulsion between the lipophilic *H*-block corona and the solvent. *F_nH_m* diblocks aggregate in either *HC* or *FC* solvents only when the antipathy between diblock and solvent is sufficiently strong. The aggregation numbers were very low, in the 2–10 range, and aggregation occurred progressively as diblock concentration increased, rather than suddenly, as usually seen for conventional surfactants in water. The variation of CAC values with chain length of *F_nH_m* and solvents broadly follows the trends expected on the basis of antipathy between diblock and solvent.³⁹

7.1.3. In Mixed Solvents

Small amounts of *F8H16* added to an *F*-octane/isooctane mixture lowered the upper critical solution temperature of the solvent mixture significantly and caused a broadening of the coexistence curve but did not prevent eventual demixing of the two solvents upon cooling.¹⁷⁷ Addition of larger amounts of the diblock to the *FC/HC* mixture produced a solid gel when cooled below a certain liquid–gel phase transition temperature, and in this case, no solvent demixing was observed upon cooling. Above the transition temperature, dynamic light scattering and SAXS measurements showed the presence of small aggregates (micelles) in the liquid, with an average hydrodynamic diameter of about 30 Å.

The aggregation behavior of an *F_nH_m* diblock in mixtures of equal amounts of an *FC* and an *HC* (*F8H16* with C_9F_{20} and $C_{16}H_{34}$ at 45 °C, *F10H16* with C_9F_{20} and $C_{16}H_{34}$ at 64 °C, and *F10H16* with C_9F_{20} and $C_{20}H_{42}$ at 64 °C) has been investigated above the Krafft point using density and refractive index measurements.³⁹ The *F_nH_m* distributions in

two-phase *FC* and *HC* solvent mixtures suggested weak diblock aggregation occurring predominantly, but not exclusively, in the *HC*-rich phase. It is noteworthy that conventional surfactant aggregates tend to partition exclusively in one or the other phase, the aqueous or the oily phase. No “third phase” bicontinuous microemulsion formation was observed.

7.1.4. In Supercritical Carbon Dioxide

Small aggregation numbers of at most four molecules have been determined by SAXS measurements for *F10H10* in supercritical CO_2 at 65 °C.²⁸⁴ The relatively high temperature at which the experiment was run may be responsible for the observed limited aggregation behavior.

7.1.5. Inclusion in β -Cyclodextrin

Solubility of diblocks inside the hydrophobic cavity of a cyclodextrin ring molecule has been demonstrated.²⁸⁵ A crystalline inclusion compound of *F8H16* and β -cyclodextrin has been precipitated in water. Inclusion only occurred above the melting point of the diblock, which likely facilitates threading of the fluid molecule into the cyclodextrin's cavity. The cross sections of the *F*-chain of the diblock guest molecule and of the host's cavity are $\sim 28 \text{ \AA}^2$ and 30.2 \AA^2 , respectively. It was expected that four cyclodextrins (cavity length $\sim 8 \text{ \AA}$) could be threaded by one *F8H16* molecule (fully extended length $\sim 33 \text{ \AA}$) in order to cover it entirely. Both nanoaggregates and larger tubular structures were seen by AFM. The latter structures were several hundred nanometers in length and appeared to result from aggregation of several inclusion adducts.

7.2. Gels

Highly viscous opaque gels have been obtained upon cooling of homogeneous fluid phases (solutions or micellar solutions) obtained by heating mixtures of *F12Hm* ($8 \leq m \leq 20$) with decane, or of *F10H12* with a number of hydrocarbons (e.g., octane, decane, hexadecane, 2-methylnonadecane, cyclodecane, and decalin).^{286,287} The transition between gel and isotropic liquid was reversible. A broad but well characterized endotherm was found by DSC at the transition temperature. When observed microscopically, the gels exhibited birefringence and microfibrillar morphology. Phase diagrams indicated intermolecular interactions between *F10H12* and the *HC* solvent that depended on the shape of the *HC* (linear vs cyclic).

Gel formation was observed for *F12H10* in octane, in dodecane, as well as in *F*-decalin (Figure 7.3a).²⁵⁵ The three diblock/solvent phase diagrams were very similar and indicated that the solvent acted simply to depress the melting point of the diblock. No discontinuity was seen at the minimum concentrations at which gel formation was observed. Upon cooling from above the melting point, pure *F12H10* solidified in the solvent in the form of very long needles, a few micrometers in diameter, which became interlocked in disarray (Figure 7.3b). This network of interdigitated crystallites enclosed large amounts of solvent. Gel formation depended on cooling rate. Fast cooling favored networks with smaller mesh size. As the gels were formed both in *HCs* and in *FCs*, it appears that the nucleation process always started with the aggregation of the *F*-chains, which tend to pack first and most regularly.

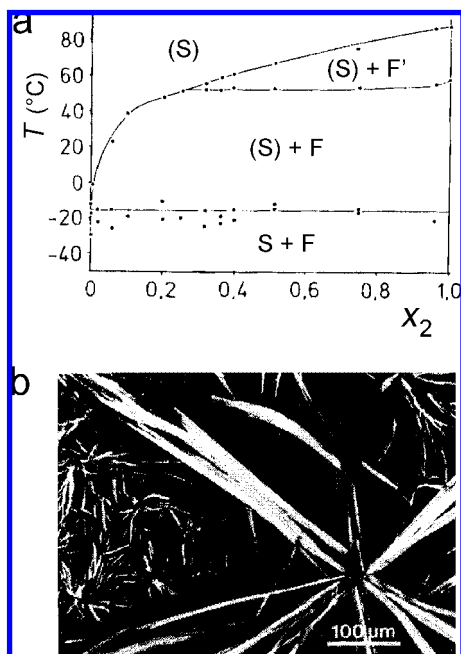


Figure 7.3. (a) Phase diagram for *F*-decalin/*F12H10* mixtures. (S) represents the solute; F and F' the crystalline solution before and after undergoing the high temperature solid–solid phase transition; S represents the crystallized solvent. (b) Birefringence micrographs showing the crystals of *F12H10* growing in a 12 wt % *F*-decalin solution. From ref 255 with permission.

Gel formation has also been observed for *F8H18* in methanol and ethanol¹⁸⁵ and for *F8H8* in methanol, ethanol, and propanol.⁹⁴ Reversible gel formation in these solvents was used as a purification method for the diblocks.

Cooling a sample of *F8H16* in an *F*-octane/isooctane mixture also resulted in formation of a white gel.¹⁷⁷ A model was proposed in which micelles, initially formed in the liquid phase, would grow, upon cooling below the liquid–gel phase transition, into an extended, ribbon-like structure, in which the diblock molecules would adopt a lamellar arrangement with closely packed *F*-blocks and interdigitated *H*-blocks. Further cooling would cause formation of lamellar layers and birefringent structures that could be seen with a polarizing microscope. SAXS experiments performed on the gel for different diblock concentrations and temperatures confirmed a ribbon structure as the most plausible model for the network of *F8H16* fibers that constitutes the solid part of the gel (Figure 7.4).²⁶⁴ Quantitative analysis of the SAXS intensities provided the following structural parameters for the ribbons: 300–350 Å wide, 13–121 Å thick, and 440–3150 Å in persistence length, depending on *F*-octane/isooctane volume ratio. Both the scattering of the crystalline *F_nH_m* fibers (with lamellar layers) and of the *F_nH_m* micelles (cylindrical, with ~20 monomers) formed in the entrapped multicomponent (but single-phase) liquid were taken into account. A mechanism for the progressive growing of cylindrical micelles into strips, followed by the aggregation and branching of these strips into curly ribbons, was proposed.

Gel formation in dense CO₂ has been observed to occur when solutions of diblocks *F10H10*, *F12H8*, *F12H12*, and *F12H16* in CO₂, obtained at room temperature at the three-phase (solid–liquid–vapor) equilibrium pressure, were expanded, causing the liquid CO₂ to evaporate and, hence, the diblock to come out of the solution.^{205,206} A network of interlocking crystalline microfibrils began to grow at the

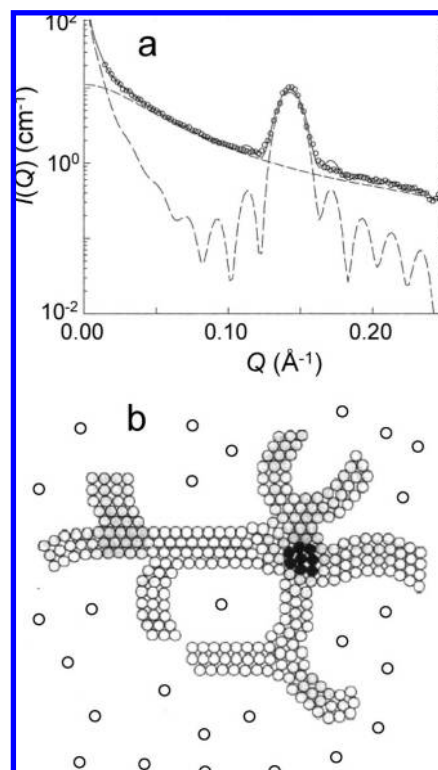


Figure 7.4. (a) SAXS data for *F8H16* in an *F*-octane/isooctane mixture. Good agreement of the experimental data (open circles) with calculations (solid line) was obtained by combining a ribbon model for the crystal (long dashed line) and a micellar model for the liquid (short dashed line). (b) Schematic ribbon-like structure (top view) for the aggregation of the diblock in the gel. The circles represent the cross sections of the *F*-chains. The structure originates from a seed (dark circles) and expands randomly, entrapping the mixed solvent between the entangled ribbons. From ref 264 with permission.

liquid–vapor interface and expanded. The opaque rigid dispersion of fibrous crystals, in whose cavities liquid CO₂ resided, had the appearance of a gel. Further expansion led to complete loss of the liquid phase while the solid microfibril network of diblock molecules subsisted. No gel was obtained from *F12H20*, likely because of too low solubility in CO₂.

Very stable gels with a continuous *FC* phase have been prepared, in which *F_nH_m* diblocks were associated with phospholipids and water as the gelifying agent.²⁸⁸ For example, a fluid opalescent dispersion was prepared by slow addition of C₈F₁₇Br to a dispersion of egg yolk phospholipids in *F6H10*. Dropwise addition of minute amounts of water resulted in immediate formation of transparent, stable, heat-sterilizable gels. A likely, but unconfirmed mechanism for their formation consists in the generation of long, wormlike entangled micelles of hydrated surfactant within the *FC*.

8. Diblocks at Interfaces—Adsorbed Films and Surface Self-Assemblies

As an effect of their amphiphilic character, *F_nH_m* diblocks in solution tend to spontaneously collect at interfaces, forming self-adsorbed Gibbs films (section 8.1). Diblocks can also be spread on the surface of water for investigation in a Langmuir trough, where they can be submitted to lateral compression (section 8.2). Deposition of a thin film of diblocks onto a solid substrate can be achieved using Langmuir–Blodgett or spin-coating techniques. Within the two-dimensional space in which they are confined, the *F_nH_m*

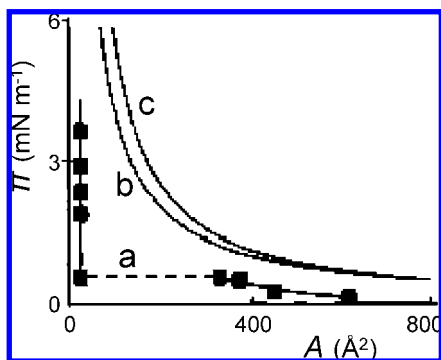


Figure 8.1. (a) Surface pressure/molecular area π/A isotherm for the strongly adsorbing *F12H14*-in-*n*-pentadecane system at 20 °C (surface pressure π is related to surface tension γ_s by $\pi = \gamma_s - \gamma_0$, with γ_0 being the surface tension of pure water). Curves b and c represent calculated ideal 2D gas surface equations of state. Curve c includes a correction for a “hard disk” excluded area. The apparent first-order phase transition between liquid expanded and liquid condensed phases is shown as the horizontal dashed line. From ref 185 with permission.

molecules can form isotropic films or can self-assemble into variously shaped discrete surface constructs (section 8.3). Dynamic film behavior is illustrated by a pressure-driven reversible vertical segregation phenomenon (section 8.4). Although Gibbs and Langmuir films can be semicrystalline in the liquid-condensed phase or crystalline in the solid phase, the notion of surface crystallization is usually reserved to single-component systems (section 6.2).

8.1. Gibbs Films or Self-Adsorbed Surface Films

Gibbs films consist of ordered monolayers of an amphiphile spontaneously adsorbed at the surface of a less ordered solution. Gibbs films can display phase transitions between gaslike, liquid expanded, liquid condensed, and solid states. *FnHm* diblocks readily adsorb at *HC*/air and *HC*/*FC* interfaces. For a diblock, driving forces for Gibbs film formation on an alkane include antipathy of *F*-chains versus *H*-chains; greater affinity of *F*-chains for air rather than for alkanes; lateral interaction among *F*-chains; and attraction between *H*-chains and the alkane solvent molecules, which, if long enough, can solvate the *H*-chain of the diblock. Gibbs films of *FnHm* diblocks are not expected to form at the surface of their solutions in a *FC*, since the surface tensions of *FC*s are lower than those of *HC*s. Adsorption of a diblock at a *FC*/air interface would indeed increase—rather than decrease—surface tension and surface energy.

Adsorption of a range of *FnHm* diblocks (*F8H16*, *iso-F9H10*, *F10H10*, *F10H16*, *F12H14*) at the surface of various *HC*s (toluene, *n*-octane, *n*-dodecane, *n*-pentadecane) has been thoroughly investigated using surface tensiometry.¹⁸⁵ Adsorption depended, as expected, on mutual phobicity between diblock and solvent and, hence, was favored by high *n* values, long chain *HC* solvents, and low temperatures. Weakly adsorbing systems (e.g., *F12H14* in octane) formed expanded, “gaslike” monolayers at 20 °C (with a minimum area per diblock of about 300 Å²), while strongly adsorbing systems (e.g., *F12H14* in dodecane, pentadecane, or toluene) formed highly condensed monolayers (with a minimum cross-sectional area that could be as low as 26 Å²), in which the *F*-chain density was similar to that found in condensed phases of *all-trans n-F*-alkanes. The surface pressure/area isotherm for *F12H14* in pentadecane (Figure 8.1) shows an abrupt change in slope at 0.6 mN m⁻¹, suggesting a first-

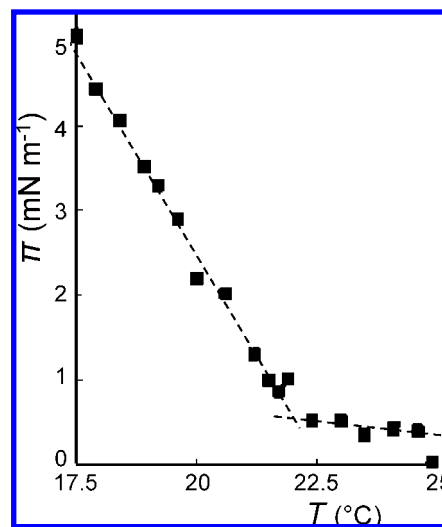


Figure 8.2. Variation of the surface pressure of *F12H14* (0.137 mol %) in *n*-dodecane with temperature; the dashed lines have been added. The sharp break indicates that formation of the liquid condensed monolayer is highly cooperative. From ref 185 with permission.

order phase transition at which liquid condensed and liquid expanded surface phases would coexist. The transition from weak to strong adsorption behavior with decreasing temperature occurred abruptly, suggesting that formation of the condensed surface monolayer happened in a highly concerted manner. Thus, Figure 8.2 shows for *F12H14* in dodecane a marked transition of surface pressure at ~22 °C upon cooling. Dependence on temperature was considerable, with lower temperatures strongly favoring the formation of a condensed surface monolayer, implying that adsorption of the diblocks at the *HC* surface was an exothermic process. At higher temperatures (but still below the Krafft point), adsorption decreased strongly and a much more dilute film was formed.

Gibbs film formation at the free surface of solutions of *F12Hm* (*m* = 12, 14, 16, and 18) in *n*-dodecane, bicyclohexyl, and *n*-hexadecane has been investigated below the Krafft temperature, using surface tension measurements¹⁹⁰ complemented by surface-sensitive X-ray techniques (X-ray reflectometry and grazing incidence X-ray diffraction).^{186,187} The surface tension $\gamma_s(T)$ curves for *F12H18* solutions in *n*-dodecane consisted of two distinct, almost linear sections with opposite signs of the slope, forming a sharp angle at a temperature T_f (Figure 8.3). The entropy of adsorption also changed discontinuously at T_f , indicating a sharp, concentration-dependent, first-order transition from a dilute gaslike state at high temperatures to a condensed state at lower temperatures.

Specular X-ray reflectivity measurements at the solution/air interface for different *F12Hm* (*m* = 14, 16, and 18) diblocks confirmed the existence of a first-order surface phase transition at T_f . T_f increased with *m* and, hence, paralleled the dependence on *m* of the bulk melting temperature T_m of the pure diblocks.¹⁸⁶ The electron density profiles derived from the reflectivity curves (Figure 8.4a) indicated that the *F12Hm* molecules were oriented with the *F12* blocks pointing toward the vapor phase. Moreover, the electron density profiles indicated that the mass centers of the *F*-blocks were not aligned in a plane but vertically distributed over a 20–30 Å-wide region, like in a smectic C film (Figure 8.4b).

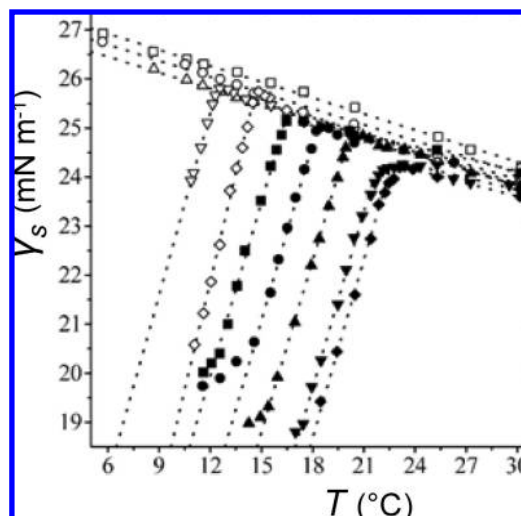


Figure 8.3. Surface tension γ_s as a function of temperature T for pure *n*-dodecane (○) and for solutions of *F12H18* in *n*-dodecane at concentrations of 0.30 (Δ), 0.60 (□), 0.90 (∇), 1.16 (◇), 1.43 (■), 1.77 (●), 2.19 (▲), 2.70 (▼), and 3.00 (◆) mmol kg⁻¹. The dotted lines are linear least-squares fits to the branches with negative or positive slopes of the respective data sets. From ref 187 with permission.

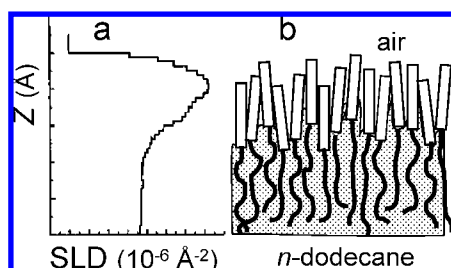


Figure 8.4. (a) Scattering length density (SLD) profile, derived from X-ray reflectivity experiments, for solutions of *F12Hm* diblocks in *n*-dodecane at a temperature below the phase transition temperature T_f ; and (b) schematic model of the condensed Gibbs layer of these diblocks at the surface of the solution. White boxes and black lines represent the *F*- and *H*-chains, respectively. From ref 186 with permission.

GIXD experiments showed markedly different patterns above and below the surface phase transition temperature (e.g., Figure 8.5). Above T_f , the scattered intensity integrated along the q_z direction essentially fell off in a monotonic way, while below T_f it showed a single pronounced diffraction peak. In the condensed films formed on *n*-dodecane or bicyclohexyl, the *F*-blocks of *F12Hm* ($m \geq 14$) were close-packed in a two-dimensional hexagonal array with a slight tilt angle.¹⁸⁷ The lattice spacing calculated from the position of the Bragg peak was $4.97 \pm 0.01 \text{ \AA}$, independently of the diblock's length. This value was comparable to the lattice spacing in PTFE (4.87 \AA) and to that found for the high-temperature 3D bulk phase of pure *F12Hm* with $m < 14$. The formation, below T_f , of a condensed monolayer of *FmHm* molecules perpendicular to the free surface of their solutions in the alkane was further evidenced by BAM experiments. The area per molecule (28.6 \AA^2) obtained from the GIXD data¹⁸⁷ was comparable to that observed for the surface-frozen layer of pure diblock ($\sim 27.6 \text{ \AA}^2$),¹⁶ but significantly lower than that derived from the surface tension isotherms of *F12H18* on dodecane ($34 \pm 2 \text{ \AA}^2$), which was attributed to the short-range nature of the positional order in the Gibbs monolayer. The in-plane positional correlation length was only on the order of 20 \AA ,¹⁸⁷ that is, smaller by several orders

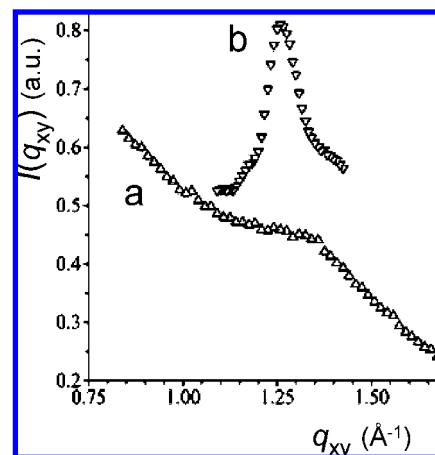


Figure 8.5. One dimensional GIXD patterns from the surface of *F12H16* in dodecane (a) at $25 \text{ }^\circ\text{C}$ (above the surface phase transition $T_1 \approx 18 \text{ }^\circ\text{C}$) and (b) at $15 \text{ }^\circ\text{C}$ (below T_1). The scattered intensities $I(q_{xy})$ were integrated along the q_z direction perpendicular to the surface and plotted against the scattering vector q_{xy} . From ref 187 with permission.

of magnitude than in the surface-frozen monolayers of long-chain *n*-alkanes.¹⁷ This rather short-range order within the films was again attributed to the packing frustration induced by the mismatch between *F*- and *H*-blocks.¹⁸⁶

The case of *F12H16* solutions in *n*-hexadecane is special because the latter solvent undergoes surface freezing upon cooling. The *F12H16*-in-*C16H34* system has been investigated in order to assess the effect of the correlation of molecular orientations that exist for *n*-alkanes, including *C16H34*, in the liquid state²⁸⁹ on the properties of the Gibbs film of the diblock. A first study, for *F12H16* molalities ranging from 0 to $4.96 \text{ mmol kg}^{-1}$, reported sharp breaks in the surface tension versus temperature and concentration plots.¹⁹⁰ Above the surface freezing temperature of *C16H34* (at $17.64 \text{ }^\circ\text{C}$; melting point $18.14 \text{ }^\circ\text{C}$), the gaseous, liquid expanded, and condensed monolayer phase behavior expected for adsorbed *F12H16* was reported as normal. When temperature was decreased, the evolution of the surface phases of *F12H16* (low *F12H16* molality, $< 1.3 \text{ mmol kg}^{-1}$) was cut off by the surface freezing of the *C16H34* subphase. *F12H16* appeared to be completely insoluble in the crystalline monolayer of *C16H34*, thus forming a crystalline monolayer on top of a surface-frozen monolayer of the alkane, with the *F12* blocks likely forming a close-packed film in the condensed state. For higher molalities ($> 1.3 \text{ mmol kg}^{-1}$), the conclusion was that the transition from the gaslike to the liquid condensed phase of the Gibbs film involved two distinct surface phase transitions, with a liquid expanded phase existing between a gaseous and a liquid condensed phase.

The conclusions of a subsequent study, using X-ray reflectivity, were at variance with the above report for the higher *F12H16* concentrations.¹⁸⁷ A concentrated (2.2 mmol kg^{-1}) solution of *F12H16* in *n*-hexadecane displayed indeed a more complex and anomalous Gibbs film behavior with, not a sharp, but a gradual, continuous transition from gaslike to condensed phase upon cooling. A surface concentration corresponding to a close-packed monolayer was not reached when freezing of the bulk sample occurred. The absence of phase transition for the Gibbs film of *F12H16* on *C16H34* indicated an interaction between diblock and solvent at such concentrations. This anomalous behavior was tentatively attributed to solvation of the *H*-blocks by hexadecane (note that the solvent length matches the *H*-block length), thus

hindering close-packing of the *F*-blocks. Partial alignment of the alkane chains of the *H*-16 block and 16-carbon-long solvent would be similar to the correlation of molecular orientations of long chain *n*-alkanes seen in their pure liquid state.²⁸⁹

When *F10H16* was present at an *F*-nonane/hexadecane interface, in a ternary system, the adsorbed film was rather expanded, with a large area per diblock molecule of $\sim 150 \text{ \AA}^2$. The data suggested that aggregation of the diblock occurred in the *H*-phase, at a critical concentration of $\sim 3 \text{ mol } \%$ with respect to the total system, once the interface was saturated with the diblock.³⁹ The partition of *F10H16* between the two solvents was preferentially in favor of the *H*-phase.

8.2. Langmuir Monolayers and Related Thin Films

Langmuir films consist of monolayers of essentially insoluble, most generally amphiphilic molecules spread on a liquid surface, ordinarily water, using a volatile solvent.^{290–296} It should be noted that the initial dogma that molecules needed to be amphiphilic in order to form stable Langmuir monolayers has been contradicted by the obtaining of stable monolayers from *F*-*n*-eicosane ($\text{C}_{20}\text{F}_{42}$)¹⁹ and even from sufficiently long linear alkanes ($n = 36$).²⁹⁷ The monolayer under investigation is confined at the air/water interface in a trough while controlled compression is exercised using one or two mobile barriers. Surface pressure (π)/area (*A*) isotherms are measured, allowing determination of monolayer characteristics and stability. Upon compression of conventional surfactants, gaseous (G), liquid expanded (LE), liquid condensed (LC), and solid (S) phases may appear as surface density increases, depending on the ordering capacity of the surfactant.^{290,292,293} Breaks or inflections in the π/A isotherms, also seen in the compression modulus C_s^{-1}/π plots, where $C_s^{-1} = -A(d\pi/dA)$, denote transitions between these phases. Coexistence domains, reflected by plateaus in the π/A isotherms, can also be observed. Monolayers can display more complicated polymorphism with, for example, several LC subphases involving different molecular orientations or unit cell sizes, and mesophases with long-range orientational order and only short-range translational order.^{298–300} Electrical properties of monolayers are determined by measuring their surface potential (ΔV), which can give access to the vertical component of the dipole moment (μ_{\perp}) of molecules within the layer. Progress in the understanding of the structure of Langmuir monolayers became decisive once surface diffraction methods using synchrotron radiation, such as grazing incidence X-ray diffraction, were applied.^{18,301–307} Langmuir monolayers can also be nanotextured, as when the constituent amphiphilic molecules organize into surface hemimicelles.^{306–310}

The capacity for *FnHm* diblocks to form Langmuir monolayers on water is well documented.^{110,157,183,304,307,309,311–317} The bulky and rigid *F*-chains of diblocks provide an element of order and tend to favor crystallinity.^{13,302} Close-packing of *F*-chains in monolayers on water is facilitated by extreme hydrophobicity, as well as by the rigidity and reduced number of kinks present in *F*-alkyl versus *H*-alkyl chains. The lattice energy of the hexagonal array of parallel *F*-chains is larger than that of the corresponding array of *H*-chains, with the difference in energy being $\sim 15 \text{ kcal per carbon atom}$.³¹⁸ *F*-chains tend to form hexagonal rather than rectangular phases, with the latter being favored for *H*-amphiphiles, due

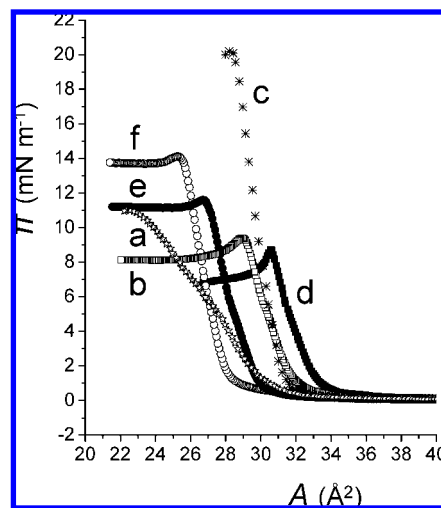


Figure 8.6. Typical examples of surface pressure π versus molecular area *A* compression isotherms for Langmuir monolayers at the air/water interface for the *FnH16* diblock series [*F6H16* (a), *F8H16* (b), and *F10H16* (c)] and for the *F8Hm* series [*F8H14* (d), *F8H16* (b), *F8H18* (e), and *F8H20* (f)] at 20 °C. Data from refs 304, 313, 315, and 468.

to stronger intermolecular interactions. The dominant mechanisms for *F*- and *H*-chain packing in monolayers thus appear to be different. Monolayers of *F*-surfactants with small polar heads (e.g., carboxylic acids) have generally less tilted molecules than monolayers of comparable *H*-surfactants.

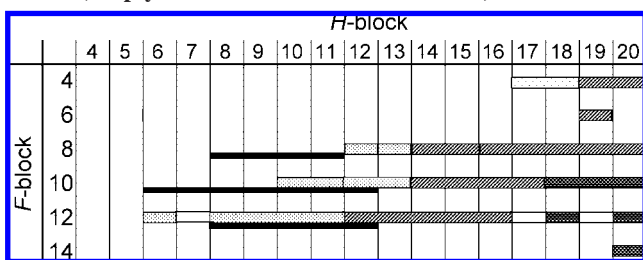
8.2.1. Diblocks at the Air/Water Interface—Langmuir Film Stability

Early exploratory work has indicated that, in spite of the absence of a hydrophilic headgroup, *FnHm* diblocks could form monolayers on the surface of water.¹⁸³ These monolayers were already fairly stable for *F12H8*, *F10H12*, and *F12H18*, with stability increasing with diblock length. A more detailed study of monolayers of *F8H12*, *F10H11*, and *F12H18* over a range of temperatures confirmed that monolayer stability increased with the length of the *F*-chain.³¹¹

Figure 8.6 represents an assortment of typical π/A isotherms measured for a series of diblocks spread as Langmuir monolayers on water at 20 °C.^{304,313,315,317} Each isotherm is primarily characterized by a collapse pressure π_c and a limiting molecular area (the area occupied by individual molecules) A_{∞} , which is obtained by extrapolation of the slope of the π/A curve. At collapse, the surface pressure of diblock monolayers remains quite constant over a large molecular area range, a situation that deserves further investigation. Hysteresis upon compression–expansion cycles can denote poor stability or slow kinetics.

The isotherms of pure *FnHm* diblocks shown in Figure 8.6 were smooth, with steep π/A variation, reflecting the rather low compressibility of the monolayer. The minimum isothermal compressibility coefficients varied only in a narrow range, from 3.2×10^{-3} to $5.2 \times 10^{-3} \text{ m mN}^{-1}$ ($\pm 1.4 \text{ m mN}^{-1}$).³¹⁰ These values suggested that the monolayers were, according to the standard classification,^{290,291} in the LC state. Highly compressible liquid expanded phases (LE), or solid phases (S) with low compressibility, have seldom been reported. The structure of the monolayers is a great deal more complex than that of the phases usually encountered with standard amphiphiles, especially in the region corresponding to large molecular areas preceding the onset of surface pressure^{169,317} (section 8.3). The usual C_s^{-1} -based

Scheme 8.1. Stability Grid for Langmuir Monolayers of F_nH_m Diblocks: Monolayer Stability Is Depicted by Increasingly Darkened Patterns, from Unstable to Highly Stable (Empty Boxes Denote Absence of Data)^a



^a Formation of a liquid crystalline mesophase in the bulk is indicated by the lower solid line. See text for references.

phase classification may therefore not apply to F_nH_m diblock monolayers, which may explain some discrepancies among the phase appellations reported in the literature.

The relative effects of the F - and H -chains on monolayer behavior are also illustrated in Figure 8.6 and summarized in Scheme 8.1. Comparison of the isotherms of $F6H16$, $F8H16$, and $F10H16$ showed a definite increase in collapse pressure and, hence, of stability, as F -chain length increased.^{310,317} While the $F6H16$ monolayer was hardly stable and progressively desorbed from the surface during compression, the cohesive energy within the monolayer increased with F -chain length (π_c was increased by ~ 5 mN m⁻¹ per CF₂), likely reflecting the lateral van der Waals interactions between rigid F -rods. The predominant effect of the F -block on stability is also illustrated by the much higher stability, for the same total number of carbons, of monolayers of $F8H14$, as compared to those of $F6H16$. Likewise, π_c for monolayers of $F10H16$ was significantly higher than for $F8H18$. Stability also increased, for a given n , with increasing m values, but to a lesser extent (by ~ 1 mN m⁻¹ per CH₂). In the $F8Hm$ series, for example, the collapse pressure increased regularly with increasing H -block length and could be fitted with a polynomial equation.³¹⁷ When comparing diblocks of the same total length, it was, not unexpectedly, the most hydrophobic compound, with the longest F -block, that gave the most stable monolayer. Interestingly, the limiting molecular area values A_∞ decreased regularly (33.2, 31.9, 29.8, and 28.0 (± 0.5) Å², for $F8H14$, $F8H16$, $F8H18$, and $F8H20$, respectively) as the length of the Hm block increased. The differences between A_∞ values, although small, were significant and indicated that the monolayers of diblocks with long Hm segments were more ordered than those with short ones. This was likely due to increased molecular freedom of the H -block, which allowed molecules to pack in a more compact way. The extrapolated area of $F10H16$ was very similar to that of $F8H16$, indicating that it was the length of the H -block that determined the area of the molecule by introducing more or less disorder in the packing.

The A_∞ values for the longer diblocks (e.g., $F8H20$, 28.0 ± 0.5 Å²) were close to those measured for common F -alkylated surfactants with small polar heads, such as C₁₀F₂₁CH₂COOH (~ 30 Å²),¹⁸ and very close to the value usually accepted for the cross section of hexagonally close-packed F -chains (28.3 Å²).^{19,305} This means that the long Hm blocks did not perturb the packing of the F -chains. Also noticeable is that these A_∞ values were significantly lower than those measured for semifluorinated carboxylic acids, C_{*n*}F_{2*n*+1}C_{*m*}H_{2*m*}COOH, which typically ranged from 33 to 40

Å²,^{162,308,319} indicating tighter film organization. The a priori surprising observation that simple F_nH_m diblocks are more condensed, less compressible, and better organized than carboxylic acids with similar hydrophobic chains likely indicates that the polar head is a factor of disorder. The minimum values of the isothermal compressibility coefficients $C_{s\min}$ ($(3.2\text{--}5.2) \times 10^{-3}$ m mN⁻¹) were also lower for F_nH_m diblocks than for partially fluorinated carboxylic acids having similar F - and H -segments.³¹⁰ $C_{s\min}$ did not vary significantly within the $F8Hm$ series, suggesting that compressibility was controlled by the F -block. The compressional moduli C_s^{-1} , which traditionally serve to characterize 2D phases,^{290,291} indicated that the monolayers of $F8Hm$ ($m = 14\text{--}20$) were all in the LC state.

It is noteworthy that the relatively short 20 to 24 carbon diblocks $F12H8$,¹⁸³ $F8H14$,³¹⁰ and $F4H20$ ³²⁰ already produced fairly stable Langmuir monolayers, while linear HCs formed stable monolayers only when the number of carbon atoms reached 36,²⁹⁷ while this number was 20 in the first published case for FCs.¹⁹ The case of $F4H20$ shows that a rather short F -block suffices to promote formation of a stable (π_c above 12 mN m⁻¹) and highly organized Langmuir monolayer. A kink at 10 °C in the C_s^{-1} plot for this diblock was assigned to a LC/S transition.

Further detailed π/A and $\Delta V/A$ isotherm studies have been published, along with Brewster angle microscopy data, for extended series of F_nH_m diblocks, under various experimental conditions.^{159,314,321} The Langmuir film formation and stability characteristics are collected in Scheme 8.1. In the $F8Hm$ diblocks series ($m = 8, 10, 12\text{--}20$, including uneven values), only $F8H8$ and $F8H10$ desorbed upon compression at 20 °C.³²¹ The films of $F8H12$ still had a low collapse pressure. Film stability increased with m , but not in a regular way. Most of the π/A isotherms exhibited a kink ($F8Hm$; $m = 13, 14, 15, 17$) or even a pseudoplateau ($m = 16$ and 18). This kink was more visible on the C_s^{-1}/π plots and $\Delta V/A$ isotherms and was assigned to a transition between two liquid phases (see next section).

In the $F10Hm$ series, the diblocks with $m = 6\text{--}10$ did not produce ordered films. Langmuir films could be investigated from $m = 9$ up.¹⁵⁹ The monolayer of $F10H10$ was unstable. For $11 \leq m \leq 14$ the monolayers were still rather unstable, while those for $15 \leq m \leq 20$ were stable. The BAM images at large molecular area were interpreted as showing structures typical of gas/liquid coexistence. A kink was again detected in the C_s^{-1}/π plots. The monolayers were described as remaining in the liquid state until they collapsed. The $F12Hm$ series ($m = 6, 8\text{--}16, 18, 20$) behaved essentially like the $F10Hm$ series, but for the expected higher stability for a given m .³¹⁴ The collapse pressure increased with m in a stepwise manner: ~ 9 mN m⁻¹ for $m \leq 11$ (the $F12H9$ film was quite unstable); ~ 15 mN m⁻¹ for $12 \leq m \leq 16$; and ~ 21 mN m⁻¹ for $m = 18$ and 20. The compression modulus indicated that the film was in a liquid state, except for $m = 13$ and 14, for which an LC phase was proposed. A kink was seen for $9 \leq m \leq 12$.

Branching of the F -chain, as in (CF₃)₂CF(CF₂)₆C_{*m*}H_{2*m*+1} ($m = 11\text{--}20$), resulted in reduced collapse pressures (i.e., lesser stability) as compared to linear analogues, indicating a disordering effect on packing. The monolayers of these diblocks were unstable until m reached 14.¹¹⁰ Among the double-branched di(F_nH_m) gemini compounds **3.49**, only the longest ones, with $n = 8, 10$ and $m = 16, 18, 20$, formed stable Langmuir films.¹⁴⁵

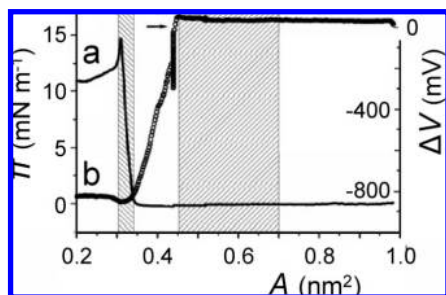


Figure 8.7. Surface pressure π (a) and surface potential ΔV (b) versus molecular area A isotherms for Langmuir monolayers of *F8H18* at the air–water interface (23 °C; compression speed ~ 3 cm² min⁻¹; the arrow indicates a 10 min stop to allow stabilization of ΔV); the two hatched areas correspond to the two phases (bilayer at the lower A values and monolayer at the higher A values) discussed in the text. From ref 157 with permission.

BAM can provide estimates of film homogeneity and thickness. In all the series investigated (with the exception of *F4H20*), the BAM data were taken to indicate a monolayer in the liquid state with the *F_nH_m* diblocks tilted with respect to the film normal.³²⁰

8.2.2. Diblocks at a Water/Air Interface—Electric Properties of Langmuir Monolayers

Surface potential/molecular area $\Delta V/A$ isotherms can easily be measured for Langmuir monolayers. The ΔV of the monolayer originates in the dipole moment of the diblocks and is therefore highly sensitive to their packing and orientation at the surface of water. ΔV is related to the vertical component of the dipole moment vector, μ_{\perp} (also called the effective dipole moment) through the Helmholtz equation, derived from the analogy between a monolayer and a parallel-plate capacitor whose plates carry the positive and negative charges of the dipole.¹⁶⁴ For a given A value, $\Delta V = \mu_{\perp}/\epsilon_0\epsilon A$, where ϵ_0 is the permittivity of vacuum and ϵ the permittivity of the monolayer, with the latter being microheterogeneous. It was suggested that the contributions of the hydrophobic tail, the hydrophilic headgroup of a surfactant, and the aqueous subphase could be treated independently, allowing replacement of the single homogeneous capacitor of the Helmholtz equation by a three-layer capacitor.²⁹¹ This model was further refined by assigning a local permittivity to each of the three layers.³²² Other models are also available.¹⁶³ The apparent dipole moment, $\mu_A = \mu_{\perp}/\epsilon$, is often provided, instead of μ_{\perp} , as the value of ϵ within the monolayer is uncertain.

Starting from 0 mV at large A values, the ΔV of Langmuir monolayers of diblocks decreased steeply at areas slightly larger than those at which the surface pressure started rising in the π/A isotherm and reached strongly negative values.^{157,159,314,321} The minimum ΔV values ranged from -700 to -1000 mV at collapse. These values are in agreement with the ΔV values measured for Langmuir monolayers of *F*-decanoic acid (-950 mV),³²³ trifluorostearic acid (-1190 mV),³²⁴ and a series of progressively fluorinated fatty acids (*F_nH_mCOOH*) (-700 mV to -970 mV).¹⁶² In comparison, the ΔV of a film of a nonfluorinated acid, myristic acid, at the same packing density, was only -50 mV.³²³ The $\Delta V/A$ isotherm of *F8H18* showed a break in the $45\text{--}30$ Å² molecular area range, while the π/A isotherm did not present any evidence for a phase transition (Figure 8.7).¹⁵⁷ The break in the $\Delta V/A$ isotherm was interpreted as

reflecting a first-order transition between a monolayer and a bilayer (see next section).

The maximum absolute value of μ_A , $|\mu_A|_{\max}$, was determined to be 0.65 ± 0.1 D for the stable monolayers formed by diblocks of the *F12H_m*, *F10H_m*, and *F8H_m* series.^{159,314,321} This value was interpreted as meaning that the molecules were tilted by 35° with respect to the surface normal. The slope of the linear ΔV versus A^{-1} curve led to estimate $|\mu_A|$ to be 0.76 D for *F8H18* and 0.60 D for *F10H10*.³²⁵ The difference between these two values was assigned to a difference in tilt angles.

The μ_{\perp} value of the CF₃ group in Langmuir monolayers of trifluorostearic acid was determined as 1.0 ± 0.2 D, i.e., about half of that measured for the dipole moment of CH₃CF₃ (2.35 D).³²⁴ An even lower value, ~ 0.5 D, was determined for μ_{\perp} of the *F_nH_m* segment in *F_nH_mCOOH*, regardless of n and m .¹⁶² In both cases, the difference in dipole moment between the molecule in its free state and when it is embedded in a Langmuir monolayer was assigned to mutual polarization between adjacent close-packed dipoles and to interactions with water molecules from the subphase. The uncertainties about the value of ϵ certainly complicate the determination of molecular dipole moments, film thicknesses, and molecular orientations from surface potential measurements.

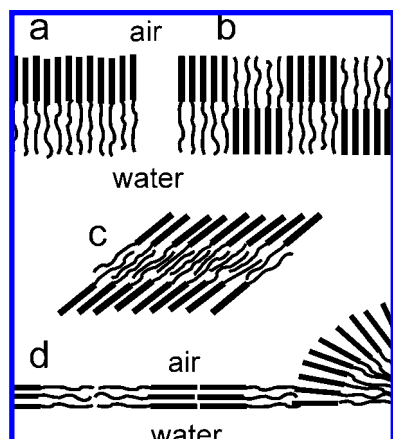
8.2.3. Diblocks at an Air/Water Interface—Film Structure and Molecular Orientation

Dependable structural investigation of Langmuir monolayers requires use of surface-sensitive techniques, such as GIXD, GISAXS, and X-ray reflectivity. The structure of the LC phase of *F*-alkylated carboxylic acids, *F*-alkylated alcohols, or *F*-eicosane has been identified as the LS phase.²⁹⁸ GIXD measurements on C₁₀F₂₁C₂H₄OH determined that its structure consisted of vertically packed molecules in a well-organized 2D hexagonal lattice with a cross section of 29.6 Å² for the *F*-chain (21.0 Å² for the *H*-chain of C₁₄H₂₉OH).²⁰

A first structural investigation of Langmuir monolayers of *F12H18* using GIXD showed the formation of an ordered structure with hexagonal close-packing of essentially untilted *F*-blocks.³¹¹ It took, however, many hours, sometimes days, for the ordered structure to form and for diffraction peaks to appear, which is much longer than for *F*-eicosane¹⁹ or *F*-acids,¹⁸ for which ordered domains were seen within minutes. Transient diffraction peaks, assignable to the *H*-chains, were observed in some samples.³¹¹ It was suggested that, during the complex monolayer relaxation process, some of the molecules went through a transient state in which the *H*-blocks would be enough aligned and over a sufficient range to generate a diffraction peak. The GIXD peak measured for *F12H18* monolayers was consistent with the first-order diffraction peak obtained for monolayers of *F*-acids (whose carboxylic acid function is unquestionably anchored on the water surface). X-ray reflectivity studies of a monolayer of *F12H18* on the surface of water concluded that the *F*-blocks were oriented toward air, with the *H*-blocks being in contact with water (Scheme 8.2a).³¹¹ The relatively large limiting area of ~ 33 Å² suggested some disorder, and possibly the coexistence of ordered and disordered phases in the *F12H18* monolayer.

An ordered structure with, however, low positional correlation length, was also found for Langmuir monolayers of the shorter *F8H16* diblock.³⁰⁴ The GIXD scans exhibited a broad Bragg peak whose position (typically at 1.25 Å⁻¹) was again consistent with the first-order diffraction peak found

Scheme 8.2. Schematic Representation of the Ordering of F_nH_m Diblocks in Langmuir Monolayers Proposed by Different Authors (Tilt Angles Not Accurately Represented): (a) F -Chain up/ H -Chain down Two-Slab Monolayer Model, in Which the Diblocks Are Essentially Oriented Vertically, Forming an F -Sublayer That Is in Contact with Air and an H -Sublayer in Contact with Water;^{304,309,311} (b) Alternating Antiparallel Orientation of Nanodomains, with about Half of the Molecules Having Their F -Chains in Contact with Water and the Other Half Having Their F -Chains in Contact with Air;^{157,326} (c) Three-Slab Hypothesis with an Antiparallel Diblock Arrangement Forming an Inner Slab Made of Interleaved H -Blocks, while the F -Blocks Are on the Outside and in Contact with Both Air and Water;³¹² (d) Coexistence of Surface Micelles (See Figure 8.11),³⁰⁹ Having Essentially Vertical F -Blocks Oriented toward the Air, with a Liquid Condensed Parallel (P) Phase in Which the Diblocks Lay Parallel to the Surface, Forming Stripes in the Lateral Direction, with Each Stripe Being a Bilayer of Oppositely Oriented Similar Blocks¹⁶⁹



for monolayers of F -acids¹⁸ and F - n -eicosane,¹⁹ suggesting a hexagonal lattice for the F -blocks. The F -chains were only slightly tilted (10° max.) and oriented toward air. The absence of peaks arising from alkyl chains indicated that the H -chains were in the liquid state.

The orientation of the diblock in Langmuir films, that is, which block is in contact with air and which with water, has nevertheless been a matter of debate. The F -chains are a priori expected to point toward air, rather than water, because of their larger hydrophobicity and higher affinity for gases as compared to H -chains. However, molecular dynamics simulations of the $F12H18$ monolayer concluded that the structure could consist of separate ordered domains with different chain orientations, with only a slightly larger fraction of diblocks having an F -block-up, H -block-down configuration (Scheme 8.2b).³²⁶

A tilted bilayer model (thickness 3.3 nm) with the diblock molecules oriented antiparallel to each other, with the F -blocks being outward and the H -blocks interleaved and inward (Scheme 8.2c), has been proposed for Langmuir films of $F8H18$ at small molecular areas (~ 0.3 nm²) on the basis of X-ray reflectivity measurements.³¹² In this arrangement the F -chains would form an external envelope for the bilayer, in contact with both the water and the air, while the interleaved H -chains would form an inner slab. This hypothesis is, however, hardly compatible with the molecular area extrapolated from the π/A isotherm (~ 0.33 nm²). The thickness of the proposed bilayer is also difficult to reconcile with the calculated length (3.65 nm) for a fully stretched $F8H18$ diblock, even if admitting a large tilt angle. The

ordering of the $F8H18$ diblock in the Langmuir monolayer was considered to have a smectic character similar to that found for solid $F12Hm$ ($8 \leq m \leq 14$) in the bulk. However, the absence, in the bulk, of contacts with air and water renders comparison with monolayers arguable. Scheme 8.1 shows no relation between Langmuir monolayer stability and aptitude at liquid crystal phase formation. The former increases steadily with F -block and total diblock lengths, while the latter is optimal for an F_n/H_m ratio around 0.9.

Further experiments on $F8H18$ were performed at very low surface pressure, before the formation of the above hypothesized bilayer.¹⁵⁷ The surface potential/molecular area isotherms $\Delta V/A$ (but not the pressure/area isotherms) detected a first-order phase transition, in the 0.45–0.30 nm² range, from a nonpolar monolayer at the large surface areas to the bilayer arrangement at higher pressures (Figure 8.7). X-ray reflectivity data in the 0.70–0.45 nm² area range found a film thickness of 2.7 nm, independent of molecular area. The data, and in particular the near-zero surface potential, were interpreted in terms of a monolayer model in which statistically half of the $F8H18$ molecules would be oriented with their F -chains in contact with water and the other half with their F -chains pointing up toward air. The in-plane organization would thus consist of oppositely oriented juxtaposed nanodomains (Scheme 8.2b). The possibility of the diblocks lying on the water surface (e.g., Scheme 8.2d)¹⁶⁹ was not considered. The film was not homogeneous and was interpreted as showing large domains of aggregated diblocks on essentially pure water. The surface fraction of void defects (50% at $A = 0.6$ nm²) would progressively fill in upon compression.¹⁵⁷ However, such an arrangement, where large area of water would exist at the interface and generate a high surface tension, would be energetically unfavorable. The subsequent discovery of the formation of surface micelles consisting mainly of upright diblocks in a sea of horizontally organized diblocks¹⁶⁹ (section 8.3) may explain some of these observations.

In the case of the diblock sulfide $F8H2SH16$, compression below 0.60 nm² led to the appearance in the FM images of dense domains dispersed in a low density monolayer.³²⁷ A uniform LC phase was formed when compression reached about 0.30 nm² per molecule. The surface pressure, which was initially practically zero, increased suddenly for molecular areas around 0.30 nm². The fact that the surface charge remained virtually zero for A values larger than 0.60 nm² was interpreted to mean that, for these A values, half of the molecules would then have their F -chains up and half their F -chains down. The sudden development of a negative surface charge for A values lower than 60 Å² was taken as indicating that all the molecules were then getting oriented with their F -chains up.

Further evidence establishing that the H -blocks were in contact with water and the F -blocks were pointing toward the air was provided for $F8H16$ by electron density distribution data from an X-ray specular reflectivity study conducted on surface micelles formed by the diblocks when compressed on water and transferred on a silicon wafer³⁰⁹ (section 8.3).

The negative surface potential values consistently measured on Langmuir films of $F8Hm$, $F10Hm$, and $F12Hm$ diblocks also indicated that the F -chains were directed toward the air.^{159,314,321} These observations are in line with those of negative surface potentials for monolayers of fluorinated³²³ or partially fluorinated^{162,324} acids and other partially fluorinated surfactants,³²⁸ for which molecular orientation is

determined by the dominant affinity of the polar head for water. Further arguments for an *F*-chain-up configuration can be derived from the fact that this orientation has been established for surface frozen diblock films and Gibbs films.

The kink that has been observed in the π/A and $\Delta V/A$ isotherms and C_s^{-1}/π plots of many diblocks has been assigned to a transition between two states with a liquid character for all the *F8Hm*³²¹ and *F12Hm* diblocks investigated.³¹⁴ In the *F10Hm* series, the kink was assigned to a transition between a liquid and a liquid condensed state or two states with liquid character.¹⁵⁹ This kink has been investigated in the case of *F10H19* using semiempirical modeling and FTIR spectroscopy performed on Langmuir monolayers after transfer on a CaF_2 substrate.¹⁶⁰ The data led to the hypothesis of a phase transition related to a conformational change from a more stable, partial double helix dimer organization to a single helix configuration. Such dimer formation had been calculated to occur for *F*-hexane and corresponded to arrangements of successive molecules in the actual crystal structure.¹⁴ Dimer clustering has also been proposed, on the basis of semiempirical calculations, to be the most stable arrangement in Langmuir monolayers of the semifluorinated alkanol $\text{C}_{34}\text{F}_{69}\text{C}_2\text{H}_4\text{OH}$.³²⁹ FTIR also indicated that the relatively long *H*-chains of *F10H19* were in a nearly crystalline (rather than liquid-like) state.

8.2.4. Langmuir–Blodgett and Other Supported Films

Exploratory experiments have indicated the capacity for *F12H18* to build Langmuir–Blodgett multilayers on oxidized silicon.¹⁸³ So far, Langmuir–Blodgett films of *F_nH_m* have essentially been formed for the purpose of transferring one monolayer on a surface appropriate for AFM, X-ray reflectivity, or FTIR studies.

Attempts at forming multilayered Langmuir–Blodgett films of *F10H19* on CaF_2 for FTIR studies were unsuccessful, as the second film transferred during immersion of the substrate through the interface detached itself during withdrawal.¹⁶⁰

Deposition of *F_nH_m* diblocks onto solid supports has also been achieved using spin coating techniques³⁰⁷ or exposure to supercritical CO_2 solutions.³¹⁶

The planar support needed for studying (and sometimes stabilizing) a diblock monolayer has also been provided by a stable and well-structured monolayer of another amphiphile that was immiscible with the diblock under investigation. The substrate or “subphase” on which diblocks are compressed can influence their film-forming behavior and film stability. Thus, *F8H16*, which formed surface micelles when the diblock was compressed alone, produced a highly ordered bilayer on top of a monolayer of DPPE, when *F8H16*/DPPE mixtures with high *F8H16*/DPPE ratios were compressed³⁰⁴ (section 8.4). Likewise, *F10H10* formed a stable monolayer on a monolayer of alamethicin (in which it did not dissolve), while no stable monolayer was obtained on water.³²⁵ Highly oriented supports, susceptible to generate epitaxy-like interactions, were observed to induce a change in morphology of the surface constructs.³¹⁶

Compressing mixtures of *F8H18* and alamethicin (a natural antibiotic peptide with a helical rodlike amphiphilic structure) resulted in the formation of a highly stable film of diblock on top of a monolayer of alamethicin.¹⁵⁸ Since the two compounds were essentially immiscible, the peptide formed a crystalline solid-like 2D substrate on which the diblock could be spread and investigated. Upon lateral compression

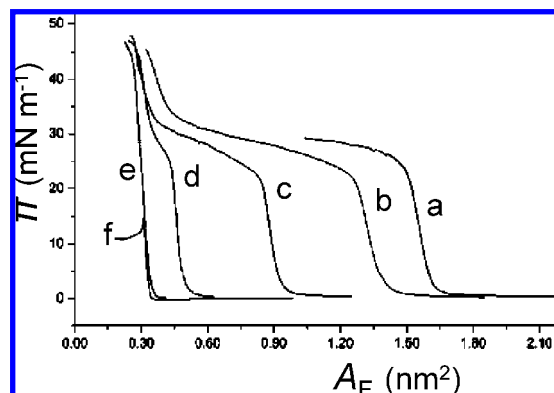


Figure 8.8. Surface pressure π versus molecular area A_F isotherms obtained by compressing *F8H18*/alamethicin (alam) mixtures with molecular *F8H18*/alam ratios of (a) 0 (pure alam), (b) 2.46, (c) 3.68, (d) 7.06, (e) 11.06, and (f) pure *F8H18*. Multiply A_F by the *F8H18*/alam ratio to convert the x axis from A_F values to $A_{F,alam}$ values, except for curve a, for which A_F values should be multiplied by 2. From ref 158 with permission.

of mixtures of alamethicin and *F8H18*, the surface pressure π increased steeply at a molecular area A of $\sim 3.2 \text{ nm}^2$, as for pure alamethicin (Figure 8.8, curve a). After the collapse of the peptide monolayer, a second rise in pressure occurred at a molecular area of $\sim 0.3 \text{ nm}^2$ (curves b–e), which is that of pure *F8H18* in its condensed phase (curve f). The density of the peptide monolayer did not change in the collapse plateau region while the diblock was compressed. The second pressure rise was attributed to compression of a monolayer of diblock alone, in agreement with the notion that the two compounds formed distinct superposed “pure” monolayers. When the *F8H18*/alamethicin ratio was 11.06, the pressure increased steadily up to 45 mN m^{-1} at a molecular area of $\sim 0.3 \text{ nm}^2$ (curve e), indicating that, at this particular ratio, the peptide monolayer was fully covered by a film of pure diblock. Grazing-incidence X-ray reflectivity experiments confirmed the formation of two monolayers stacked on top of each other but could not determine the structure and orientation of the diblock. The *F*-chain-up orientation was selected on the basis of surface potential measurements.

A subsequent study investigated the structure of Langmuir films of *F8H18* and *F10H10* diblocks compressed on top of an alamethicin monolayer.³²⁵ *F10H10* formed a stable monolayer on the hydrophobic peptide monolayer, while no stable monolayer was obtained on water. Again, no mixed Langmuir monolayer was formed at any point. The negative surface potential measured at high *F_nH_m* densities confirmed an *F*-block-up, *H*-block-down orientation. The π/A isotherm of the *F10H10*/alamethicin mixture showed again a first increase in π , corresponding to the onset of formation of the alamethicin monolayer, and a second break, corresponding to formation of a layer of *F10H10* on top of the above one. This situation is different from that observed when compressing mixtures of *F8H16* and phospholipids since, in the latter case, the two components initially formed a *mixed* monolayer from which the diblock was progressively ejected upon compression.³⁰⁴ GIXD experiments indicated that the *F8H18* molecules were organized with their long axis close to perpendicular to the surface in a quasi-rectangular 2D lattice, while no long-range positional order could be detected for the *F10H10* monolayer.³²⁵ The quasi-absence of diffraction peaks in the latter case probably reflected a liquid-like state. An increase of surface potential at small molecular areas for *F10H10* was interpreted as due

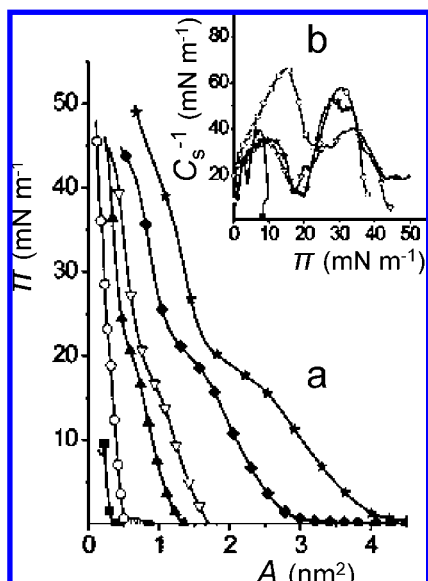


Figure 8.9. (a) Surface pressure π versus molecular area A isotherms for monolayers of $F6H18$ /gramicidin mixtures with increasing mole fractions of gramicidin, 0.1 (\circ), 0.3 (\blacktriangle), 0.5 (∇), and 0.7 (\blacklozenge), along with those measured for the pure components, $F6H18$ (\blacksquare) and gramicidin (\star); (b) some compression modulus/surface pressure C_s^{-1}/π plots. From ref 332 with permission.

to the build up of a second layer of diblocks on top of the first one. The diblocks would then adopt an unfavorable antiparallel arrangement with their H -blocks in contact with air.

8.2.5. Langmuir Monolayers of Mixtures of Diblocks with Other Compounds

Langmuir film studies of mixtures of F_nH_m diblocks with other types of amphiphiles revealed new and often complex types of behaviors, especially a novel dynamic and reversible pressure-dependent vertical phase separation phenomenon (section 8.4).

Pressure/area isotherm and BAM studies of mixtures of F_nH_m diblocks with long-chain alcohols provided phase diagrams for such two-dimensional binary systems. For example, $F10H20$ was miscible with $C_{18}H_{37}OH$, completely immiscible with $C_{18}F_{37}OH$, and partially miscible with $F18H10OH$; branching of the F -chain in $iF9H10OH$ resulted in reduced miscibility.³³⁰ Concerning the series comprising $iF3H20$, $F4H20$, $iF9H20$, and $F10H20$, miscibility was larger with the longer $C_{22}H_{45}OH$ alcohol than with $C_{14}H_{29}OH$ and increased with the length of the F -block.³³¹

Langmuir monolayers of $F6H18$ have been investigated as a matrix for Gramicidin A, a polypeptide antibiotic forming transmembrane ion channels for monovalent cations.³³² The objective was the transfer of such a mixed monolayer onto a solid support to serve as a biosensor. Gramicidin and $F6H18$ were found miscible in all proportions. The stability of the diblock monolayer increased considerably, as indicated by a remarkable increase of its collapse pressure from ~ 10 to ~ 36 mN m^{-1} upon addition of 0.1 mol fraction of the peptide (Figure 8.9). The phenomenon and the V/A isotherms have been interpreted as due to strong dipole–dipole attraction between the two species, favoring their association over that of like molecules. The possibility of maintaining π values of ~ 30 mN m^{-1} for gramicidin/ $F6H18$ mixtures should allow preservation of the peptide's bioactive vertical conformation, as this pressure is

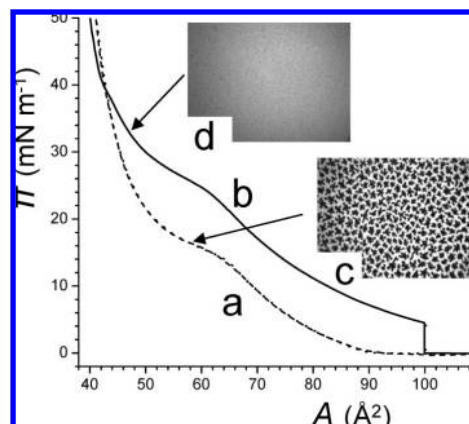


Figure 8.10. Effect of an $F8H2$ -saturated nitrogen atmosphere on the compression isotherm of a monolayer of DPPC on water at 25 °C (b, solid line); the control isotherm measured under an atmosphere of N_2 alone is also represented (a, dashed line); fluorescence images of (c) the DPPC monolayer under pure N_2 at 15 mN m^{-1} , showing the crystalline domains, and (d) the DPPC monolayer in contact with $F8H2$ (32 mN m^{-1}). The diblock vapor prevents formation of semicrystalline domains. From ref 334.

above the transition normally observed for gramicidin at ~ 16 – 21 mN m^{-1} to its inactive horizontal conformation when π is reduced.

8.2.6. Monolayers in Contact with Diblock Gases

The structure and behavior of Langmuir monolayers of phospholipids can be profoundly modified when contacted with FC gases. Figure 8.10 shows that the compression isotherm on water of a monolayer of DPPC changed drastically when an atmosphere of nitrogen (a) was replaced by an atmosphere of N_2 saturated with diblock $F8H2$ (b).^{333,334}

The LE/LC transition at $\pi \sim 13$ mN m^{-1} found for DPPC under N_2 or air disappeared, and two kinks appeared at $\pi \sim 28$ and ~ 38 mN m^{-1} . Below $\pi \sim 38$ mN m^{-1} , the π/A isotherm was shifted toward the large molecular areas, indicating that the $F8H2$ molecules were incorporated into the DPPC monolayer. The transition at $\pi \sim 28$ mN m^{-1} was no longer of the LE/LC type, as assessed by bright and featureless fluorescence microscopy images. Upon compression, the $F8H2$ molecules incorporated into the DPPC monolayer were progressively squeezed out from the DPPC monolayer until π reached ~ 38 mN m^{-1} . At high π values, the FM images showed the presence of very small crystalline domains, suggesting that the LE/LC transition occurred at ~ 38 mN m^{-1} . For $\pi > \sim 38$ mN m^{-1} , the isotherm became steeper and the limiting area (~ 50 \AA^2) was similar to that of DPPC compressed in the absence of $F8H2$. It is likely that the $F8H2$ molecules ejected from the DPPC monolayer respread on top of that monolayer, as in the case of the DPPE/ $F8H16$ mixed monolayer. The DPPC monolayer contacted with $F8H2$ was stable until ~ 71 mN m^{-1} , indicating that near-zero surface tensions were achieved. Upon expansion below $\pi = 40$ mN m^{-1} , the isotherm was again shifted toward larger molecular areas, reflecting the reincorporation of the diblock into the DPPC monolayer. These experiments demonstrated that the $F8H2$ diblock interacted dynamically with the phospholipid molecules, preventing the formation of the LC phase and inducing a fluidizing effect in the monolayer.

In order to assess the effect of $F8H2$ on LC domains that were already formed, a DPPC monolayer was compressed

to 13 mN m^{-1} and *F8H2*-saturated N_2 was then allowed to flush the gas-tight box that enclosed the Langmuir through, with π being maintained at 13 mN m^{-1} .³³³ The FM images showed that the LC domains had totally disappeared after only 5 min, leaving a totally fluid monolayer. These results were confirmed by GIXD experiments using synchrotron radiation, which also showed complete disappearance of the diffraction peaks due to the semicrystalline DPPC domains within 5 min after the monolayer had been contacted with *F8H2*.

Such behavior has also been found with other FCs having similar vapor pressures (C_8F_{18} , $\text{C}_8\text{F}_{17}\text{Br}$, $\text{F}_4\text{CH}=\text{CHF}_4$, *F*-decalin), but the diblock compound was the most effective, possibly in relation with its slightly lipophilic character. The finding that FC gases can prevent or revert crystallization of a DPPC monolayer has potential in lung surfactant therapy (section 10.2.4).

8.2.7. Black Lipid Membranes

Although not Langmuir monolayers, it should be mentioned that exceptionally long-lived and sturdy planar fluorinated black lipid membranes (BLMs) have been obtained from combinations of phospholipids and *F_nH_m* diblocks. The capacitances of these membranes were at least two times larger than those in the absence of the diblock component. For example, bilayers made of equimolar amounts of egg yolk phospholipids and *F6H10* or *F8H10* had capacitances of 0.55 ± 0.01 and $0.72 \pm 0.02 \mu\text{F cm}^{-2}$, respectively, as compared to $0.28 \pm 0.003 \mu\text{F cm}^{-2}$ for EYP alone.³³⁵

8.3. Patterned Surface Films—Surface Micelles

Close examination of monolayers of diverse *F_nH_m* diblocks discovered that their structure actually involved arrays of variously shaped discrete surface micelles. These arrays have been observed directly on the surface of water,³⁰⁶ in films deposited by Langmuir–Blodgett or spin-coating techniques on solid surfaces,^{307,309,310,315,317} in monolayers deposited from solutions in *sc*- CO_2 ,³¹⁶ and in monolayers formed on top of a monolayer of a distinct amphiphile.^{158,336,337}

8.3.1. Characterization of Surface Micelles of Diblocks after Transfer of a Langmuir Monolayer onto Solid Supports

Langmuir films of *F_nH_m* diblocks ($n = 6, 8, 10$ and $m = 14, 16, 18, 20$), when examined by AFM after transfer onto silicon wafers, were found to actually consist of large self-assembled surface micelles (hemimicelles) of different morphologies and dimensions, rather than of classical, featureless isotropic monolayers.^{309,310,315,317} The AFM images showed that, depending on diblock constitution, the surface micelles were circular or elongated or coiled (Figure 8.11) and could feature pits or tips in their middle (Figure 8.12). *F6H16* and *F8H14* produced almost exclusively highly monodisperse circular hemimicelles. The other diblocks investigated also displayed elongated micelles that coexisted with the circular ones (Figure 8.11d). Even when transferred at low surface pressures (a few mN m^{-1}), the micelles were organized in well-ordered hexagonal networks. These constructs were remarkably sturdy and resisted well, for soft organic self-assembled nano-objects, to the tip of the AFM cantilever. A noticeable observation was that the surface micelles did not

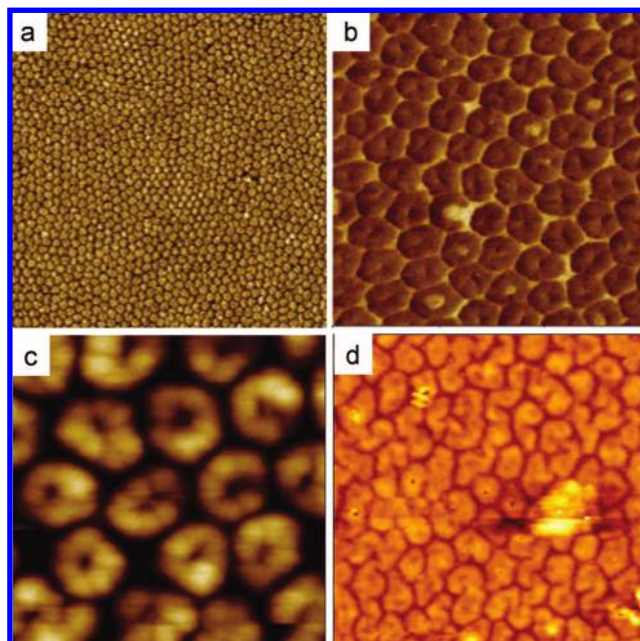


Figure 8.11. AFM images (tapping mode) of Langmuir films of (a) *F8H16* transferred onto a silicon wafer at 7 mN m^{-1} ($1 \times 1 \mu\text{m}^2$, topography);³³⁷ (b) phase image for the same diblock ($300 \times 300 \text{ nm}^2$); (c) the typical hexagonal array formed by *F8H16* surface micelles ($d \sim 30 \pm 1 \text{ nm}$); it is noteworthy that the surface micelles are robust enough to allow AFM imaging at such a small scale ($150 \times 150 \text{ nm}^2$; transfer pressure $\sim 6 \text{ mN m}^{-1}$) as, under these conditions, the frequency of contacts applied by the cantilever on the surface is high, which usually leads to destruction of soft organic self-assemblies;⁴⁶⁹ and (d) *F8H20* transferred onto a silicon wafer at 5 mN m^{-1} ($440 \times 440 \text{ nm}^2$). While the surface micelles are almost exclusively circular in the case of *F8H16*, a significant amount of elongated, wormlike surface micelles is present in the monolayers of *F8H20*. From ref 315.

shrink or coalesce and retained their shape when compressed (but, in some cases, for some deformation from circular to hexagonal at high lateral pressures, e.g., Figure 8.11b), even at pressures close to collapse. It is also interesting to note that the π/A isotherms of the monolayers of these diblocks (e.g., Figure 8.6) did not present any feature that foretold the existence of surface structures.

The mean diameter of the circular surface micelles, in the 20–35 nm range, was much larger than those of the micelles (circular or elongated) obtained in solution from standard surfactants (typically $\sim 5 \text{ nm}$ wide, $\sim 1 \text{ nm}$ high).³³⁸ The size of the transferred micelles of *F_nH_m* diblocks was shown to be controlled by the density mismatch between the *F*- and *H*-blocks.³¹⁰ It depended mainly on and increased with the length of the *H*-block. By contrast, micelle diameter was essentially independent of *F*-chain length, an observation in line with theoretical calculations based on statistical physics.¹⁶⁹ Increasing the length of *F_nH_m* favored the formation of elongated micelles at the expense of the circular ones, with both the length of the *H*-block and of the *F*-block having a strong influence.³¹⁰ The decrease in molecular area measured on compression isotherms increasing *H*-block length indicated increased ordering within micelles, likely due to increased molecular freedom, thereby allowing more compact packing.

The width of the elongated micelles, when present, was very close to the radius of the circular micelles, suggesting that the latter could arise from a partition of elongated micelles, followed by coalescence of the edges of the

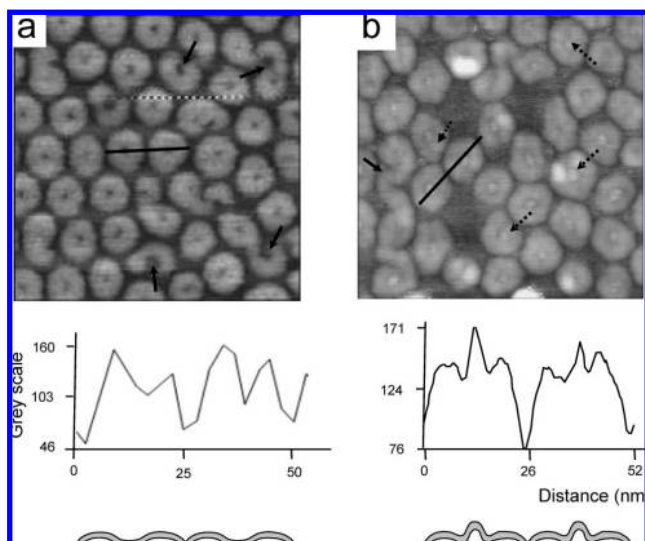
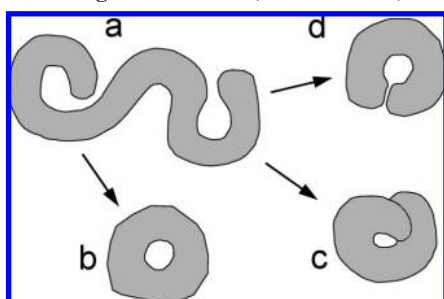


Figure 8.12. Surface micelles with a pit or a tip at their center. AFM images ($336 \times 336 \text{ nm}^2$) of films of *F8H18* transferred at (a) 8 mN m^{-1} and (b) 12 mN m^{-1} . Below each panel are the corresponding image analyses of the AFM profiles along the solid line shown on the images, as well as schematic representations of surface micelles displaying (a) a pit and (b) a tip at their center. In part a, the arrows show croissant-shaped surface micelles that are not completely closed up. In part b, the solid arrow points to an elongated micelle with coiled ends, and the dotted arrows point to micelles with a tip at their center; the latter may result from the protrusion of one of the edges during curling. From ref 310.

Scheme 8.3. Schematic Representation of the Partition of an Elongated (Wormlike) Surface Micelle (a), Yielding (b) a Pit-Centered (or Doughnut- or Toroid-Shaped) Circular Micelle and (c) a Coiled or Tip-Centered Micelle; (d) Incomplete Closing Is Also Seen (From ref 310)



resulting fragments (Scheme 8.3). This hypothesis is supported by the fact that the occurrence of elongated micelles was reduced and that they became shorter when the surface pressure of transfer was increased.³¹⁰ Incomplete coalescence of the edges would result in the open doughnut-shaped and coiled or tipped or spiral-shaped structures also seen on the AFM images. It was suggested that one extremity of the sectioned elongated micelle could stay in contact with the substrate, while the other would spiral upward. The interconversion between circular and elongated hemimicelles was reversible. In the case of *F8H18*, low surface pressures of transfer clearly induced the formation of pits, while high pressures favored curling and the formation of tips.

A detailed X-ray specular reflectivity study has been conducted on Langmuir–Blodgett films of *F8H16*.³⁰⁹ The experimental data were in good agreement with a two-layer model. The variation of the electron density as a function of the micelle's height is shown in Figure 8.13. The electron density distribution (Figure 8.13b) consisted of a 1.00 nm thick upper layer with an electron density of 487 e nm^{-3} (a

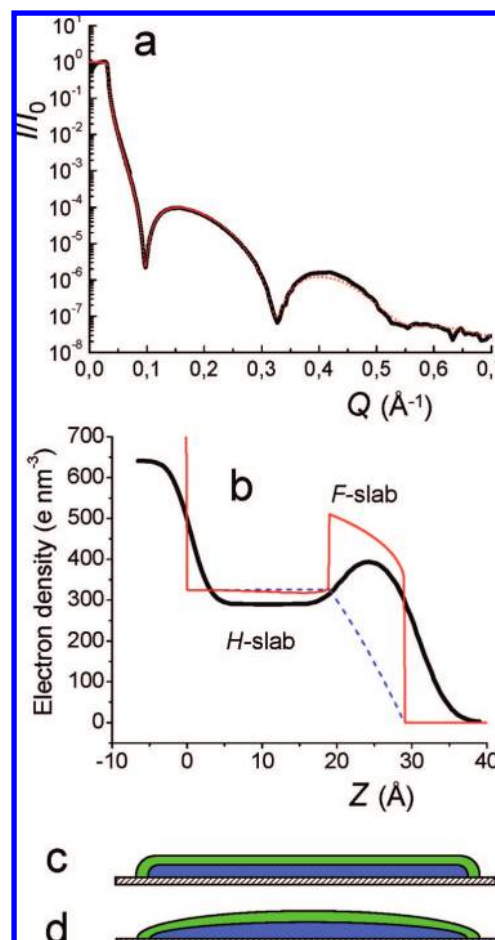


Figure 8.13. (a) Experimental X-ray reflectivity curve obtained from a Langmuir monolayer of *F8H16* transferred onto a silicon wafer at 7 mN m^{-1} ; the red dotted curve (almost completely overlaid by the experimental curve) is the fit obtained with the two-layer model (Parrat software); (b) variation of the electron density D , as a function of the height Z within the hemimicelle, derived from the experimental data, showing a definite difference in electron density (290 and 487 e nm^{-3} , respectively) between an inner- and an upper-slab (therefore characterized as F - and H -slabs, respectively); the thin solid red line corresponds to the theoretical electron profile for the disklike model (c), and the dotted blue line corresponds to the profile for the ellipsoidal model (d); the F - and H -slabs are in green and blue, respectively. From ref 309.

fluorinated layer) and a 1.93 nm thick lower layer with an electron density of 290 e nm^{-3} (a hydrogenated layer). These data establish unambiguously that the H -blocks were in contact with the silicon wafer and the F -blocks were pointing toward the air. The height of the surface micelles (2.93 nm) was somewhat shorter than the length of a fully extended *F8H16* molecule (3.32 nm), with the difference likely reflecting the liquid-like state of the H -chains. A disklike shape (Figure 8.13c) was proposed for the micelles on the basis of electron density calculations. The model was based on the fact that the interfacial area between the two layers (an F -layer and an H -layer) within a circular surface micelle should be equal to the product of the cross-sectional area of the F_nH_m molecule by the number of molecules per micelle. This diameter was independent of surface density and was solely determined by the density mismatch between F - and H -blocks.³⁰⁹ The model allowed a reasonably accurate prediction of the micelle diameter for a given F_nH_m diblock (Figure 8.14).

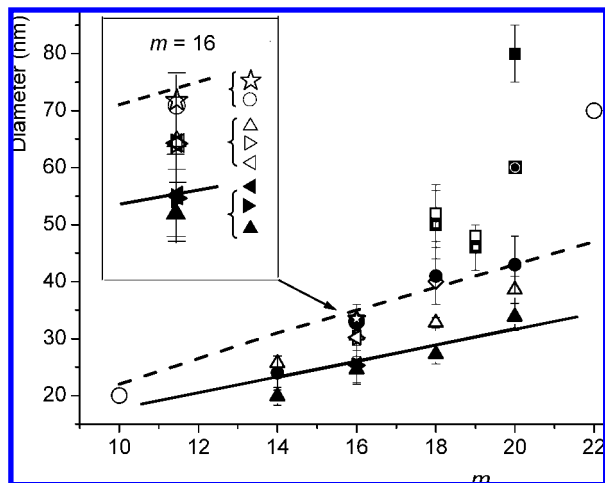


Figure 8.14. Dependence of the surface micelle diameter of F_nH_m diblocks on the length of the H -block. Experimental data: diameter (33.5 nm) measured by GISAXS, directly on the surface of water (\star), in monolayers of $F8H16$ at surface pressures of 0.5, 5, and 7 mN m^{-1} .³⁰⁶ Diameters obtained from AFM images after transfer of monolayers of $F8H_m$ ($m = 14, 16, 18, 20$) on a silicon wafer at pressure of transfer $\pi_t = 5 \text{ mN m}^{-1}$, diameters estimated using the (\blacktriangle) Visilog or (\triangle) Nanoscope software;³¹⁰ (\bullet) from AFM images of monolayers of $F8H_m$ transferred on silicon wafers at $\pi_t = 0 \text{ mN m}^{-1}$ at 49 and 41 \AA^2 for $m = 14$ and 16, and at $\pi_t = 0.5 \text{ mN m}^{-1}$ for $m = 18$ and 20;³¹⁷ from SFM images of monolayers of $F14H20$ cast on mica from a solution of hexafluoroxylene by spin coating (\blacksquare) or by Langmuir–Blodgett transfer at $\pi_t = 4.9 \text{ mN m}^{-1}$ (solid box containing a circle);³⁰⁷ from SFM images of structures deposited from solutions of $F12H19$ and $F14H18$ on mica (\square) or on HOPG (solid box containing a square) by exposure to a solution of the diblocks in scCO_2 [image analysis used the Femtoscan software³¹⁶]; from AFM images of a monolayer of $F8H18$ formed on a polystyrene–poly(ethylene oxide) copolymer and transferred on glass at $\pi_t = 25 \text{ mN m}^{-1}$ (\diamond);³³⁶ and (\circ) for $F_nH_m\text{COOH}$ acids ($n = 8, m = 10, 16, 22; n = 4, m = 22; n = 6, m = 22$) formed on a Cd^{2+} -containing subphase and transferred on glass at $\pi_t = 35 \text{ mN m}^{-1}$.³⁰⁸ Inset: enlargement of data for $m = 16$ (triangle pointing right, $n = 6$; \blacktriangle , $n = 8$; solid triangle pointing left, $n = 10$ for Visilog treatment; open signs for corresponding Nanoscope treatment). The solid and dashed lines represent the calculated diameter variations predicted according to models by refs 309, 310, and 316, respectively. These data also show that micelle diameter is much less dependent on F -chain length than on H -block length.

The mechanism of self-assembly of diblocks into surface micelles within Langmuir monolayers has been unraveled for a series of $F8H_m$ ($m = 14, 16, 18, 20$) diblocks.³¹⁷ It was established that micelle formation did not result from nucleation induced by evaporation of the spreading solvent and was not promoted by surface pressure but depended on the surface area available prior to transfer and, hence, on a critical surface concentration.

Evidence has indeed been provided for the presence of isolated micelles even at zero surface pressure (large molecular area) for certain diblocks after transfer onto silicon wafers. Thus, isolated disklike surface micelles were seen on AFM images (Figure 8.15) for $F8H14$ and $F8H16$ (diameters $\sim 26 \text{ nm}$ and $\sim 30 \text{ nm}$, respectively) for molecular area values A below 49 \AA^2 and 41 \AA^2 , respectively. At such large A values, the surface pressure experienced by the molecules is essentially null. Again, compression did not affect the diameter of the micelles. No surface aggregates were seen at $\pi = 0$ for the longer H_m diblocks $F8H18$ and $F8H20$, but well defined surface micelles were found for all the diblocks investigated when transfer was done at $\pi =$

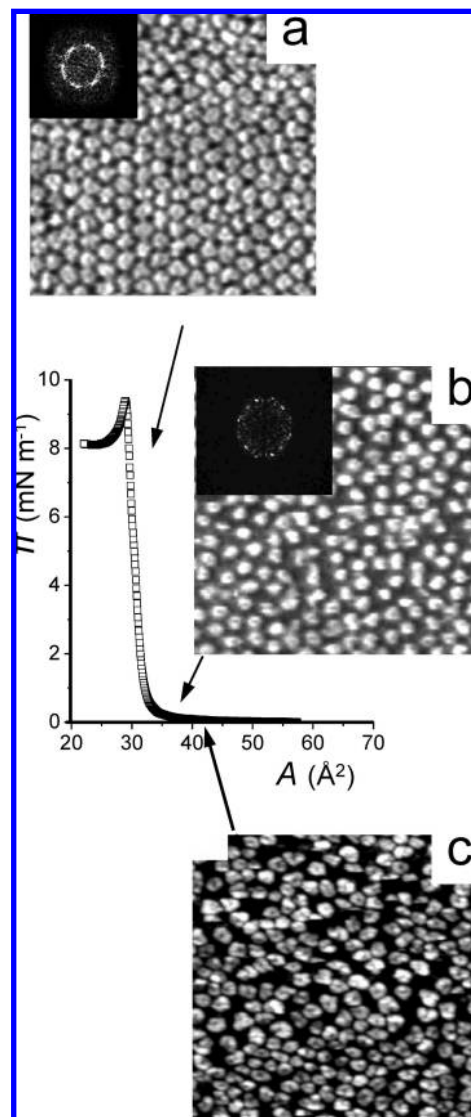


Figure 8.15. Surface micelles have been observed, after transfer of Langmuir monolayers of $F8H16$ on silicon wafers, at all the surface pressures investigated (20 $^\circ\text{C}$). AFM images (500 \times 500 nm^2 , tapping mode, z range 5 nm) of Langmuir–Blodgett films of $F8H16$ transferred on silicon wafers at (a) $\pi = 7 \text{ mN m}^{-1}$, data from ref 309; (b) $\pi = 0.5 \text{ mN m}^{-1}$, data from ref 337; and (c) $\pi = 0 \text{ mN m}^{-1}$, data from ref 317 at 41 \AA^2 . At the very large molecular areas, π is essentially null, yet isolated micelles are clearly seen that have the same size and morphology as those obtained at surface pressures near collapse. Notice that two diffusion rings are seen in part a and one in part b, while none were seen in part c.

0.5 mN m^{-1} . It has also been shown that the morphology (disklike vs elongated) of the hemimicelles was essentially determined by the diblock's molecular structure, independently of compression conditions. No surface aggregates were seen at very large surface areas (i.e., 120–60 \AA^2) after transfer onto a silicon wafer, likely indicating that there is a critical surface concentration required for diblock aggregation.

A theoretical treatment confirmed that large circular hemimicelles of $F8H16$ diblocks could be stable and monodisperse and organize in a hexagonal array at the water/air interface.¹⁶⁹ A two-phase liquid–liquid model was proposed in which a high-density phase, consisting of disklike surface micelles whose molecules were perpendicular to the interface with their F -chains pointed toward air, coexisted with a lower density matrix of diblock molecules lying on the surface of water within the Langmuir film. The stability and size of

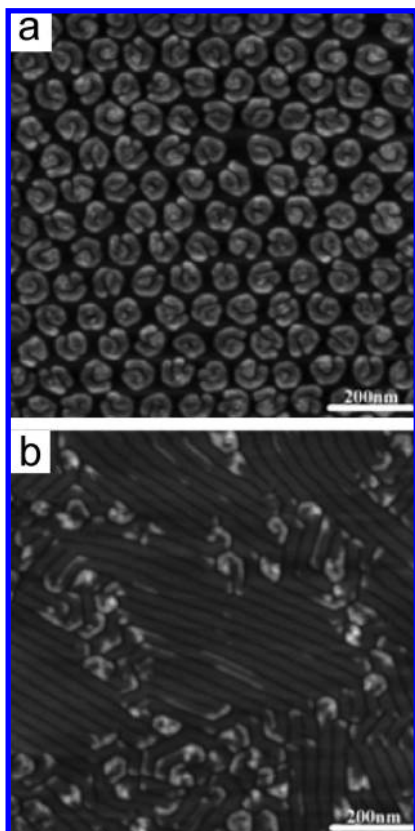


Figure 8.16. Scanning force microscopy images (tapping-mode) of *F14H20* deposited on mica by spin coating from 1 g L^{-1} solutions of the diblock (a) in hexafluoroxylylene, showing spiral/toroidal structures, and (b) in decalin, showing straight ribbons along with spirals. From ref 307 with permission.

the micelles, much larger than the molecule's length, called for long-range electrostatic interactions. These interactions were determined to arise from the permanent dipole of the diblocks. Electrostatic repulsion between micelles was established as the cause for low polydispersity at high surface pressures.

The surface aggregates most closely related to *F_nH_m* hemimicelles are those observed in Langmuir monolayers of partially fluorinated carboxylic acids.³⁰⁸ However, the experiments were performed in the presence of cations in the aqueous subphase. The observed surface patterns were increasingly sharp and well organized when turning from K^+ to Cd^{2+} and to La^{3+} . Metallic ions are indeed known to induce organization of organic molecules at the air/water

interface.³³⁹ It may, therefore, be that formation of surface micelles of partially fluorinated fatty acids was driven by interactions between the carboxylic group and the cations present in the subphase.

Spontaneous organization in regular nanoscopic surface patterns has also been identified by scanning force microscopy (SFM, i.e., AFM) and X-ray reflectivity on films of *F14H20* deposited by spin coating or by Langmuir–Blodgett transfer on mica or silicon wafers.³⁰⁷ Depending on the solvent used to cast the film of diblock, hexagonal arrays of spiral/toroidal structures (in hexafluoroxylylene) or of straight ribbons coexisting with spirals (in decalin or *F*-decalin) were formed (Figure 8.16). The spirals had an average diameter of $\sim 80 \text{ nm}$ and consisted of coiled short ribbons with a width of $\sim 35 \text{ nm}$ and height of $\sim 3.0 \text{ nm}$. Lateral compression reversibly yielded faceted hexagonal toroids having a size comparable to that of the initial spirals. The width and height of the ribbons were identical to those of the strands found in the spirals. These values are almost twice those found for the surface micelles of *F8H16* (Figure 8.14).^{309,310}

Quite remarkably, the spirals/toroids changed into straight ribbons when exposed to decalin or *F*-decalin vapor (Figure 8.17), while the ribbons transformed into toroids when exposed to hexafluoroxylylene.³⁰⁷ X-ray reflectivity determined identical heights (3.61 nm) for both types of structures. The data were consistent with an arrangement in which the *F*-chains were oriented perpendicular to the surface (and in contact with the air), while the *H*-chains would be tilted by 122° (and in contact with the support), allowing dense packing of the *H*-chains, thus compensating for the larger section of the *F*-chains. The GIXD data measured on both doughnut and ribbon monolayers indicated that both *F*- and *H*-blocks were largely in a liquid-like state. However, another series of samples, which was exposed to lower temperatures, showed a crystalline in-plane diffraction peak that was assigned to untilted crystalline *F*-chains. The finite width of the ribbons and stepwise turn of the spirals were explained by the amphiphilic character of the diblocks. Their interconversion would result partly from selective uptake of the solvent within the aggregates and partly from coadsorption of the solvent at the substrate, thus modifying the adhesive interactions of the diblocks.

Surface micelles have also been observed in Langmuir–Blodgett and spin-coated films of the gemini diblocks di(*F8H20*) and di(*F10Hm*) with $m = 14\text{--}20$ **3.49**. AFM imaging indicated a morphology similar to that observed for *F8H16* films (mainly circular with pits, $\sim 35 \text{ nm}$ in diameter).¹⁴⁵

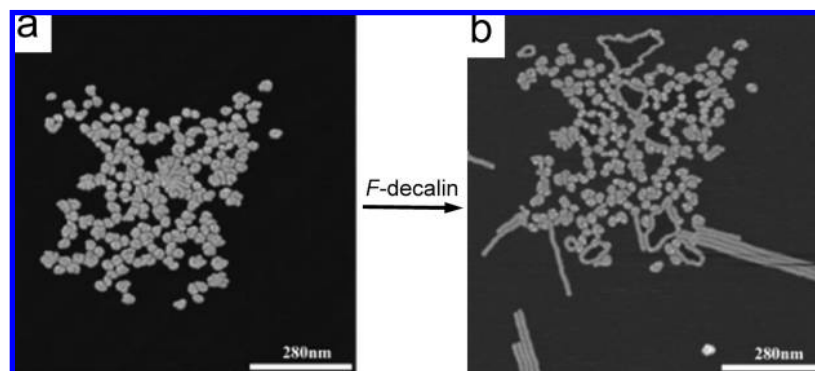


Figure 8.17. (a) As-cast film from a 0.1 mg mL^{-1} solution of *F14H20* in hexafluoroxylylene deposited by spin-coating at 2000 rpm, and (b) the same film after exposure to *F*-decalin vapor for 20 h, showing the development of ribbon structures from spirals/toroids. From ref 307 with permission.

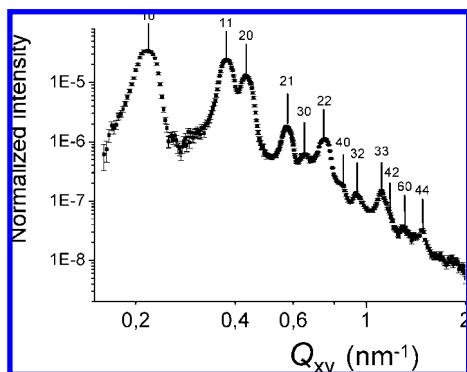


Figure 8.18. GISAXS diffraction spectrum measured directly on the surface of water, using the ESRF synchrotron source, of a monolayer of *F8H16* compressed at 5 mN m^{-1} . Note the exceptionally large number of reflections obtained. The intensity is integrated along Q_z from 0 to 5 nm^{-1} . The peaks were indexed in the hexagonal lattice of parameter 33.5 nm . From ref 306.

8.3.2. Direct Observation of *FnHm* Micelles on the Surface of Water

The key question whether the surface micelles of diblocks were formed at the free air/water interface or were induced by transfer of the Langmuir film onto the silicon or other solid substrate was solved by GISAXS experiments performed directly in the Langmuir trough on the surface of films of *F8H16* deposited on water.³⁰⁶

Measurements at surface pressures ranging from 0.5 to 7 mN m^{-1} definitely established the existence, directly at the air/water interface, of circular domains of $\sim 30 \text{ nm}$ in diameter. These domains formed highly organized hexagonal arrays. At 5 mN m^{-1} , an exceptional set of 12 peaks that were fitted by Lorentzian curves was obtained (Figure 8.18). Their indexation established that the observed 2D pattern consisted of circular structures of 33.5 nm in diameter positioned on a hexagonal lattice. To our knowledge, this was the first time that domains of such large size were characterized using GISAXS. The method involves generation and propagation of an evanescent wave formed when the X-ray beam hits the surface of water at an angle lower than the critical angle of water (2.5 mrad). The evanescent wave is diffracted and Bragg peaks are obtained when nanometric ordered domains are present on the water surface.

Similar results were obtained at 3 mN m^{-1} and even at pressures as low as 0.5 mN m^{-1} .³⁰⁶ The size of the hemimicelles formed on the water surface was independent of pressure and was close to that measured after transfer on silicon wafers ($30.5 \pm 1.2 \text{ nm}$).^{309,310,317} These data demonstrated unambiguously that surface micelles of *F8H16* diblocks existed on the surface of water. Their self-assembly and the regular nanoscale surface patterning found in transferred Langmuir films were definitely not caused by the transfer procedure and were not induced by a solid support.

8.3.3. Surface Micelles of Diblocks Deposited on Solid Supports from Solutions in Supercritical Carbon Dioxide

The use of sc-CO_2 , rather than a standard liquid solvent, for deposition of materials on a solid substrate has several advantages.³¹⁶ As CO_2 can be transferred directly from the supercritical to the gaseous phase, without formation of a liquid, formation of moving interfaces of drying droplets is avoided. The influence of solvent evaporation on the morphology of the deposited structures is therefore mini-

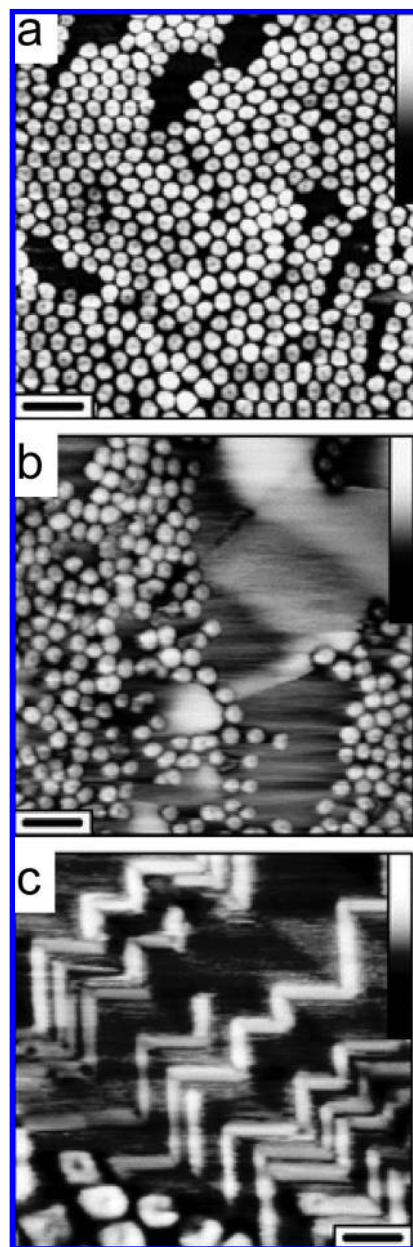


Figure 8.19. (a) Scanning force microscopy images (bar size, 150 nm ; height scale, 10 nm) of surface structures formed by *F12H19* on mica exposed to a solution of *F12H19* in scCO_2 ; (b and c) SFM images of structures formed by *F12H19* on mica (b) and on HOPG (c), with the substrates being simultaneously exposed to *F12H19* solutions in scCO_2 and slowly depressurized (bar size, 75 nm ; height scale, 10 nm). From ref 316 with permission.

mized. Possible deposition of structures formed at the solvent/vapor interface is also avoided. High-quality ultrathin coatings and self-assembled monolayers can thus be obtained.

Toroidal self-assembled structures were observed by SFM immediately after deposition of *F12H19* and *F14H18* on mica or on highly oriented pyrolytic graphite (HOPG) by exposure to solutions (dip-coating) of the diblocks in sc-CO_2 (Figure 8.19).³¹⁶ The images displayed a high degree of regularity regarding size, shape, and packing of the objects in a monolayer. The toroids had an outer diameter of $\sim 50 \text{ nm}$ and a height of $\sim 4\text{--}5 \text{ nm}$, independently of substrate. A double-layered arrangement was suggested to account for the slightly higher height of the toroids as compared to the length of the diblock molecules. Use of sc-

CO₂ deposition of diblocks on a solid support thus confirmed the observation made directly on water,³⁰⁶ that surface micelle formation and morphology was a true molecular self-assembly process and was not controlled by the substrate. Toroid formation on mica was also independent from decompression and CO₂ removal rate. However, in the case where HOPG was the substrate and when decompression was achieved slowly or annealing was allowed, another morphology was observed.³¹⁶ The *FnHm* diblocks then organized in stripes along the main crystallographic axis of the substrate, which was indicative of a strong interaction of the *H*-blocks with the substrate. A model was proposed for disk formation from *FnHm*, based on close-packing principles, with the amphiphilic and amphisteric characters of the diblocks being key factors.

8.3.4. Surface Micelles from Mixtures of Diblocks with Other Amphiphiles

Mixed monolayers on DPPE/*F8H16* (1:1.3) transferred on silicon wafers demonstrated lateral phase separation and showed domains of circular *F8H16* hemimicelles in coexistence with domains of DPPE.³³⁷ This system and its dynamics are the subject of section 8.4.

Vertical separation led to bi- or trilayered films whose structure was determined using GIXD.³⁰⁴ The diffraction patterns and contour plots for *F8H16*/DPPE (1:1) at low pressure showed a strong impact of the diblock on the ordering of the monolayer. GISAXS and AFM experiments made on the *F8H16*/DPPE system spread on water³⁴⁰ and AFM experiments after transfer on a silicon wafer demonstrated that, at high surface pressure, the size and ordering of the surface micelles formed on the lipophilic substrate constituted by the hydrophobic surface of the DPPE-only monolayer were essentially identical to those formed by *F8H16* on water.^{306,337} These experiments further demonstrated that surface micelle formation is an intrinsic property of *FnHm* diblocks, independent, among others, of substrate.

Langmuir films of mixtures of *F8H18* and of a poly(styrene)–poly(ethylene oxide) block copolymer (40 and 123 monomers, respectively) have been investigated using isotherm determinations and AFM experiments.³³⁶ It was shown that *F8H18* segregated and formed a film on top of the copolymer for all copolymer densities. After transfer on a glass substrate for AFM examination, the film exhibited a surface structure that was described as honeycombs (periodicity of ~40 nm) with a hump at their center (diameter of ~30 nm). These structures were actually comparable in size and shape to the pitted disks or toroids described by other authors in the absence of copolymer.^{307,309,310} Nevertheless, their formation was assigned to interactions between the diblock molecules and the copolymer interface, rather than to an inherent property of *FnHm* diblocks.

Nanoscale circular domains of about 40 nm in size and ~2.6 nm in thickness have also been identified by AFM after transfer on a silicon substrate of a film of *F8H18* supported by an alamethicin monolayer.¹⁵⁸

8.3.5. Surface Micelle Formation: an Inherent Behavior of *FnHm* Diblocks

A solid body of data leads to the conclusion that formation of self-assembled surface micelles is an intrinsic property of *FnHm* diblocks in 2D surface films. These surface micelles can adopt various shapes/morphologies, including disks,

toroids (doughnuts), tip-centered hemimicelles, coils (nanospirals), worms, ribbons, etc. (Figures 8.11, 8.12, and 8.16). Structural investigations performed directly on the surface of water (Figure 8.18) determined that self-assembly was not caused by transfer of the monolayer on a solid support. Self-assembly did not result from compression, since the existence of surface micelles was demonstrated at zero surface pressure (Figure 8.15), but depended on the surface area available prior to transfer and, hence, on a critical surface concentration. Micelle formation did not result from nucleation induced by evaporation of the spreading solvent. The structures, when transferred on a solid, did not appear to be affected by the nature of the substrate (which were, for example, hydrophilic in the case of silicon wafers and hydrophobic in the case of phospholipid monolayers), unless there was a specific epitaxy-like interaction (Figure 8.16). On the other hand, exposure to different solvents led to modifications of the morphology of the constructs (Figure 8.17).

The size of circular (or toroidal) surface micelles is primarily dependent on the length of the *H*-chain and much less on that of the *F*-chain (Figure 8.14). It is essentially independent of pressure and support. On the other hand, the *F*-chain length and the *FnHm* ratio appear to influence the morphology, elongated versus circular, for example, of the constructs. The formation of such stable, large nanometric ordered surface patterns from simple “nonpolar” molecular *FnHm* diblocks may provide new organic templates with tunable periodicity for the controlled elaboration of arrays of nanoparticles (section 10.3).

8.4. Diblock-Induced, Pressure-Controlled Film Dynamics

A new type of pressure-induced *vertical* phase separation phenomenon has been observed upon compression of Langmuir films made of combinations of *FnHm* diblocks and phospholipids and other fatty acids.^{304,313,334} In these binary systems, pressure caused the diblocks to be reversibly expelled from an initially mixed monolayer and to organize separately on top of a monolayer of the other component. Extensive investigation of monolayers of mixtures of *FnHm* diblocks with phospholipids was triggered by the observation of an unexpectedly strong stabilization of *FC* emulsions^{191,341} and vesicles^{9,12,342,343} upon incorporation of such diblocks in phospholipid films.

Compression isotherms of mixed Langmuir monolayers of dipalmitoylphosphatidylethanolamine (DPPE) and diblock *F8H16* spread on water are shown in Figure 8.20.³⁰⁴ For DPPE/*F8H16* ratios between 1:1.3 and 2:1, the isotherms featured a transition at about 10 mN m⁻¹, above which the area occupied by the diblocks (the difference in *A* between the DPPE-only and the mixed monolayers) decreased and became very small. The limiting area was then very similar to that of pure DPPE. The isotherms were fully reversible (with hysteresis), indicating that no significant amount of diblock was lost during the compression/expansion cycle. These observations strongly suggested the formation of multilayers.

Grazing incidence X-ray diffraction patterns measured for DPPE/*F8H16* 1:1 and 1:1.3 mixtures at low pressure showed a strong impact of the diblock on the ordering of the DPPE monolayer, resulting in a more dense, but less organized packing.³⁰⁴ At 10 mN m⁻¹, which corresponds to the collapse pressure of *F8H16*, the diblocks started being ejected from

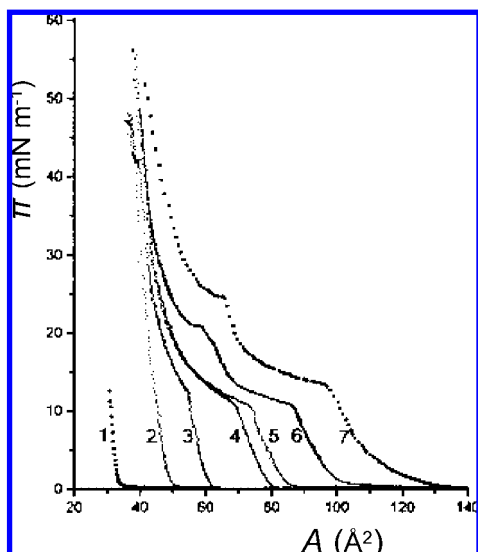


Figure 8.20. Surface pressure π versus molecular area A isotherms of Langmuir monolayers of *F8H16* (1), DPPE (2), and DPPE/*F8H16* mixtures with molar ratios of 2:1 (3), 1:1 (4), 1:1.3 (5), 1:1.5 (6), and 1:2 (7).³⁰⁴ At high surface pressure, the molecular area for the DPPE/*F8H16* combination is close to that of DPPE alone, suggesting that the diblock has been expelled from the water surface.

the monolayer toward the air. At high pressure (38 mN m^{-1}), a strong and sharp diffraction peak (1.52 \AA^{-1}) characteristic of the untilted LS lattice of a DPPE-only monolayer was observed, indicating complete expulsion of the diblock. A broad Bragg peak at 1.25 \AA^{-1} showed that the *F*-blocks were ordered on top of the DPPE monolayer, with a rather low positional correlation length ($\sim 25 \text{ \AA}$), very similar to that found in monolayers of pure *F8H16*.

The 1:1.3 ratio for a DPPE/*F8H16* mixture is critical, as it corresponds to the maximum molar ratio for which, owing to their respective cross sections, a dense *F8H16* monolayer can be accommodated atop a close-packed DPPE monolayer.

A second transition appeared on the isotherms of Figure 8.20 for DPPE/*F8H16* ratios of 1:1.5 and 1:2. (at 20 and 25 mN m^{-1} , respectively), with an extrapolated molecular area corresponding to that of pure DPPE. The isotherms were again reversible. The diffraction peaks became narrower as pressure increased. At 45 mN m^{-1} , DPPE was again fully organized in its hexagonal lattice. The thickness of the mixed layer became significantly larger than that of pure DPPE (3.3 vs 2.1 nm) and increased upon compression. Up to the second transition, the ejection of *F8H16* occurred similarly to what was observed for DPPE/*F8H16* ratios $\leq 1:1.3$. However, when the ratio exceeded the critical 1:1.3 value, the surface concentration of diblocks became too high for all the diblock molecules to be engaged in one single upper monolayer and the diblocks were forced to form an additional layer on top of the two already formed. GIXD studies of a 1:2 DPPE/*F8H16* monolayer at 38 mN m^{-1} showed a highly structured pattern of Bragg peaks for the *F*-blocks, indicating that the layer of diblocks formed on top of the DPPE layer was highly organized.³⁰⁴

AFM studies were performed on DPPE/*F8H16* (1:1.3) mixed monolayers transferred on silicon wafers (Figure 8.21).³³⁷ Below surface pressures of transfer π_t of 10 mN m^{-1} , the images presented a lateral phase separated topology, with monodisperse domains of *F8H16* hemimicelles coexisting with a monolayer of DPPE (d). The density of the network

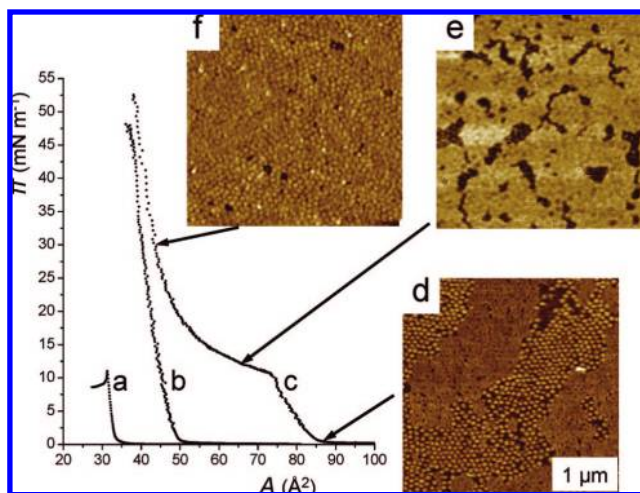
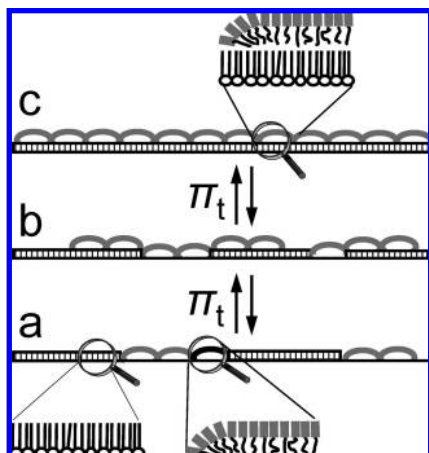


Figure 8.21. Lateral and vertical phase separation of *F8H16* surface micelles within and on top of a monolayer of DPPE. Surface pressure π versus molecular area A isotherms of (a) *F8H16*, (b) DPPE, and (c) a DPPE/*F8H16* 1:1.3 mixture (the molar ratio that corresponds to the threshold at which the *F8H16* surface concentration allows a dense monolayer of the diblock to form on top of a dense monolayer of DPPE). Isotherm c presents a transition at $\sim 10 \text{ mN m}^{-1}$, above which the limiting area is very similar to that of pure DPPE. AFM images ($1 \times 1 \mu\text{m}^2$) of mixed 1:1.3 DPPE/*F8H16* monolayers transferred on silicon wafers at (d) 0.5 mN m^{-1} , (e) 10 mN m^{-1} on the coexistence plateau, and (f) 30 mN m^{-1} . In image (d), the domains of circular micelles of *F8H16* coexist with phase-separated flat DPPE monolayer domains; in image (e), depicts higher and lower regions, with the topology of the higher regions being identical to that of surface micelles of pure *F8H16*, with the same diameter and height, while the lower region is similar to the image seen in part d. The proportion of the surface covered by *F8H16* surface micelles increases with transfer pressure; in image (f), the surface micelles of *F8H16* cover totally the DPPE monolayer; the topology of the film is then indistinguishable from that observed for monolayers of pure *F8H16* transferred at 7 mN m^{-1} . From ref 337.

of *F8H16* surface micelles increased as π_t increased, but their size remained the same. Around 10 mN m^{-1} , the images depict higher and lower regions (e). The network of surface micelles started to glide onto the DPPE monolayer, progressively overlying it as π_t increased, until full coverage was achieved (f). At π_t of 30 mN m^{-1} , the surface micelles completely covered the DPPE monolayer and the observed pattern was identical to that obtained for monolayers of pure *F8H16*. Throughout the experiment, the surface micelles retained the same size (30 nm) and height ($2.3 \pm 0.5 \text{ nm}$), the same as those observed for pure *F8H16* monolayers on water.³⁰⁶ X-ray reflectivity experiments at various pressures confirmed that the thickness of the mixed film was comparable to that of a DPPE-only monolayer at low surface pressure (5 mN m^{-1}), while at higher pressures (15 and 40 mN m^{-1}) the height (5.50 nm) of the composite *F8H16*/DPPE film corresponded to the sum of those of the lower DPPE monolayer (2.50 nm) and of the layer of *F8H16* surface micelles (2.93 nm).

Scheme 8.4 summarizes the pressure-controlled dynamics of a *F8H16*/DPPE 1:1.3 Langmuir monolayer transferred onto silicon wafers. At low surface pressures (a), the film was laterally phase-separated with domains of monodisperse surface micelles of *F8H16*, identical to those found in monolayers of pure diblock, coexisting with a monolayer of DPPE. When pressure attained $\sim 10 \text{ mN m}^{-1}$, the surface micelles started being ejected and started gliding above the DPPE monolayer (b), until complete coverage was achieved

Scheme 8.4. Pressure-Controlled Dynamics of Mixed *F8H16*/DPPE Langmuir Monolayers—Schematic Representation of the Structure of DPPE/*F8H16* (1:1.3) Langmuir Monolayers Transferred onto Silicon Wafers as a Function of Transfer Pressure (π_t): (a) At Low Surface Pressure of Transfer, the Film Is Laterally Phase-Separated, with Domains of Monodisperse, Essentially Circular Surface Micelles of *F8H16* Coexisting with a Flat Monolayer of DPPE (Striated Layer); (b) When π_t Attains $\sim 10 \text{ mN m}^{-1}$, the Surface Micelles Start Being Ejected from the Water Surface and Start Gliding on Top of the DPPE Monolayer, until (c), at Still Higher π_t , Complete Coverage of the DPPE Monolayer by Surface Micelles of *F8H16* Is Eventually Achieved^a

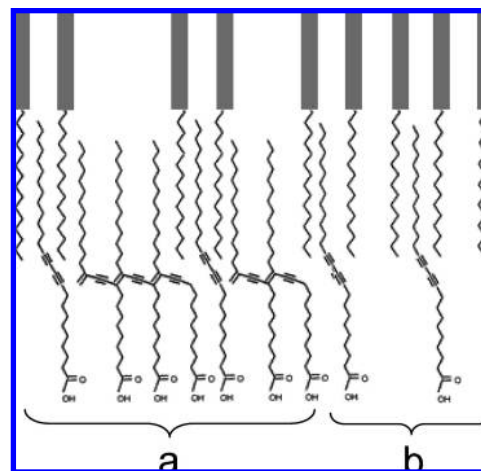


^a The sequence can be fully reversed upon decompression.³³⁷ The *F8H16* micelles on top of the DPPE film are identical in diameter (30 nm) and height (3 nm) to those obtained from pure *F8H16* on water.³⁰⁶

(c). These pressure-driven lateral and vertical phase separation phenomena were fully reversible.

Another example involving vertical phase separation of diblocks upon compression concerns mixtures of *F8H16* with 10,12-pentacosadiynoic acid (PDA) and the effect of the diblock on polymerization of the diynoic fatty acid in a monolayer. Langmuir compression studies on water have demonstrated that *F8H16* and $\text{C}_{13}\text{H}_{27}\text{C}\equiv\text{CC}\equiv\text{CC}_8\text{H}_{16}\text{COOH}$ were fully miscible at low pressures.³¹³ Lower isotherm slopes indicated that the mixed monolayers were more compressible than those of both individual components. The limiting molecular area for the mixture was significantly smaller than the mean molecular area obtained from the additivity law, indicating stronger intermolecular interactions. These data, complemented by BAM and UV–visible spectroscopy studies, suggested an unusual packing arrangement in which surface pressure would cause the *F*-chains to be squeezed out from the monolayer to the top of the alkyl chains of PDA, thus forming an additional half-layer on top of the PDA monolayer (Scheme 8.5). The PDA molecules would be anchored on the water surface, with the *F*-chains of *F8H16* in contact with air and the *H*-blocks intercalated with the PDA chains. Optimum packing was reached for a PDA/*F8H16* ratio of 1:2, which corresponds to each PDA being surrounded by six diblock molecules. The isotherms were fully reversible, indicating reversibility of the vertical separation phenomenon. The influence of the diblock on PDA polymerization was clear-cut (Scheme 8.5): PDA could be polymerized within the mixed film upon UV irradiation up to a PDA/*F8H16* molar ratio of 1:2 (a). Higher diblock proportions made polymerization impossible, as it prevented contacts between PDA molecules (b).

Scheme 8.5. Suggested Molecular Packing of a Mixed *F8H16*/10,12-Pentacosadiynoic Acid (PDA) Monolayer.^a



^a Segregation of the *F*-chains (gray rectangles) causes formation of a fluorinated half-layer on top of the PDA monolayer. (a) When the molar fraction of *F8H16* is lower than 0.67, PDA can still be polymerized; (b) when it is larger than 0.67, polymerization is no longer possible, as all PDA molecules are separated. From ref 313.

A further example of dynamic, pressure-driven reversible vertical separation was provided by the earlier described reversible ejection/reincorporation of *F8H2* diblocks in DPPC monolayers contacted with diblock gas.³³⁴

Driving forces for vertical phase separation of *F_nH_m* diblocks from mixtures with nonfluorinated amphiphiles include the limited miscibility of the monolayer components, the propensity for *F*-chains to segregate and self-assemble in an orderly manner, and the decrease in surface tension that follows expulsion of the *F*-chains toward air above the lipid or other nonfluorinated layer. The screwlike shape and low friction or “slippery” surface of the *F*-chains could facilitate such dynamic structural transformations.

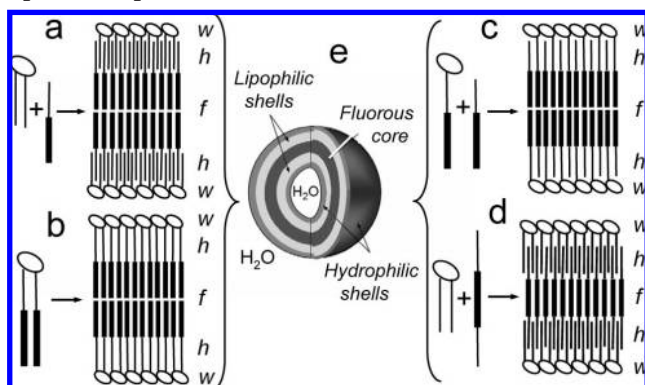
9. Diblocks at Interfaces—Discrete Dispersed Particles

The pronounced tendency for *F_nH_m* diblocks to collect and organize at interfaces has been put to advantage to prepare, stabilize, and control the properties of colloidal systems made of dispersed discrete objects, such as dispersions of vesicles (liposomes) and emulsions. The latter include *FC*-in-water emulsions and microemulsions, *HC*-in-*FC* emulsions, and multiple emulsions. In these systems, diblocks can participate in interfacial film or bilayer membrane structuring and/or provide the dispersed or the continuous phase. Diblocks also have a vocation as components of tubules, microbubble walls, and other supramolecular constructs.

9.1. Bilayer Membranes—Fluorinated Vesicles

Fluorinated vesicles (*F*-vesicles) consist typically of vesicles made from amphiphiles that have a hydrophilic polar headgroup and one or more hydrophobic *F*-chains. *F*-Vesicles are uniquely characterized by the presence of a well-organized highly hydrophobic fluorinated layer or sheet within their liposomal membrane (Scheme 9.1). *F*-Vesicles have been prepared from a large variety of single- and double-chain amphiphiles.^{9,12,13,46,47} When compared to standard vesicles obtained from nonfluorinated surfactants,

Scheme 9.1. Bilayer Membranes of Fluorinated Vesicles Made of (a) a Diblock/Phospholipid Combination and, for Comparison; (b) an *F*-Alkylated Phospholipid (e.g., compound 9.2); (c) a Diblock/Single Chain *F*-Alkylated Phosphocholine (e.g., 9.1) Combination, with the Diblock Providing a “Crutch” That Reconstitutes the Double-Chain Hydrophobic Part of an *F*-Alkylated Phospholipid; (d) Bilayer Phospholipid Membranes Can Also Be Reinforced Using *HmFnHm* Triblocks That Play the Role of “Tie-Bars” between the Two Phospholipid Monolayers; (e) All the Fluorinated Vesicles Share an Essential Common Element: the Presence of a Highly Organized, Strongly Hydrophobic Fluorinated Core within Their Membrane That Induces Specific Properties^a



^a The hydrophilic, lipophilic, and fluorophilic sublayers or shells of these membranes are denoted *w*, *h*, and *f*, respectively.

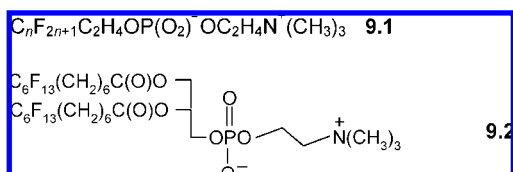
F-vesicles generally display higher thermal stability, lesser membrane permeability, and substantially different behavior, including in a biological medium.

Incorporation of *F*-alkyl/*H*-alkyl diblocks into a classical (nonfluorinated) liposomal membrane provides an alternative means of building an internal fluorinated sheet, thus imparting to this membrane some of the properties obtained with complete hydrophilic/fluorophilic *F*-surfactants, although generally to a lesser extent. Such diblock incorporation can allow modulation and control of vesicle membrane properties.

9.1.1. Preparation and Stability

9.1.1.1. Combinations of *FnHm* Diblocks with Standard Phospholipids. The first *F*-vesicles based on a *FnHm*/phospholipid association were obtained serendipitously, along with phospholipid-coated diblock droplets, while preparing highly concentrated emulsions of diblock compounds. Formulation optimization led to obtaining solely small unilamellar *F*-vesicles, about 20 nm in diameter.³⁴⁴ Like *F*-vesicles prepared from complete *F*-amphiphiles (e.g., the *F*-alkylated phosphocholines 9.1 and *F*-alkylated phosphatidylcholines 9.2), these vesicles possess a highly hydrophobic, as well as lipophobic, fluorinated internal core, typically 1–2 nm thick, within their membrane (Scheme 9.1e).⁹

This fluorinated core is flanked by two lipophilic shells,



contributed by both the *H*-chains of the diblocks and the fatty chains of the phospholipids, and then by the hydrophilic

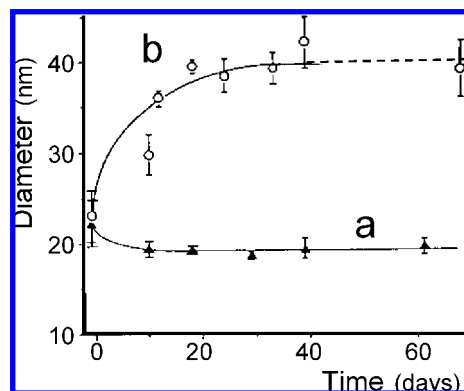


Figure 9.1. Evolution of size (photon correlation spectroscopy) as a function of time in a phosphate buffer at 25 °C of (a) vesicles made from a DMPC/*F*4CH=CHH10 (1:2) combination, as compared to (b) vesicles made of DMPC alone. From ref 344.

shells formed by the phospholipids' polar head groups. The *F*-vesicles made from *FnHm*/phospholipid combinations, like those obtained from *F*-phospholipids, display increased physical stability (for example, liposomes made from DMPC and diblock *F*4CH=CHH10 resisted better to heat sterilization), reduced membrane permeability, and reduced fusion kinetics.

The case of the *Fn*CH=CHH10/DMPC vesicles has been investigated in some detail.³⁴⁴ A typical preparation of such vesicles involved codissolution of equimolar amounts of DMPC and diblock in CHCl₃; removal of the solvent on a rotoevaporator; thorough drying of the thin film left on the inside surface of the flask; hydration of that film, for example, with a phosphate buffer; and dispersion by sonication until particle sizes reached a plateau. This procedure, when applied to *Fn*CH=CHH10 (*n* = 4, 6, 8)/DMPC mixtures (1:2 to 2:1), yielded a largely predominant population (87–99%, depending on diblock and processing) of small unilamellar vesicles (SUVs), 20–30 nm in average diameter, as determined by photon correlation spectroscopy, and a second population (1–13%) of larger particles, with mean diameters of 70–160 nm. A 2:1 *F*4CH=CHH10/DMPC mixture produced, after ultracentrifugation, a narrowly dispersed single population of 19 nm particles. Quantitative analysis established that 80% of the phospholipid was contained in SUVs and that the DMPC/diblock ratio in these SUVs was essentially 1:1, as for the vesicles obtained from an initial 1:1 *F*4CH=CHH10/DMPC mixture. This indicates that, under the conditions used, formation of 1:1 *F*4CH=CHH10/DMPC SUVs was favored over other structures.³⁴⁴ Further *F*-vesicles were obtained from combinations of DMPC with *F*4H12 and *F*6H12, and displayed similar behavior.³⁴⁵

The stability of *F*4CH=CHH10/DMPC vesicles, in terms of particle coarsening over time, was substantially increased with respect to that of liposomes made of DMPC only (Figure 9.1). There was no significant change in mean particle size after two months in a phosphate buffer at 25 °C, whereas the DMPC-only liposomes went from a mean diameter of 22 nm to about 39 nm within ~20 days, which was accompanied by flocculation and sedimentation.³⁴⁴ Several factors likely contributed to vesicle stabilization, including tight *F*-chain segregation and rigidity, reduction of packing defects, and improved resistance to buckling and delipidation.

The presence of the *F*-core of *F*4CH=CHH10 diblocks within the liposomal bilayer membrane also modified the vesicle's thermotropic behavior. A phase behavior study by

steady state fluorescence anisotropy determined a slight lowering of the liposomes' gel-to-fluid phase transition temperature T_c and a broadening of the transition.³⁴⁴ The magnitude of the T_c shift increased as the F_n/H_m ratio decreased. The behavior of these F_nH_m -reinforced vesicles in a biological milieu is discussed in section 9.1.5.

9.1.1.2. Combinations of F_nH_m Diblocks with Single Chain Amphiphiles. Single-chain H -surfactants, when dispersed in water, do usually not form vesicles, but micelles, while analogous single-chain F -surfactants can provide stable vesicles.^{12,231}

The stability of single-chain phosphocholine-derived F -surfactant **9.1** ($n = 8$) was further increased by using equimolar amounts of **9.1** and diblock $F8H2$.³⁴⁶ The hydrophobic effect-driven cohesion of the F -chains of the two components likely led to the reconstitution of a pseudo-double-tailed amphiphile (some sort of a "molecular crutch" effect) and to tightening of the packing of the bilayer membrane (Scheme 9.1). Contrary to the F -vesicles formed by single-chain amphiphile **9.1** alone, which are highly stable and heat sterilizable in water²³¹ but not in a HEPES/NaCl buffer (a buffer commonly used when assessing colloids for drug delivery), the diblock-reinforced vesicles resisted destruction in the buffer. No significant change in average diameter and particle size distribution was seen after three months at 25 °C.³⁴⁶ This may indicate that incorporation of the diblock prevented the dehydration of the polar headgroup that commonly results from addition of electrolytes on bilayer membranes made of single-chain surfactants and is held responsible for their destruction.

9.1.1.3. Combinations of Phospholipids with $H_mF_nH_m$ Triblocks. Another strategy for building a fluorinated core within a liposomal membrane has consisted of admixing standard phospholipids with "reverse" $H_mF_nH_m$ triblocks, such as $C_mH_{2m+1}C_nF_{2n}C_mH_{2m+1}$ and $C_mH_{2m+1}-(CF_2)_2O(CF_2)_2C_mH_{2m+1}$. These triblocks were expected to function as "tie-bars" between the two leaflets of the phospholipid bilayer membrane (Scheme 9.1d). Combinations of such triblocks with distearoylphosphatidylcholine (DSPC) or egg yolk phospholipids (EYP) provided heat-sterilizable vesicles with diameters in the 60–90 nm range that were substantially more stable than those obtained with the phospholipids alone.¹⁴⁴

9.1.2. Structural Studies

Direct experimental evidence of the location of the diblock within the vesicle's bilayer membrane has been provided by cryo-TEM, high sensitivity micro-DSC, and SAXS data.³⁴³ Cryo-TEM demonstrated that a sonicated 1:1 molar codispersion of dioleoylphosphatidylcholine (DOPC) and $F6H10$ consisted of a homogeneous population of SUVs, ~30 nm in diameter, with no $F6H10$ emulsion droplets present. The bilayer of these SUVs appeared as a single, thick, and dark ring in the micrographs, as fluorine scatters electrons much more effectively than hydrogen (Figure 9.2). This aspect is very similar to that found for F -vesicles made from an F -alkylated phospholipid (e.g., **9.2**)³⁴⁷ and very different from the two thin concentric rings seen for DOPC-alone vesicles,³⁴⁸ establishing the presence of a fluorine core within the bilayer.

Micro-DSC experiments on DMPC/ $F6H10$ SUVs showed a broadening and a lowering of the DMPC main phase transition peak (Figure 9.3), indicating that the diblock had a disordering effect on the phospholipid bilayer, which

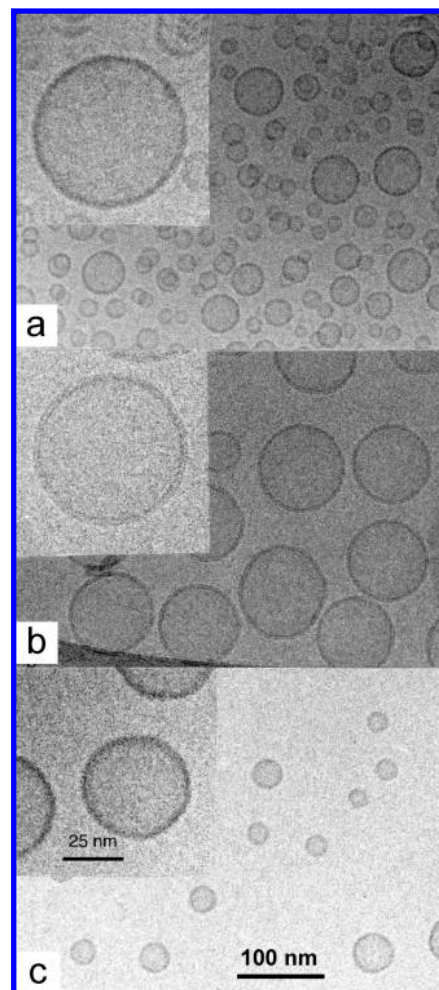


Figure 9.2. Cryo-TEM micrographs of vesicles made of (a) a DOPC/ $F6H10$ (1:1) combination, (b) DOPC alone, and (c) the F -phospholipid $F6H6$ -phosphatidylcholine (F -PC). Part a shows that the DOPC/ $F6H10$ sample is exclusively composed of SUVs, without occurrence of phospholipid-coated $F6H10$ emulsion droplets. The vesicles made of DOPC/ $F6H10$ (a) and those made of F -PC (c) show identical, thick, dark central rings due to the strongly electron scattering F -chains; the two narrower and less intense concentric rings typical of standard phospholipid bilayers seen in part b are not observed in the F -vesicles (a, c) because they are obscured by the much stronger central ring due to the F -chains. From ref 343.

implied its presence within that bilayer.³⁴³ Additionally, $F6H10$ was observed to undergo a gel-to-fluid transition at ~25 °C when incorporated in the bilayer, while it is liquid in the bulk at that temperature, providing further evidence for an organized F -film within the bilayer.

Finally, the SAXS experiments concurred with a hollow spherulike particle model (Scheme 9.2), comprising a ~3 nm thick central F -shell and indicated that the F -chains adopted an extended configuration and were not interdigitated. The above results all supported the formation of an organized core of diblocks within the bilayer membrane, as shown in Scheme 9.1a.

Investigation of large unilamellar vesicles made of EYP and the short $F6H2$ diblock, using fluorescence anisotropy and zeta-potential and light scattering measurements, also found that the diblock was incorporated inside the bilayer.³⁴⁹ Three different probes were used to locate the diblocks. The fatty chains within the bilayer showed lower viscosity than in the absence of diblock, indicating increased motion.

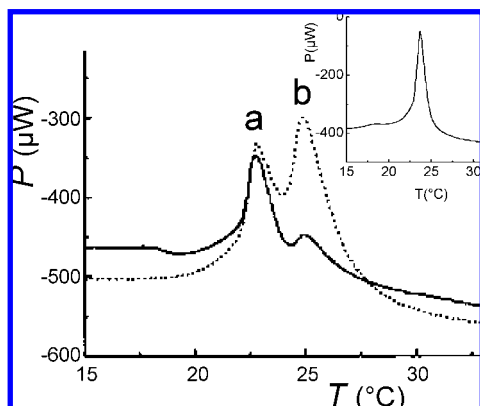
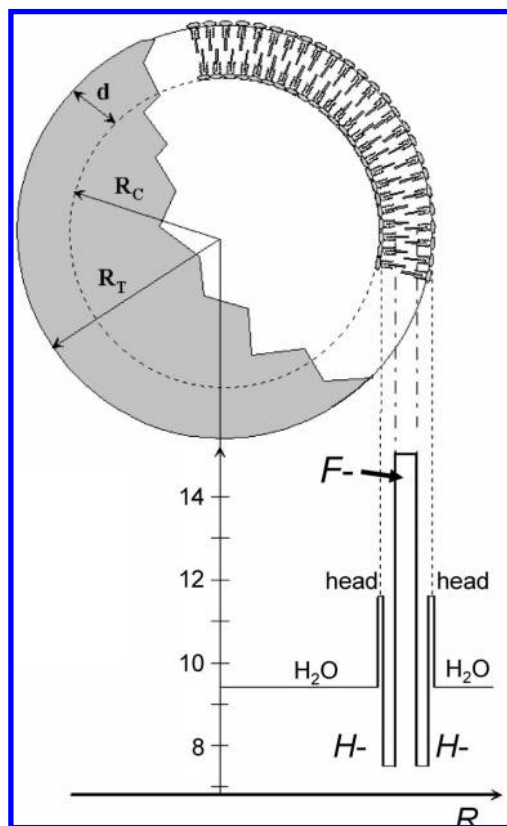


Figure 9.3. Micro-DSC heating curves (power P vs temperature T) of SUVs of DMPC/ $F6H10$ in 1:1 (solid line) and 1:3 (dashed line) molar ratio mixtures. Peak a originates from DMPC and is broadened and slightly shifted with respect to that of pure DMPC (inset); peak b is characteristic of a gel-to-fluid transition for $F6H10$. From ref 343.

Scheme 9.2. Concentric Shell Model for an F -Vesicle, along with Its Radial Scattering Density Profile, as Determined by SAXS^a



^a Each motif on the upper right side schematically depicts a phospholipid/diblock combination; F - and H - represent the F - and H -chain shell thicknesses; R_C is the particle core radius, R_T the overall radius, and d the total shell thickness. From ref 343.

9.1.3. Permeability–Encapsulation Stability

An important feature for effective liposomal drug delivery is the extent to which entrapped agents are retained within the liposome. Encapsulation stability depends on the characteristics of the membrane, on the encapsulated substance, and on the surrounding biological milieu. Endowing the liposomal membrane with the uniquely high hydrophobic and lipophobic characters of FC s was expected to reduce the

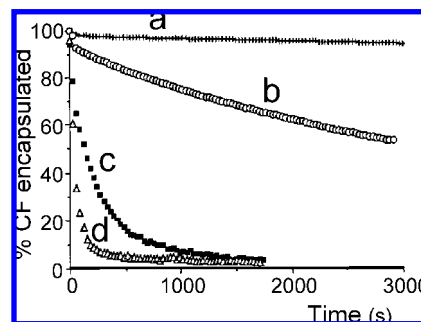


Figure 9.4. Incorporation of diblocks into a liposome's membrane can slow down release of entrapped material. Release of 5,6-carboxyfluorescein (CF) from vesicles composed of a 1:2 mixture of DMPC and $F4CH=CHH10$ (curves a and c) and from DMPC alone (curves b and d), in a HEPES/ Na_2SO_4 buffer (curves a and b) and in human serum (curves c and d). From ref 350.

solubility of encapsulated nonfluorinated material in and diffusion across the fluorinated core and, hence, to slow down its release. These features, which have been established for standard F -vesicles,^{9,48} have also been observed to some degree with F -vesicles comprising F_nH_m diblocks.

Incorporation of $F_nCH=CHH_m$ into DMPC liposomes has resulted in markedly decreased permeability of the liposomal membrane for 5,6-carboxyfluorescein (CF) and calcein (two classical fluorescent markers in permeation studies), both in a buffer and in human serum at 37 °C.³⁵⁰ Half-leakage times of CF from DMPC and $F4CH=CHH10$ /DMPC vesicles in HEPES buffer were 55 min and 15 h, respectively (Figure 9.4). Interestingly, the double bond of the diblock appeared to play some role: in its absence (i.e., with $F4H12$), the encapsulation half-life of CF was only 4.3 h.³⁴⁵ The same diffusion barrier effect was noted for adriamycin encapsulation: the decrease in permeability was significant for both $F6CH=CHH10$ and $F6H12$ incorporation but was larger in the former case. On the other hand, for the same H -chain length, the encapsulation half-time was, surprisingly, seen to decrease for $F_nCH=CHH10$ along the series $n = 4$ (15 h), $n = 6$ (207 min), and $n = 8$ (170 min),³⁴⁴ possibly reflecting increasing perturbation of the H -layers.

Human serum is known to strongly destabilize liposomes.³⁵¹ This was also true for diblock-reinforced liposomes. Nonetheless, the half-leakage time of CF was increased from 41 ± 7 s for DMPC alone to 141 ± 8 s for $F4CH=CHH10$ /DMPC liposomes (Figure 9.4).³⁴⁴ Likewise, the half-leakage times of calcein from DMPC and $F4CH=CHH10$ /DMPC liposomes in serum were 30 ± 4 s and 210 ± 30 s, respectively.³⁵⁰ Such encapsulation stabilization effects, although substantial, remain insufficient for practical purposes. Addition of diblocks to cholesterol-stabilized liposomes provided no further encapsulation stability.

In another series of experiments, the rate of Ca^{2+} -induced release in a buffer of CF from vesicles made of bovine brain phosphatidylserine (PS) and $F6H10$ was 40 times slower than when phospholipid was the sole vesicle component.³⁴²

Likewise, equimolar mixtures of the single-chain F -alkylated phosphocholine **9.1** and $F8H2$ yielded vesicles with substantially reduced membrane permeability to CF, as compared to those made of **9.1** only.³⁴⁶ From less than 1 min, the half-life of encapsulated CF went to ca. 2 h in a NaCl/HEPES buffer. The tightly packed highly hydrophobic F -chains were expected to reduce membrane permeability, which was born out experimentally. In human serum, the stability results were, however, disappointing.

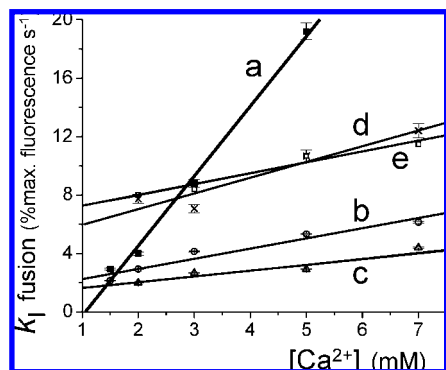


Figure 9.5. Initial rates (k_f , in % of maximum fluorescence s^{-1}) of Ca^{2+} -induced fusion of phosphatidylserine (PS) and PS/*FnH10* vesicles (monitored by the terbium citrate/sodium dipicolinate assay) as a function of Ca^{2+} concentration; the final lipid concentration was 100 μ M; (a) PS alone, (b) PS/*F4H10* (1:1), (c) PS/*F6H10* (1:1), (d) PS/*F8H10* (1:1), (e) PS/*F4H10* (1:2). From ref 342.

Vesicle membrane permeability with respect to CF release has also been strongly reduced by incorporation of certain *HmFnHm* triblock “tie-bars”.¹⁴⁴ For example, only 35% of the encapsulated CF was released from DSPC/*H12F2OF2H12* (1:1) vesicles suspended in PBS buffer, after 22 days at 37 °C, as compared to 60% for DSPC/cholesterol vesicles. Under the same conditions, 100% of the CF was released after only 2.5 days when DSPC was the sole membrane component. DSPC/*H14F8H14* (1:1) vesicles exhibited comparable permeability as DSPC/cholesterol vesicles. The capacity for some other tie-bars (*H5F2OF2H5*, *H6F6H8*, and *H16F6H16*) to stabilize DSPC vesicles against CF leakage was slightly lower, but these vesicles were significantly more stable against content release than those made of pure DSPC. In human serum, the efficacies of *H12F2OF2H12* and *H5F2OF2H5* in stabilizing DSPC vesicles were comparable but did not exceed that of cholesterol (~85% of the CF still encapsulated after 7 days at 37 °C). *H14F8H14* and *H10F8H10* were slightly less efficacious (~80% of CF still encapsulated). All the tie-bars investigated increased the probe retention time, as compared to vesicles made of DSPC only.

9.1.4. Vesicle Fusion

Incorporation of *FnH10* diblocks ($n = 4, 6, 8$) in vesicles made from bovine brain PS has resulted in much lesser tendency for these vesicles to undergo fusion or exchange components.³⁴² Thus, the initial rate of Ca^{2+} -induced fusion of PS/*F6H10* (1:1) *F*-vesicles, as monitored by the terbium/dipicolinic acid fluorescence assay in a buffer, was an order of magnitude slower than the rate for those made of PS alone (Figure 9.5). Also, contrary to the case of the PS-alone vesicles, this rate became almost independent from Ca^{2+} concentration when the diblock was present. A dual action was proposed for the diblock’s inhibitory effect that involved both the presence of a hydrophobic and lipophobic *F*-core within the bilayer membrane and an increase in the van der Waals interactions within the *HC* regions of the bilayer.

9.1.5. Behavior in Biological Media

The presence of a fluorinated core within its bilayer membrane can have surprising repercussions on a vesicle’s behavior in vivo or in a biological milieu.¹² Thus, introduction of appropriate *FnHm* diblocks into the membrane of DMPC or DPPC liposomes has resulted in a dramatic

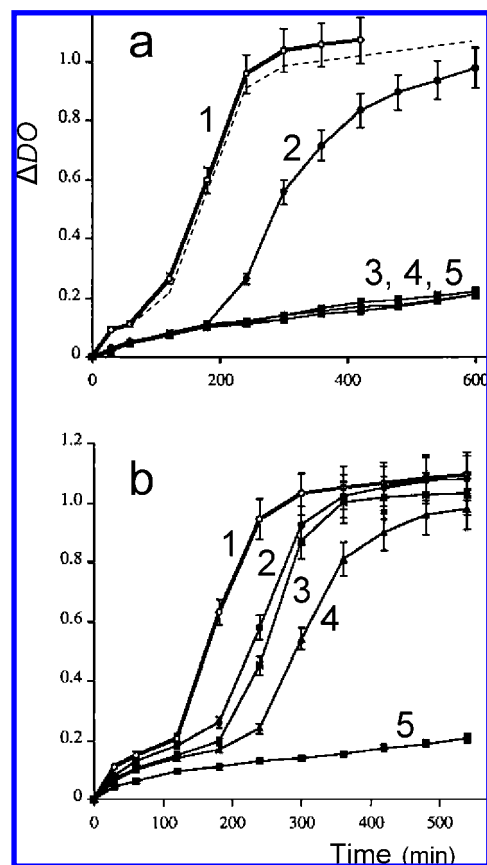


Figure 9.6. Hindering the enzymatic hydrolysis of phospholipids in liposomes by incorporation of *FnHm* diblocks into the bilayer membrane: Incorporation of *FnHm* diblocks (equimolar amounts) in (a) DMPC or (b) DPPC vesicles results in a drastic reduction of the rate of enzymatic hydrolysis of the phospholipids by porcine pancreatic phospholipase A_2 , as measured by monitoring the release of fatty acids using a pH indicator (absorbance, ΔDO at 595 nm) at 30 °C for (a) and 46 °C for (b). The effect depends very precisely on the relative length of the *H*-chain of the diblock and of the fatty chain of the phospholipid: (a) 1, DMPC alone; 2, DMPC + *F8H8*; 3, DMPC + *F6H10*; 4, DMPC + *F8H10*; and 5, DMPC + *F4H12*; (b) 1, DPPC alone; 2, DPPC + *F8H8*; 3, DPPC + *F8H10*; 4, DPPC + *F6H10*; and 5, DPPC + *F4H12*. The alkane $C_{16}H_{34}$ (same length as *F8H8*, *F6H10*, and *F4H12*), when added to DMPC, has no hydrolysis hindering effect (dotted line). From ref 352.

reduction of the rate of enzymatic hydrolysis of the phospholipid by porcine pancreatic phospholipase A_2 (Figure 9.6).³⁵² Quite remarkably, this effect was exquisitely sensitive to the relative lengths of the *Hm* segment of the diblock and of the phospholipid’s fatty acid chains. For a given fatty acid chain length, there was a precise minimal *H*-alkyl chain length in the *FnHm* diblock for this rate reduction effect to occur. The number of C atoms in the *H*-block needed to be at least 10 when the phospholipid was DMPC and 12 when it was DPPC, probably meaning that the *H*-segment needed to be inserted deep enough in between the fatty acid chains in order to hinder the approach of the enzyme near to the ester function. This effect was not observed in the absence of the *F*-chain (i.e., upon incorporation of $C_{10}H_{22}$ or $C_{16}H_{34}$), demonstrating a key role for the diblock in the structuration of the bilayer membrane. The parallel with the destabilization of *FC* emulsions induced by a mismatch between phospholipid chain length and diblock *H*-chain length (section 9.2) is striking.

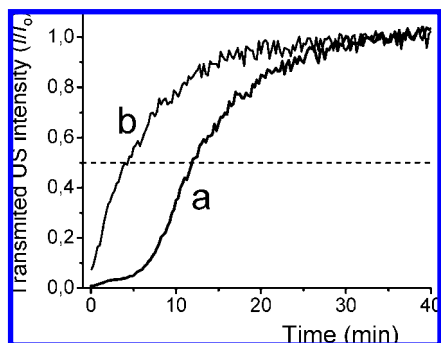


Figure 9.7. Variation over time of the ultrasound (US) intensity I transmitted through a suspension of microbubbles $14\ \mu\text{m}$ in diameter, at $25\ ^\circ\text{C}$ (I_0 being the US intensity measured in the absence of bubbles). (a) Incorporation of diblock $F6H10$ in gas bubbles with a DMPC shell results in significantly prolonged bubble persistence in the ultrasound beam (half-life 12 min) as compared with (b) bubbles similarly prepared, but without diblock (half-life 4 min). From ref 355.

9.2. Gas Bubble Dispersions and Foams

Injectable microbubbles are useful for ultrasound diagnostics and as ultrasound-triggered therapeutic agents.^{353,354} The lifetime and, hence, the efficacy of the presently commercialized FC -gas-stabilized ones is, however, still limited. Incorporation of diblock $F6H10$ in the DMPC wall of gas bubbles stabilized by F -hexane caused a delay in transmitted U.S. intensity increase, reflecting a significant prolonged persistence of an aqueous suspension of such bubbles in the ultrasound beam (Figure 9.7).³⁵⁵ Greatly enhanced stabilization of gas bubbles was subsequently obtained through a synergistic effect of an internal FC gas and an F -phospholipid shell.³⁵⁶

The aptitude for some star-shaped triblocks (two F -chains and one H -chain) to induce foaming when shaken in various HC solvents, including decane, dodecane, cyclohexane, and decalin and, to a lesser extent, toluene, has been noted, reflecting surface activity.¹¹⁶

9.3. Fluorocarbon-in-Water Emulsions

FC -in-water emulsions have received sustained attention owing to their potential for in vivo O_2 delivery (“blood substitutes”), diagnosis (contrast agents for ultrasound and MRI), molecular imaging, and drug delivery (section 10.2).

Key issues in the development of injectable FC -based O_2 -carriers include selection of a well defined, rapidly excretable FC and the formulation of a stable, small-sized, heat-sterilizable biocompatible emulsion.²¹⁰ The FC s most investigated as the O_2 -carrying dispersed phase were F -decalin and, subsequently, F -octyl bromide. Some development efforts have focused on α,ω -dichloro- F -octane. The triblock $F4CH=CHF4$ has also received some attention.^{130,357} Use of diblocks as the dispersed phase (e.g., $F8H2$, $F10H2$, $F8CH=CH_2$, $F6H8$, etc.) has been proposed.^{358–361}

Egg yolk phospholipids were the most commonly used emulsifier. Incorporation of F -alkyl/ H -alkyl diblocks in EYP has been found to provide a simple and highly effective means of stabilizing FC -in-water emulsions and of controlling their droplet sizes. The latter is essential because several important physical and biological properties of the emulsions, including oxygen diffusion, intravascular persistence, toxicity, and side effects, depend on droplet sizes and size distribution.

9.3.1. Stabilization and Particle Size Control

Achieving prolonged stability is essential for injectable FC emulsions to be practical. The primary mechanism of droplet size increase over time in such emulsions has been determined to be molecular diffusion (Ostwald ripening),^{362–365} including in concentrated FC emulsions.^{207,366–368} Molecular diffusion originates from the difference in chemical potential between differently sized droplets. The chemical potential and, hence, the solubility of the dispersed phase in the aqueous continuous medium depends on droplet curvature according to the Kelvin equation. Large droplets grow at the expense of smaller ones as a result of the higher solubility of the latter in water and consequent diffusion of individual FC molecules through the continuous aqueous phase. The process is thermodynamically favored, as it decreases the system’s interfacial energy by decreasing the interfacial area. The Lifshitz–Slezov theory,³⁶⁹ when applied to emulsions,³⁷⁰ predicts that droplet volume increases linearly over time according to eq 9.1:

$$\frac{d\bar{r}^3}{dt} = \omega = \frac{8VmC_{\infty}^{\text{eq}}D\gamma_i}{9RT}f(\varphi) = \frac{4}{9}\alpha DC_{\infty}^{\text{eq}}f(\varphi) \quad (9.1)$$

where ω is the Ostwald ripening rate (droplet volume growth rate), C_{∞}^{eq} the dimensionless solubility of the bulk dispersed FC in water, D the diffusion coefficient of the FC in the aqueous phase, γ_i the FC /water interfacial tension, $f(\varphi)$ a factor that introduces the effect of the volume fraction φ of the dispersed FC on ω , and α the capillary length.³⁷⁰

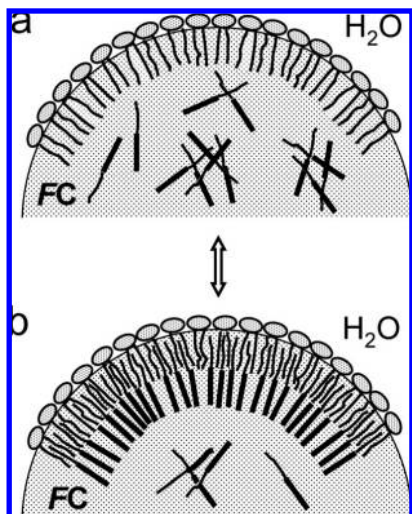
Indeed, FC droplet volume has consistently been observed to increase linearly with time, and growth rate has been observed to increase nearly proportionally with FC volume fraction. This was also the case for diblock-stabilized emulsions.^{191,207} Another characteristic of diffusion-controlled droplet growth is that the particle size distribution function is time-invariant. It should be noted, however, that eq 9.1 does not take into account the presence of the surfactant film, which can hinder diffusion of FC molecules and supposes that the two phases are isotropic, which may not necessarily be the case, especially in the vicinity of the interfacial film for a multicomponent FC phase or surfactant system.

FC emulsion stabilization can be gained in various ways. The most commonly used has consisted of adding a small amount of a higher molecular weight, less soluble, and less diffusible secondary FC that reduces C and D in eq 9.1.^{362,370,371} For example, addition of a small percentage of $\text{C}_{10}\text{F}_{21}\text{Br}$ was shown to effectively stabilize an emulsion of $\text{C}_8\text{F}_{17}\text{Br}$,³⁷² likewise for the addition of triblock $F6CH=CHF6$.³⁶⁷ Another way of stabilizing a FC -in-water emulsion is to reduce γ_i and, therefore, to use a more effective surfactant or surfactant system, for example a fluorinated surfactant.^{48,196,373}

F_nH_m diblocks were subsequently found to provide a convenient means of strongly stabilizing FC emulsions when used in conjunction with phospholipids as the emulsifier.^{341,374} It was hypothesized that at least part of the amphiphilic F_nH_m molecules would concentrate at the interface between the FC droplets and the phospholipid film that surrounds them. The H -blocks were expected to meddle with the phospholipids’ fatty chains, while the F -blocks would anchor themselves into the FC droplet (Scheme 9.3b). The diblocks would then behave as “molecular dowels” at this interface.

Highly stable concentrated emulsions of $\text{C}_8\text{F}_{17}\text{Br}$, diblock $F8H2$, and triblock $F4CH=CHF4$ have, for example, been

Scheme 9.3. The Two Likely Mechanisms for FC-in-Water Emulsion Stabilization by *FnHm* Diblocks Depend on the Localization of the Diblocks. (a) The Diblock Is Dispersed Randomly within the FC Droplets, Possibly Forming Micelles. (b) Due to Its Amphiphilic Character, the Diblock Collects Preferentially at the Interface between the FC Droplets and the Surfactant Monolayer (e.g., Phospholipids) That Coats Them. The *H*-Chain of the Diblock Would Then Meddle with the Fatty *H*-Chains of the Emulsifier while the *F*-Chains Would Extend in the FC Phase.^a



^a In case a, the diblock can contribute to stabilization only if less soluble and less diffusible in water than the dispersed FC. In case b, the diblock would primarily contribute to stabilization by acting as a cosurfactant of the phospholipid, reducing the interfacial tension γ_i between FC and water. Experimental evidence supports that a significant part of the diblock is located at the interface and expresses surfactant activity. Molecules and interface curvature not at scale.

obtained by using equimolar mixtures of *F8CH=CHH8* and EYP as the emulsifier. No significant particle size increase was seen over at least nine months of accelerated aging at 40 °C.^{341,374,375} A typical formulation and preparation procedure for an injectable diblock-stabilized emulsion will be given in section 10.2. It is noteworthy that use of diblocks also facilitated emulsification, as less energy was required to achieve small particle sizes. The evolution of the average particle sizes over time for identically formulated emulsions of *F*-octyl bromide with and without incorporation of *F6H10* or with the less soluble and less diffusible, but nonamphiphilic “heavy” *F*-alkane $C_{16}F_{34}$ is shown in Figure 9.8.³⁷⁶ It is remarkable that the droplets of the diblock-stabilized emulsion were still below 100 nm in average diameter after over 2 years of storage at 25 °C. Simple hand shaking sufficed then to resuspend the emulsion completely; no deposit was left in the vials.

Pluronic F68 (a polyethylene oxide–polypropylene oxide block copolymer)/diblock combinations have also been investigated, but proved much less effective. For example, the most stable *F*-decalin emulsions obtained with a Pluronic/*F10H2* combination lasted only about 80 days at 6 °C.³⁶⁰

Use of EYP/diblock combinations also allowed close control of emulsion droplet size over a remarkably wide range of diameters, from 0.12 to 16 μm poststerilization.³⁷⁷ An essentially linear correlation was found between the logarithm of average droplet diameter and the reciprocal of the logarithm of *F8CH=CHH8*/EYP (1:1) concentration (Figure 9.9). Heat-sterilizable, 90% w/v concentrated $C_8F_{17}\text{Br}$ /EYP/*F8CH=CHH8* emulsions with a large average droplet

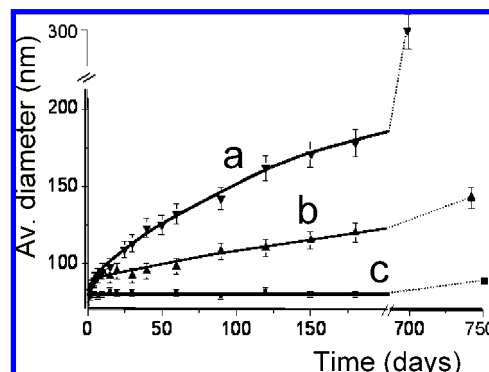


Figure 9.8. Average droplet size evolution over time at 25 °C in 60% w/v-concentrated *F*-octyl bromide/EYP (3% w/v) emulsions prepared with (a) EYP as the sole emulsifier; (b) equimolar amounts of EYP and the less soluble and less diffusible $C_{16}F_{34}$; and (c) an equimolar combination of EYP and the amphiphilic *F6H10* diblock; the two stabilizing additives have very close boiling points. It is remarkable that the droplets of emulsion c are still below 100 nm in diameter after 2 years at 25 °C. Emulsions b and c resuspend completely upon simple hand shaking, leaving no deposit in the vials.³⁸⁰

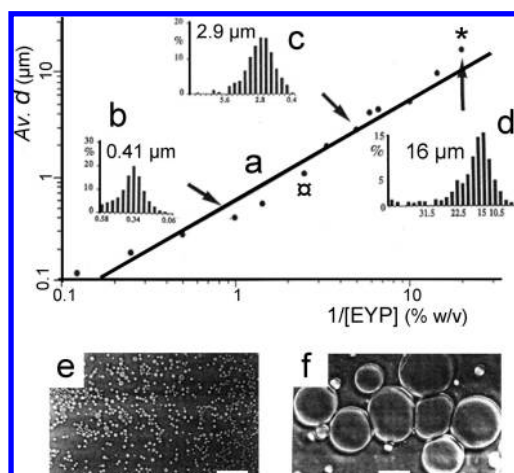


Figure 9.9. Control over particle sizes in a heat-sterilized 90% w/v *F*-octyl bromide emulsion using an equimolar combination of *F8CH=CHH8* diblock and EYP. (a) Particle sizes increase linearly with $1/[\text{EYP}]$ (% w/v) on the log–log chart; the particle size histograms (b, c, and d) were measured after 3 months of storage of the emulsions at 40 °C and reflect shelf stability, including for the largest droplet emulsions; the amounts of EYP/*F8CH=CHH8* (% w/v) in the emulsion, related to that of the FC, were 1.0/0.7% for image (b), 0.2/0.14% for image (c), and 0.05/0.036% for image (d); images (e) and (f) are phase contrast optical micrographs of emulsions obtained with 0.4% EYP/0.3% diblock (\odot , $\sim 1.12 \mu\text{m}$ avg) and 0.05% EYP/0.036% diblock (\ast , $16 \mu\text{m}$ avg), respectively; the bar represents 10 μm . From ref 377.

size of 16 μm have been obtained with as little as 0.05% w/v of EYP and 0.036% w/v of *F8CH=CHH8* (equimolar amounts). Yet, these emulsions showed essentially no increase in droplet size after 6 months at 40 °C.

Highly stable high internal phase ratio emulsions (HIPRE) have been prepared from a number of FCs and related compounds, including diblock *F8H2*, using a water-soluble *F*-surfactant (e.g., the *F*-alkylated amine oxide $C_7F_{15}C(O)NH(CH_2)_3N(O)(CH_3)_2$).³⁷⁸ These emulsions provided stable, heat-sterilizable, highly viscous, and elastic gels, in which the internal fluorine phase could exceed 99% v/v. Their structure consisted of micron-sized polyhedral domains (polyaphrons) of liquid FC or diblock, separated by a water-stabilized (hydrated) surfactant bilayer film.

9.3.2. Mechanism of Diblock-Induced Emulsion Stabilization

Two distinct mechanisms could, a priori, be invoked for the diblock-induced stabilization of *FC*/phospholipid emulsions against molecular diffusion (Scheme 9.3). The diblocks could either reduce the solubility C and diffusibility D of the dispersed phase in eq 9.1, as observed upon addition of a nonamphiphilic heavier *FC*,^{207,365,367,370,372} or they could act as a cosurfactant, along with the phospholipids, and reduce γ_i .^{379,380} An effect on the energy barrier to mass transfer across the interface could also be involved.³⁸¹

When *F*-octyl bromide (bp 143 °C, solubility in water: $\sim 5 \times 10^{-9}$ mol L⁻¹) was used as the main *FC* to be emulsified, the boiling point of the added diblock (e.g., *F6H10*, bp 243 °C) was higher than that of the *FC* used, and its solubility in water (estimated at 3.4×10^{-11} mol L⁻¹) was lower. Stabilization could then simply reflect a reduced rate of molecular diffusion consequent to lowered C and D of the *FC* phase in the aqueous phase. For this mechanism to operate, it suffices that the stabilizer molecule be dispersed randomly, as individual molecules or as micelles, within the bulk of the *FC* droplet, with no particular involvement at the interface (Scheme 9.3a). Deviation from Raoult's law of diblock/*FC* mixtures could further reduce the solubility of the fluorous phase in water.¹⁹⁷ Excess thermodynamic stabilization with respect to ideality increased with diblocks having a high F_n/H_m ratio and for lipophilic *FC*s, such as *F*-octyl bromide.

The second mechanism, which relies on a cosurfactant effect that would lower γ_i , implies a direct interaction of a certain proportion of the diblock molecules with the interfacial film (Scheme 9.3b). This would also increase the concentration of high MW component near the interface, thereby further amplifying the C and D reducing effect. Whether the added diblock induces such an interfacial effect or not has been a matter of debate.^{191,193,382}

A substantial body of experimental evidence has now been collected that supports a direct involvement of the diblock at the *FC*/water interface. Diblocks were found to be more effective emulsion stabilizers than a "heavy" *FC* additive of similar MW (hence, to a first approximation, of comparable water solubility), and a direct impact of their presence on the characteristics of the phospholipid film has been demonstrated.

A first notable observation is that stabilization of *FC*/EYP ($C_8F_{17}Br$, *F8H2*, *F4CH=CHF4*, *F*-decalin) emulsions upon addition of diblock *F6H10* attained maximum efficacy as soon as an equimolar diblock/phospholipids ratio was reached³⁶¹ (Figure 9.10), and this *independently* of the phospholipids/*FC* ratio. Effective stabilization could, for example, be achieved with molar fractions of EYP and *F8CH=CHH8* as low as 0.003 with respect to the *FC*, provided the *F8CH=CHH8*/EYP molar ratio was 1:1.³⁷⁷ In contrast, when nonamphiphilic stabilizing adducts with boiling points lower than that of $C_8F_{17}Br$ (e.g., $C_{10}F_{21}Br$, or $C_{16}F_{34}$, the latter having roughly the same boiling point (242 °C) as *F6H10* (243 °C)) were used, the stabilization effect increased more progressively with additive/*FC* ratio (Figure 9.10).

Figure 9.11 compares the average particle sizes measured after 6 months for emulsions prepared with decreasing amounts of EYP/*FC* ratios with or without an equimolar amount of stabilizing additive (*F6H10* or $C_{10}F_{21}Br$).³⁸³ The diblock continued to stabilize the emulsions even when

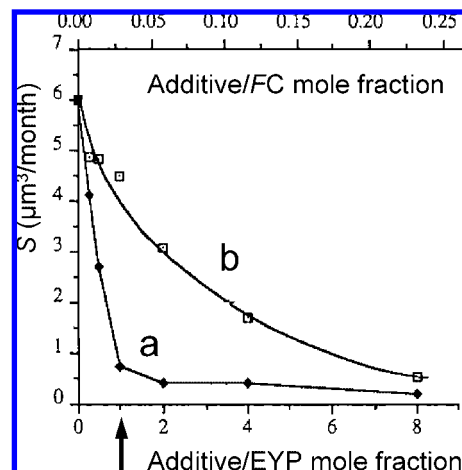


Figure 9.10. Stabilization S of 90% w/v *F*-octyl bromide/EYP emulsions (data after six months at 40 °C) by diblock *F6H10* (a) already reaches maximum efficacy for an *F6H10*/EYP molar ratio of about 1:1 (arrow), while stabilization by *F*-decyl bromide (b) is much more progressive and shows no break for any particular additive/EYP ratio.⁴⁷⁰

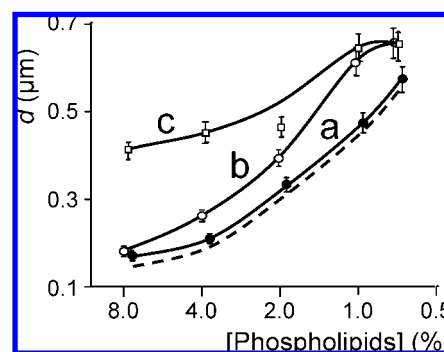


Figure 9.11. Average droplet sizes after six months at 40 °C in 90% w/v-concentrated emulsions of $C_8F_{17}Br$ stabilized by equimolar amounts of EYP and (a) diblock *F6H10* or (b) alkane $C_{16}H_{34}$, as compared to (c) EYP alone, for decreasing EYP/ $C_8F_{17}Br$ ratios; the dashed line represents the initial average droplet sizes of emulsions a, b, and c. The differences in variation profiles are significant (Krafft et al., unpublished).

present in very small amounts (provided that the diblock/EYP ratio remained close to 1), which was not the case for $C_{10}F_{21}Br$, indicating different stabilization mechanisms. Stable particles as large as 16 μm , poststerilization, could thus be prepared with 0.05% of EYP and 0.036% w/v of *F8CH=CHH8*, while EYP alone (0.2% w/v) allowed only reaching 3.4 μm .³⁷⁷ No stable emulsion could be obtained with 0.1 w/v of EYP, even after incorporation of the heavier *FC* $C_{10}F_{21}Br$. Furthermore, diblock-stabilized emulsions resisted better to heat sterilization than the reference emulsions. Thus, the particle size (0.12 μm) of an *F*-decalin/EYP/*F8CH=CHH8* (100/4.5/3.2% w/v) emulsion remained unchanged during sterilization (121 °C, 15 lb/in², 15 min), while the reference *F*-decalin/EYP (100/4.5% w/v) emulsion underwent a droplet size increase from 0.13 to 0.21 μm .³⁷⁴

Improved resistance to forced coalescence through shaking has also been noted for *F6H10*-stabilized emulsions, including for very large particle sizes, relative to those prepared with EYP alone or with an EYP/ $C_{10}F_{21}Br$ combination (Figure 9.12).³⁸⁴ These observations all point to distinct stabilization mechanisms by diblocks versus nonamphiphilic higher MW *FC*s.

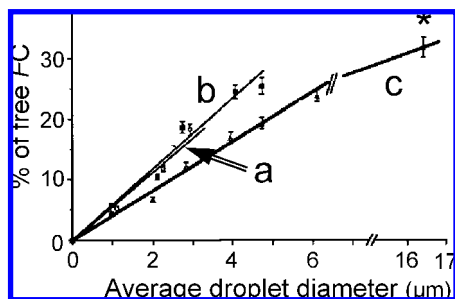


Figure 9.12. Incorporation of diblocks augments resistance of an *FC* emulsion (90% w/v $C_8F_{17}Br$ in water) to accelerated coalescence provoked by shaking (200 strokes/min, 30 mm amplitude, 45 min, room temperature), including for very large size emulsions that can only be obtained when diblocks are present, even in very small amounts (0.03% w/v in the largest size emulsion (*)). The amount of free *FC* released by shaking was measured after centrifugation as a function of particle size for three surfactant systems consisting of (a) EYP alone or equimolar amounts of (b) EYP/ $C_{10}F_{21}Br$ or (c) EYP/*F6H10*. From ref 384.

Definite evidence for a direct involvement of diblock molecules in the surfactant film that coats the *FC* droplets has been provided by the observation that the magnitude of the emulsion stabilization effect of a given diblock was exquisitely sensitive to the length of the lipid's fatty acid chains.¹⁹¹ Inadequate fit between diblock and phospholipid alkyl chain length could even lead to emulsion *destabilization*. Figure 9.13a depicts the variation of the average droplet volume as a function of time for $C_8F_{17}Br$ emulsions stabilized by DPPC alone or by equimolar amounts of DPPC/ $C_{10}F_{21}Br$ or of DPPC/*F8H16*. In all three cases, the linear variation of the droplet volume over time was characteristic of molecular diffusion-controlled particle growth. The time independence of the distribution functions was also established. Figure 9.13a shows that *F8H16* stabilized the emulsion more effectively against Ostwald ripening than $C_{10}F_{21}Br$, which is known to stabilize the emulsion by reducing *C* and *D*.³⁷² Similar behavior and results have been obtained when the phospholipid was DMPC or EYP. In these cases, the fatty acid chains of DMPC and DPPC are 14 and 16 C atom long, respectively, and hence comparable in length with the *H16* moiety of the diblock, probably resulting in the formation of a tightly organized mixed interfacial film.

A strikingly different situation was observed with the shorter phospholipids DLPC and PLC8 (Figure 9.13b,c). For these phospholipids, $C_{10}F_{21}Br$ still acted as a stabilizer, while incorporation of *F8H16*, in spite of its high MW, strongly *destabilized* the emulsions.¹⁹¹ Furthermore, the droplet volume increase over time was no longer linear and, hence, no longer determined solely by molecular diffusion. The exponential volume increase indicated that a coalescence-driven droplet coarsening mechanism was at play. This destabilization effect suggested a mismatch between the length of the diblock's *H*-chain and that of the phospholipid's fatty chains. The fact that stabilization, or destabilization, was conditioned by the adequacy between these two lengths implied the presence of diblock molecules at the interfacial film. By contrast, the stabilization effect of $C_{10}F_{21}Br$, which simply reduces the solubility of the *FC* phase in water, was insensitive to the phospholipid's chain length.¹⁹¹

Independent critical evidence for an interfacial tension reducing effect and, hence, for an involvement of the diblock at the interface includes the sharp decrease in γ_i (from about 24 to about 2 mN m^{-1}) between *F*-octyl bromide and an aqueous phospholipid solution, observed when a diblock was

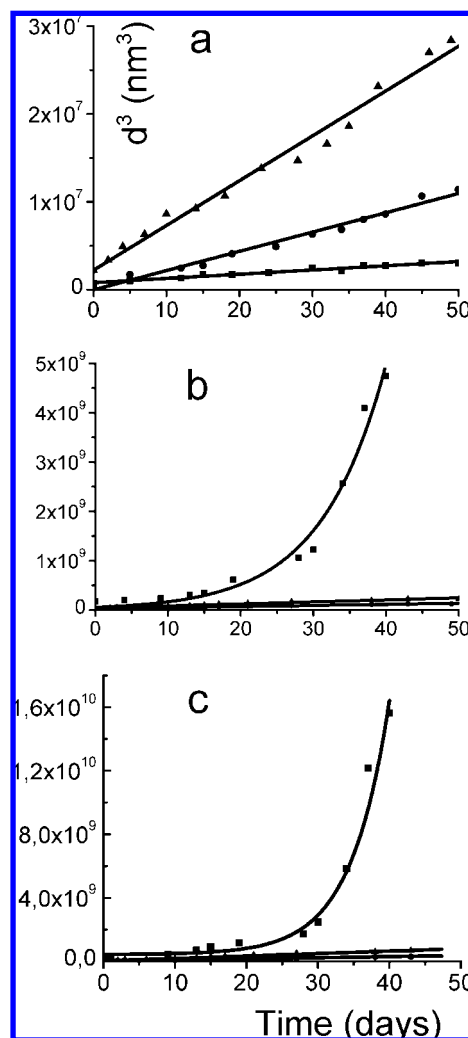


Figure 9.13. Stabilization or destabilization of an *F*-octyl bromide-in-water emulsion by incorporation of diblocks depends on a proper match between fatty chain length of phospholipids and *H*-block length of diblock. Variation of the cube of the average droplet diameter as a function of time at 40 °C; (a) the emulsions were prepared with DPPC alone (triangles), with an equimolar mixture of DPPC and $C_{10}F_{21}Br$ (circles), or with an equimolar mixture of DPPC and *F8H16* (squares); (b) *destabilization* by droplet coalescence observed for the emulsion prepared with the shorter-chain phospholipid DLPC (12 carbon fatty chains) upon incorporation of *F8H16* diblock (same meaning for symbols as above, but for DPPC being replaced by DLPC); (c) similar destabilization was observed when equimolar amounts of PLC8 (8 carbon fatty chains) and *F8H16* were used, while stabilization was again achieved with $C_{10}F_{21}Br$ (same meaning for symbols as above, but for DPPC being replaced by PLC8). From ref 191.

added to the *FC* phase (Figure 4.5).¹⁹¹ On the other hand, there was no break and no significant decrease of γ_i when $C_{10}F_{21}Br$ was added to the *FC* phase, confirming the absence, in this case, of significant cosurfactant activity. The capacity for *F_nH_m* diblocks to act as cosurfactants with phospholipids and reduce γ_i in eq 9.1 has thus been definitely established. Interestingly, the γ_i decrease curves (Figure 4.5) were very similar for all the phospholipids investigated. In particular, the slopes of all the curves were similar, meaning that the interfacial concentrations of diblock (calculated from these slopes to be $\sim 1.3 \pm 0.1$ molecules nm^{-2}) depended solely on diblock/EYP ratio and were essentially independent from phospholipid chain length. The molecular area occupied by

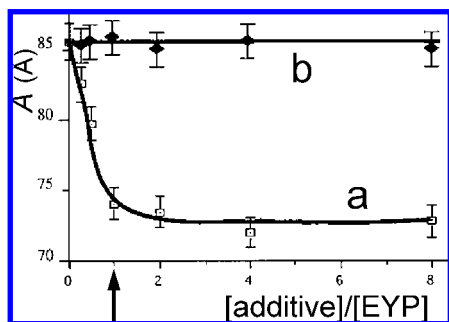


Figure 9.14. Effect of diblock incorporation on the absorption of phospholipids at the *FC*/water interface in *FC* emulsions. (a) Decrease (from $85.8 \pm 1.3 \text{ \AA}^2$ to $74.1 \pm 1.1 \text{ \AA}^2$ per molecule) of the surface area *A* occupied by EYP upon incorporation of *F6H10* in the formulation of a $\text{C}_8\text{F}_{17}\text{Br}/\text{EYP}$ (90/4% w/v) emulsion, as a function of *F6H10*/EYP ratio; the surface area reduction effect levels off as soon as the diblock/EYP molar ratio reaches 1:1 (arrow); (b) no effect on *A* is seen when the diblock is replaced by $\text{C}_{10}\text{F}_{21}\text{Br}$. From ref 471.

the diblocks at the interface was $0.8 \pm 0.2 \text{ nm}^2$, comparable to that occupied by phospholipids in emulsions ($0.7 \pm 0.2 \text{ nm}^2$).³⁸⁵

A clear deviation of experimental stability curves from those calculated for the reduction of Ostwald ripening rate expected from a nonsurface-active, higher MW stabilizing adduct has also been reported for diblock-stabilized *F*-decalin/Pluronic F68 emulsions.³⁶⁰ Interestingly, even *F8H2*, which is lighter than *F*-decalin, when incorporated in an *F*-decalin/Pluronic F68 emulsion, already showed a stabilization effect. Also noteworthy is that stabilization of such an emulsion was similar using *F10H2* and *F6H10*, in spite of differences of 88 mass units and of $\sim 80 \text{ }^\circ\text{C}$ in boiling points, which would not be expected if only *C* and *D* were involved.

Several other experiments support an interfacial role for diblock compounds in phospholipid-based *FC* emulsions. Thus, partition coefficient determinations for $F_n\text{CH}=\text{CH}H_m$ diblocks ($n = 6$ or 8 ; $m = 6, 8,$ or 10) between *FC*s (*F*-decane, *F*-octyl bromide, bis-1,2-(*F*-butyl)ethene) and hexadecane (intended to mimic the fatty chains of phospholipids) indicated no marked preference or phobicity for either phase, meaning that such diblocks could indeed bridge and improve the cohesiveness between the *FC* droplets and the surrounding corona of fatty chains of the phospholipid film.²⁰⁴ Incorporation of a diblock in a *FC*-in-water emulsion emulsified with EYP increased the amount of phospholipid molecules adsorbed on the *FC* droplets and caused a reduction of the area occupied by the phospholipids at the droplets' surface, providing evidence for tighter packing.¹⁹³ The polar head surface area for EYP thus decreased from $85.6 \pm 1.3 \text{ \AA}^2$ to $74.0 \pm 1.1 \text{ \AA}^2$ per molecule when *F6H10* was added to an *F*-octyl bromide/EYP emulsion, until the diblock/EYP ratio was around 1, after which it leveled off (Figure 9.14). No such effect was seen upon addition of *F*-decyl bromide.

Altogether, the array of experimental evidence discussed above consistently supports the conclusion that there exists, in the case of the diblock-induced *FC* emulsion stabilization effect, a substantial interfacial contribution. This contribution involves lowering of the *FC*/water interfacial tension and adds to the previously established contribution that arises from a lowering of the solubility and diffusibility of the dispersed phase in the continuous phase.

9.4. Other Emulsions

9.4.1. Microemulsions

Microemulsions (usually defined as thermodynamically stable self-emulsifying systems) of *F8H2* and $F8\text{CH}=\text{CH}_2$ (up to 50% by weight) have been obtained over a narrow composition domain using relatively large amounts of the nonionic *F*-surfactant $\text{C}_7\text{F}_{15}\text{CH}_2(\text{OC}_2\text{H}_4)_6\text{OH}$.²¹³ These microemulsions had particle sizes below 500 \AA , long-term stability, and very high O_2 solubility. SANS measurements on microemulsions of $F8\text{CH}=\text{CH}_2$ indicated a core of ~ 4300 diblock molecules surrounded by ~ 2000 surfactant molecules for a droplet size of $\sim 100 \text{ \AA}$. Further microemulsions of *F8H2*, $F6\text{CH}=\text{CH}_2$, $F8\text{CH}=\text{CH}_2$, and $F4\text{CH}=\text{CHF}_4$ were prepared using a mixture of fluorinated surfactants (e.g., $\text{C}_8\text{F}_{17}\text{SO}_3\text{Li}/\text{C}_7\text{F}_{15}\text{COOH}$) or a surfactant/cosurfactant system (e.g., $\text{C}_8\text{F}_{17}\text{C}_2\text{H}_4\text{SO}_3\text{H}/\text{C}_4\text{H}_9\text{OH}$).³⁸⁶

Viscoelastic transparent gels with very high water content have been produced from $F8\text{CH}=\text{CH}_2$ and $F4\text{CH}=\text{CHF}_4$ using a relatively hydrophobic nonionic *F*-surfactant ($\text{C}_6\text{F}_{13}\text{C}_2\text{H}_4\text{SC}_2\text{H}_4(\text{OC}_2\text{H}_4)_2\text{H}$).³⁸⁷ Structural investigation by SANS determined that these gels consisted of water-in-(water-in-oil microemulsion) emulsions.

Microemulsions with greatly improved O_2 solubilities have also been produced using the diblock $\text{C}_8\text{F}_{17}\text{CH}_2\text{CH}=\text{CHC}_4\text{H}_9$ as the dispersed phase, along with a pharmaceutical grade nonfluorinated nonionic sorbitan-derived surfactant (Montanox 80).^{214,359}

On the other hand, phase diagrams of the *F4H4*/ and *F8H16*/water/didodecyltrimethylammonium bromide ternary systems revealed no microemulsion domain.³⁸⁸ In the case of *F4H4*, some coarse and polydisperse, but stable, water-in-oil emulsions were obtained.

9.4.2. "Apolar" Hydrocarbon-in-Fluorocarbon Emulsions

Stable *HC*-in-*FC* emulsions (Scheme 9.4) have been obtained using F_nH_m diblocks as the sole emulsifier. *n*-Hexane (36% v/v) has, for example, been dispersed in *F*-octane, using *F8H16* (7.8% w/v) as the surfactant.³⁸⁹ Likewise, dodecane (3.6% v/v) has been dispersed in *F*-octyl bromide, using *F6H10* (0.03% v/v).

No evidence has been found for the formation of microemulsions when F_nH_m diblocks were incorporated in two-phase mixtures of *HC* and *FC* solvents (e.g., *F10H16* in a C_9F_{20} and $\text{C}_{16}\text{H}_{34}$ mixture).³⁹

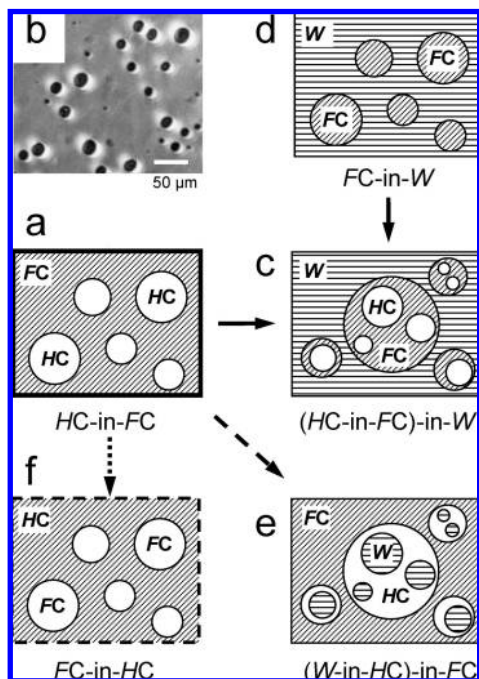
9.4.3. Reverse Emulsions and Multiple Emulsions

F8H2 has been used as the continuous phase of "reverse" water-in-*FC* emulsions, using an *F*-alkyldimorpholinophosphate surfactant ($\text{C}_n\text{F}_{2n+1}(\text{CH}_2)_m\text{OP}(\text{O})[\text{N}(\text{C}_2\text{H}_4)_2\text{O}]_2$) as the emulsifier.^{390,391} Highly stable, micron-size emulsions were obtained. In vitro release of an encapsulated probe, 5,6-carboxyfluorescein, was significantly slower than that from a water-in-*HC* emulsion. Such emulsions have potential for drug delivery through the pulmonary route. *HC*-in-*FC*-in-water and *HC*-in-water-in-*FC* multiple emulsions (Scheme 9.4) have also been produced.^{389,392}

10. Application Potential

The unique, multifaceted properties of molecular *F*-alkyl/alkyl diblocks and multiblocks entail a rich application potential. However, in these increasingly environmentally

Scheme 9.4. Stable Apolar HC-in-FC Emulsions (a) Can Be Obtained with an *FnHm* Diblock as the Sole Surfactant. (b) Phase Contrast Optical Micrograph of a 5% Water-in-*F8H2* Emulsion, Emulsified with *F8H2OP(O)₂[N(C₂H₄)₂O]₂*, after 10 Days at 25°C. Multiple HC-in-FC-in-Water (W) Emulsions (c) and Water-in-HC-in-FC Emulsions (e) Are Obtained by Re-emulsification According to Part d or a. Preparation of FC-in-HC Emulsions (f), Using a Diblock Surfactant, and HC-in-Water-in FC Emulsions Should Also Be Possible.



conscious times, a word is here in order about the potential impact of highly fluorinated materials on the environment. FCs and *FnHm* diblocks that do not contain heavier halogens have essentially no ozone-depleting potential but still participate in global warming. However, the greenhouse effect of the combined present emissions of FCs and hydrofluorocarbons (HFCs) is about 6 orders of magnitude less than that of CO₂ and can therefore be reasonably ignored.³⁹³ Nevertheless, it is clear that only low tonnage uses of FCs and highly fluorinated materials will be sustainable and only if the properties induced by these materials cannot be matched with more easily degradable materials. This is essentially the case of the products presently commercialized or under development, if only because of the relatively high cost of highly fluorinated material. There is a definite trend to avoid the nonindispensable use of *F*-surfactants, some of which (e.g., *F*-decanoic acid and *F*-octyl sulfonate) have been associated with side effects and bioaccumulation.

The biodegradability of *FnHm* diblocks is low and, as yet, still poorly documented, which could hinder the development of some of their possible applications. On the other hand, acceptance of molecular *FnHm* diblocks, when appropriate, could be much easier than acceptance of fluorosurfactants, in particular because of their biological inertness, which is close to that of the better documented FCs. In any case, according to the recent REACH regulations, companies will need (before June 2018 for annual volumes of 1–100 tons) to establish that use of any product is adequately controlled and that the socioeconomic benefit of its use outweighs potential risks.

Following the Montreal and Kyoto Protocols, some short chain hydrofluoroether diblocks, principally CF₃OCH₃ (also

known as HFE-143a), C₃F₇OCH₃ (HFE-7000), C₄F₉OCH₃ (HFE-7100), C₄F₉OC₂H₅ (HFE-7200), and C₇F₁₅OC₂H₅ (HFE-7500) have been developed as alternatives to chlorofluorocarbons (CFCs) and HFCs. These compounds have nearly zero ozone depletion potential, much shorter atmospheric lifetimes, and lower global warming potential. Their applications encompass use as heat transfer agents for refrigeration, blowing agents, cleaning agents for electronic devices and precision equipment, and carriers for lubricant deposition. The atmospheric chemistry and fate of these substitutes^{393–395} and of industrial FCs³⁹⁶ is being actively investigated.

10.1. Research Tools

Unsaturated and iodinated diblocks and multiblocks provide a range of starting materials or intermediates for building *F*-moieties with *H*-spacers (i.e., *FnHm*-moieties) into molecules, polymers, colloids, interfaces, and other constructs, for the purpose of introducing hyperhydrophobic (fluorophilic) sites, rigid segments, and smectogenic moieties into these molecules and structures. Many fluorinated surfactants and functional *F*-alkylated compounds comprise a diblock segment consisting of a terminal *F*-chain and a *HC* spacer with two or more carbon atoms. From a reactivity standpoint, the *H*-spacer located between the polar or functional head-group and the *F*-chain functions as an insulator against the electron-withdrawing character of the *F*-chain, while the latter fully displays its surface active and other specific properties. Likewise, telechelic monomers allow positioning of *F*-blocks within multiblock polymers and other constructs.

Iodinated or brominated diblocks are also instrumental building blocks for the engineering of complex supramolecular self-assemblies based on fluorophobic effects.

F-Chains play a fundamental role in fluorosynthesis and separation, where “ponytail” grafting on reagents and catalyzers is a major activity^{172,397–399} (one might, however, fancy that rigid rod *F*-chains evoke drumsticks rather than the supple and elegant movement of pony tails chasing flies). “Fluorous” essentially describes an affinity for FCs and highly fluorinated phases. To become “fluorous”, molecules need to be fitted with an adequate number of *F*-alkyl chains (or tags). Diblock iodides have, for example, been used to prepare triazacyclononane ligands.¹²¹ Iodinated diblocks and unsaturated diblocks (e.g., *F8H3*CH=CH₂) led to phosphane ligands with (*F*-alkyl)alkyl chains.¹²² In turn, these ligands allowed preparation of metal–phosphane complexes soluble in fluoros media. The *H*-block provided nearly complete insulation of the metallic center from the electron withdrawing influence of the *F*-chains. Likewise, the ligand properties of triblock dithioethers (*F8Hm*)₂S (*m* = 2 and 3) have allowed fitting multiple *F*-chains onto palladium complexes, providing precursors of active catalysts for fluoros media.¹⁴⁰ More broadly, (*F*-alkyl)alkyl iodides and bromides supply the fluoros tags needed for the effective synthesis and separation of libraries of compounds (see, for example, ref 400).

As adjuncts, diblocks can provide modulation and control over solubilities, solvent characteristics, surface properties, membrane viscosity and permeability, self-assembling ability, nanocompartmentation of self-assembled systems, etc.^{13,52,222} Thus, adjunction of *FnHm* diblocks to a FC allowed substantial modification of and control over the latter’s solvent properties.¹⁷⁷ Application to liquid–liquid separations of reaction products has been achieved by tuning the

fluorophilic character of the solvent, rather than that of the reagents.¹⁷⁸ *FnHm* diblocks can be instrumental for this purpose.

Specific diblocks have been identified that can fulfill specific purposes. For example, the branched diblock ether $C_2F_5C_2H_4OCH(CH_3)CH_2CH(CH_3)_2$, because it is miscible with a wide range of common solvents and partitions about equally between acetone and *F*-hexanes, was proposed as an effective, easily recyclable, high boiling amphiphilic solvent for fluorine/organic biphasic workup.^{117,401} A commercial mixture of *n*- and *i*- $C_4F_9OCH_3$ (HFE-7100) that is soluble in most organic solvents at room temperature, phase separates upon addition of small amounts of water (which greatly enhances the fluorophobicity of the organic phase).¹⁷⁸ Partition could also be modulated by adding these diblock ethers to *F*-hexanes (which increases the solubility of organic material in the fluorine phase). Partition coefficients of certain fluorine compounds between organic and fluorine phases could thus be changed by 3 orders of magnitude. $C_8F_{17}CH_2CH_2SCH_3$ has been identified as a convenient and recyclable BH_3 carrier, in the form of the solid $C_8F_{17}CH_2CH_2S(BH_3)CH_3$ adduct, for hydroboration in fluorine media.¹¹⁹

The engineering of supramolecular self-assemblies, colloids, and interfaces could benefit more widely from the “superhydrophobic” character, exceptionally strong gregarious instinct and organizing capacity of *F*-chains. The eminently dynamic and reversible character of their intermolecular interactions (solvophobic van der Waals) also qualifies *F*-components for participating in constitutional dynamic chemistry,⁴⁰² an emerging field where the potential of *F*-compounds remains to be explored.

Diblocks should offer unique, tunable environments, unknown to Nature that could help control or interfere with living material and processes.²²² *FnHm* diblocks and related *F*-compounds are highly effective in generating organized compartmented (cellular) molecular devices with controlled complexity (e.g., Scheme 9.1) It is noteworthy that high enzymatic activity (e.g., lipase-catalyzed alcoholysis) can be preserved and even enhanced in a fluorine medium.⁴⁰³

Dispersed micro- or nanosized fluorine compartments with properly tuned solvent characteristics can be devised in the form of micelles, emulsions, microemulsions, reverse emulsions, bubbles, and other compartmented self-assembled systems. These systems can provide new media for fluorine chemistry that could, for example, circumvent solubility issues encountered with fluorine-tagged reagents and catalysts. Diblocks can play a decisive role as continuous or dispersed phases, as stabilizers of membranes and films, and for tuning of surface properties, membrane viscosity, permeability, etc. *FnHm* diblocks (in particular *F8H2* and, to a lesser extent, *F6H2* and *F8CH=CH2*) and some essentially inert triblocks such as *FnCH=CHFn* (in particular *F4CH=CHF4*, also known as F-44E) have often been used as “fluorocarbons” or listed in series of *FCs* investigated in a study, in part because the *F*-chain largely outweighs the *H*-chain, thus enhancing the *FC* character of the diblock, and also because of easy availability. Such compounds have, for example, provided the continuous phase of *FC*-in-water emulsions¹³⁰ and microemulsions,^{213,386} reverse water-in-*FC* emulsions,³⁹⁰ and gels³⁷⁸ and have been investigated as lung surfactant replacement preparations.⁴⁰⁴ These systems can provide carriers, microreactors, templates, etc. The apolar *HC*-in-*FC* emulsions^{13,389,392} may, for example, help protect

water-sensitive reactants and products, and serve as isolated microreactors. Water-in-*FC* emulsions proved useful for physical studies of confined water molecules,⁴⁰⁵ a concept that could be applied to larger molecules. They should, for example, allow isolation and investigation of isolated single proteins.

10.2. Biomedical

The biomedical potential of fluorine materials has recently been reviewed.^{222,406,407} Semifluorinated alkanes with large *F*-chains share some of the attributes of *FCs*, including exceptional chemical and biological inertness. However, the *H*-chain can critically modify certain parameters. For example, because they are substantially more lipophilic than *FCs*, *FnHm* diblocks, when injected parenterally, are excreted much faster than *FCs* of similar molecular weight.²¹⁰

10.2.1. Biological Characteristics

In the absence of functional groups, *FnHm* diblocks are expected to be chemically and biologically rather inert. They also withstand high-shear emulsion processing and heat sterilization conditions. However, the *HC* moiety is susceptible to enzymatic attack under certain circumstances. Also, some very short diblocks that can be soluble in membranes may express specific pharmaceutical activity. Thus, as a borderline example, the short compound $CF_3CH_2OCH=CH_2$ (fluoroxene) was the first fluorinated anesthetic to be developed.

Generally, grafting of an *F*-chain to a molecule tended to reduce hemolytic activity and toxicity.^{408,409} There are, however, some notable exceptions to biological innocuousness. Short chain compounds with branched *F*-alkyl groups that could serve for diblock synthesis can display high inhalation toxicities. LD₅₀ values (1 h, in mice) of less than 100 ppm have been measured for $(CF_3)_3Cl$, $(CF_3)_2C=CFCF_5$, $C_2F_5(CF_3)_2Cl$, $C_3F_7(CF_3)_2Cl$, $C_3F_7(CF_3)_2CBr$, $C_3F_7(CF_3)_2CH$, and $C_3F_7(CF_3)C=CF_2$.¹⁰⁸ The toxicity of these compounds may be related to their increased susceptibility to nucleophilic attack.⁴¹⁰ It is reminiscent of that of *F*-isobutene $(CF_3)_2C=CF_2$, the most toxic *F*-compound known so far.

10.2.1.1. Biocompatibility. The data presently available on the toxicity of *FnHm* diblocks indicate a behavior close to that of *FCs* when the length of the *F*-chain is comparable to, or larger than, that of the *H*-chain. Acute toxicity in mice and rats was found to be very low. No hemolytic activity has been detected. No indication of metabolism has been reported.

Toxicological data for commercial *F*(alkyl)alkyl ethers (HFEs) show very low acute inhalation toxicity and no significant evidence for mutagenicity, carcinogenicity, reproductive/developmental, and other effects.³⁹⁵

Incubation for 4 days of various neat *FnCH=CHHm* triblocks with Namalva lymphoblastoid cell cultures did not affect the growth and viability of these cells (Table 7).^{84,341} Likewise, contact of HeLa-carcinoma cells with a series of *FnHm* diblocks ($n = 6, 8, 10$; $m = 2, 4, 6, 8, 10$) did not inhibit cell proliferation.³⁶⁰ No significant toxic effects were detected when cell cultures were contacted with purified diblocks (e.g., *F6H2*, *F8H8*, *F8CH2CH=CHCH2CH(CH3)2*) destined for ophthalmological uses.⁴¹¹ In these uses, lack of long-term biocompatibility can, however, originate from

Table 7. Effect of Diblock Compounds on Cell Cultures and on Mice Survival Following Intraperitoneal Administration

diblock	cell cultures ^{a,b} growth/viability (% vs controls)	i.p. injection in mice dose survival ratio (g kg ⁻¹ body weight) ³⁴¹	
<i>F6H2</i>	97 ^b		
<i>F6H6</i>	96 ^b		
<i>F6H10</i>	70/89 ^a	30	10/10
<i>F8H10</i>	81/81 ^a		
<i>F6CH=CHH8</i>		23	10/10
<i>F6CH=CHH10</i>	125/76 ^a	28	10/10
<i>F8H2</i>	96 ^b		
<i>F8CH=CHH6</i>		33	10/10
<i>F8CH=CHH8</i>	69/87 ^a	30	9/10
<i>F10H2</i>	100 ^b		

^a Namalva cells.⁸⁴ ^b HeLa cells.³⁶⁰

mechanical effects, possibly linked to density and surface activity. Specific tests are then performed on rabbit or pig eyes.²⁰³

No overt toxicity or effects on the survival and growth of mice have been noted after intraperitoneal injection of 30 g kg⁻¹ body weight (b.w.; protocol-allowed limit) of neat diblocks (Table 7).³⁴¹

Survival of mice administered intraperitoneally with 25 mL (~50 g) per kilo b.w. of the neat iodinated diblocks C_nF_{2n+1}CH=CIC₆H₁₃ (*n* = 6, 8) and triblocks C_nF_{2n+1}CH=CIC_nF_{2n'+1} (*n* = 2, 4, 6, 8; *n'* = 4, 6, 8) was 10 out of 10.^{123,124} This figure dropped to 2/10 with C₈F₁₇CI=CH₂ (5 mL kg⁻¹ b.w.), in which the iodine atom is more exposed. Emulsions of the radiopaque iodinated diblock C₆F₁₃CH=CIC₆H₁₃ were tolerated at an intravenous dose of 8 g kg⁻¹ b.w. of the diblock iodide in rats (survival 10/10).⁴¹² This dose was 15 times larger than that required for effective contrast enhancement. Histological examinations and blood analysis demonstrated normal functioning of the liver, even at such high doses of diblock.

Emulsions of *F*-octyl bromide stabilized with the *F6H10* diblock were evaluated for their effects on cultured human endothelial cells, the first cells to come in contact with the emulsion when organs are perfused with them.⁴¹³ The objective was to achieve room temperature or body temperature organ perfusion with an O₂-carrying emulsion in order to prevent damage related to reoxygenation of preserved organs after hypothermic hypoxia. The diblock-stabilized emulsions were not affected by dilution with the cell culture media or organ preservation fluids. The cells grew and multiplied normally, and their morphology was unaffected, indicating absence of toxicity. Prolonged contact of the emulsion with rat small bowel grafts showed no deleterious effects either.⁴¹⁴ The histological score was actually better than that after preservation with a standard commercial preservation medium.

A huge dose (52 mL kg⁻¹ b.w., limit allowed by the protocol) of the 90% concentrated, diblock (1.4% w/v)-stabilized emulsion described below in Table 8 has been injected intravenously to mice as a tolerance test.³⁴¹ This dose was well tolerated, and all the animals survived the one month observation period.

The same emulsion was tested in a close-to-total isovolemic exchange-perfusion experiment in rats (over 90% of the blood replaced by the emulsion).³⁴¹ For this purpose, the emulsion was diluted to 50% w/v with a solution of albumin and salts, allowing adjustment of oncotic pressure. The O₂-breathing rats were conscious and unrestricted during the exchange perfusion and showed no sign of stress or concern

while the red blood cell content (hematocrit, vol %) of their "blood" went from ca. 44% down to 3–4%. Under these extreme conditions, the survival ratio after 10 days was 73% (*n* = 15), while none of the control animals receiving an albumin and salt solution survived. These experiments demonstrated both *in vivo* tolerance and O₂ delivery efficacy.

10.2.1.2. Distribution, Metabolism, and Excretion. Studies of the adsorption, distribution, metabolism, and excretion of *F_nH_m* diblocks are still limited. The short diblock *F2H4* was submitted to *in vitro* incubation with rat liver microsomal preparations.⁴¹⁵ These preparations contained at least three oxygenases active in the metabolism of saturated aliphatic *H*Cs. Only one metabolite was detected by GC in the case of the diblock, and it was shown by mass spectrometry to be the 5-hydroxy derivative C₂F₅CH₂CH₂CH(OH)CH₃. When compared to microsomal hydroxylation of *n*-hexane, the C₂F₅ group was seen to completely inhibit hydroxylation at positions 3 and 4. There was no indication of modification of the *F*-moiety.

Excretion rate, after intravenous (i.v.) administration of diblocks in the form of emulsions to rats, depends on molecular weight, fluorophilic/lipophilic balance, and dose. The rate-determining step in the elimination of *FC*s has indeed been determined to be their dissolution into lipid carriers (lipoproteins, chylomicrons) in the blood.⁴¹⁶ *In vivo* studies investigated more particularly the biodistribution and excretion of *F6CH=CHH10* (MW = 486).^{341,417} The diblock was therefore formulated as a 25% (w/v) heat-sterilized, injectable emulsion prepared with EYP. This emulsion was administered parenterally at the massive dose of 14.4 mL kg⁻¹ b.w. (3.6 g kg⁻¹ b.w. of diblock) through the jugular vein of anesthetized female rats. The treated rats behaved normally, and none of the 33 animals treated died prior to the programmed sacrifice date. The diblock present in the blood, liver, spleen, kidneys, or lungs was quantified by ¹⁹F NMR after 2, 4, 8, 24, and 48 h; 4, 10, 15, and 21 days; 1, 2.5, 3, and 4 months. For this 3.6 g kg⁻¹ b.w. dose, the diblock distribution, one day after injection, was 70% in the liver, 20% in the spleen, 4% in the lungs, 2% in the kidneys, and 2% in the blood. The variation of these concentrations over time is shown in Figure 10.1. The maximum concentration in the liver and spleen, the main organs of the reticuloendothelial system, in charge of clearing the blood from foreign particles, was reached after 1 and 7 days, respectively. The half-life of *F6CH=CHH10* in the liver was 25 ± 5 days. Altogether, the diblock's organ retention half-life was significantly shorter than that for a nonlipophilic *FC* of comparable MW. The injected diblock was the only fluorinated compound detected in all the spectra recorded, even after having resided for four months in liver tissue, indicating that metabolism was either absent or at a very low level, beneath detection by high resolution ¹⁹F NMR (<10⁻⁴ M, i.e. 0.02% of the injected dose). The dose administered in these studies was about 2 orders of magnitude larger than the amount of diblock required to effectively stabilize a clinically relevant dose of i.v.-administered *F*-octyl bromide emulsion.

In the series of *F_nCH=CHF_{n'}* triblocks, the organ retention half-lives, *T*_{1/2} (days), increased exponentially with MW, as expected from increasing lipophobia (*n* = *n'* = 4: 7 days; *n* = *iso*-3, *n'* = 6: 23 days; *n* = 4, *n'* = 6: 43 days; *n* = *n'* = 6: >600 days).^{130,132} As for the diblocks, the largest load of fluorinated material was found in the liver, the second largest in the spleen, and the longest lasting in the adipose

Table 8. Formulation of a Typical Diblock-Stabilized Injectable FC Emulsion for in Vivo Oxygen Delivery (Avg Particle Size Poststerilization = 250 nm ± 12, pH = 6.8, Osmolarity = 288 mOsm, Viscosity = 15 cP)³⁴¹

ingredient	amount	function
<i>F</i> -octyl bromide	90 g (47 mL)	O ₂ carrier
EYP	2.0 g	emulsifier
<i>F6H10</i> (equimolar to EYP)	1.4 g	stabilizer diblock
NaH ₂ PO ₄ ·H ₂ O	0.052 g	
Na ₂ HPO ₄ ·7H ₂ O	0.355 g	
NaCl	0.25 g	buffered, osmotically adjusted aqueous phase
water for injection	q.s.ad 100 mL	

tissues. In view of their acceptable excretion rates and large tonnage feasibility in highly pure form, *F4CH=CHF4* (F-44E) and *iso-F3CH=CHF6* (F-136E) have been recommended for parenteral emulsion preparation, and *F6CH=CHF6* for tissue and organ preservation.^{418,419}

10.2.2. Oxygen Carriers

The topic of injectable oxygen delivery systems (“blood substitutes”) has been extensively reviewed.^{210,357,420,421} Reasons for developing injectable O₂-carriers include insufficient blood collection to meet the augmenting needs of an aging population; a reluctance in certain countries and cultures against allogeneic (donor blood) transfusion; the realization that banked blood becomes rapidly less effective than fresh blood as a result of consequential biochemical changes (so-called “storage lesions”),^{422,423} the risks carried by blood transfusion, for example of transfusion-associated acute lung injury;⁴²⁴ evidence that donor blood may reduce the immune responsiveness of the organism;⁴²⁵ and the possibility of providing the developing countries with an alternative to blood transfusion. The transfusion of “older” blood units (stored for more than 14 days, the FDA-allowed storage time for packed red blood cells being 45 days) has been associated with significantly increased risk of postoperative complications, as well as reduced survival for surgical cardiac patients.^{426–428}

The present aim has shifted for a large part from “blood substitutes” to “oxygen therapeutics”, for example, the correction of hemodynamic instability consequent to surgery in order to prevent organ ischemia; reduction of gaseous microembolism frequently observed during cardiopulmonary bypass surgery; treatment of sickle-cell crisis; resuscitation from hemorrhagic shock; or preservation of tissues and

organs destined for transplantation.²¹⁰ Use of a synthetic O₂ carrier rather than blood in surgery remains nevertheless an important goal. Only some recent papers dealing with diblock-containing FC emulsions will be considered here.

The *F_nH_m*-stabilized and particle size-controlled FC emulsions described in section 9.3 may provide the basis for a future generation of FC-based O₂ carriers. *F*-octyl bromide was usually chosen as the FC because of a favorable combination of excretion rate, emulsion stability, O₂ solubility, and industrial feasibility.²¹⁰ Several *F*-decalin/diblock formulations have also been investigated, but with Pluronic as the emulsifier, resulting in lesser stability.³⁶⁰

A typical formulation of a diblock-stabilized injectable emulsion is given in Table 8. The *F*-octyl bromide concentration chosen (90% w/v or 60% w/v) reflects optimization of balance between O₂ transport efficacy, fluidity, stability, and user convenience.⁴²⁹ The high 90% w/v concentration was often selected for research emulsions, as it allows flexibility in terms of addition of electrolytes, oncotic agent, nutrients, etc., prior to administration. EYP was used because it is a well documented, effective emulsifier, well accepted in pharmaceuticals. As indicated earlier, formulation optimization studies found that maximum emulsion stabilization was attained when the diblock and EYP were in equimolar proportions. The EYP was first dispersed in the buffered aqueous phase, the diblock was then added, and the mixture was further codispersed with a low energy device. Dropwise addition of the FC was achieved using first a rotor/stator low energy mixer. The final stage of emulsification required a high-pressure homogenizing procedure, such as microfluidization, in order to achieve the small droplet size and narrow size distribution needed for parenteral use.^{207,430} Oxygen exclusion during processing and sterilization minimized EYP oxidation. Heat sterilization was performed under standard conditions (121 °C, 1 atm, 15 min). When equilibrated with O₂ under atmospheric pressure, the emulsion of Table 8 dissolved ~25 vol % of O₂, while water dissolved ~2.3 vol % of O₂ under the same conditions.

Normovolemic aerobic preservation of “multiple organ blocks” from rats was significantly improved when such a 90% w/v-concentrated emulsion (supplemented with albumin and electrolytes and diluted to 36% w/v FC) was used, as compared to a standard, nonoxygen carrying preservation solution (albumin-supplemented Krebs solution).⁴³¹ Lactate, amylase, and creatine kinase levels were lower, indicating lesser suffering of the organs. PaO₂ was significantly higher, allowing full aerobic metabolism to be maintained. Diuresis was also higher, evidencing better organ preservation. One should note that blood cannot be used for this purpose because of rapid hemolysis. Use of the diblock-stabilized emulsion also allowed improved long-term hypothermic (4 °C, 48 h) preservation of rat small bowel grafts.⁴¹⁴

A diblock-stabilized FC emulsion has been investigated for preservation of β-cell lines (mouse insulinoma-6 line)

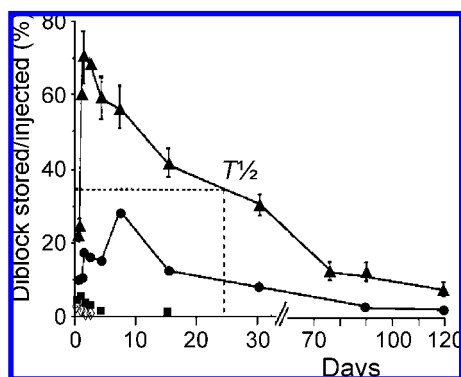


Figure 10.1. Organ distribution over time after administration of diblock *F6CH=CHH10* in rats (3.6 g kg⁻¹ b.w. dose) in the form of a phospholipid-stabilized emulsion (25% w/v of diblock; average droplet diameter 0.22 μm after heat sterilization). Percent of the total injected diblock dose (each point is the average of 3 animals) found in (▲) liver (half-life $T_{1/2}$ = 25 ± 5 days), (●) spleen, (■) lungs, and (◇) kidneys. From ref 417.

and Langerhans islets from pig pancreas destined for treatment of type 1 diabetes.⁴³² The O₂ carrying capacity of the *FC* emulsion led to prolonged, improved islet preservation. Additionally, the study discovered an unexpected antiadhesion phenomenon: the *FC* emulsion prevented adhesion of the β -cells onto tissue culture plastic and induced their aggregation into well formed pseudoislets. Contrary to the adhering cells, the pseudoislets produced insulin under glucose stimulation, thus demonstrating a beneficial effect on cell functionality. The emulsion also proved capable of inducing the detachment of already adhering cells. The detachment effect was more pronounced for the diblock-containing emulsions and varied with diblock structure.

Further in vivo experimentation of emulsions of the type described in Table 8 has included, for example, improved tissue oxygenation in a rabbit model of resuscitation from acute hemorrhagic shock.⁴³³

Use of a diblock-stabilized emulsion allowed dramatic improvement of in vivo two-photon microscopy imaging of the brain of rats after near-total (5% hematocrit) substitution of their blood by the emulsion.⁴³⁴ Subcellular resolution was achieved, including in areas usually obscured by blood vessels. Replacement of the blood by the emulsion circumvented the limitation due to the strong absorption of light by hemoglobin and strong scattering by red blood cells, which both considerably reduce image quality.

Emulsions using solely diblocks as the dispersed phase have also been investigated. Emulsions of *F6H10* and *F10H2* were more stable than those obtained with *F*-decalin, even when the latter was stabilized by adjunction of diblocks.³⁶⁰ However, Pluronic F68 was used as the emulsifier and stability was considerably less than that for emulsions of *F*-octyl bromide with phospholipids as the emulsifier. The slightly lipophilic *F8H2*, in many respects similar to *F*-octyl bromide, is also a prime candidate for O₂ delivery formulations. Preliminary biocompatibility data have been obtained on microemulsions of C₈F₁₇CH₂CH=CHC₄H₉.⁴³⁵

Finally, the neat (nonemulsified) oxygenated diblock *F6H8* has been used for storage by incubation of rat pancreas prior to islets isolation and was found superior to *F*-decalin.⁴³⁶

10.2.3. Ophthalmologic Uses

Use of *FC* gases (e.g., *F*-ethane, *F*-propane, and sulfur hexafluoride) and liquids (e.g., *F*-octane, *F*-decalin) has become part of standard procedures in vitreoretinal surgery, such as for intraoperative manipulation (e.g., unfolding) of the detached retina, as tamponade agents to hold the retina in position, and to achieve reattachment of the retina.^{203,411,437–439} However, neat liquid *FC*s, when used for long-term vitreous tamponade, can cause damage to the retina, which was assigned to excessive specific gravity.^{438,440} Extensive emulsification within the eye has also been observed, hence the evaluation of the less dense *F_nH_m* diblocks.^{201,441} In a multicenter clinical study, *F6H8* (specific gravity 1.35 g cm⁻³) was reportedly effective for the management of complicated retinal detachments and no obvious signs of side effects were seen after several months of internal tamponade.⁴⁴¹ However, some emulsification was still reported, as well as other adverse reactions, resulting in poor long-term tolerance.^{442–444} Use of *F6H2* also led to emulsification, as well as inflammatory reactions.⁴⁴⁵ Whether specific gravity was the reason for retinal degeneration in long-term tamponade with *F6H8* has been questioned.^{446,447} There was no evidence that higher density led to more pronounced side

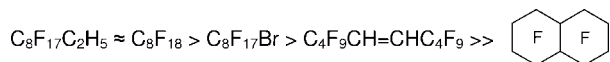
effects in the series *F4H4*, *F6H2*, *F*-octane, and *F*-decalin (densities of 1.24, 1.62, 1.78, and 1.92, respectively).⁴¹¹ Liquid diblocks have also been used as intraocular washes to remove residual silicone oil from intraocular silicon lenses or after silicone oil tamponade,^{200,201} although their efficacy has been questioned,⁴⁴⁸ and for the flotation and removal of dislocated intraocular lens components. A series of semifluorinated symmetrical diethers, CF₃CH₂O(CH₂)_{3–10}OCH₂CF₃, provided material that had a chemical inertness, O₂ solubility, and transparency close to those of *FC*s, but with substantially lower and adjustable specific gravity (1.06–1.23 g cm⁻³);¹³⁷ the biocompatibility results were, however, disappointing.

Subsequently, mixtures of *F_nH_m* diblocks and polydimethylsiloxane oils (so-called heavy silicon oils) were developed in order to mitigate the side effects observed with either a silicon oil or a diblock alone. The lower-than-water density of silicon oils, which causes them to float atop of vitreous fluids, was remedied by admixing an inert higher density compound. The advantage of diblocks over *FC*s in this respect is their much larger solubility in silicon oils. Clinical studies of an admixture of C₈F₁₇CH₂CH=CHCH₂CH(CH₃)₂ and a silicone oil, with a compounded density of 1.03 g cm⁻³ and a viscosity of 3700 cSt (Oxane Hd), on patients suffering from complicated retinal detachment, concluded that the product was safe and effective as a long-term tamponade agent,^{203,449,450} while another study still found inflammatory responses.⁴⁵¹ Another preparation consists of an admixture of *F6H8* and polydimethylsiloxane 5000 with a specific gravity of 1.06 g cm⁻³ and a viscosity of ~1400 mPa s (Densiron 68).²⁰² It allowed successful long-term tamponade in pilot studies on patients with complex retinal detachment and showed a promising surgical outcome with minimal side effects.⁴⁵² Multicentered trials are now underway to compare this product with standard silicon oil. Diblock *F4H5*, which is more easily dissolved in silicon oils than *F6H8*, also appeared promising for the preparation of “heavy” silicone oils.⁴⁵³ Comparison with *F4H6* and *F4H8* indicated that tolerance may depend on lipophilic character.

10.2.4. Lung Surfactant Replacement Preparations

DPPC is the main component of the native lung surfactant, which plays a vital role in respiration. However, DPPC alone is inadequate as a lung surfactant replacement because it tends to form rigid monolayers upon compression (i.e., during expiration) that contain semicrystalline domains (Figure 10.2a). Such crystallization opposes effective respreading of the phospholipids on the alveolar surface upon inspiration. *FC* gases were found to produce a highly effective fluidizing effect on a Langmuir monolayer of DPPC and prevented the undesirable formation of the semicrystalline phase during compression (mimicking the expiration phase of the respiratory cycle). The *F8H2* diblock was among the most effective compounds in this respect (section 8.2).^{333,334,404} Near zero surface tensions have been achieved for DPPC monolayer contacted with N₂ saturated with *F8H2*. The *F4CH=CHF4* triblock also proved effective. Moreover, these compounds were shown to dissolve the liquid-condensed domains of DPPC that were already formed and helped respread the DPPC molecules at the air/water interface. Figure 10.2 shows complete disappearance of the semicrystalline LC domains of DPPC only 5 min after the monolayer had been exposed to *F8H2*-saturated nitrogen. The monolayer was then totally fluid. The *FC*s investigated were ranked according to the

rate at which they achieved suppression of semicrystalline domains, providing the following efficacy scale:



Only *F*-decalin could not achieve complete dissolution of the domains even after more than 1 h at room temperature and in spite of its slightly higher vapor pressure (13.5 Torr at 37 °C) as compared to *F8H2* and $\text{C}_8\text{F}_{17}\text{Br}$ (11.5 and 10.5 Torr at 37 °C, respectively). *F*-octane was deemed too volatile for convenient use (v.p. of 52–64 Torr at 37 °C). *F8H2* and $\text{C}_8\text{F}_{17}\text{Br}$ share together the presence of a lipophilic extremity that attenuates the overall lipophobicity of *FC*s. *F*-decalin displays the most pronounced lipophobic character within the series, as expressed by a critical solution temperature in hexane that is about 40 °C higher than those for *F8H2* and $\text{C}_8\text{F}_{17}\text{Br}$.²⁰⁷ Also noteworthy is that both *F8H2* and $\text{C}_8\text{F}_{17}\text{Br}$ have positive spreading coefficients, meaning that they spread spontaneously when deposited on water, while the spreading coefficient of *F*-decalin is negative.²¹⁰ *F*-decalin may also be hampered by its bicyclic, somewhat globular shape that does not facilitate insertion into a phospholipids monolayer. The above-discussed features, along with a vapor pressure around 10 Torr at 37 °C, appear to constitute practical criteria for the selection of *FC*s destined to serve in lung surfactant replacement compositions.³³⁴

Experimentation on premature rabbits with $\text{C}_8\text{F}_{17}\text{Br}/\text{F6H10}/\text{EYP}$ emulsions demonstrated a significant increase in alveolar tidal volume (from 20 to 140 μL within 50 min) for the treated animals.⁴⁵⁴ The diblock-containing emulsions were significantly superior to reference emulsions that did not contain the diblock. The presently used lung surfactant

substitutes consist of fractions of bovine or porcine lung surfactant. Use of synthetic *DPPC/FnHm* diblock compositions may thus represent a new approach to lung surfactant therapy and a treatment for neonatal respiratory distress syndrome.

10.2.5. Drug Delivery Systems

Numerous fluorinated colloids have been investigated as drug delivery systems.⁴⁰⁶ Antibiotics, corticosteroids, and antitumor agents have been incorporated into apolar *HC-in-FC* emulsions stabilized by *FnHm* diblocks as the surfactant.¹³ Reverse water-in-*FC* emulsions have been investigated for drug delivery through the pulmonary route, including via metered-dose inhalers. *F8H2* was among the *FC*s investigated.³⁹⁰ *F8H2* was advocated for use in pulmonary applications, in particular because its positive spreading coefficient facilitates dispersion over the surface of the pulmonary alveolar membrane.⁴⁸

The stable highly concentrated gels, consisting of high internal phase ratio emulsions, described in section 9.3, used, among others, *F8H2* as the internal phase.³⁷⁸ Such gels could serve for topical applications. Further gels, but with a continuous *FC* phase, obtained by dispersing combinations of diblocks with phospholipids, have potential for topical use as low friction, gas-permeant, repellent dressings and barrier creams.²⁸⁸ Topical uses could also be found for the water-rich gel emulsions of $\text{F8CH}=\text{CH}_2$ and $\text{F4CH}=\text{CHF4}$.³⁸⁷

Targeted *FC* emulsions, traceable by ultrasound or MRI, are being investigated for drug delivery and other biomedical applications.^{455–458} The drug is primarily located in the droplet shell. The dissolving capacity of the dispersed *FC* for lipophilic drugs could be considerably augmented by use or adjunction of *FnHm* diblocks.

10.2.6. Contrast Agents for Diagnostic

Several internally iodinated diblocks of type $\text{FnCH}=\text{CIHm}$ have been evaluated both as contrast agents for X-ray radiography and for stabilizing emulsions of other radiopaque molecules. A series of *F*-alkylated bromo- and iodoethenes, including $\text{F6CI}=\text{CH}_2$, $\text{F6CBr}=\text{CBr}_2$, and $\text{FnCH}=\text{CIFn}'$ ($n = 2, 4, 6; m = 4, 6, 8$) showed the radiopacity expected from the presence of the heavy halogen atoms.¹²⁴ No degradation was detected after heating for 24 h at 121 °C with water. Effective and persistent contrast enhancement was achieved in the liver and spleen of rabbits after intravenous administration of an emulsion of $\text{F6CH}=\text{CIH6}$.⁴¹² The iodinated diblocks $\text{FnCH}=\text{CIHm}$ ($n = 6$ or 8; $m = 6$) have also been used to stabilize concentrated emulsions of $\text{F4CH}=\text{CIF4}$, according to the principles outlined in section 9.3.¹²³

Diblocks could also play a role in stabilizing and controlling the characteristics of parenterally injectable microbubbles that serve as contrast agents for ultrasound diagnosis, thrombolytic agents, and ultrasound-triggered drug delivery systems.³⁵⁵

10.3. Materials Science

Various hydrofluoroethers, including $\text{C}_4\text{F}_9\text{OCH}_3$ and $\text{C}_4\text{F}_9\text{OC}_2\text{H}_5$, have been developed in an effort to phase out *CFC*s and *HCFC*s. These ether diblocks have no ozone-depleting potential and an atmospheric lifetime of, respec-

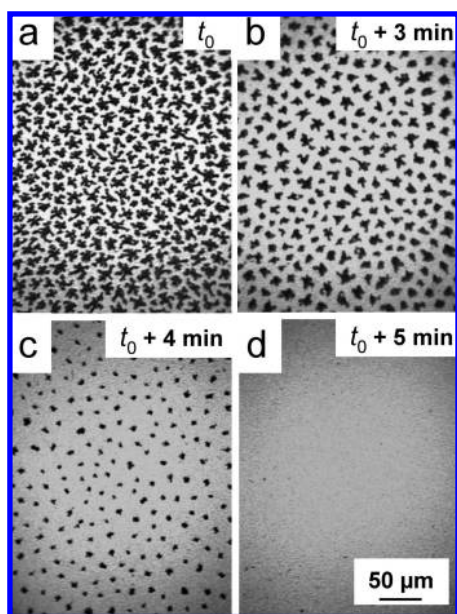


Figure 10.2. Dissolving rigid semicrystalline domains in a *DPPC* monolayer. Fluorescence images of a *DPPC* monolayer (the major lung surfactant component) compressed at 13 mN m^{-1} on water under N_2 (a, mimicking expiration) at 26 °C. The images were obtained using the fluorescent dye $\text{NBDC}_6\text{-HPC}$, which is preferentially soluble in the disordered regions of the monolayer. As a result, liquid expanded regions appear bright, while the semicrystalline liquid condensed domains appear dark. At time t_0 , the atmosphere of N_2 above the monolayer was saturated with *F8H2*. The *LC* domains disappeared rapidly (b, c). After 5 min, the monolayer was totally fluidized (d). From ref 333.

tively, about four years and one year only.⁴⁵⁹ They are now commercially available for use in metal and electronics cleaning, in lubricant deposition formulations, as heat transfer fluids, and as aerosol components. $(\text{CF}_3)_2\text{CFOCH}_3$ has been investigated as a new, chlorine-free cleaning solvent.²⁸⁰

The smectogenic character of the rigid-rod *F*-blocks confers to diblocks and multiblocks definite liquid crystal phase behavior (section 5). New mesophases with ferroelectric properties have been obtained from mixtures of polyphilic multibloc molecules.¹⁶⁸ These compounds were actually the first *nonchiral* compounds to form liquid crystals that exhibited ferroelectricity.⁴⁶⁰ Therefore, the mechanism for ferroelectricity is likely different from that at play in conventional chiral smectic phases.

(*F*-Alkyl)alkyl diblocks are known to promote and provide additional stability and sturdiness to self-assembled systems, as well as control over aggregation type, dimensions, and properties. Most nonfluorinated compounds are excluded from fluorinated domains.

Self-assemblies of *F_nH_m* diblocks have been used as templates to prepare functional nanoporous membranes.⁴⁶¹ In a first step the diblock (e.g., *F12H12*) was dissolved into a monomer (e.g., methacrylate). Cooling induced thermoreversible gelation of the diblock; the bundles of cylindrical aggregates (section 7) formed a template. Covalent cross-linking and polymerization were then initiated within the cold gel. The *F_nH_m* diblock was eventually extracted from the resulting resin with a suitable solvent (e.g., hexane), leaving a thermostable microporous polymer membrane. Pore size (7–145 nm) depended on diblock, diblock concentration, the temperature at which gelation was induced, and cooling rate. The reaction of methacrylate ester groups present on the pore walls allowed preparation of microporous polyelectrolyte membranes.

Surface patterning by self-assembly is sought after for the purpose of producing semiconductor integrated circuits, light-emitting displays (LEDs), photonic crystals, devices for data storage, special coatings for controlling cell growth, mobility and adhesion, tissue engineering, biosensor development, etc.⁴⁶² Regular arrays of surface micelles of *F_nH_m* diblocks, the radius of which can be preordained by adjusting the length of the *F*- and *H*-blocks, have provided a means of decorating surfaces with clusters of predetermined size in the nanometer range.^{309,310,315} Preliminary experiments have indicated that deposition of metals (e.g., Au and Ag) in the interstices between micelles transferred on a silicon wafer was possible. The template, once removed by evaporation or solvent leaching, left a regular pattern of metal dots.⁴⁶³

A series of diblock sulfides $(\text{C}_n\text{F}_{2n+1}\text{C}_m\text{H}_{2m})\text{S}$ and disulfides $(\text{C}_n\text{F}_{2n+1}\text{C}_m\text{H}_{2m}\text{S})_2$ has been prepared for self-assembled monolayer (SAM) studies.^{138,139}

Sensor engineering often involves embedding of the sensing molecule in a film that protects it and organizes its environment, thereby controlling its conformation and interactions. For example, constructs incorporating a monolayer of functionalized conjugated polydiacetylenic lipids fitted with carbohydrate residues afforded chromatic sensors for detection of receptor–ligand interactions.⁴⁶⁴ Addition of *F8H16* to 10,12-pentacosadiynoic acid (PDA) provided a means of precisely controlling the kinetics and yield of a PDA surface photopolymerization reaction in a Langmuir monolayer, thus allowing control of the chromatic properties of PDA and potentially useful in the preparation of chromatic sensor films.^{313,465}

A monolayer of *F6H18* has been used as a matrix for Gramicidin A, a polypeptide antibiotic that forms transmembrane ion channels, in view of transfer onto a solid support to serve as a biosensor for monovalent cation detection. Stable homogeneous mixed monolayers were obtained in which the peptide was protected from the environment (section 8.2).³³² Preliminary experiments indicated that, when admixed with the diblock, gramicidin could be transferred onto solid supports without losing its ion conducting properties.

Triblock disulfides $[\text{FnCH}_2\text{CH}_2\text{S}]_2$ **3.42** ($n = 6$ and 8) showed superior friction reducing properties on sliding surfaces.¹³⁸ *F_nH_m* diblocks, because they combine outstanding lubrication and water repellency properties, are being used in ski-wax preparations. The *H*-block facilitates incorporation in paraffinic wax preparations and provides adhesion to polyethylene ski soles. Commercial products incorporate *F_nH_m* diblocks with $n = 3–17$ and $m = 15–20$.⁴⁶⁶ Multiblocks with four *F*-blocks grafted on a six carbon branched central *H*-block,⁹⁸ as well as a series of *F_nH_mF_n* triblocks,¹²⁸ have also been synthesized for this purpose. The latter compounds exhibited surface energies comparable to those of *FC*s, but with lower melting points, which facilitates application of the wax on ski soles.

There is little doubt that *F_nH_m* diblocks and multiblocks will continue to intrigue scientists, producing new knowledge and useful applications. A strong case can be made for such diblocks when the specific functional properties of *F*-alkyl chains are needed, in view of their relative biological and environmental innocuousness among highly fluorinated amphiphiles.

11. Abbreviations

AFM	atomic force microscopy
AIBN	2,2'-azobis-(isobutyronitrile)
ARDS	acute respiratory distress syndrome
a.u.	arbitrary units
BAM	Brewster angle microscopy
BLM	black lipid membrane
BSA	bovine serum albumin
b.w.	body weight
CAC	critical aggregation concentration
CF	5,6-carboxyfluorescein
CFC	chlorofluorocarbon
CMC	critical micelle concentration
CRYO-TEM	cryogenic transmission electron microscopy
DLPC	dilauroyl- <i>sn</i> -glycero-3-phosphocholine
DMPC	dimyristoyl- <i>sn</i> -glycero-3-phosphocholine
DOPC	dioleoyl- <i>sn</i> -glycero-3-phosphocholine
DPPC	dipalmitoyl- <i>sn</i> -glycero-3-phosphocholine
DSPC	distearoyl- <i>sn</i> -glycero-3-phosphocholine
DSC	differential scanning calorimetry
ESRF	European Synchrotron Radiation Facility
EYP	egg yolk phospholipids
<i>F</i> -	perfluoro
<i>FC</i>	fluorocarbon
FDA	Food and Drug Administration (U.S.)
FF-TEM	freeze-fracture transmission electron microscopy
FID	free induction decay
FITS	(<i>F</i> -alkyl)phenyliodonium trifluoromethanesulfonate
FM	fluorescence microscopy
<i>F_n</i>	$\text{C}_n\text{F}_{2n+1}$
<i>F_nH_m</i>	$\text{C}_n\text{F}_{2n+1}\text{C}_m\text{H}_{2m+1}$
FT	Fourier transform
FTIR	Fourier transform infrared spectroscopy
GC	gas chromatography
GISAXS	grazing incidence small-angle X-ray scattering

H-	perhydro
HC	hydrocarbon
HFC	hydrofluorocarbon
HFE	hydrofluoroether
HIPRE	high internal phase ratio emulsion
Hm	C_mH_{2m+1}
HOPG	highly oriented pyrolytic graphite
i.v.	intravenous
LC	liquid condensed
LD	lethal dose
LE	liquid expanded
MAS NMR	magic-angle solid NMR
MD	molecular dynamics
MW	molecular weight
NMR	nuclear magnetic resonance
PBS	phosphate buffered saline
PLC8	dioctanoyl- <i>sn</i> -glycero-3-phosphocholine
PDA	10,12-pentacosadiynoic acid
PE	poly(ethylene)
PS	phosphatidylserine
PTFE	poly(tetrafluoroethylene)
PVDF	poly(vinylidene fluoride)
QELS	quasi-elastic light scattering
REACH	registration, evaluation, authorization, and restriction of chemicals
SANS	small-angle neutron scattering
SAXS	small-angle X-ray scattering
scCO ₂	supercritical CO ₂
SFM	scanning force microscopy (i.e., AFM)
SUV	small unilamellar vesicles
TEM	transmission electron microscopy
TMSC	temperature-modulated scanning calorimetry
UV	ultraviolet
WAXD	wide-angle X-ray diffraction

12. Acknowledgments

We thank Daniel Guillon and Bertrand Donnio (Institut de Physique et de Chimie des Matériaux de Strasbourg) for helpful discussions about liquid crystals. M.P.K. thanks her co-workers at the Institut Charles Sadron, and the Centre National de la Recherche Scientifique, for support.

13. References

- Haszeldine, R. N. *J. Chem. Soc.* **1949**, 285, 6–2861.
- Henne, A. L.; Nager, M. *J. Am. Chem. Soc.* **1951**, 73, 5527–5528.
- Brace, N. O. *J. Org. Chem.* **1962**, 27, 3033–3038.
- Tiers, G. V. D. *J. Org. Chem.* **1962**, 27, 2261–2262.
- Brace, N. O. *J. Fluorine Chem.* **1999**, 93, 1–25.
- Rabolt, J. F.; Russel, T. P.; Twieg, R. T. *Macromolecules* **1984**, 17, 2786–2794.
- Mahler, W.; Guillon, D.; Skoulios, A. *Mol. Cryst. Liq. Cryst. Lett.* **1985**, 2, 111–119.
- Reed, T. M. In *Fluorine Chemistry*; Simmons, J. H., Ed.; Academic Press: New York, 1964; Vol. 5, pp 133–221.
- Riess, J. G. *J. Drug Target.* **1994**, 2, 455–468.
- Smart, B. E. In *Organofluorine Chemistry: Principles and Commercial Applications*; Banks, R. E., Smart, B. E., Tatlow, J. C., Eds.; Plenum Press: New York, 1994; Chapter 3, pp 57–88.
- Smart, B. E. In *Chemistry of Organic Fluorine Compounds II*; Hudlicky, M., Pavlath, A. E., Eds.; American Chemical Society: Washington, DC, 1995; Chapter 6, pp 979–1010.
- Krafft, M. P.; Riess, J. G. *Biochimie* **1998**, 80, 489–514.
- Riess, J. G. *Tetrahedron* **2002**, 58, 4113–4131.
- Dunitz, J. D. *ChemBioChem* **2004**, 5, 614–621.
- Bondi, A. *J. Phys. Chem.* **1964**, 68, 441–451.
- Gang, O.; Ellmann, J.; Möller, M.; Kraak, H.; Sirota, E. B.; Ocko, B. M.; Deutsch, M. *Europhys. Lett.* **2000**, 49, 761–767.
- Ocko, B. M.; Wu, X. Z.; Sirota, E. B.; Sinha, S. K.; Gang, O.; Deutsch, M. *Phys. Rev. E* **1997**, 55, 3164–3182.
- Barton, S. W.; Goudot, A.; Bouloussa, O.; Rondelez, F.; Lin, B.; Novak, F.; Acero, A.; Rice, S. A. *J. Chem. Phys.* **1992**, 96, 1343–1351.
- Li, M.; Acero, A. A.; Huang, Z.; Rice, S. A. *Nature* **1994**, 367, 151–153.
- Takiue, T.; Vollhardt, D. *Colloids Surf., A: Physicochem. Eng. Aspects* **2002**, 198–200, 797–804.
- Tournilhac, F. G.; Bassoul, P.; Cortès, R. *Mol. Cryst. Liq. Cryst.* **2001**, 362, 45–65.
- Miller, T. M.; Bederson, B. *Adv. Atom. Mol. Phys.* **1978**, 13, 1–55.
- Pauling, L. *Nature of the Chemical Bond*, 3rd ed.; Cornell University Press: Ithaca, NY, 1960.
- Bunn, C. W.; Howells, E. R. *Nature* **1954**, 174, 549–551.
- Schwickert, H.; Strobl, G. R.; Kimmig, M. *J. Chem. Phys.* **1991**, 95, 2800–2808.
- Campos-Vallette, M.; Rey-Lafon, M. *J. Mol. Struct.* **1983**, 101, 23–45.
- Albrecht, T.; Elben, H.; Jaeger, R.; Kimmig, M.; Steiner, R.; Strobl, G.; Stühn, B.; Schwickert, H.; Ritter, C. *J. Chem. Phys.* **1991**, 95, 2807–2816.
- Knochenhauer, G.; Penacorada, F.; Reiche, J.; Barberka, T. A.; Brehmer, L.; Tredgold, R. H. *Mater. Sci. Eng. C* **1999**, 8–9, 231–235.
- Wang, J.; Ober, C. K. *Liq. Cryst.* **1999**, 26, 637–648.
- Piaggio, P.; Francese, P. G.; Masetti, G.; Dellepiane, G. *J. Mol. Struct.* **1975**, 26, 421–428.
- Knochenhauer, G.; Reiche, J.; Brehmer, L.; Barberka, T.; Woolley, M.; Tredgold, R.; Hodge, P. *J. Chem. Soc., Chem. Commun.* **1995**, 1619–1620.
- Strobl, G. R.; Schwickert, H.; Trzebiatowski, T. *Ber. Bunsen-Ges. Phys. Chem.* **1983**, 87, 274–279.
- Hildebrand, J. H.; Prausnitz, J. M.; Scott, R. L. *Regular and Related Solutions*; Van Nostrand Reinhold Co.: New York, 1970.
- Tanford, C. *The Hydrophobic Effect: Formation of Micelles and Biological Membranes*, 2nd ed.; Wiley: New York, 1980.
- Tiddy, G. J. T. In *Modern Trends of Colloid Science in Chemistry and Biology*; Eicke, H. F., Ed.; Birkhäuser Verlag: Basel, 1985; pp 148–159.
- Mukerjee, P. *Colloids Surf., A: Physicochem. Eng. Aspects* **1994**, 84, 1–10.
- Gao, J.; Qiao, S.; Whitesides, G. M. *J. Med. Chem.* **1995**, 38, 2292–2301.
- Mukerjee, P.; Handa, T. *J. Phys. Chem.* **1981**, 85, 2298–2303.
- Binks, B. P.; Fletcher, P. D. I.; Kotsev, S. N.; Thompson, R. L. *Langmuir* **1997**, 13, 6669–6682.
- Bedford, R. G.; Dunlap, R. D. *J. Am. Chem. Soc.* **1958**, 80, 282–285.
- Dunlap, R. D.; Bedford, R. G.; Woodbrey, J. C.; Furrow, S. D. *J. Am. Chem. Soc.* **1959**, 81, 2927–2930.
- Young, C. L. *Trans. Faraday Soc.* **1969**, 65, 2639–2644.
- Mukerjee, P. *J. Am. Oil Chem. Soc.* **1982**, 59, 573–578.
- Dorset, D. L. *Macromolecules* **1990**, 23, 894–901.
- Lo Nostro, P. *Adv. Colloid Interface Sci.* **1995**, 56, 245–287.
- Ringsdorf, H.; Schlarb, B.; Venzmer, J. *Angew. Chem., Int. Ed. Engl.* **1988**, 27, 113–158.
- Kunitake, T. *Angew. Chem., Int. Ed. Engl.* **1992**, 31, 709–726.
- Riess, J. G. *Colloids Surf., A: Physicochem. Eng. Aspects* **1994**, 84, 33–48.
- Fletcher, P. D. I. In *Specialist Surfactants*; Robb, I. D., Ed.; Blackie: London, 1997; Chapter 5, pp 104–140.
- Hoffmann, H.; Würtz, J. *J. Mol. Liq.* **1997**, 72, 191–230.
- Kissa, E. *Fluorinated Surfactants and Repellents*; Marcel Dekker: New York, 2001.
- Krafft, M. P. In *Handbook of Fluorous Chemistry*; Gladysz, J. A., Curran, D. P., Horvath, I. T., Eds.; Wiley-VCH: Weinheim, 2004; Chapter 12, pp 478–490.
- Krafft, M. P.; Riess, J. G. In *Advances in Fluorine Science—Fluorine and Health. Molecular Imaging, Biomedical Materials and Pharmaceuticals*; Tressaud, A., Haufe, G., Eds.; Elsevier: Amsterdam, 2008; Chapter 11, pp 447–486.
- Turberg, M. P.; Brady, J. E. *J. Am. Chem. Soc.* **1988**, 110, 7797–7801.
- Haszeldine, R. N. In *Fluorine—The First Hundred Years*; Banks, R. E., Sharp, D. W. A., Tatlow, J. C., Eds.; Elsevier Sequoia: Lausanne, 1986; pp 307–313.
- Dolbier, W. R. *Chem. Rev.* **1996**, 96, 1557–1584.
- Haszeldine, R. N. *Nature* **1951**, 167, 139–140.
- Haszeldine, R. N. *J. Chem. Soc.* **1953**, 3761–3768.
- Wakselman, C.; Lantz, A. In *Organofluorine Chemistry: Principles and Commercial Applications*; Banks, R. E., Smart, B. E., Tatlow, J. C., Eds.; Plenum Press: New York, 1994; Chapter 8, pp 177–194.
- Ameduri, B.; Boutevin, B. *Well-Architected Fluoropolymers: Synthesis, Properties and Applications*; Elsevier: Amsterdam, 2004.
- Napoli, M. *J. Fluorine Chem.* **1996**, 79, 59–69.
- Burton, D. J.; Kehoe, L. J. *J. Org. Chem.* **1970**, 35, 1339–1342.

- (63) von Werner, K. *J. Fluorine Chem.* **1985**, *28*, 229–233.
- (64) Chen, Q.-Y.; Yang, Z.-Y. *J. Chem. Soc., Chem. Commun.* **1986**, 498–499.
- (65) Calas, P.; Moreau, P.; Commeyras, A. *J. Chem. Soc., Chem. Commun.* **1982**, 433–434.
- (66) Andrieux, C. P.; Gélis, L.; Médebielle, M.; Pinson, J.; Savéant, J.-M. *J. Am. Chem. Soc.* **1990**, *112*, 3509–3520.
- (67) Médebielle, M.; Pinson, J.; Savéant, J.-M. *J. Am. Chem. Soc.* **1991**, *113*, 6872–6879.
- (68) Dapremont, C.; Calas, P.; Commeyras, A.; Amatore, C. *J. Fluorine Chem.* **1992**, *56*, 249–258.
- (69) Huang, W.-Y.; Zhang, H.-Z. *J. Fluorine Chem.* **1990**, *50*, 133–140.
- (70) Lumbierres, M.; Moreno-Manas, M.; Vallribera, A. *Tetrahedron* **2002**, *58*, 4061–4065.
- (71) Brace, N. O. *J. Org. Chem.* **1984**, *49*, 2361–2368.
- (72) Avila, D. V.; Ingold, K. U.; Luszyk, J.; Dolbier, W. R.; Pan, H.-Q.; Muir, M. *J. Am. Chem. Soc.* **1994**, *116*, 99–104.
- (73) Calas, P.; Gomez, C.; Amatore, C.; Commeyras, A. *J. Fluorine Chem.* **1990**, *49*, 247–261.
- (74) Brace, N. O. *J. Org. Chem.* **1966**, *31*, 2879–2885.
- (75) Brace, N. O. *J. Fluorine Chem.* **1999**, *96*, 101–127.
- (76) Brace, N. O.; Van Elswyk, J. E. *J. Org. Chem.* **1976**, *41*, 766–771.
- (77) Twieg, R. J.; Rabolt, J. F. *Macromolecules* **1988**, *21*, 1806–1811.
- (78) Lo Nostro, P.; Chen, S.-H. *J. Phys. Chem.* **1993**, *97*, 6535–6540.
- (79) van der Puy, M.; Poss, A. J.; Persichini, P. J.; Ellis, L. A. S. *J. Fluorine Chem.* **1994**, *67*, 215–224.
- (80) Brace, N. O. *J. Fluorine Chem.* **2001**, *108*, 147–175.
- (81) Rábai, J. In *Handbook of Fluorous Chemistry*; Gladysz, J. A., Curran, D. P., Horváth, I. T., Eds.; Wiley-VCH: Weinheim, 2004; Chapter 9, pp 156–174.
- (82) Umemoto, T.; Kuriu, Y.; Nakayama, S. *Tetrahedron Lett.* **1982**, *23*, 1169–1172.
- (83) Umemoto, T. *Chem. Rev.* **1996**, *96*, 1757–1777.
- (84) Le Blanc, M.; Riess, J. G.; Poggi, D.; Follana, R. *Pharm. Res.* **1985**, *2*, 246–248.
- (85) Napoli, M.; Conte, L.; Gambaretto, G. P. *J. Fluorine Chem.* **1997**, *85*, 163–167.
- (86) Brace, N. O. U.S. Patent 3,145,222, 1964.
- (87) Bloechl, W. Netherlands Patent 6,506,069, 1969.
- (88) Brace, N. O. *J. Org. Chem.* **1979**, *44*, 212–217.
- (89) Kuroboshi, M.; Ishihara, T. *J. Fluorine Chem.* **1988**, *39*, 299–303.
- (90) Davis, C. R.; Burton, D. J.; Yang, Z.-Y. *J. Fluorine Chem.* **1995**, *70*, 135–140.
- (91) Johansson, G.; Percec, V.; Ungar, G.; Zhou, J. P. *Macromolecules* **1996**, *29*, 646–660.
- (92) Coe, P. L.; Milner, N. E. *J. Organomet. Chem.* **1972**, *39*, 395–402.
- (93) Yagupolskii, L. M.; Maletina, I. I.; Kondratenko, N. V.; Orda, V. V. *Synthesis* **1978**, 835–837.
- (94) Napoli, M.; Conte, L.; Guerrato, A. *J. Fluorine Chem.* **2001**, *110*, 47–58.
- (95) Viney, C.; Russel, T. P.; Depero, L. E.; Twieg, R. J. *Mol. Cryst. Liq. Cryst.* **1989**, *168*, 63–82.
- (96) Araki, K.; Satoh, K.; Kondo, S. *Mol. Cryst. Liq. Cryst.* **1997**, *302*, 369–377.
- (97) Szlavik, Z.; Tárkányi, G.; Gömör, Á.; Rábai, J. *Org. Lett.* **2000**, *2*, 2347–2349.
- (98) Gambaretto, G.; Conte, L.; Fornasieri, F.; Zantonello, C.; Tonei, D.; Sassi, A.; Bertani, R. *J. Fluorine Chem.* **2003**, *121*, 57–63.
- (99) Bravo, A.; Borsvik, H.-R.; Fontana, F.; Liguori, L.; Mele, A.; Minisci, F. *J. Org. Chem.* **1997**, *62*, 7128–7136.
- (100) Escoula, B.; Rico, I.; Laval, J. P.; Lattes, A. *Synth. Commun.* **1985**, *15*, 35–38.
- (101) Haszeldine, R. N.; Leedham, K. *J. Chem. Soc.* **1952**, 3483–3490.
- (102) Cullen, W. R.; Waldman, M. C. *Can. J. Chem.* **1969**, *47*, 3093–3098.
- (103) Baum, K.; Bedford, C. D.; Hunadi, R. J. *J. Org. Chem.* **1982**, *47*, 2251–2257.
- (104) Fuchikami, T.; Ojima, I. *Tetrahedron Lett.* **1984**, *25*, 303–306.
- (105) Henne, A. L.; Nager, M. *J. Am. Chem. Soc.* **1951**, *73*, 1042–1043.
- (106) Le Blanc, M.; Santini, G.; Jeanneaux, F.; Riess, J. G. *J. Fluorine Chem.* **1976**, *7*, 525–530.
- (107) Bak, B.; Christensen, D.; Hansen-Nygaard, L.; Tannenbaum, E. *J. Chem. Phys.* **1957**, *26*, 241–243.
- (108) Probst, A.; Raab, K.; Ulm, K.; von Werner, K. *J. Fluorine Chem.* **1987**, *37*, 223–245.
- (109) Höpken, J.; Möller, M. *Macromolecules* **1992**, *25*, 2482–2489.
- (110) Broniatowski, M.; Dynarowicz-Latka, P. *J. Colloid Interface Sci.* **2006**, *299*, 916–923.
- (111) Dmowski, W.; Wozniacki, R. *J. Fluorine Chem.* **1987**, *36*, 385–394.
- (112) Boutevin, B.; Youssef, B.; Boileau, S.; Garnault, A. M. *J. Fluorine Chem.* **1987**, *35*, 399–410.
- (113) Boutevin, B.; Youssef, B. *J. Fluorine Chem.* **1989**, *44*, 395–412.
- (114) Höpken, J.; Möller, M.; Lee, M.; Percec, V. *Makromol. Chem.* **1992**, *193*, 275–284.
- (115) Höpken, J.; Möller, M.; Boileau, S. *New Polym. Mater.* **1991**, *2*, 339–356.
- (116) Huang, W.; Jin, C.; Derzon, D. K.; Huber, T. A.; Last, J. A.; Provencio, P. P.; Gopalan, A. S.; Dugger, M.; Sasaki, D. Y. *J. Colloid Interface Sci.* **2004**, *272*, 457–464.
- (117) Matsubara, H.; Yasuda, S.; Sugiyama, H.; Ryu, I.; Fujii, Y.; Kita, K. *Tetrahedron* **2002**, *58*, 4071–4076.
- (118) Szonyi, F.; Cambon, A. *J. Fluorine Chem.* **1989**, *42*, 59–68.
- (119) Crich, D.; Neelamkavil, S. *Org. Lett.* **2002**, *4*, 4175–4177.
- (120) Portella, C.; Shermolovich, Y. G.; Tschenn, O. *Bull. Soc. Chim. Fr.* **1997**, *134*, 697–702.
- (121) Vincent, J.-M.; Rabion, A.; Yachandra, V. K.; Fish, R. H. *Angew. Chem., Int. Ed. Engl.* **1997**, *36*, 2346–2349.
- (122) Alvey, L. J.; Meier, R.; Soós, T.; Bernatis, P.; Gladysz, J. A. *Eur. J. Inorg. Chem.* **2000**, *9*, 1975–1983.
- (123) Sanchez, V.; Greiner, J.; Riess, J. G. *J. Fluorine Chem.* **1995**, *73*, 259–264.
- (124) Sanchez, V.; Manfredi, A.; Greiner, J.; Riess, J. G. *Bull. Soc. Chim. Fr.* **1994**, *131*, 648–657.
- (125) Santini, G.; Le Blanc, M.; Riess, J. G. *J. Organomet. Chem.* **1975**, *102*, C21–24.
- (126) Brace, N. O. *J. Am. Chem. Soc.* **1964**, *86*, 523–524.
- (127) Delest, B.; Shtarev, A. B.; Dolbier, W. R. *Tetrahedron* **1998**, *54*, 9273–9280.
- (128) Conte, L.; Zaggia, A.; Sassi, A.; Seraglia, R. *J. Fluorine Chem.* **2007**, *128*, 493–499.
- (129) Le Blanc, M.; Riess, J. G. In *Oxygen Carrying Colloidal Blood Substitutes*; Frey, R., Beisbarth, H., Stossek, K., Eds.; Zuckschwerdt Verlag: München, 1982; pp 43–49.
- (130) Jeanneaux, F.; Le Blanc, M.; Riess, J. G.; Yokoyama, K. *Nouv. J. Chim.* **1984**, *8*, 251–257.
- (131) Santini, G.; Le Blanc, M.; Riess, J. G. *Tetrahedron* **1973**, *29*, 2411–2414.
- (132) Arlen, C.; Gauffreteau, Y.; Jeanneaux, F.; Le Blanc, M.; Riess, J. G. *Bull. Soc. Chim. Fr.* **1985**, 562–567.
- (133) Le Blanc, M.; Santini, G.; Guion, J.; Riess, J. G. *Tetrahedron* **1973**, *29*, 3195–3201.
- (134) Jeanneaux, F.; Santini, G.; Le Blanc, M.; Cambon, A.; Riess, J. G. *Tetrahedron* **1974**, *30*, 4197–4200.
- (135) Schulte, A.; Hallmark, V. M.; Twieg, R.; Song, K.; Rabolt, J. F. *Macromolecules* **1991**, *24*, 3901–3905.
- (136) McLoughlin, V. C. R.; Thrower, J. *Tetrahedron* **1969**, *25*, 5921–5940.
- (137) Dinkelmann, S.; Geister, U.; Röhlke, W.; Meinert, H.; Northoff, H. *Artif. Cells, Blood Substitutes, Immobil. Biotechnol.* **2001**, *29*, 71–83.
- (138) Brace, N. O. *J. Fluorine Chem.* **2000**, *105*, 11–23.
- (139) Naud, C.; Calas, P.; Blancou, H.; Commeyras, A. *J. Fluorine Chem.* **2000**, *104*, 173–183.
- (140) Rocaboy, C.; Gladysz, J. A. *Tetrahedron* **2002**, *58*, 4007–4014.
- (141) Anselmi, E.; Blazejewski, J. C.; Tordeux, M.; Wakselman, C. *J. Fluorine Chem.* **2000**, *105*, 41–44.
- (142) McLoughlin, V. C. R. *Tetrahedron Lett.* **1968**, *9*, 4761–4762.
- (143) Ameduri, B.; Boutevin, B. *J. Fluorine Chem.* **1999**, *100*, 97–116.
- (144) Cornélius, C.; Krafft, M. P. To be published.
- (145) de Gracia Lux, C.; Krafft, M. P. In preparation.
- (146) Wilson, L. M.; Griffin, A. C. *Macromolecules* **1993**, *26*, 6312–6314.
- (147) Pensec, S.; Tournilhac, F.-G.; Bassoul, P.; Durliat, C. *J. Phys. Chem. B* **1998**, *102*, 52–60.
- (148) Tournilhac, F.; Bosio, L.; Nicoud, J. F.; Simon, J. *Chem. Phys. Lett.* **1988**, *145*, 452–454.
- (149) Sanchez-Dominguez, M.; Benoit, N.; Krafft, M. P. *Tetrahedron* **2008**, *64*, 522–528.
- (150) Hirao, A.; Sugiyama, K.; Yokoyama, H. *Prog. Polym. Sci.* **2007**, *32*, 1393–1438.
- (151) *Organofluorine Chemistry: Principles and Commercial Applications*; Banks, R. E., Smart, B. E., Tatlow, J. C., Eds.; Plenum Press: New York, 1994.
- (152) Al-Ajda, G. N. D.; Beagley, B.; Jones, M. O. *J. Mol. Struct.* **1980**, *65*, 271–276.
- (153) Hariharan, A.; Harris, J. G. *J. Chem. Phys.* **1994**, *101*, 4156–4165.
- (154) Mahler, W. *Langmuir* **1991**, *7*, 3054–3056; cited by G. L. Gaines.
- (155) Shulman, R. G.; Dailey, B. P.; Townes, C. H. *Phys. Rev.* **1950**, *78*, 145–148.
- (156) Rudaya, M. N.; Saloutin, V. I.; Pashkevich, K. I. *Russ. Chem. Bull.* **1984**, *33*, 1653–1655.
- (157) El Abed, A.; Fauré, M.-C.; Pouzet, E.; Abillon, O. *Phys. Rev. E* **2002**, *65*, 051603-1-4.
- (158) El Abed, A. I.; Ionov, R.; Daoud, M.; Abillon, O. *Phys. Rev. E* **2004**, *70*, 51607-1-8.
- (159) Broniatowski, M.; Sandez Macho, I.; Minones, J.; Dynarowicz-Latka, P. *J. Phys. Chem. B* **2004**, *108*, 13403–13411.

- (160) Dynarowicz-Latka, P.; Pérez-Morales, M.; Munoz, E.; Broniatowski, M.; Martín-Romero, M. T.; Camacho, L. *J. Phys. Chem. B* **2006**, *110*, 6095–6100.
- (161) Goodwin, A. R. H.; Mehl, J. B. *Int. J. Thermophys.* **1997**, *18*, 795–806.
- (162) Burnett, M. K.; Zisman, W. A. *J. Phys. Chem.* **1963**, *67*, 1534–1540.
- (163) Vogel, V.; Möbius, D. *J. Colloid Interface Sci.* **1988**, *126*, 408–420.
- (164) Taylor, D. M.; Bayes, G. F. *Phys. Rev. E* **1994**, *49*, 1439–1449.
- (165) Shafirin, E. G.; Zisman, W. A. *J. Phys. Chem.* **1962**, *66*, 740–748.
- (166) Barriet, D.; Lee, T. R. *Curr. Opin. Colloid Interface Sci.* **2003**, *8*, 236–242.
- (167) Clément, C.; Thoai, N. *C. R. Acad. Sci. C. Paris* **1978**, *287*, 227–230.
- (168) Tournilhac, F. G.; Bosio, L.; Simon, J.; Blinov, L. M.; Yablonsky, S. V. *Liq. Cryst.* **1993**, *14*, 405–414.
- (169) Semenov, A. N.; González-Pérez, A.; Krafft, M. P.; Legrand, J.-F. *Langmuir* **2006**, *22*, 8703–8717.
- (170) Geppi, M.; Pizzanelli, S.; Veracini, C. A.; Cardelli, C.; Tombari, E.; Lo Nostro, P. *J. Phys. Chem. B* **2002**, *106*, 1598–1605.
- (171) Araki, K.; Satoh, K.; Kondo, S. *Mol. Cryst. Liq. Cryst.* **1996**, *281*, 123–134.
- (172) *Handbook of Fluorous Chemistry*; Gladysz, J. A., Curran, D. P., Horváth, I., Eds.; Wiley-VCH: Weinheim, 2004.
- (173) Freed, B. K.; Biesecker, J.; Middleton, W. J. *J. Fluorine Chem.* **1990**, *48*, 63–75.
- (174) Kabalnov, A. S.; Makarov, K. N.; Shcherbakova, O. V. *J. Fluorine Chem.* **1990**, *50*, 271–284.
- (175) Wilhelm, E.; Battino, R. *Chem. Rev.* **1973**, *73*, 1–9.
- (176) Riess, J. G.; Le Blanc, M. *Pure Appl. Chem.* **1982**, *54*, 2383–2406.
- (177) Lo Nostro, P.; Ku, C.; Chen, S.; Lin, J. *J. Phys. Chem.* **1995**, *99*, 10858–10864.
- (178) Yu, M. S.; Curran, D. P.; Nagashima, T. *Org. Lett.* **2005**, *7*, 3677–3680.
- (179) Kiss, L. E.; Kövesdi, I.; Rábai, J. *J. Fluorine Chem.* **2001**, *108*, 95–109.
- (180) Rosen, M. J. *CHEMTECH* **1985**, 292–298.
- (181) Sadtler, V. M.; Giulieri, F.; Krafft, M. P.; Riess, J. G. *Chem.—Eur. J.* **1998**, *10*, 1952–56.
- (182) Handa, T.; Mukerjee, P. *J. Phys. Chem.* **1981**, *85*, 3916–3920.
- (183) Gaines, G. L. *Langmuir* **1991**, *7*, 3054–3056.
- (184) Napoli, M.; Fraccaro, C.; Scipioni, A.; Alessi, P. *J. Fluorine Chem.* **1991**, *51*, 103–115.
- (185) Binks, B. P.; Fletcher, P. D. I.; Sager, W. F. C.; Thompson, R. L. *Langmuir* **1995**, *11*, 977–983.
- (186) Marczuk, P.; Lang, P.; Möller, M. *Colloids Surf.* **2000**, *163*, 103–113.
- (187) Marczuk, P.; Lang, P.; Findenegg, G. H.; Mehta, S. K.; Möller, M. *Langmuir* **2002**, *18*, 6830–6838.
- (188) Greiner, J.; Riess, J. G.; Vierling, P. In *Organofluorine Compounds in Medicinal Chemistry and Biomedical Applications*; Filler, R., Kobayashi, Y., Yagupolskii, L., Eds.; Elsevier: New York, 1993; pp 339–380.
- (189) Binks, B. P.; Fletcher, P. D. I.; Sager, W. F. C.; Thompson, R. L. *J. Mol. Liq.* **1997**, *72*, 177–190.
- (190) Hayami, Y.; Findenegg, G. H. *Langmuir* **1997**, *13*, 4865–4869.
- (191) Marie Bertilla, S.; Thomas, J.-L.; Marie, P.; Krafft, M. P. *Langmuir* **2004**, *20*, 3920–3924.
- (192) Trinh Dang, T. T.; Gerber, F.; Vandamme, T. F.; Krafft, M. P. In preparation.
- (193) Cornélus, C.; Krafft, M. P.; Riess, J. G. *J. Colloid Interface Sci.* **1994**, *163*, 391–394.
- (194) Le, T. D.; Arlauskas, R. A.; Weers, J. G. *J. Fluorine Chem.* **1996**, *78*, 155–163.
- (195) Grec, J.-J.; Riess, J. G.; Devallez, B. *Nouv. J. Chim.* **1985**, *9*, 637–643.
- (196) Riess, J. G.; Arlen, C.; Greiner, J.; Le Blanc, M.; Manfredi, A.; Pace, S.; Varescon, C.; Zarif, L. *Biomater. Artif. Cells Artif. Organs* **1988**, *16*, 421–430.
- (197) Solé-Violan, L.; Devallez, B. *New J. Chem.* **2004**, *28*, 1526–1530.
- (198) Dos Ramos, M. C.; Blas, F. J. *Mol. Phys.* **2007**, *105*, 1319–1334.
- (199) Morgado, P.; Tomas, R.; Zhao, H.; dos Ramos, M. C.; Blas, F. J.; McCabe, C.; Filipe, E. J. M. *J. Phys. Chem. C* **2007**, *111*, 15962–15968.
- (200) Langefeld, S.; Kirchhof, B.; Meinert, H.; Roy, T.; Aretz, A. *Graefes Arch. Clin. Exp. Ophthalmol.* **1999**, *237*, 201–206.
- (201) Meinert, H.; Roy, T. *Eur. J. Ophthalmol.* **2000**, *10*, 189–197.
- (202) Kim, Y. K.; Günther, B.; Meinert, H. *Eur. J. Ophthalmol.* **2005**, *15*, 627–637.
- (203) Rico-Lattes, I.; Quintyn, J. C.; Pagot-Mathis, V.; Benouaich, X.; Mathis, A. In *Advances in Fluorine Science—Fluorine and Health. Molecular Imaging, Biomedical Materials and Pharmaceuticals*; Tressaud, A., Haufe, G., Eds.; Elsevier: Amsterdam, 2008; Chapter 9, pp 407–420.
- (204) Solé-Violan, L.; Devallez, B.; Postel, M.; Riess, J. G. *New J. Chem.* **1993**, *17*, 581–583.
- (205) Wikramanayake, R.; Enick, R.; Turberg, M. *Fluid Phase Equilib.* **1991**, *70*, 107–118.
- (206) Iezzi, A.; Bendale, P.; Enick, R. N.; Turberg, M.; Brady, J. *Fluid Phase Equilib.* **1989**, *52*, 307–317.
- (207) Krafft, M. P.; Riess, J. G.; Weers, J. G. In *Submicronic Emulsions in Drug Targeting and Delivery*; Benita, S., Ed.; Harwood Academic Publishers: Amsterdam, 1998; Chapter 10, pp 235–333.
- (208) Arlauskas, R. A.; Weers, J. G. *Langmuir* **1996**, *12*, 1923–1925.
- (209) Devallez, B.; Gauffreteau, Y.; Le Blanc, M.; Riess, J. G. *J. Chim. Phys.* **1988**, *85*, 947–952.
- (210) Riess, J. G. *Chem. Rev.* **2001**, *101*, 2797–2920.
- (211) Hamza, M. A.; Serratrice, G.; Stébé, M. J.; Delpuech, J.-J. *J. Am. Chem. Soc.* **1981**, *103*, 3733–3738.
- (212) Pierotti, R. A. *Chem. Rev.* **1976**, *76*, 717–726.
- (213) Mathis, G.; Leempoel, P.; Ravey, J. C.; Selve, C.; Delpuech, J.-J. *J. Am. Chem. Soc.* **1984**, *106*, 6162–6171.
- (214) Cecutti, C.; Novelli, A.; Rico, I.; Lattes, A. *J. Dispersion Sci. Technol.* **1990**, *11*, 115–123.
- (215) Hoefling, T. A.; Enick, R. M.; Beckman, E. J. *J. Phys. Chem.* **1991**, *95*, 7127–7129.
- (216) Johnston, K. P.; Harrison, K. L.; Clarke, M. J.; Howdle, S. M.; Heitz, M. P.; Bright, F. V.; Carlier, C.; Randolph, T. W. *Science* **1996**, *271*, 624–626.
- (217) Eastoe, J.; Gold, S. *Phys. Chem. Chem. Phys.* **2005**, *7*, 1352–1362.
- (218) Lawson, D. D.; Moacanin, J.; Scherer, K. V.; Terranova, T. F.; Ingham, J. D. *J. Fluorine Chem.* **1978**, *12*, 221–236.
- (219) Deschamps, J.; Gomes, M. F. C.; Padua, A. A. H. *J. Fluorine Chem.* **2004**, *125*, 409–413.
- (220) Padua, A. A. H. *J. Phys. Chem. A* **2002**, *106*, 10116–10123.
- (221) Grec, J.-J.; Riess, J. G.; Devallez, B. *Nouv. J. Chim.* **1985**, *9*, 109–117.
- (222) Krafft, M. P.; Riess, J. G. *J. Polym. Sci., Part A: Polym. Chem.* **2007**, *45*, 1185–1198.
- (223) Fendler, J. H. *Membrane Mimetic Chemistry. Characterization and Applications of Micelles, Microemulsions, Monolayers, Bilayers and Vesicles, Host-Guest Systems*; John Wiley: New York, 1982.
- (224) Tanford, C. *The Hydrophobic Effect: Formation of Micelles and Biological Membranes*, 2nd ed.; Krieger Publishing Co.: Malabar, FL, 1991.
- (225) Gelbart, W. M.; Ben-Shaul, A.; Roux, D. *Micelles, Membranes, Microemulsions and Monolayers*; Springer-Verlag: New York, 1994.
- (226) Evans, D. F.; Wennerström, H. *The Colloidal Domain*, 2nd ed.; Wiley-VCH: Weinheim, 1999.
- (227) Krafft, M. P. *J. Polym. Sci., Part A: Polym. Chem.* **2006**, *44*, 4251–4258.
- (228) Fung, B. M.; Mamrosh, D. L.; O’Rear, E. A.; Fresh, C. B.; Afzal, J. *J. Phys. Chem.* **1988**, *92*, 4405–4411.
- (229) Oda, R.; Huc, I.; Danino, D.; Talmon, Y. *Langmuir* **2000**, *16*, 9759–9769.
- (230) Friedemann, R.; Naumann, S.; Brikmann, J. *Phys. Chem. Chem. Phys.* **2001**, *3*, 4195–4199.
- (231) Krafft, M. P.; Giulieri, F.; Riess, J. G. *Angew. Chem., Int. Ed. Engl.* **1993**, *32*, 741–743.
- (232) Giulieri, F.; Krafft, M. P.; Riess, J. G. *Angew. Chem., Int. Ed. Engl.* **1994**, *33*, 1514–1515.
- (233) Krafft, M. P.; Giulieri, F.; Riess, J. G. *Colloids Surf., A: Physicochem. Eng. Aspects* **1994**, *84*, 113–119.
- (234) Janulis, E. P.; Novack, J. C.; Papapolymerou, G. A.; Tristani-Kendra, M.; Huffman, W. A. *Ferroelectrics* **1988**, *85*, 375–384.
- (235) Arehart, V. V.; Pugh, C. *J. Am. Chem. Soc.* **1997**, *119*, 3027–3037.
- (236) Dahn, U.; Erdelen, C.; Ringsdorf, H.; Festag, R.; Wendorff, J. H.; Heiney, P. A.; Maliszewskij, N. C. *Liq. Cryst.* **1995**, *19*, 759–764.
- (237) Tschierske, C. *Chem. Soc. Rev.* **2007**, *36*, 1930–1970.
- (238) Lee, H.-Y.; Lee, K.-H.; Al-Hashimi, H. M.; Marsh, E. N. G. *J. Am. Chem. Soc.* **2006**, *128*, 337–343.
- (239) Son, S.; Tanrikulu, I. C.; Tirrell, D. A. *ChemBioChem* **2006**, *7*, 1251–1257.
- (240) Guillon, D.; Skoulios, A. *J. Phys. (Paris)* **1984**, *45*, 607–621.
- (241) Skoulios, A.; Guillon, D. *Mol. Cryst. Liq. Cryst.* **1998**, *165*, 317.
- (242) Friedel, G. *Ann. Phys. Fr.* **1922**, *18*, 273–474.
- (243) de Gennes, P.-G.; Prost, J. *The Physics of Liquid Crystals*, 2nd ed.; Clarendon Press: Oxford, 1993.
- (244) *Handbook of Liquid Crystals*; Demus, D., Goodby, J., Gray, G. W., Spiess, H.-W., Vill, V., Eds.; Wiley-VCH: Weinheim, 1998.
- (245) Dierking, I. *Textures of Liquid Crystals*; Wiley-VCH: Weinheim, 2003.
- (246) Ewen, B.; Strobl, G. R.; Richter, D. *Faraday Discuss. Chem. Soc.* **1980**, *69*, 19–31.
- (247) Doucet, J.; Denicolo, I.; Craievich, A. F.; Germain, C. *J. Chem. Phys.* **1984**, *80*, 1647–1651.

- (248) Sirota, E. B.; King, H. E., Jr.; Hughes, G. J.; Wan, W. K. *Phys. Rev. Lett.* **1992**, *68*, 492–495.
- (249) Mukherjee, P. K. *J. Chem. Phys.* **2000**, *113*, 4472–4474.
- (250) Sirota, E. B.; King, H. E., Jr.; Shao, H. H.; Singer, D. M. *J. Phys. Chem.* **1995**, *99*, 798–804.
- (251) Starkweather, H. W. *Macromolecules* **1986**, *19*, 1131–1134.
- (252) Kimmig, M.; Steiner, R.; Strobl, G.; Stühn, B. *J. Chem. Phys.* **1993**, *99*, 8105–8114.
- (253) Nakamura, N.; Uno, K.; Ogawa, Y. *Acta Crystallogr.* **2001**, *C57*, 585–586.
- (254) Russell, T. P.; Rabolt, J. F.; Twieg, R. T.; Siemens, R. L.; Farmer, B. L. *Macromolecules* **1986**, *19*, 1135–1143.
- (255) Höpken, J.; Pugh, C.; Richtering, W.; Möller, M. *Makromol. Chem.* **1988**, *189*, 911–925.
- (256) Marx, A.; Krüger, J. K.; Unruh, H.-G. *Z. Phys. B: Condens. Matter* **1989**, *75*, 101–107.
- (257) Mita, S.; Fujiwara, M.; Kondo, S. *Mol. Cryst. Liq. Cryst.* **1999**, *330*, 1281–1288.
- (258) Broniatowski, M.; Dynarowicz-Latka, P.; Witko, W. *Mol. Cryst. Liq. Cryst.* **2006**, *460*, 63–74.
- (259) Fujiwara, M.; Satoh, K.; Kondo, S.; Ujije, S. *Macromolecules* **2006**, *39*, 5836–5842.
- (260) Pugh, C.; Höpken, J.; Möller, M. *Polym. Prepr.* **1988**, *29*, 460–461.
- (261) Viney, C.; Twieg, R. J.; Russell, T. P. *Mol. Cryst. Liq. Cryst.* **1990**, *182B*, 291–297.
- (262) Viney, C.; Twieg, R. J.; Russell, T. P.; Depero, L. E. *Liq. Cryst.* **1989**, *5*, 1783–1788.
- (263) Marczuk, P.; Lang, P. *Macromolecules* **1998**, *31*, 9013–9018.
- (264) Ku, C.-Y.; Nostro, P. L.; Chen, S.-H. *J. Phys. Chem. B* **1997**, *101*, 908–914.
- (265) Chen, J. T.; Thomas, E. L.; Ober, C. K.; Hwang, S. S. *Macromolecules* **1995**, *28*, 1688.
- (266) Sun, W.-J.; Tristram-Nagle, S.; Suter, R. M.; Nagle, J. F. *Proc. Natl. Acad. Sci. U.S.A.* **1996**, *93*, 7008–7012.
- (267) Núñez, E.; Clark, C. G.; Cheng, W.; Best, A.; Floudas, G.; Semenov, A. N.; Fytas, G.; Müllen, K. *J. Phys. Chem.* **2008**, *112*, 6542–6549.
- (268) Dorset, D. L. *Chem. Phys. Lipids* **1977**, *20*, 13–19.
- (269) Starkweather, H. W.; Zoller, P.; Jones, G. A.; Vega, A. J. *J. Polym. Sci., B: Polym. Phys.* **1982**, *20*, 751–761.
- (270) Clark, E. S.; Muus, L. T. *Z. Kristallogr.* **1962**, *117*, 119–127.
- (271) Escobedo, F. A.; Chen, Z. *J. Chem. Phys.* **2004**, *121*, 11463–11473.
- (272) Fujiwara, M.; Satoh, K.; Mita, S. *Mol. Cryst. Liq. Cryst.* **2005**, *441*, 307–317.
- (273) Song, K.; Twieg, R. J.; Rabolt, J. F. *Macromolecules* **1990**, *23*, 3712–3714.
- (274) Viney, C.; Twieg, R. J.; Gordon, B. R.; Rabolt, J. F. *Mol. Cryst. Liq. Cryst.* **1991**, *198*, 285–289.
- (275) Marx, A.; Krüger, J. K.; Kirfel, A.; Unruh, H.-G. *Phys. Rev. B* **1990**, *42*, 6642–6650.
- (276) Davidson, T.; Griffin, A. C.; Wilson, L. M.; Windle, A. H. *Macromolecules* **1995**, *28*, 354–357.
- (277) Wilson, L. M. *Macromolecules* **1995**, *28*, 325–330.
- (278) Dietzmann, E.; Weissflog, W.; Markscheffel, S.; Jakli, A.; Lose, D.; Diele, S. *Ferroelectrics* **1996**, *180*, 341–354.
- (279) Beagley, B.; Jones, M. O.; Zanjanchi, M. A. *J. Mol. Struct.* **1979**, *56*, 215–219.
- (280) Tochigi, K.; Satou, T.; Kurihara, K.; Ochi, K.; Yamamoto, H.; Mochizuki, Y. *J. Chem. Eng. Data* **2001**, *46*, 913–917.
- (281) Morgado, P.; Zhao, H.; Blas, F. J.; McCabe, C.; Rebelo, L. P. N.; Filipe, E. J. M. *J. Phys. Chem. B* **2007**, *111*, 2856–2863.
- (282) Pierce, F.; Tsige, M.; Borodin, O.; Perahia, D.; Grest, G. S. *J. Chem. Phys.* **2008**, *128*, 214903.
- (283) Sloutskin, E.; Kraack, H.; Ocko, B.; Ellmann, J.; Möller, M.; Lo Nostro, P.; Deutsch, M. *Langmuir* **2002**, *18*, 1963–1967.
- (284) Fulton, J. L.; Pfund, D. M.; McClain, J. B.; Romack, T. J.; Maury, E. E.; Combes, J. R.; Samulski, E. T.; DeSimone, J. M.; Capel, M. *Langmuir* **1995**, *11*, 4241–4249.
- (285) Lo Nostro, P.; Santoni, I.; Bonini, M.; Baglioni, P. *Langmuir* **2003**, *19*, 2313–2317.
- (286) Twieg, R. J.; Russell, T. P.; Siemens, R.; Rabolt, J. F. *Macromolecules* **1985**, *18*, 1361–1362.
- (287) Rabolt, J. F.; Russell, T. P.; Siemens, R.; Twieg, R. J.; Farmer, B. *Polymer Prepr.* **1986**, *27*, 223–224.
- (288) Krafft, M. P.; Riess, J. G. French Patent 2,737,135, 1994.
- (289) Bothorel, P.; Such, C.; Clément, C. *J. Chim. Phys. Fr.* **1972**, *69*, 1453–1461.
- (290) Harkins, W. D. *The Physical Chemistry of Surface Films*; Reinhold Publishing Corp.: New York, 1952.
- (291) Davies, J. T.; Rideal, E. K. *Interfacial Phenomena*, 2nd ed.; Academic Press: New York, 1963.
- (292) Gaines, G. L. *Insoluble Monolayers at Liquid-Gas Interfaces*; Interscience: New York, 1966.
- (293) Knobler, C. M. *Adv. Chem. Phys.* **1990**, *77*, 397–449.
- (294) Adamson, A. W.; Gast, A. P. *Physical Chemistry of Surfaces*, 6th ed.; Wiley-Interscience: New York, 1997.
- (295) *Organized Monolayers and Assemblies: Structures, Processes and Function*; Möbius, D., Miller, R., Eds.; Elsevier: Amsterdam, 2002.
- (296) *Advanced Chemistry of Monolayers and Interfaces. Trends in Methodology and Technology*; Imae, T., Ed.; Academic Press: 2007.
- (297) Weinbach, S. P.; Weissbuch, I.; Kjaer, K.; Bouwman, W. G.; Als-Nielsen, J.; Lahav, M.; Leiserowitz, L. *Adv. Mater.* **1995**, *7*, 857–862.
- (298) Bibo, A. M.; Knobler, C. M.; Peterson, I. R. *J. Phys. Chem.* **1991**, *95*, 5591–5599.
- (299) Schwartz, D. K.; Knobler, C. M. *J. Phys. Chem.* **1993**, *97*, 8849–8851.
- (300) Dutta, P. In *Organized Monolayers and Assemblies: Structure, Processes and Function*; Möbius, D., Miller, R., Eds.; Elsevier: Amsterdam, 2002; Chapter 1, pp 1–12.
- (301) Helm, C. A.; Möhwald, H.; Kjaer, K.; Als-Nielsen, J. *Biophys. J.* **1987**, *52*, 381.
- (302) Jacquemain, D.; Wolf, S. G.; Leveiller, F.; Deutsch, M.; Kjaer, K.; Als-Nielsen, J.; Lahav, M.; Leiserowitz, L. *Angew. Chem., Int. Ed. Engl.* **1992**, *31*, 130–152.
- (303) Möhwald, H. In *Phospholipids Handbook*; Cevc, G., Ed.; Marcel Dekker: New York, 1993; Chapter 16, pp 579–602.
- (304) Krafft, M. P.; Giulieri, F.; Fontaine, P.; Goldmann, M. *Langmuir* **2001**, *17*, 6577–6584.
- (305) Krafft, M. P.; Goldmann, M. *Curr. Opin. Colloid Interface Sci.* **2003**, *8*, 243–250.
- (306) Fontaine, P.; Goldmann, M.; Muller, P.; Fauré, M.-C.; Kononov, O.; Krafft, M. P. *J. Am. Chem. Soc.* **2005**, *127*, 512–513.
- (307) Mourran, A.; Tartsch, B.; Gallyamov, M. O.; Magonov, S.; Lambrea, D.; Ostrovskii, B. I.; Dolbnya, I. P.; de Jeu, W. H.; Moeller, M. *Langmuir* **2005**, *21*, 2308–2316.
- (308) Kato, T.; Kameyama, M.; Ehara, M.; Limura, K. *Langmuir* **1998**, *14*, 1786–1798.
- (309) Maaloum, M.; Muller, P.; Krafft, M. P. *Angew. Chem., Int. Ed.* **2002**, *41*, 4331–4334.
- (310) Zhang, G.-F.; Marie, P.; Maaloum, M.; Muller, P.; Benoit, N.; Krafft, M. P. *J. Am. Chem. Soc.* **2005**, *127*, 10412–10419.
- (311) Huang, Z.; Acero, A. A.; Lei, N.; Rice, S. A.; Zhang, Z.; Schlossman, M. L. *J. Chem. Soc., Faraday Trans.* **1996**, *92*, 545–552.
- (312) El Abed, A.; Pouzet, E.; Fauré, M.-C.; Sanière, M.; Abillon, O. *Phys. Rev. E* **2000**, *62*, R5895–5898.
- (313) Wang, S.; Lunn, R.; Krafft, M. P.; Leblanc, R. M. *Langmuir* **2000**, *16*, 2882–2886.
- (314) Broniatowski, M.; Minones, J.; Dynarowicz-Latka, P. *J. Colloid Interface Sci.* **2004**, *279*, 552–558.
- (315) Zhang, G.; Maaloum, M.; Muller, P.; Benoit, N.; Krafft, M. P. *Phys. Chem. Chem. Phys.* **2004**, *6*, 1566–1569.
- (316) Gallyamov, M. O.; Mourran, A.; Tartsch, B.; Vinokur, R. A.; Nikitin, L. N.; Khokhlov, A. R.; Schaumburg, K.; Möller, M. *Phys. Chem. Chem. Phys.* **2006**, *8*, 2642–2649.
- (317) González-Pérez, A.; Contal, C.; Krafft, M. P. *Soft Matter* **2007**, *3*, 191–193.
- (318) Acero, A. A.; Li, M.; Lin, B.; Rice, S. A.; Goldmann, M.; Ben Azouz, I.; Goudot, A.; Rondelez, F. *J. Chem. Phys.* **1993**, *99*, 7214–7220.
- (319) Lehmler, H.; Oyewumi, M.; Jay, M.; Bummer, P. *J. Fluorine Chem.* **2001**, *107*, 141–146.
- (320) Broniatowski, M.; Dynarowicz-Latka, P. *J. Fluorine Chem.* **2004**, *125*, 1501–1507.
- (321) Broniatowski, M.; Sandez Macho, I.; Dynarowicz-Latka, P. *Thin Solid Films* **2005**, *493*, 249–257.
- (322) Demchak, R. J.; Fort, T. J. *J. Colloid Interface Sci.* **1974**, *46*, 191–202.
- (323) Davies, J. T.; Rideal, E. *Can. J. Chem.* **1955**, *33*, 947–960.
- (324) Fox, H. W. *J. Phys. Chem.* **1957**, *61*, 1058–1062.
- (325) El Abed, A. I.; Ionov, R.; Goldmann, M. *Phys. Rev. E* **2007**, *76*, 041606-1-7.
- (326) Kim, N.; Shin, S. *J. Chem. Phys.* **1999**, *110*, 10239–10242.
- (327) El Abed, A.; Fauré, M.-C.; Hamdani, M.; Guitard, F.; Billard, J.; Peretti, P. *Mol. Cryst. Liq. Cryst.* **1999**, *329*, 283–292.
- (328) Shibata, O.; Krafft, M. P. *Langmuir* **2000**, *16*, 10281–10286.
- (329) Vysotsky, Y. B.; Bryantsev, V. S.; Boldyreva, F. L.; Fainerman, V. B.; Vollhardt, D. *J. Phys. Chem. B* **2005**, *109*, 454–462.
- (330) Broniatowski, M.; Dynarowicz-Latka, P. *Langmuir* **2006**, *22*, 2691–2696.
- (331) Broniatowski, M.; Vila Romeu, N.; Dynarowicz-Latka, P. *J. Phys. Chem. B* **2006**, *110*, 3078–3087.
- (332) Broniatowski, M.; Suarez, M. N.; Vila Romeu, N.; Dynarowicz-Latka, P. *J. Phys. Chem. B* **2006**, *110*, 19450–19455.
- (333) Gerber, F.; Krafft, M. P.; Vandamme, T. F.; Goldmann, M.; Fontaine, P. *Biophys. J.* **2006**, *90*, 3184–3192.
- (334) Gerber, F.; Vandamme, T. F.; Krafft, M. P. *C. R. Acad. Sci. (Chimie)* **2009**, *12*, 180–187.

- (335) Krafft, M. P.; Cohen, J. A. Unpublished.
- (336) Simões Gamboa, A. L.; Filipe, E.; Brogueira, P. *Nano Lett.* **2002**, *2*, 1083–1086.
- (337) Maaloum, M.; Muller, P.; Krafft, M. P. *Langmuir* **2004**, *20*, 2261–2264.
- (338) Patrick, H. N.; Warr, G. G.; Manne, S.; Aksay, I. A. *Langmuir* **1999**, *15*, 1685–1692.
- (339) Kmetko, J.; Datta, A.; Evmenenko, G.; Dutta, P. *J. Phys. Chem. B* **2001**, *105*, 10818–10825.
- (340) Fontaine, P.; Goldmann, M.; Krafft, M. P.; Waton, G.; Bardin, L. To be published.
- (341) Riess, J. G.; Cornélus, C.; Follana, R.; Krafft, M. P.; Mahé, A. M.; Postel, M.; Zarif, L. *Adv. Exp. Med. Biol.* **1994**, *345*, 227–234.
- (342) Ferro, Y.; Krafft, M. P. *Biochim. Biophys. Acta* **2002**, *1581*, 11–20.
- (343) Schmutz, M.; Michels, B.; Marie, P.; Krafft, M. P. *Langmuir* **2003**, *19*, 4889–4894.
- (344) Trevino, L.; Frézard, F.; Rolland, J. P.; Postel, M.; Riess, J. G. *Colloids Surf., A: Physicochem. Eng. Aspects* **1994**, *88*, 223–233.
- (345) Trevino, L.; Krafft, M. P.; Frézard, F.; Giulieri, F.; Riess, J. G. *Proc. Int. Symp. Controlled Release Bioact. Mater.* **1994**, p 606–607.
- (346) Krafft, M. P.; Giulieri, F. *Am. Chem. Soc. Symp. Ser.* **2001**, *787*, 48–56.
- (347) Krafft, M. P.; Schieldknecht, L.; Marie, P.; Giulieri, F.; Schmutz, M.; Poulain, N.; Nakache, E. *Langmuir* **2001**, *17*, 2872–2877.
- (348) Lepault, J.; Pattus, F.; Martin, N. *Biochim. Biophys. Acta* **1985**, *820*, 315.
- (349) Sabin, J.; Ruso, J. M.; Gonzalez-Pérez, A.; Prieto, G.; Sarmiento, F. *Colloids Surf., B: Biointerfaces* **2006**, *47*, 64–70.
- (350) Trevino, L.; Frézard, F.; Postel, M.; Riess, J. G. *J. Liposome Res.* **1994**, *4*, 1017–1028.
- (351) Allen, T. M.; Cleland, L. G. *Biochim. Biophys. Acta* **1980**, *597*, 418–426.
- (352) Privitera, N.; Naon, R.; Riess, J. G. *Biochim. Biophys. Acta* **1995**, *1254*, 1–6.
- (353) Riess, J. G. *Curr. Opin. Colloid Interface Sci.* **2003**, *8*, 259–266.
- (354) Schutt, E. S.; Klein, D. H.; Mattrey, R. M.; Riess, J. G. *Angew. Chem., Int. Ed.* **2003**, *42*, 3218–3235.
- (355) Gerber, F.; Krafft, M. P. Unpublished.
- (356) Gerber, F.; Krafft, M. P.; Waton, G.; Vandamme, T. F. *New J. Chem.* **2006**, *30*, 524–527.
- (357) Riess, J. G.; Krafft, M. P. In *Blood Substitutes*; Winslow, R. M., Ed.; Elsevier: Amsterdam, 2006; Chapter 24, pp 259–275.
- (358) Clark, L. C.; Wesseler, E. P.; Miller, M. L.; Kaplan, S. *Microvasc. Res.* **1974**, *8*, 320–340.
- (359) Cecutti, C.; Rico, I.; Lattes, A.; Novelli, A.; Rico, A.; Marion, G.; Gracia, A.; Lachaise, J. *Eur. J. Med. Chem.* **1989**, *24*, 485–492.
- (360) Meinerth, H.; Knoblich, A. *Biomater. Artif. Cells Immob. Biotechnol.* **1993**, *21*, 583–595.
- (361) Riess, J. G.; Cornélus, C.; Krafft, M. P.; Postel, M. L.; Solé-Violan, L.; Trevino, L.; Zarif, L. In *Proceedings of the International Symposium on Blood Substitutes*; Vorobyev, S. I.; Ivanitsky, G. R., Ed.; Russian Academy of Sciences: Pushchino, 1994.
- (362) Davis, S. S.; Round, H. P.; Purewal, T. S. *J. Colloid Interface Sci.* **1981**, *80*, 508–511.
- (363) Riess, J. G. *Artif. Organs* **1984**, *8*, 44–56.
- (364) Kabalnov, A. S.; Aprosina, Y. D.; Pavlova-Verevkina, O. B.; Pertsov, A. V.; Shchukin, E. D. *Kolloidn. Zh. Acad. Nauk. U.S.S.R.* **1986**, *58*, 27–32.
- (365) Kabalnov, A. S.; Shchukin, E. D. *Adv. Colloid Interface Sci.* **1992**, *38*, 69–97.
- (366) Varescon, C.; Arlen, C.; Le Blanc, M.; Riess, J. G. *J. Chim. Phys.* **1989**, *86*, 2111–2117.
- (367) Trevino, L.; Solé-Violan, L.; Daumur, P.; Devallez, B.; Postel, M.; Riess, J. G. *New J. Chem.* **1993**, *17*, 275–278.
- (368) Weers, J. G.; Arlauskas, R. A. *Langmuir* **1995**, *11*, 474–477.
- (369) Lifshitz, I. M.; Slezov, V. V. *Sov. Phys. J. Phys.* **1959**, *35*, 331–339.
- (370) Higuchi, W. I.; Misra, J. *J. Pharm. Sci.* **1962**, *51*, 459–466.
- (371) Kabalnov, A. S.; Aprosina, Y. D.; Pavlova-Verevkina, O. B.; Pertsov, A. V.; Shchukin, E. D. (*translated from*) *Kolloidn. Zh.* **1986**, *48*, 27–32.
- (372) Weers, J. G.; Liu, J.; Fields, T.; Resch, P.; Cavin, J.; Arlauskas, R. A. *Artif. Cells, Blood Substitutes, Immob. Biotechnol.* **1994**, *22*, 1175–1182.
- (373) Riess, J. G.; Greiner, J. *Carbohydr. Res.* **2000**, *327*, 147–168.
- (374) Riess, J. G.; Solé-Violan, L.; Postel, M. *J. Disp. Sci. Technol.* **1992**, *13*, 349–355.
- (375) Riess, J. G.; Krafft, M. P. *Chem. Phys. Lipids* **1995**, *75*, 1–14.
- (376) Riess, J. G.; Weers, J. G. *Curr. Opin. Colloid Interface Sci.* **1996**, *1*, 652–659.
- (377) Cornélus, C.; Krafft, M. P.; Riess, J. G. *Artif. Cells, Blood Substitutes, Immob. Biotechnol.* **1994**, *22*, 1183–1191.
- (378) Krafft, M. P.; Riess, J. G. *Angew. Chem., Int. Ed. Engl.* **1994**, *33*, 1100–1101.
- (379) Riess, J. G. *Biomater. Artif. Cells Immob. Biotechnol.* **1992**, *20*, 183–202.
- (380) Marie Bertilla, S.; Marie, P.; Krafft, M. P. In *Artificial Oxygen Carriers: Its Frontline*; Keio Univ. Int. Symp. Life Sci. Med. Series, Vol. 12; Springer: Tokyo, Japan, 2005; pp 237–251.
- (381) Peña, A. A.; Miller, C. A. *Adv. Colloid Interface Sci.* **2006**, *123*, 241–257.
- (382) Weers, J. G. In *Modern Aspects of Emulsion Science*; Binks, B. P., Ed.; The Royal Society of Chemistry: Cambridge, U.K., 1998; Chapter 9, pp 292–327.
- (383) Krafft, M. P.; Cornélus, C.; Riess, J. G. Unpublished.
- (384) Cornélus, C.; Krafft, M. P.; Riess, J. G. *Artif. Cells, Blood Substitutes, Immob. Biotechnol.* **1994**, *22*, 1267–1272.
- (385) Kabalnov, A.; Weers, J.; Arlauskas, R.; Tarara, T. *Langmuir* **1995**, *11*, 2966–2974.
- (386) Ceschin, C.; Roques, J.; Malet-Martino, M. C.; Lattes, A. *J. Chem. Technol. Biotechnol.* **1985**, *35A*, 73–82.
- (387) Ravey, J. C.; Stébé, M. *Prog. Colloid Polym. Sci.* **1990**, *82*, 218–228.
- (388) Olla, M.; Monduzzi, M.; Ambrosone, L. *Colloids Surf., A* **1999**, *160*, 23–36.
- (389) Krafft, M. P.; Dellamary, L.; Tarara, T.; Riess, J. G.; Trevino, L. PCT WO 97/21425, 1997.
- (390) Sadtler, V. M.; Krafft, M. P.; Riess, J. G. *Angew. Chem., Int. Ed. Engl.* **1996**, *35*, 1976–1978.
- (391) Sadtler, V. M.; Krafft, M. P.; Riess, J. G. *Colloids Surf., A* **1999**, *147*, 309–315.
- (392) Riess, J. G.; Krafft, M. P. *Biomaterials* **1998**, *19*, 1529–1539.
- (393) McCulloch, A. *J. Fluorine Chem.* **2003**, *123*, 21–29.
- (394) Wallington, T. J.; Schneider, W. F.; Sehested, J.; Bilde, M.; Platz, J.; Nielsen, O. J.; Christensen, L. K.; Molina, M. J.; Molina, L. T.; Wooldridge, P. W. *J. Phys. Chem. A* **1997**, *101*, 8264–8274.
- (395) Tsai, W.-T. *J. Hazardous Mater.* **2005**, *A119*, 69–78.
- (396) Shine, K. P.; Gohar, L. K.; Hurley, M. D.; Marston, G.; Martin, D.; Simmonds, P. G.; Wallington, T. J.; Watkins, M. *Atmos. Environ.* **2005**, *39*, 1759–1763.
- (397) Horváth, I. T. *Acc. Chem. Res.* **1998**, *31*, 641–650.
- (398) Gladysz, J. A.; Curran, D. P. Fluorous Chemistry, a Special Issue of *Tetrahedron*, 2002.
- (399) Curran, D. P. *Science* **2008**, *321*, 1645–1646.
- (400) Curran, D. P.; Zhang, Q.; Richard, C.; Lu, H.; Gudipati, V.; Wilcox, C. S. *J. Am. Chem. Soc.* **2006**, *128*, 9561–9573.
- (401) Fukuyama, T.; Arai, M.; Matsubara, H.; Ryu, I. *J. Org. Chem.* **2004**, *69*, 8105–8107.
- (402) 2403; Lehn, J.-M. *Chem. Soc. Rev.* **2007**, *36*, 151–160.
- (403) Maruyama, T.; Kotani, T.; Yamamura, H.; Kamiya, N.; Goto, M. *Org. Biomol. Chem.* **2004**, *2*, 524–527.
- (404) Gerber, F.; Krafft, M. P.; Vandamme, T. F.; Goldmann, M.; Fontaine, P. *Angew. Chem., Int. Ed.* **2005**, *44*, 2749–2752.
- (405) Brubach, J.-B.; Mermet, A.; Filabozzi, A.; Gerschel, A.; Lairez, D.; Krafft, M. P.; Roy, P. *J. Phys. Chem. B* **2001**, *105*, 430–435.
- (406) Krafft, M. P. *Adv. Drug Delivery Rev.* **2001**, *47*, 209–228.
- (407) Riess, J. G. In *Handbook of Fluorous Chemistry*; Gladysz, J. A., Curran, D. P., Horváth, I., Eds.; Wiley-VCH: Weinheim, 2004.
- (408) Riess, J. G.; Pace, S.; Zarif, L. *Adv. Mater.* **1991**, *3*, 249–251.
- (409) Mahé, A. M.; Manoux, J.; Valla, A.; Follana, R.; Zarif, L.; Greiner, J.; Vierling, P.; Riess, J. G. *Biomater. Artif. Cells Immob. Biotechnol.* **1992**, *20*, 1025–1027.
- (410) Cook, E. W.; Pierce, J. S. *Nature* **1973**, *242*, 337–338.
- (411) Menz, D.-H.; Dresch, J. H. In *Advances in Fluorine Science: Fluorine and Health*; Tressaud, A., Haufe, G., Eds.; Elsevier: Amsterdam, 2008; Chapter 10, pp 421–445.
- (412) Sanchez, V.; Zarif, L.; Greiner, J.; Riess, J. G.; Cippolini, S.; Bruneton, J. N. *Artif. Cells, Blood Substitutes, Immob. Biotechnol.* **1994**, *22*, 1421–1428.
- (413) Mathy-Hartert, M.; Krafft, M. P.; Deby, C.; Deby-Dupont, G.; Meurisse, M.; Lamy, M.; Riess, J. G. *Artif. Cells, Blood Substitutes, Immob. Biotechnol.* **1997**, *25*, 563–575.
- (414) DeRoover, A.; Krafft, M. P.; Deby-Dupont, G.; Riess, J. G.; Jacquet, N.; Lamy, M.; Meurisse, M.; D'Silva, M. *Artif. Cells, Blood Substitutes, Immob. Biotechnol.* **2001**, *29*, 225–234.
- (415) Baker, M. H.; Foster, A. B.; Hegedus, L.; Jarman, M.; Rowlands, M. G.; Coe, P. L.; Troth, J. *Biomed. Mass Spectrom.* **1984**, *11*, 512–521.
- (416) Obratsov, V. V.; Kabalnov, A. S.; Sklifas, A. N.; Makarov, K. N. *Biophysics* **1992**, *37*, 298–302.
- (417) Zarif, L.; Postel, M.; Septe, B.; Trevino, L.; Riess, J. G.; Mahé, A.-M.; Follana, R. *Pharm. Res.* **1994**, *11*, 122–127.
- (418) Dellacherie, E.; Labrude, P.; Vigneron, C.; Riess, J. G. *Crit. Rev. Ther. Drug Carrier Syst.* **1987**, *3*, 41–94.
- (419) Riess, J. G. *La Trasfusione del Sangue* **1987**, *32*, 316–334.
- (420) Riess, J. G. In *Fluorine at the Millennium*; Banks, R. E., Ed.; Elsevier: Amsterdam, 2000; Chapter 23, pp 385–431.

- (421) Krafft, M. P.; Chittofrati, A.; Riess, J. G. *Curr. Opin. Colloid Interface Sci.* **2003**, *8*, 251–258.
- (422) Ho, J.; Sibbald, W. J.; Chin-Yee, I. H. *Crit. Care Med.* **2003**, *31* (Suppl.), S687–S697.
- (423) Bennett-Guerrero, E.; Veldman, T. H.; Doctor, A.; Telen, M. J.; Ortel, T. L.; Reid, T. S.; Mulherin, M. A. H.; Zhu, R. D. B.; Califf, R. M.; McMahon, T. J. *Proc. Natl. Acad. Sci. U. S. A.* **2007**, *104*, 17063–17068.
- (424) Silliman, C. C.; Ambruso, D. R.; Boshkof, L. K. *Blood* **2005**, *105*, 2266–2273.
- (425) Vamvakas, E. C.; Blajchman, M. A. *Blood Rev.* **2007**, *21*, 327–348.
- (426) Tinmouth, A.; Fergusson, D.; Yee, I. C.; Hébert, P. C. *Transfusion* **2006**, *46*, 2014–2027.
- (427) Koch, C. G.; Li, L.; Sessler, D. I.; Figueroa, P.; Hoeltge, G. A.; Mihaljevic, T.; Blackstone, E. H. *New Engl. J. Med.* **2008**, *358*, 1229–1239.
- (428) Marik, P. E.; Corwin, H. L. *Crit. Care Med.* **2008**, *36*, 2667–2674.
- (429) Riess, J. G.; Dalfors, J. L.; Hanna, G. K.; Klein, D. H.; Krafft, M. P.; Pelura, T. J.; Schutt, E. G. *Biomater. Artif. Cells Immob. Biotechnol.* **1992**, *20*, 839–842.
- (430) Riess, J. G.; Krafft, M. P. *Adv. Exp. Med. Biol.* **1992**, *317*, 465–472.
- (431) Voiglio, E. J.; Zarif, L.; Gorry, F. C.; Krafft, M. P.; Margonari, J.; Martin, X.; Riess, J. G.; Dubernard, J. M. *J. Surg. Res.* **1996**, *63*, 439–446.
- (432) Sanchez-Dominguez, M.; Krafft, M. P.; Maillard, E.; Siegrist, S.; Belcourt, A. *ChemBioChem* **2006**, *7*, 1160–1163.
- (433) Audonnet-Blaise, S.; Krafft, M. P.; Smani, Y.; Mertes, P.-M.; Marie, P.-Y.; Labrude, P.; Longrois, D.; Menu, P. *Resuscitation* **2006**, *70*, 124–132.
- (434) Haiss, F.; Jolivet, R.; Wyss, M. T.; Reichold, J.; Scheffold, F.; Krafft, M. P.; Weber, B. Submitted.
- (435) Lattes, A.; Rico-Lattes, I. *Artif. Cells, Blood Substitutes, Immob. Biotechnol.* **1994**, *22*, 1007–1018.
- (436) Brandhorst, H.; Muehling, B.; Yamaya, H.; Henriksnaes, J.; Carlsson, P. O.; Korsgren, O.; Brandhorst, D. *Transplant. Proc.* **2008**, *40*, 393–394.
- (437) Peyman, G. A.; Schulman, J. A.; Sullivan, B. *Surv. Ophthalmol.* **1995**, *39*, 375–395.
- (438) Colthurst, M. J.; Williams, R. L.; Hiscott, P. S.; Grierson, I. *Biomaterials* **2000**, *21*, 649–665.
- (439) Wong, D.; Lois, N. *Sem. Ophthalmol.* **2000**, *15*, 25–35.
- (440) Stolba, U.; Krepler, K.; Velikay-Parel, M.; Binder, S. *Graefe's Arch. Clin. Exp. Ophthalmol.* **2004**, *242*, 931–936.
- (441) Kirchhof, B.; Wong, D.; Van Meurs, J. C.; Hilgers, R. D.; Macek, M.; Lois, N.; Schrage, N. F. *Am. J. Ophthalmol.* **2002**, *133*, 95–101.
- (442) Roeder, J.; Hoerauf, H.; Kobuch, K.; Gabel, V.-P. *Graefe's Arch. Clin. Exp. Ophthalmol.* **2002**, *240*, 965–971.
- (443) Vote, B.; Wheen, L.; Cluroe, A.; Teoh, H.; McGeorge, A. *Clin. Exp. Ophthalmol.* **2003**, *31*, 408–414.
- (444) Schatz, B.; El-Shabrawi, Y.; Haas, A.; Langmann, G. *Retina* **2004**, *24*, 567–573.
- (445) Hoerauf, H.; Roeder, J.; Kobuch, K.; Laqua, H. *Retina* **2005**, *25*, 479–488.
- (446) Wong, D.; Williams, R.; Stappler, T.; Groenewald, C. *Graefe's Arch. Clin. Exp. Ophthalmol.* **2005**, *243*, 474–477.
- (447) Mackiewicz, J.; Maaijwee, K.; Lüke, C.; Kociok, N.; Hiebl, W.; Meinert, H.; Jousseen, A. M. *Graefe's Arch. Clin. Exp. Ophthalmol.* **2007**, *245*, 665–675.
- (448) Klär-Dissars, U.; Hoerauf, H. *Graefe's Arch. Clin. Exp. Ophthalmol.* **2004**, *242*, 218–222.
- (449) Wolf, S.; Schon, V.; Meier, P.; Wiedemann, P. *Retina* **2003**, *23*, 335–342.
- (450) Pagot-Mathis, V.; Benouaich, X.; Mathis, A.; Rico-Lattes, I.; Dumoulin, A. *J. Franc. Ophthalmol.* **2006**, *29*, 137–145.
- (451) Theelen, T.; Tilanus, M. A. D.; Klevering, B. J. *Graefe's Arch. Clin. Exp. Ophthalmol.* **2004**, *242*, 617–620.
- (452) Wong, D.; Van Meurs, J. C.; Stappler, T.; Groenewald, C.; Pearce, I. A.; McGalliard, J. N.; Manousakis, E.; Herbert, E. N. *Br. J. Ophthalmol.* **2005**, *89*, 662–665.
- (453) Mackiewicz, J.; Mühling, B.; Hiebl, W.; Meinert, H.; Maaijwee, K.; Kociok, N.; Lüke, C.; Zagorski, Z.; Kirchhof, B.; Jousseen, A. M. *Invest. Ophthalmol. Vis. Sci.* **2007**, *48*, 1873–1883.
- (454) Gerber, F.; Krafft, M. P.; Vandamme, T.; van Ryn, J.; Jung, B. In preparation.
- (455) Cyrus, T.; Winter, P. M.; Caruthers, S. D.; Wickline, S. A.; Lanza, G. M. *Future Drugs—Expert Rev. Cardiovasc. Ther.* **2005**, *3*, 705–715.
- (456) Morawski, A. M.; Lanza, G. A.; Wickline, S. A. *Curr. Opin. Biotechnol.* **2005**, *16*, 89–92.
- (457) Winter, P. M.; Cai, K.; Caruthers, S. D.; Wickline, S. A.; Lanza, G. M. *Expert Rev. Med. Devices* **2007**, *4*, 137–145.
- (458) Soman, N. R.; Lanza, G. M.; Heuser, J. M.; Schlesinger, P. H.; Wickline, S. A. *Nano Lett.* **2008**, *8*, 1131–1136.
- (459) Koenig, T.; Owens, J. G. *Proc. Int. Conf. Ozone Protection Technol., St-Paul, MN 1996*, 1–8.
- (460) Tournilhac, F.; Blinov, L. M.; Simon, J.; Yablonsky, S. V. *Nature* **1992**, *359*, 621–623.
- (461) Gankema, H.; Hempenius, M. A.; Möller, M.; Johansson, G.; Percec, V. *Macromol. Symp.* **1996**, *102*, 381–390.
- (462) Gates, B. D.; Xu, Q.; Stewart, M.; Ryan, D.; Willson, C. G.; Whitesides, G. M. *Chem. Rev.* **2005**, *105*, 1171–1196.
- (463) Charraut, E.; Muller, P.; Maaloum, M.; Krafft, M. P.; Petit, C.; Petit, P. *Journées Matière Condensée, Société Française de Physique, Nancy, France, 2004*.
- (464) Charych, D. H.; Nagy, J. O.; Spevak, W.; Bednarski, M. D. *Science* **1993**, *261*, 585–588.
- (465) Charych, D. H.; Cheng, Q.; Reichert, A.; Kuziemko, G.; Stroh, M.; Nagy, J. O.; Spevak, W.; Stevens, R. C. *Chem. Biol.* **1996**, *3*, 113.
- (466) Rogowski, I.; Gauvrit, J.-Y.; Léonard, D.; Lanteri, P. *Cold Regions Sci. Technol.* **2005**, *43*, 140–149.
- (467) Chandra Sekhar, G.; Venkatesu, P.; Hofman, T.; Prabhakara Rao, M. V. *Fluid Phase Equilib.* **2002**, *201*, 219–231.
- (468) Gonzalez, P.; Hackney, A. C.; Jones, S.; Strayhorn, D.; Hoffman, E. B.; Hughes, G.; Jacobs, E. E.; Orringer, E. P. *J. Invest. Med.* **1997**, *45*, 258–264.
- (469) Gonzalez-Pérez, A.; Contal, C.; Benoit, N.; Krafft, M. P. To be published.
- (470) Riess, J. G.; Krafft, M. P. Unpublished.
- (471) Riess, J. G. *New J. Chem.* **1995**, *19*, 891–909.

CR800260K